Biophysical studies on the structure-function relationship of membrane-active peptides.



Marc-Philipp Pfeil

St Edmund Hall

University of Oxford

A thesis submitted for the degree of

Doctor of Philosophy

Trinity 2016

Abstract

It is becoming evident that protein conformation and function are sensitive to the local environment. Structural models are often reported, out of technical necessity, in environments only partially related to the native environment of the protein of interest. This is a major challenge for structural biology of membrane proteins, which are predicted to be highly sensitive to their local environment. The structural plasticity of membrane-active alpha helical peptides and proteins is explored in native-like model membranes in this thesis. On the one hand, alpha helical antimicrobial peptides (AMPs) and their destructive membrane insertion mode are characterised, and on the other, the viroporin p7 (Hepatitis C Virus), expected to form oligomeric channels, is investigated in a endoplasmic reticulum mimicking model membrane.

(I) AMPs: An engineering approach, which alters the antimicrobial insertion motif, is used to characterise distinct structure-function relationships linked between the primary and secondary peptide structures. Data is presented on different timescales and resolutions in order to understand the direct peptide location and orientation with respect to the membrane normal using solid-state NMR. Equally important are the global effects on the membrane bilayer and bacteria examined using atomic force microscopy (AFM) and fluorescence microscopy. Detailed dynamical changes and membrane order are explored by continuous wave EPR and solid-state NMR. Design principles that altered a pore-forming transmembrane AMP into a sequence that develops its potency in the membrane interface and shows broad-spectrum antimicrobial activity are reported.

(II) Different structural models of p7 have been reported in the literature, most of which are in a detergent or organic solvent environment. A single-constraint approach is presented in order to probe their plausibility in an endoplasmic reticulum-like model membrane using pulsed EPR. This is combined with angular constraints from solid-state NMR experiments in the same membrane composition. The results point towards an ensemble hairpin structure in the environment probed. Further to this, the drug-membrane interaction of the p7 inhibitor, *N*N-DNJ (an iminosugar), is investigated, and a membrane interaction is observed with a pK_a of 6.3 for the membrane-partitioned inhibitor.

Both systems are described in simplified models. While not yielding high resolution structures, these models are still an important consideration for the understanding of protein

structure, topology and oligomerisation, which directly relates to protein function. The functionalities of the two systems explored in this thesis differ significantly, AMPs are naturally occurring antibiotics that compromise membrane integrity, whereas p7, with a defined channel architecture, is essential to the viral life cycle of Hepatitis C Virus. Hence, a structural spectrum of membrane-activity with relevance to infectious diseases is explored.

Acknowledgements

I would like to thank my supervisor Prof Anthony Watts for supporting this D. Phil thesis and the presented work therein. I am grateful for his optimism, the scientific freedom and associated trust to allow me to develop and follow up my own ideas. He always provided very constructive feedback and highly valued guidance throughout. I thank him for his collaborative approach to science that allowed me to present my work on many occasions. I truly enjoyed my time in his laboratory.

I also want to express my gratitude to my industrial co-supervisor, Dr Maxim Ryadnov, for supporting this D.Phil, especially during my stay at the National Physical Laboratory (NPL, Teddington). His ideas were always fascinating and created and interesting environment for scientific exploration and learning.

I am grateful to Dr Peter Judge, who provided guidance and discussion to all parts of the work presented in this thesis. His constant confidence was always reassuring during the process of the D. Phil.. Dr Juan Bolívar Gonzáles, supervised the overall scope of the Hepatitis C p7 work. His positive attitude and cheerfulness, even late at night and despite occasional setbacks, were always uplifting.

Many parts of this thesis were done in collaboration with various laboratories. At NPL, I would especially like to thank Baptiste Lamarre and Dr Angelo Bella for supervision in the laboratory and general guidance on the projects presented. The constant optimism of both of them and the ongoing scientific discussions generated an enjoyable and supportive atmosphere while working at NPL. Baptiste provided excellent guidance and help for most of the biophysical studies presented in Chapter 3. Angelo taught me the skills required for peptide synthesis and purification presented in Chapter 3. I would also like to thank both of them for their patience with me in the laboratory. I thank Dr Santanu Ray for collaboration with atomic force microscope (AFM) image acquisition and data analysis; data presented in Chapter 3.

The EPR work presented in Chapter 7 was an collaborative effort with Prof Nicole Zitzmann's laboratory (University of Oxford) and I would like to especially thank Dr Juan Bolìvar Gonzàles and Mario Hensen, who did most of the expression and reconstitution work presented in this Chapter. I thank Dr Patricia Dijkman who taught me to set-up DEER

experiments and provided guidance for all EPR studies. Dr William Myers (CAESR, University of Oxford) helped with the set-up of Gadolinium DEER and was always approachable and very helpful with technical and general questions regarding pulsed and continuous wave EPR. I am grateful to the CAESR EPR facility for generous provision of EPR measurement time. I thank Dr Jason Schnell (University of Oxford) for providing the pMM-LR1 plasmid used for expression of HCV p7. I also thank him for kindly providing his Rosetta model of HCV p7 for comparison to data presented in this thesis (Chapter 6 and 7). I want to express my gratitude to Dr Ben Oestringer for guidance on the expression and isotope labelling of p7, part of the work presented in Chapter 6. Further to this, I am very thankful to both Juan and Ben for the many constructive discussion on HCV and viroporins.

The PISEMA studies presented in Chapter 6 were performed in collaboration with Prof Burkhard Bechinger's laboratory (University of Strasbourg, France). I thank him for his generosity of measurement time to record PISEMA spectra on his 750 MHz set-up. I am very grateful to Dr Christopher Aisenbrey and Dr Jesus Raya who performed the experiments, I also thank them for their patience in explaining the methodology and teaching me about solid-state NMR in general. Most of all I would like to thank Dr Louic Vermeer who supervised my stay in Strasbourg and made these experiments possible. Louic also taught me how to use SIMMOL and SIMPSON simulation tools to analyse the recorded spectra reported in Chapter 6, he also took patience to teach and discuss many aspects of NMR in general. His excellent support continued after my visit to Strasbourg and was of great help for data analysis. I thank Dr Evgeniy Salnikov for discussion and help with oriented ^{2}H NMR.

The MD simulations presented in Chapter 4 were performed in collaboration with Dr Juan Muñoz García, Dr Peter Judge and Benjamin Little (University of Edinburgh) with support from Prof Jason Crain (University of Edinburgh).

I thank Dr Philip Williamson (University of Southampton) for introducing me to the *Spinach* software library.

I thank my students Samantha Woerner and James Harris that contributed to the HCV p7 work, and the entire Watts' and Ryadnov labs for their friendly and welcoming atmospheres, and general helpfulness. I thank my fellow graduate student in lab, Daniel Yin, for collaboration and general support throughout the D. Phil.. I also thank him for the many travels together to conferences presenting our combined projects.

To my funding bodies the BBSRC and industrial collaborator NPL.

To my college St Edmund Hall that supported me with funding for conferences.

To my family and friends for their great support throughout.

List of publications and presented work

Publications from *D. Phil.*

Pyne, A.‡, **Pfeil, M. P.**‡, Bennett, I., Ravi J., Iavicoli, P., Lamarre, B., Roethke, A., Ray, S., Jiang, H., Bella, A., Reisinger, B., Yin, D., Little, B.,Munoz-Garcia, J., Cerasoli, E., Judge, P., Faruqui, N., Calzolai, L., Henrion, A., Martyna, G., Grovenor, C., Crain, J., Hogenboom, B., Watts, A. and Ryadnov, M.,(2016) **Engineering monolayer poration for rapid exfoliation of microbial membranes**, Chemical Science, in press.

Dannatt, H. R., Taylor, G. F., Varga, K., Higman, V. A., **Pfeil, M. P.**, Asilmovska, L., Judge, P.J. and Watts, A. (2015). **^{13}C-and ^{1}H-detection under fast MAS for the study of poorly available proteins: application to sub-milligram quantities of a 7 trans-membrane protein.** Journal of biomolecular NMR, 62(1), 17-23.

Publications prior to *D. Phil.*

Fernandes, H., Leen, E. N., Cromwell Jr, H., **Pfeil, M. P.**, and Curry, S. (2015). **Structure determination of Murine Norovirus NS6 proteases with C-terminal extensions designed to probe protease-substrate interactions.** PeerJ, 3, e798.

Publications in preparation

Oestringer, B. P., Bolivar Gonzalez, J., Claridge, J. K., Pfeil, M. P., Hensen, M., Almanea, L., Watts, A., Schnell, J. R., Zitzmann, N. (in preparation). **Structural and dynamic properties compare the conformational and oligomeric state of HCV p7 from genotypes 1b and 5a**.

Sanders, M.R., Yin, D. J., Clifton, L.A., Judge, P. J., Pfeil, M. P., Watts, A., Frazier, R. A., Green R. J., (in preparation). **The interaction of tryptophan-rich puroindoline-b wild-type and mutant proteins with liposome models of biological membranes**.

Presentations

Oral presentation at the following meetings:

- EBSA Biophysics Course on Membrane Biophysics and Lipid Protein Interactions (2015)

Informal seminars:

- Goethe-Universität Frankfurt, Germany. Prof Clemens Glaubitz group
- Université de Strasbourg, France. Prof Burkhard Bechinger group
- Physikalisch-Technische Bundesanstalt, Germany.

Posters presented at the following conferences:

- British Biophysical Society meeting, Warwick, U.K. (2014).
- European Biophysics Congress, Lisbon, Portugal (2013).
- International Symposium: Connecting EPR, ssNMR and DNP for the study of complex Biomolecules, Castle Ringberg, Germany (2016).

Other achievements

Runner-up at the BBSRC Impact Awards 2016; Category: *social impact*.

Contents

List of Figures **xiii**

List of Abbreviations **xviii**

1 Introduction **1**

1.1 Biological membranes 1

1.1.1 Membrane characteristics and components 1

1.1.2 Lipids 3

1.1.3 Membrane asymmetry 7

1.1.4 The bacterial cell envelope 9

1.1.5 Lipid-protein interactions 12

1.2 Membrane proteins and peptides 15

1.2.1 Viral ion channels 15

1.2.1.1 Pharmacological relevance of viroporins 19

1.2.2 Membrane-active peptides 22

1.2.2.1 Antimicrobial peptides (AMPs) 22

1.2.2.2 Therapeutic potential of AMPs and resistance 29

1.2.2.3 Cell-penetrating peptides (CPPs) 32

1.3 Aims of this thesis 33

2 Experimental Principles **35**

2.1 Solid-state Nuclear Magnetic Resonance (ssNMR) 35

2.1.1 NMR experiments of I = 1/2 nuclei used in this thesis 40

2.1.1.1 Phosphorus (^{31}P) 40

2.1.1.2 Nitrogen (^{15}N) 42

2.1.2 NMR experiments of quadrupolar nuclei nuclei used in this thesis . . . 44
2.2 EPR . . . 45
2.2.1 Continuous wave EPR (cwEPR) . . . 46
2.2.2 Pulsed EPR (DEER) . . . 50
2.3 Fluorescence . . . 57
2.3.1 Tryptophan fluorescence . . . 58
2.3.2 Förster Resonance Energy Transfer (FRET) . . . 58

I Antimicrobial peptides 62

3 Peptide design, synthesis and activity 63
3.1 Introduction . . . 63
3.2 Peptide sequence design . . . 64
3.2.1 Sequence design principles of tilamin . . . 64
3.2.2 Sequence design principles of ChoM . . . 68
3.2.3 Solid phase peptide synthesis of antimicrobial peptides . . . 70
3.3 Activity of tilamin . . . 73
3.3.1 Minimum Inhibitory Concentration (MIC) . . . 73
3.3.2 Confocal Microscopy . . . 74
3.3.3 Atomic Force Microscopy (AFM) . . . 77
3.3.4 Circular Dichroism (CD) . . . 79
3.4 Activity of ChoM . . . 81
3.4.1 Minimum Inhibitory Concentration (MIC) . . . 81
3.4.2 Confocal Microscopy . . . 82
3.5 Conclusion . . . 84

4 Peptide - membrane interaction by magnetic resonance 85
4.1 Tilamin - lipid interaction investigated by cwEPR . . . 85
4.1.1 Introduction to cwEPR techniques . . . 85
4.1.1.1 Segmental order and dynamics probed by cwEPR . . . 87

4.1.2 Results . . . 90
4.1.2.1 Lipid acyl chain perturbation upon tilamin interaction probed by 5-SASL and 14-SASL . . . 90
4.1.2.2 Lipid acyl chain perturbation upon tilamin interaction probed by 5-PCSL and 12-PCSL . . . 94
4.2 Tilamin - lipid interaction investigated by solid-state NMR . . . 99
4.2.1 Introduction to experimental solid-state NMR techniques (^{2}H and ^{15}N) 99
4.2.1.1 Lipid order and orientation dependence of ^{2}H & ^{15}N . . . 100
4.2.2 Results . . . 106
4.2.2.1 Acyl - chain perturbation probed by ^{2}H NMR . . . 106
4.2.2.2 Peptide orientation probed by ^{2}H & ^{15}N NMR . . . 110
4.2.2.3 Simulation of ^{2}H spectra . . . 122
4.2.2.4 Molecular dynamics (MD) simulation of probed interaction . 125
4.3 ChoM - lipid interaction investigated by ssNMR . . . 128
4.3.1 Acyl - chain perturbation probed by ^{2}H NMR . . . 128
4.3.2 Peptide orientation probed by ^{2}H NMR . . . 129
4.4 Discussion . . . 133
4.4.1 Tilamin - lipid interaction based on cwEPR . . . 134
4.4.2 Tilamin - lipid interaction based on ^{2}H and ^{15}N ssNMR . . . 135
4.4.3 Membrane perturbation upon tilamin interaction by ^{2}H NMR . . . 137
4.4.4 ChoM - lipid interaction . . . 139
4.5 Conclusion . . . 139

II The viroporin p7 **143**

5 *N*N-DNJ-membrane interaction probed by ^{2}H ssNMR **144**

5.1 Introduction . . . 144
5.1.1 ^{2}H NMR of headgroup deuterated lipids . . . 147
5.2 Results . . . 148
5.3 Discussion . . . 152

6 PISEMA studies of p7 topology 155

6.1 Introduction . . . 155

6.1.1 Detergent- and solvent-based p7 structures in literature . . . 155

6.1.2 Oriented systems for solid-state NMR . . . 158

6.1.3 PISEMA . . . 159

6.2 Results . . . 161

6.2.1 Expression and uniform ^{15}N labelling of p7 . . . 161

6.2.2 Reconstitution of p7 . . . 164

6.2.3 Membrane alignment for oriented solid-state NMR . . . 165

6.2.4 Oriented solid-state NMR of p7 . . . 167

6.2.4.1 PISEMA . . . 168

6.2.4.2 2^4-SEMA Experiments . . . 171

6.3 Discussion . . . 174

7 Towards the oligomeric state of p7 in a membrane 180

7.1 Introduction . . . 180

7.1.1 p7 mutants . . . 183

7.1.2 Stoichiometric analysis based on ensemble FRET . . . 186

7.1.3 Introduction to DEER techniques used . . . 190

7.2 Results . . . 192

7.2.1 Oligomeric stoichiometry by FRET . . . 192

7.2.2 p7 mobility profile by cwEPR . . . 194

7.2.3 Oligomeric state and protomer conformation by DEER . . . 197

7.2.3.1 Modulation depth behaviour based on spins within the nano-object . . . 197

7.2.3.2 Channel stoichiometry based on inter- and intra-monomer distance constraints . . . 199

7.2.4 DEER of Gadolinium (Gd^{3+}) ions . . . 214

7.3 Discussion . . . 216

8 Conclusion and Discussion 220

Appendices

A Appendix **225**

A.1 Material and Methods . . . 225

A.1.1 Chapter 3 . . . 225

A.1.2 Chapter 4 . . . 228

A.1.3 Chapter 5 . . . 233

A.1.4 Chapter 6 . . . 234

A.1.5 Chapter 7 . . . 239

A.1.6 Media and Buffers . . . 244

A.2 Additional information . . . 246

A.2.1 Chapter 3 . . . 246

A.2.1.1 Solid-phase peptide synthesis . . . 246

A.2.1.2 Peptide purity by MALDI-TOF . . . 250

A.2.2 Chapter 4 . . . 252

A.2.2.1 ^{2}H-NMR . . . 252

A.2.2.2 ^{31}P-NMR . . . 253

A.2.2.3 MD simulations of tilamin . . . 254

A.2.3 Chapter 7 . . . 256

A.2.3.1 Stitched 3p and 4p DEER trace of N-terminally labelled p7 . 256

A.2.3.2 Static ^{31}P of p7 in DOPC:POPE(4:1, wt:wt) . . . 256

A.2.3.3 p7 S21C L51C mutation illustrated on PDB models . . . 256

A.2.3.4 p7 K33R L51C mutation illustrated on PDB models . . . 258

A.2.3.5 Construction of Chirp pulse for Gd^{3+} DEER . . . 260

Bibliography **261**

List of Figures

1.1 Fluid mosaic model of a membrane 2
1.2 Lipid phase transition 5
1.3 General lipid shapes 5
1.4 Lipid phases 6
1.5 Lipid asymmetry of the plasma membrane 7
1.6 Bacterial cell envelope 10
1.7 Peptide-lipid interaction: Hydrophobic mismatch 13
1.8 3D structures of selected viroporins 16
1.9 Effects of viroporins on cellular live cycle 18
1.10 HCV genome and polyprotein processing 20
1.11 Statistical information of AMPs 23
1.12 Mechanisms of action (AMPs) 26
1.13 Antimicrobial resisitance 29

2.1 Chemical shift anisotropy (CSA) of simulated static phosphate spectra 41
2.2 Heteronuclear dipolar coupling in a powder 43
2.3 Simulated ^{2}H spectrum ($S=1$) 45
2.4 The hyperfine energy splitting of a nitroxide radical 47
2.5 Simulated cwEPR spectra at different correlation times 49
2.6 Illustration of a Hahn echo 51
2.7 Absorption spectrum of a nitroxide at Q-band 52
2.8 3p and 4p DEER pulse sequences 52
2.9 Illustration of background correction 54
2.10 Nuclear modulation averaging in a 4p DEER experiment 56

2.11 Cy3 and Cy5 dyes as a FRET pair 59
2.12 Jablonski diagram 60

3.1 Peptide sequence design principles of tilamin 65
3.2 Helical wheel representation of AMPs 67
3.3 Peptide sequence design principles of ChoM 69
3.4 Semi - prep HPLC trace of tilamin 71
3.5 Analytical HPLC traces of all peptide sequences 72
3.6 Tilamin-Membrane interactions by confocal microscopy 76
3.7 AFM of *E. coli* upon tilamin interaction 78
3.8 *E. coli* cross sections upon tilamin interaction 79
3.9 Secondary structure by CD 80
3.10 ChoM-membrane interaction by confocal microscopy 83

4.1 Nitroxide spin probes 86
4.2 Spectral splittings of nitroxide (cwEPR) 88
4.3 Dipolar broadening in frozen cwEPR 90
4.4 Tilamin-lipid interactions probed by SASL 91
4.5 Segmental acyl chain oder probed by by SASL 91
4.6 De-convolution of multicomponent cwEPR spectra 92
4.7 Slow exchange between lipid environments 93
4.8 5-PCSL spectra at a temperature range 95
4.9 5-PCSL and 12-PCSL spectra upon tilamin interaction 96
4.10 Segmental acyl chain oder probed by by PCSL 96
4.11 Segmental acyl chain dynamics probed by by PCSL 97
4.12 Side-directed spin labelled tilamin 98
4.13 Geometric relationships in an alpha helix 102
4.14 Quadrupolar splitting as a function of rotation and tilt angles 103
4.15 ^{15}N CSA 105
4.16 Orientational constraints of tilamin 106

4.17 ^{2}H spectra of chain-deuterated POPC 107

4.18 ^{2}H spectra of chain-deuterated POPG 108

4.19 Acyl chain order probed by ^{2}H 108

4.20 Ala-d_3 orientational constraints of tilamin 110

4.21 Exemplar ^{2}H spectrum 111

4.22 Oriented bilayer in the absence of peptide 112

4.23 Selectively deuterated tilamin at different peptide to lipid ratios by ^{2}H NMR 112

4.24 Different deuterated position of tilamin by ^{2}H NMR 115

4.25 RMSD plot analysis of multiple constraints 117

4.26 Rotational peptide diffusion by ^{2}H 118

4.27 Static ^{15}N spectra of tilamin 120

4.28 Combined RMSD analysis ^{2}H and ^{15}N constraints 121

4.29 ^{2}H orientational dependance by simulation 123

4.30 ^{2}H spectra by simulation 124

4.31 MD simulation of single tilamin peptide in a DLPC:DLPG(3:1,molar ratio) bilayer 126

4.32 MD simulation of tilamin pore structure 127

4.33 ^{2}H NMR of acyl chain deuterated POPC and POPG upon ChoM and ChoC interaction 128

4.34 Segmental order parameters upon ChoM and ChoC interaction by ^{2}H NMR . 129

4.35 Illustration of labelled (^{2}H) sites of ChoM 130

4.36 ^{2}H NMR of selectively deuterated ChoM 131

4.37 RMSD plot of ChoM orinetation based on ^{2}H constraints 132

4.38 Summary of techniques 133

4.39 Tilamin orientation as a model 136

4.40 AFM and SIMS of supported bilayers 140

4.41 Proposed tilamin insertion mode 141

5.1 Chemical structure of *N*N-DNJ 146

5.2 Charge deposition in a POPC bilayer 148

5.3 Chemical structure of DOPC-d_4 . . . 149
5.4 $\Delta\nu_Q$ at different *N*N-DNJ concentrations . . . 150
5.5 ^{2}H-NMR of headgroup deuterated lipids . . . 151
5.6 $\Delta\nu_Q$ at different pH levels . . . 152

6.1 Schematic p7 topology . . . 156
6.2 Illustration of PISA-wheels . . . 160
6.3 PISEMA pulse sequence . . . 161
6.4 p7 expression and purification . . . 162
6.5 p7 ^{15}N labelling . . . 163
6.6 Reconstitution by dilution . . . 164
6.7 Mechanically aligned bilayers . . . 166
6.8 ^{31}P NMR spectrum of aligned lipids . . . 167
6.9 PISEMA spectrum . . . 168
6.10 PISEMA simulation strategy . . . 169
6.11 PISEMA analysis by simulation . . . 170
6.12 2^4-SEMA spectrum of p7 . . . 172
6.13 Comparison of 2^4-SEMA spectrum to a powder . . . 173
6.14 2^4-SEMA analysis . . . 174
6.15 SAMMY of p7 in aligned bicelles . . . 176
6.16 Solution and solid-state NMR structure of p7 . . . 177
6.17 Secondary structural elements across different p7 structures . . . 178

7.1 Structural and stoichiometric information on p7 oligomerisation . . . 181
7.2 p7 sequence allignment and mutations . . . 183
7.3 E_{app} dependancy on n . . . 188
7.4 Corrections of FRET signal . . . 189
7.5 Multi-spin effects in a symmetric hexamer . . . 191
7.6 Stoichiometry based on FRET . . . 193
7.7 Deconvoluted cwEPR . . . 196

7.8 Modulation depth analysis 198
7.9 DEER pump-pulse reduction 200
7.10 DEER spin dilution of N-terminally labelled p7 201
7.11 DEER of spin-labelled C- and N-terminus 203
7.12 Model based analysis of N - terminus 205
7.13 Model based analysis of C - terminus 207
7.14 Theoretical distance separation of p7 S21C L51C 208
7.15 p7 S21C L51C in 27 mM cyclofos-6 209
7.16 p7 S21C L51C in different bilayer environments 211
7.17 Fitted distributions of p7 S21C L51C in different bilayer environments 212
7.18 p7 K33R L51C in DOPC:POPE (4:1; wt;wt) 213
7.19 DEER of Gd^{3+} ions 215

A.1 Solid phase peptide synthesis 247
A.2 Orthogonal protection scheme 249
A.3 Mass spectrometry of ChoM and QAELA 250
A.4 Mass spectrometry of tilamin 251
A.5 ^{2}H NMR on tilamin interaction in DLPC:DLPG(3:1, molar ratio) 252
A.6 Representative ^{31}P static NMR monitoring lipid alignment 253
A.7 Tilamin assemblies used as starting points for MD 254
A.8 MD simulations of tilamin assemblies 255
A.9 3p and 4p DEER stitched 256
A.10 Static ^{31}P NMR of p7 (Gt1b J4) in DOPC:POPE(1:4. wt:wt) 256
A.11 p7 S21C L51C illustrated in different models 257
A.12 p7 S21C L51C in PDB: 2M6X 257
A.13 p7 K33R L51C illustrated in different proposed models 258
A.14 p7 K33R L51C in PDB: 2M6X 259
A.15 Construction of chirp pulse 260

List of Abbreviations

12-PCSL . . . . Phosphatidylcholine spin labelled at position 12

14-SASL . . . . Stearic acid spin labelled at position 14

3p DEER . . . 3-pulse DEER

4p DEER . . . 4-pulse DEER

14-0-PC 1,2-di-O-tetradecyl-*sn*-glycero-3-phosphocholine

16-0-PC 1,2-di-O-hexadecyl-*sn*-glycero-3-phosphocholine

5-PCSL . . . . . Phosphatidylcholine spin labelled at position 5

5-SASL . . . . . Stearic acid spin labelled at position 5

AFM . . . . . Atomic force microscopy

AMP . . . . . Antimicrobial peptide

ARV . . . . . Avian reovirus

ATP . . . . . Adenosine triphosphate

BVDV . . . . . Bovine viral diarrhea virus

CD . . . . . Circular dichroism

CecB . . . . . Cecropin B

CFU . . . . . Colony forming unit

ChoC . . . . . N-temrinal 21 amino acids of CecB

ChoM . . . . . ChoC with G14I G20K mutations

CL . . . . . Cardiolipin

CMC . . . . . Critical micelle concentration

CoV . . . . . Coronavirus

CP . . . . . Cross-polarisation

CPP . . . . . Cell-penetrating peptides

CSA . . . . . Chemical shift anisotropy

cwEPR . . . . . Continous wave EPR

DAA . . . . . Direct acting antiviral

DEER . . . . . Double electron-electron resonance

DGJ . . . . . Deoxygalactonojirimycin

DHB . . . . . 2,5-Dihydroxybenzoic acid matrix

DHPC 1,2-Dihexanoyl-*sn*-glycero-3-phosphocholine

DIPEA . . . . . N,N-Diisopropylethylamine

DLPC 1,2-dilauroyl-*sn*-glycero-3-phosphocholine

DLPG 1,2-Dilauroyl-*sn*-glycero-3-phosphoglycerol

DMF . . . . . Dimethylformamide

DMPC 1,2-dimyristoyl-*sn*-glycero-3-phosphocholine

DMPE 1,2-dimyristoyl-*sn*-glycero-3-phosphoethanolamine

DMPG 1,2-dimyristoyl-*sn*- glycero-3-phosphoglycerol

DNA . . . . . Deoxyribonucleic acid

DNJ . . . . . Deoxynojirimycin

DOPC 1,2-dioleoyl-*sn*-glycero-3-phosphocholine

DOPC-d_4 . . . . 1,2-dioleoyl-*sn*-glycero-3-phosphocholine-d_4

DPC Fos-choline-12

DPG . . . . . Diphosphatidylglycerol

DTT . . . . . Dithiothreitol

E5 . . . . . Viroporin human papilloma virus

EDT 1,2-Ethanedithiol

EDTA . . . . . Ethylenediaminetetraacetic acid

EI-MS . . . . . Electron ionization mass spectrometery

EM . . . . . Electron microscope

EPR . . . . . Electron paramagnetic resonance

ER . . . . . Endoplasmic reticulum

ERG . . . . . Ergosterol

ESEEM . . . . . Electron spin echo envelope modulation

FID . . . . . Free induction decay

FPLC . . . . . Fast protein liquid chromatography

FQRP . . . . . *Fluoroquinolone-resistant Pseudomonas Aeruginosa*

FRET . . . . . Förster resonance energy transfer

GFP . . . . . Green fluorescent protein

GPCR . . . . . G-protein coupled receptor

GUV . . . . . Giant unilamellar vesicle

HBTU . . . . . 3-[Bis(dimethylamino)methyliumyl]-3H-benzotriazol-1-oxide hexafluorophosphate

HCV . . . . . Hepatitis C virus

HEPES . . . . . 4-(2-Hydroxyethyl)piperazine-1-ethanesulfonic acid

HIV-1 . . . . . Human immunodeficiency virus 1

HMA . . . . . Hexamethylene amiloride

HPLC . . . . . High Performance Liquid Chromatography

HRSV . . . . . Human respiratory syncytial virus

IAV . . . . . Influenza virus A

IPTG . . . . . Isopropyl β-D-1-thiogalactopyranoside

IRES . . . . . Internal ribosome entry site

JCV . . . . . JC polyomavirus

L:P . . . . . Lipid-to-protein ratio

lacY . . . . . Lactose permease

LB . . . . . Lysogeny broth

LDS . . . . . Lithium dodecyl sulfate

LPA . . . . . Lipoteichoic acid

LPG . . . . . Lysyl-phosphatidylglycerol

LPS . . . . . Lipopolysaccharide

M2 . . . . . Matrix-2 protein

MALDI . . . . . Matrix-assisted laser desorption/ionization

MAS . . . . . Magic angle spinning

MBHA . . . . . 4-Methylbenzhydrylamine hydrochloride

MD . . . . . Molecular dynamics

MIC . . . . . Minimal inhibitory concentration

MMM . . . . . Multiscale modeling of macromolecular systems software

MRSA . . . . . Methicillin-resistant *Staphylococcus aureus*

MS . . . . . Mass spectrometry

MTSL . . . . . S-(1-oxyl-2,2,5,5-tetramethyl-2,5-dihydro-1H-pyrrol-3-yl)methyl methanesulfonothioate

MWCO . . . . . Molecular weight cut-off

***N*B-DGJ** . . . . N-butyldeoxygalactonojirimycin

***N*B-DNJ** . . . . N-Butyldeoxynojirimycin

NHS . . . . . N-Hydroxysuccinimide

NMR . . . . . Nuclear magnetic resonance

***N*N-DGJ** . . . . N-Nonyl)-deoxygalactonojirimycin

***N*N-DNJ** . . . . N-nonyl deoxynjirimycin

NOE . . . . . Nuclear Overhauser effect

NPL . . . . . National Physical Laboratory

OMP . . . . . Outer membrane protein

OS . . . . . Oriented sample

Oxyl-1-NHS . . 1-Oxyl-2,2,5,5-tetramethylpyrroline-3-carboxylate NHS ester

p7 . . . . . Protein 7 kDa

PA . . . . . Phosphatidic acid

PBS . . . . . Phosphate buffered saline

PC . . . . . Phosphatidylcholine

PDB . . . . . Protein data bank

PE . . . . . Phosphatidylethanolamine

PEG-IFN-α . . Pegylated interferon α

PELDOR . . . . Pulsed electron double resonance

PG . . . . . Phosphatidylglycerol

PI . . . . . Phosphatidylinositol

PISA . . . . . Polar Index Slant Angle

PISEMA . . . . Polarisation inversion spin exchange at the magic angle

POPC 1-palmitoyl-2-oleoyl-*sn*-glycero-3-phosphocholine

POPE 1-Palmitoyl-2-oleoyl-*sn*- glycero-3-phosphoethanolamine

POPG 1-palmitoyl-2-oleoyl-*sn*-glycero-3-phosphoglycerol

ppm . . . . . Part per million

PS . . . . . Phosphatidylserine

PV . . . . . Poliovirus

RBV . . . . . Ribavirin

REDOR . . . . Rotational-echo, double-resonance nuclear magnetic resonance

rf . . . . . Radio-frequency

RMSD . . . . . Root-mean-square deviation

RNA . . . . . Ribonucleic acid

RP-HPLC . . . Reversed phase HPLC

RV . . . . . Rotavirus

SARS CoV . . Severe acute repiratory syndrom CoV

SASL . . . . . Stearic acid spin labelled

SDS . . . . . Sodium dodecyl sulfate

SDS-PAGE . . Sodium dodecyl sulfate polyacrylamide gel electrophoresis

$\mathbf{S_{eff}}$ . . . . . Effective order parameter

SEMA . . . . . Spin exchange at the magic angle

SIMS . . . . . Secondary ion mass spectrometry

sNMR . . . . . Solution NMR

SRT . . . . . Shot repetition time

$\mathbf{S_{seg}}$ . . . . . Segmental order parameter

ssNMR . . . . . Solid-state NMR

SUV . . . . . Small unilamellar vesicle

SV . . . . . Sindbis virus

$\mathbf{T_1}$ . . . . . Spin-lattice relaxation

$\mathbf{T_2}$ . . . . . Spin-spin relaxation

TB . . . . . Terrific Broth

TCEP . . . . . Tris(2-carboxyethyl)phosphine

TEM . . . . . Transmission electron microscopy

TFA . . . . . Trifluoroacetic acid

TFE . . . . . Tetrafluoroethylene

Tis . . . . . Triisopropylsilane

$\mathbf{T_m}$ . . . . . Transisiton temperature (bilayer)

TM1 . . . . . Trans-membrane helix 1

TM2 . . . . . Trans-membrane helix 2

TOF . . . . . Time- of-flight

$\mathbf{\nu_{obs}}$ . . . . . Observer frequency (for DEER)

vol:vol . . . . . Volume-to-volume ratio

VpU . . . . . Viral Protein Unique

$\mathbf{\nu_{pump}}$ . . . . . Pump frequency (for DEER)

VRE . . . . . *Vancomycin-resistant Enterococci*

wt:wt . . . . . Weight-to-weight ratio

1 Introduction

Contents

1.1 Biological membranes 1
1.1.1 Membrane characteristics and components 1
1.1.2 Lipids 3
1.1.3 Membrane asymmetry 7
1.1.4 The bacterial cell envelope 9
1.1.5 Lipid-protein interactions 12
1.2 Membrane proteins and peptides 15
1.2.1 Viral ion channels 15
1.2.2 Membrane-active peptides 22
1.3 Aims of this thesis 33

1.1 Biological membranes

1.1.1 Membrane characteristics and components

Compartmentalisation is a fundamental principle for life. Phospholipids possess distinct characteristics that allow the formation of bilayers, highly dynamic structures that separate distinct biochemical environments. Biological membranes facilitate organised and highly selective chemical and information exchange between compartments [1]. These distinct characteristics are essential to Biology.

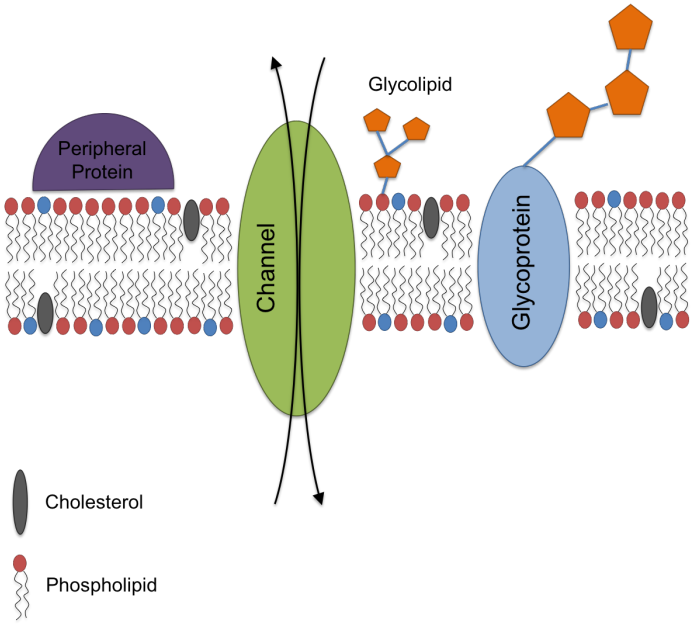

Figure 1.1: A schematic illustrating the different main components of a complex membrane.

Membranes are formed of three major components:

- Phospholipids
- Proteins
- Sugars

All three membrane components show a high degree of versatility and form a dynamic relationship with each other. This gives rise to the generic structure of a membrane with two lipid leaflets in opposing orientation that have integral membrane proteins embedded as well as peripheral proteins associated with the membrane surfaces. This basic assembly of a biological membrane has been described as the fluid mosaic model (Figure 1.1, [2]), which depicts the membrane as a "sea" of lipids that provide a dynamic two dimensional solvent for integral membrane proteins.

The main thermodynamic driving force for a membrane structure is the non-covalent hydrophobic effect of amphiphilic lipids forming the characteristic shielded hydrophobic membrane core minimising contact to the aqueous solvent. The hydrophobic effect causes the hydrophilic head-group and the hydrophobic acyl chains to cluster together, two opposing

leaflets ensure that all hydrophobic regions are covered from aqueous exposure. Electrostatic interactions between head groups and van der Waal forces between the individual acyl chains strengthen the assembly. Phospholipids build the structural framework for membranes, whilst depicting a membrane as a simple lipid bilayer would be a drastic oversimplification. In the past, lipids were often regarded as a solvent that provides support for membrane proteins to "float" in, yet in recent years it became evident that phospholipid bilayers might be much more than this, and indeed are not only a vehicle for biological function but might also have a more direct involvement. Thus, membranes are highly specialised functional assemblies containing different types of phospholipids, integral transmembrane proteins as well as peripheral proteins. Oligosaccharides can be carried by both lipids and proteins for various reasons. There is an asymmetry between the inner and outer leaflet of a membrane adding to its complexity. In spite of all these things a biological membrane remains highly dynamic allowing for membrane budding, fission, fusion,diffusion and domain formation; processes that are of importance for transportation, chemical exchange and signalling events as well as cellular reproduction [1; 3].

1.1.2 Lipids

Lipids are a class of molecules that are essential to Biology. The function of lipids can be categorised in three main areas: (I) energy conservation (II) signal transduction and (III) the inherent ability to form spontaneous membranes as a structural and functional platform. All of these functions require a diverse set of molecules and hence it is hardly surprising that 5% of eukaryotic genes are involved in lipid biosynthesis, which leads to the existence of >1 000 different lipid species in a eukaryotic cell [4]. A total of 40 000 lipids species are known to date, which resembles broadly the number of encoding genes in a eukaryotic cell. Unlike many other biologically relevant molecules, lipids are amphiphilic, with a small hydrophilic head-group and an associated hydrophobic hydrocarbon chains, typically 12-22 carbon in length.

Glycerophospholipids together with sphingolipids are responsible for the structural backbone of a membrane. Glycerophospholipids share the common feature of a glycerol backbone that acts as the connection and interface of the hydrophilic head moiety and the hydrophobic acyl chains. Both the acyl chains and head group moiety vary and give rise to distinct lipid species. The precise membrane composition varies between organisms and organelles

(Table 1.1), which dictates intrinsic membrane characteristics that support biological function in specific environments.

Table 1.1: Glycerophopholipid composition (%) of representative members of different organism

Phospholipid		Erythrocyte (human)	Barley (plant)	Torulaspora delbruekii (yeast)	Escherichia coli (Gram-negative bacteria)	Staphylococcus aureus (Gram-positive bacteria)	Haloferax volcanii (archae)
Glycerophospholipid	PC	26	40	29	-	10	-
	PE	28	33	37	74	-	-
	PS	11	7	5	-	-	-
	PI	[d]	5	10	-	-	-
	PG	[d]	5	-	20	57	91
	LPG					38	
	DPG	-	2	7	6	5	6
	PA	[d]	7	2	-	-	3
Sphingolipid	SM	28	-	-	-	-	-

Numbers are percentages of main lipids other lipids are not included. PE: Phosphatidylethanolamine; PS: Phosphatidylserine; PI: Phosphatidylinositol; PG: Phosphatidylglycerol; DPG:Diphosphatidylglycerol; PA: Phosphatic acid [d] all other lipids add up to a total of 8%. (Table adapted from [5]) and extended with data from [6]).Note that membrane composition can vary across different organelles within the cell.

Lipid bilayers can exist in different polymorphic phases, which are characterised by the phase transition temperature (T_m) specific to each individual lipid and chemical composition. Phase influences lipid organisation in a bilayer, for example the spacial arrangement of lipids and consequently also their motional freedom, in turn strongly affecting the membrane characteristics as a whole. Above the specific T_m lipids change from a highly ordered solid phase (the gel phase) to a liquid crystalline phase; this can occur via a pre-state where the bilayer adapts characteristics of both phases (Figure 1.2). Biophysical characterisation of this phenomenon showed that it is possible for two phases to coexist in a model membrane and form specific domains that might serve a functional purpose [7; 8]. Lateral local lipid domains are characterised by lipid composition variation across a bilayer that affect key characteristics like membrane shape and fluidity, which is the basis for the formation of lateral micro-domains often called lipid rafts. Phase transitions are a complex process that increase in complexity for multi-component systems and can be described by phase diagrams [9].

The hydrophobic acyl tails of lipids can vary in length and their degree of saturation. This affects mostly the T_m of a single distinct lipid, where lipids with shorter acyl chains and unsaturation have lower T_m. This phenomenon adds to the adaptability of organisms to local environment. It has been shown that *E. coli* grown at different temperatures adjust their membrane composition ensuring a sufficiently mobile bilayer across all temperature ranges [10].

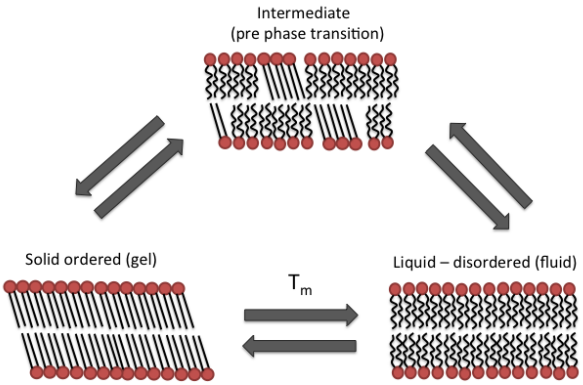

Figure 1.2: A schematic illustrating the different polymorphic phases and their basic characteristics.

In addition to the carbon acyl chains, the headgroup moiety varies across lipid species, where the main headgroups are:

1. Phosphatidylcholine (PC)
2. Phosphatidylserine (PS)
3. Phosphatidylethanolamine (PE)
4. Phosphatidylglycerol (PG)
5. Phosphatidylinositol (PI)

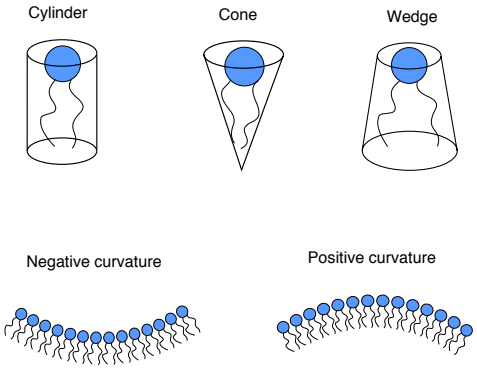

Figure 1.3: A schematic illustrating different lipid shapes depending on head-group moiety and acyl chain character and the influence on lipid assemblies

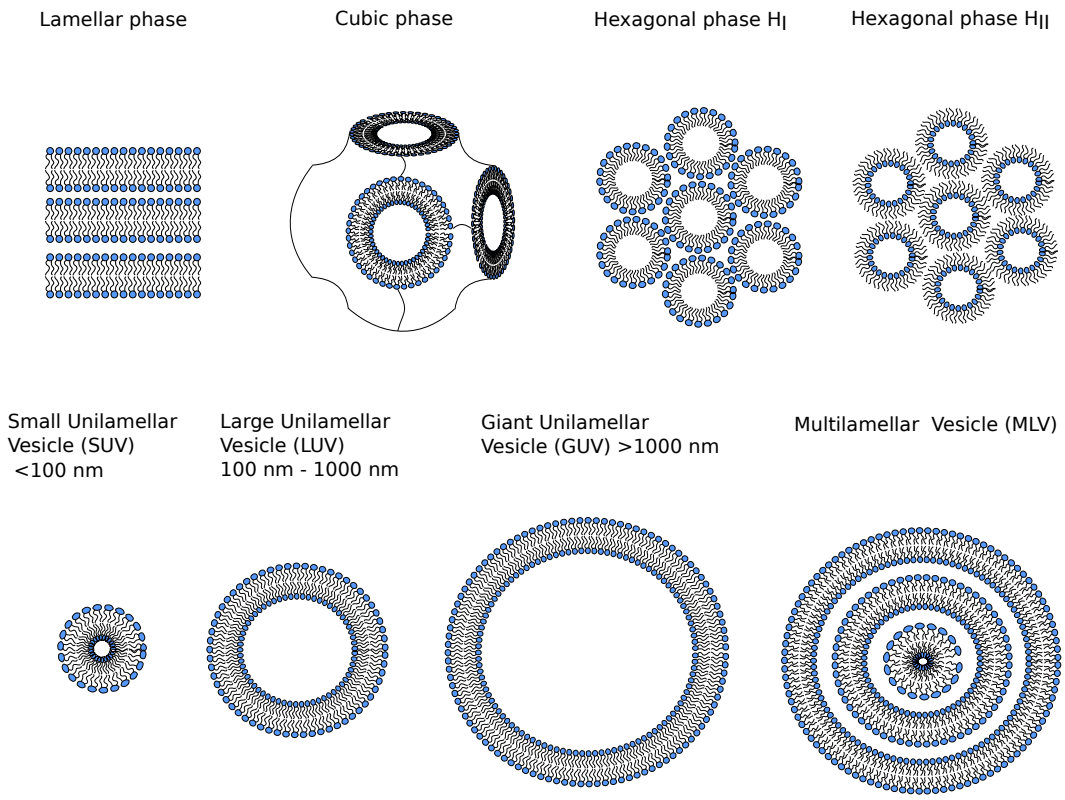

Figure 1.4: Top: a schematic illustrating different lipid phases, which can broadly be characterised in 4 main classes. Bottom: the major lamellar forms that are relevant for the study of membrane protein systems

Each headgroup moiety has distinct characteristics like charge, size and shape. Depending on this leaflets can posses an overall charge and adapt to polymorphic forms (Figure 1.3 and 1.4). Hence, to study biological membranes it is important to understand their individual components and composition.

The "amphiphile shape hypothesis" postulates that lipid shape is related to the polymorphic form that a lipid assembly will adopt. Lipid shape is defined by a form factor S, where a perfectly cylindrical shape is described by S =1; e.g. lipids with a smaller head-group moiety like PE (S < 1), are described by a "wedge' like appearance and will favour negative curvature and an overall structure of a hexagonal phase (H_{II}) will be favoured (Figure 1.3 and 1.4; [11]). The overall bilayer curvature is the result of the interplay of many forces such as acyl chain motions and electrostatic effects of headgroup moieties in close proximity. This is an important consideration both for biology and when considering biological mimetics to study lipids and lipid-protein systems.

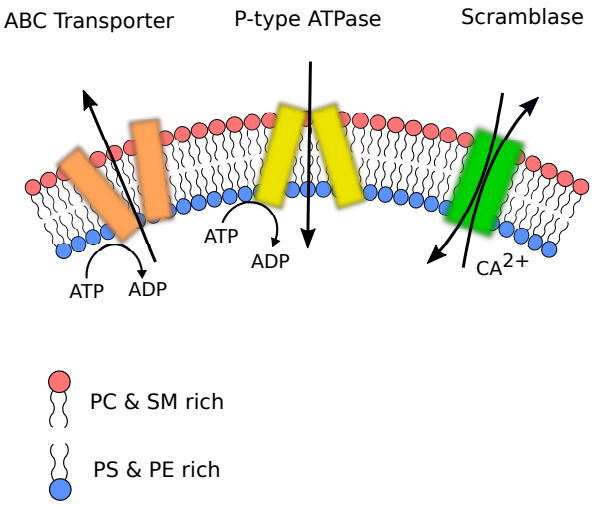

Figure 1.5: Summary of the main enzymes involved in the establishment and disruption of lipid asymmetry of the eukaryotic plasma membrane

1.1.3 Membrane asymmetry

Most cellular membranes characterised to date have an asymmetric distribution of lipid species between the two leaflets. This asymmetry is of biological relevance for processes like programmed cell death [12], the inherent mechanical bilayer stability [13] and the electrostatic membrane potential [14]. As an example, the outer leaflet of the eukaryotic plasma membranes is rich in choline phospholipids like phosphatidylcholine and sphingomyelin, whereas the corresponding inner leaflet is rich in the aminophospholipds like phophatidylserine and phosphatidylethanolamine, leading to an asymmetric charge distribution across the leaflets [15; 16].

Eukaryotic membrane asymmetry is established by two ATP-depending translocases. The ATP-binding cassette (ABC) transporter moves lipids from the inner to the outer leaflet whereas the faster aminophospholipid translocase moves PS and PE from the outer to the inner leaflet, showing no specificity towards choline lipids [17; 18; 19]. The third important player is the ATP-independent but Ca^{2+}-dependent scramblase that allows for bidirectional phospholipid transport and hence disrupts asymmetry (Figure 1.5). The asymmetry can also be disrupted by calcium influx triggered scramblase activity and in turn causes PS accumulation in the outer leaflet, attracting macrophages to the plasma membrane and thus triggering cell death [17; 20; 21]. Nevertheless, lipid flip-flop can also be facilitated in the absence of enzyme activity by the general membrane potential or thermally induced.

Membrane asymmetry is also important for specific membrane protein function. The negatively charged PS on the inner leaflet is known to cause accumulation of enzymes like protein kinase C to the inner side of the plasma membrane. PS is also known to be an essential co-factor for ATPases [22].

Similar to eukaryotic membranes, bacterial membranes possess an intrinsic asymmetry too. The outer membrane of Gram-negative bacteria has an unusual asymmetry in lipopolysaccharide (LPS), a unique component of this system, found exclusively on the outer leaflet, whilst most of the phospholipids are found on the inner leaflet. LPS forms an important barrier protecting the bacteria from external stress factors. Asymmetries across the individual cytoplasmic membrane leaflets are summarised in Table 1.2.

Table 1.2: Relative membrane composition of the individual leaflets of the cytoplasmic membrane of different organism (in %)

	E. coli		*S. aureus*		*B. subtilis*		*C. albicans*		Erytrocyte	
constituent	outer	inner	outer	inner	outer	inner	outer	inner	outer	inner
CL	20	10	30	5	35	10	-	-	-	-
PG	5	15	45	5	-	-	-	-	-	-
PE	10	40	-	-	5	5	5	40	5	20
PC	-	-	5	5	5	5	5	5	5	20
SM	-	-	-	-	-	-	5	15	5	30
ST	-	-	-	-	-	-	10	10	10	10

Relative distribution of different membrane constituents across the bilayer leaflets of different pathogens (bacterial and fungi). Constituents are PG: Phosphotatidylglycerol; PE: Phosphatidylethanaolamine; PC: Phosphatidtylcholine; SM: Sphingomyelin and ST: Sterols. The percentages are +/- 5% and taken from [23]. Note the differences in architecture across different organism which is believed to be one driving force in selective toxicity of antimicrobial peptides.

Membrane asymmetry also presents a potential target for antibiotic agents, as neutralising the negative charge alters the intrinsic surface potential that often leads to cell death or to the onset of antibacterial mechanisms. This together with membrane depolarisation, is the likely mechanism of action for many naturally occurring peptide antibiotics. Indeed early studies of a simple poly-Lys peptides showed local PE segregation from lipopolysaccheride (LPS), thus causing lateral asymmetry in the membrane [24]. Further to this, magainin 2 (an antimicrobial peptide from the african frog *Xenopus laevis*) was reported to induce lipid flip-flop across the bilayer, which in turn was linked to peptide translocation towards the hydrophobic core [25].

The model peptides WALP and KWALP were shown to translocate fluorescently tagged phospholipids at the bacterial cytoplasmic membrane without the need for scramblases, similar observations were made in the presence of the potassium channel KscA [26; 27]. The authors postulated that lipid translocation across the bilayer is caused by lipid interactions with a fully transmembrane alpha helix. It has been argued that naturally occurring peptide antibiotics disrupt inter-leaflet asymmetry by similar mechanisms. The resulting altered electrostatic potential of an asymetric membrane are important considerations for selective toxicity of peptide-based antibiotics, thus rendering membrane asymmetry an important consideration for therapy [23; 28].

1.1.4 The bacterial cell envelope

All bacteria share the common feature of having a complex cell envelope consisting of the cytosolic membrane and an associated cell wall, which is distinct from higher living multicellular organisms. The cellular envelope differs between species and the most basic classification is in Gram-staining (Gram-positive) and non-Gram-staining (Gram-negative) bacterial classes (Figure 1.6). In the most simple picture the cellular wall is made of polysaccharides and peptidoglycan in addition to the cytoplasmic lipid bilayer, which ensures an overall tight, yet flexible cell envelope. The cytosolic membrane itself is composed of phospholipids in both scenarios, however their charge, head-group and fatty acid tails differ. Broadly, Gram-positive bacteria contain a larger fraction in PG lipids whereas the Gram-negative bacteria are richer in the zwitterioninc PE component but also contain some PG lipids. The acyl chain characteristics differ between both cytosolic membranes and are summarised in Table 1.3. The cytosolic membrane of Gram-positive bacteria and the outer membrane of Gram-negative bacteria together with the associated LPS layer contain a high degree of negative charge, which is characteristic for the bacterial cell envelope.

The periplasm, the space between the cytosolic membrane and the cell wall, differs between Gram-positive and Gram-negative bacteria. In the case of Gram-positive bacteria this space separates the cytoslic membrane from the thick peptidoglycan layer and is comparably narrow. In Gram-negative bacteria the periplasm separates the inner from the outer membrane and is much larger [6]. The presence of the outer membrane in Gram-negative bacteria is also one of the main differences of the cell envelope between Gram-positive and Gram-negative species.

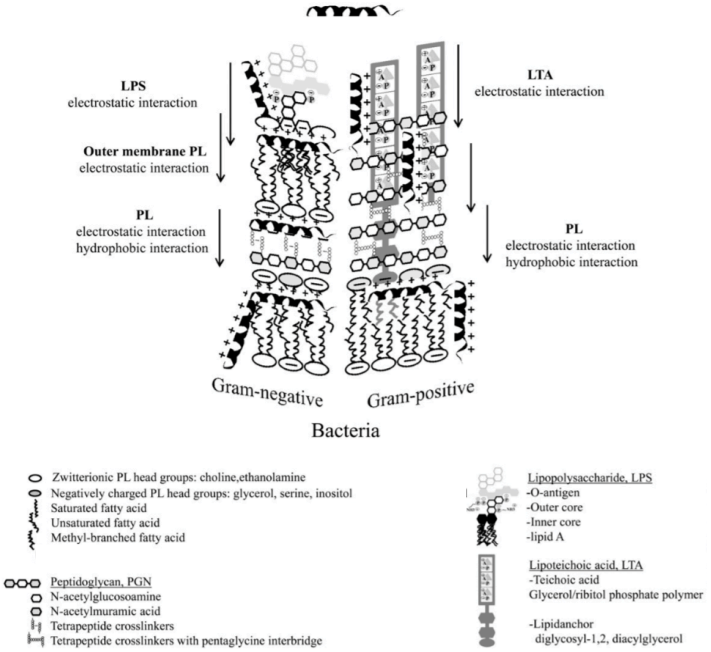

Figure 1.6: Schematic illustrations of the bacterial cell envelopes for Gram-negative and Gram-positive bacteria. Note the additional outer membrane with an associated LPS layer for Gram-negative bacteria and the thick peptidoglycan layer of Gram-positive bacteria. The proposed interaction profile of antimicrobial peptides during their penetration process to inner membrane are shown. Figure taken from [6]

The outer membrane of Gram-negative bacteria is an asymmetric phospholipid bilayer. The inner leaflet is rich in phospholipids and the outer leaflet contains the characteristic lipid A and the associated LPS layer. Here the hydrated hydrophilic saccharide chains portray a barrier to hydrophobic molecules whereas the hydrophobic core excludes hydrophilic substances and thus this forms an overall tight barrier [29]. The anionic LPS is cross-linked via divalent cations, which strengthens this network barrier. The selective permeability of the outer membrane is achieved via integral outer membrane proteins (OMPs).

The peptidoglycan layer is common to both bacterial classes, yet it is this characteristic that led to the initial classification of Gram-positive and Gram-negative species as the thick pepdidoglycan layer of Gram-positive bacteria (40-80 nm) allows for successful Gram staining. This comparably larger pepdidoglycan layer of Gram-positive bacteria contributes ca. 90% to the bacterial dry weight [6]. The peptidoglycan layer of Gram-negative bacteria is thinner (7-8 nm) and is located in the periplasmic space between the inner and outer membranes and does not allow for staining with Gram [30]. The bacterial shape is attributed to the

Table 1.3: Phospholipid composition in Gram + and Gram - bacteria compared to human membranes

		Gram-negative bacteria		Gram-positive bacteria		Human	
		E. coli	*P. aeuriginosa*	*S. aureus*	*B. subilis*	*Erythrocyte*	*Fibroblast*
Phospholipid	PG	25	21	57	70	-	-
	LPG			38			
	PE	75	60	-	12	27.5	31.8
	CL	-	11	5	4	-	-
	PS	-	-	-	-	14.8	5.9
	PI	-	-	-	-	0.6	2.5
	PC	-	-	-	-	29.2	43.7
	LPC					1.0	
	SP	-	-	-	-	26.2	13.8
	PA	-	-	-	-	n.a.	2.4
Sterol	ERG	-	-	-	-	0.8	0.16
Fatty acid		C16:0	C16:0	a-C15:0	a-C15:0	C16:0	C16:0
		C16:1	C16:1	C18:0	i-C17:0	C18:1	C18:1
		C18:1	C18:1	a-C17:0		C18:2	C18:2
				C20:0	C20:4	C20:4	

Relative distribution of different membrane constituents in Gram-positive and Gram-negative bacteria compared to eukaryotic human cells reported in percentages. Constituents are PG: Phosphotatidylglycerol; LPG: Lysylphosphatidylglyerol; PE: Phosphatidylethanaolamine; CL: Cardiolipin; PS: Phosphatidylserine; PI: Phosphatidylinositol; PC: Phosphatidytlcholine; LPC: Lysylphosphatidylcholine; SP: Sphingolipid; PA: Phosphatidic acid; ERG: Ergosterol. The table was adapted from [6].

stiffness of the peptidoglycan layer, which is lost in spheroplast that lack this layer in both Gram-positive and Gram-negative bacteria [31; 32].

The Gram-positive bacterial cell wall contains lipoteichoic acid (LPA), which is linked via a glycolipid anchor to the plasma membrane. LPA possesses negatively charged phosphate groups that contribute to the overall membrane charge. Around 1.6% of the dry weight of Gram-positive bacteria is composed of LPA [33].

As for all membranes, the cytosolic membrane is a barrier to the exterior and separates the microenvironment of the bacterium. This makes the cytosolic membrane an attractive drug target that is exploited by innate immune functions. Most antimicrobial peptides (AMPs), that form part of the innate immune system, are predicted to act directly on the cytosolic membrane and thus the cell envelope needs to be considered when investigating AMP action. It has been suggested that the bacterial cell wall portrays a network of high electrostatic charge that captures AMPs as a first contact to the bacteria (Figure 1.6, [34; 35]). More

recent advances have recreated the asymmetry of the bacterial envelope, which is a much needed step to study these interactions in a more holistic scenario [36].

1.1.5 Lipid-protein interactions

It has become evident that protein-lipid interactions are important for biological mechanisms and protein topology. The annular lipid shell surrounding a membrane protein needs to form a tight interaction with the protein in order to maintain membrane integrity and yet be dynamic enough to allow for function. The bulk lipids are only slightly affected by integral membrane proteins. The third class of lipids to consider are non-annular lipids that are trapped within a protein or at interfacial regions between individual subunits, these are often described as lipid-cofactors [37; 38; 39]. Protein-lipid interactions represent a bilateral relationship where both components impact each other. Lipids can cause changes of protein backbone topology, oligomerisation, rotational and tilt angles of transmembrane domains as well as changes of side chain orientations (Figure 1.7, [40]). Lipids can also change 2D diffusion patterns directing proteins into specific lipid domains. On the other hand proteins can impact bilayer thickness and lateral lipid organisation or cause lipid movement across leaflets [40; 41; 42]. Complex proteins with multiple transmembrane domains can show multifaceted lipid interactions and thus are highly complex and still poorly understood. For this reason simple model transmembrane peptides have been used in order to understand and characterise protein-lipid interactions in more detail.

The impact of hydrophobic mismatch, an imperfect alignment of the membrane hydrophobic core and the hydrophobic transmembrane domain, on both lipid and protein organisation has been extensively studied using the model peptide WALP (a simple peptide containing membrane anchoring tryptophan residues at either terminus that are separated by a hydrophobic alanine and leucine cluster; [43]). The alanine rich transmembrane cluster is ideal for the characterisation by deuterium (^{2}H) NMR (section 2.1.2) using selectively deuterated side chains to investigate conformational peptide changes like tilt [44; 45]. WALP has been shown to adapt to positive mismatch by tilting, however the change in tilt observed is not enough to fully compensate for the hydrophobic mismatch suggesting that lipid stretching or ordering might have an additional contribution (Figure 1.7). Indeed ^{2}H NMR studies of acyl chain deuterated

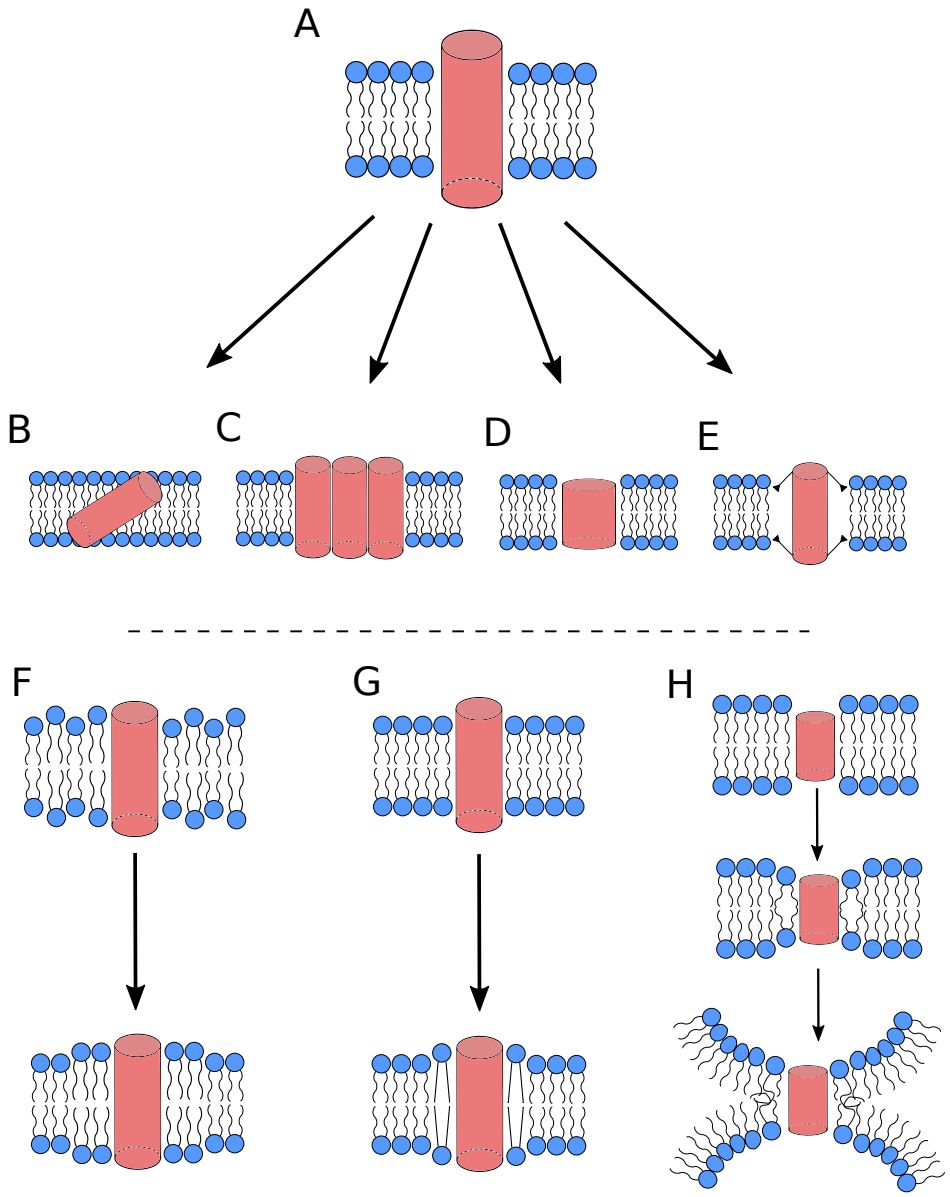

Figure 1.7: Possible peptide and lipid adaptations to both positive and negative hydrophobic mismatch of an alphahelical model peptide. The hydrophobic peptide region is represented by a red cylinder (A). Part I: Peptide adaption to bilayers with positive hydrophobic mismatch. (B) Peptide tilting to accommodate the entire hydrophobic mismatch in the membrane. (C) Peptide oligomerisation to minimise the overall exposed hydrophobic region. (D) Changes in peptide backbone configuration to adapt to the bilayer thickness. (E) Changes in side chain orientation and conformation to adapt to the hydrophobic mismatch. Part II: Lipid adaptations to hydrophobic mismatch. (F) In a membrane of mixed sizes of lipids, peptide interaction can cause lateral phase separation by interacting exclusively with lipids of best hydrophobic thickness match. (G) Lipids can stretch to cause a local bilayer thickening to accommodate the peptide. (H) In a negative hydrophobic mismatch scenario lipid acyl chains can become disordered, in extreme cases forming non-lamellar lipid phases. (Figure adapted from [40])

phospholipids confirmed a slight but consistent acyl chain ordering upon WALP interaction. Nevertheless an overall thickening of the membrane could not be confirmed [43; 46].

In contrast, studies on VpU (a single span channel forming transmembrane peptide from human immunodeficiency virus (HIV)-1) showed that the transmembrane helix can sufficiently tilt to fully compensate for hydrophobic mismatch [47]. Furthermore gramicidin has been reported to increase or decrease bilayer thickness in cases of positive and negative hydrophobic mismatch respectively [48]. These different responses to hydrophobic mismatch by different peptide systems can be explained by different intrinsic peptide characteristics such as their ability to tilt or the propensity for oligomerisation (Figure 1.7).

The flanking Tryptophan residues of WALP peptides were shown to have a strong preference for the interface region between the hydrophobic core and the aqueous environment anchoring the peptide in a preferred orientation that limits its intrinsic ability to tilt [49]. This is facilitated by the comparably rigid side chain structure and the π electronic structure favourably residing in the electrostatic network of the interface. Tryptophan residues also limit the helical reorientation around the peptide longitude axis but interestingly still allow for fast reorientation around the bilayer normal [45; 50; 51]. Experimental conditions are also an important consideration as differences in hydration and lipid packing might force the peptide to respond in different ways.

In addition to hydrophobic mismatch, electrostatic interactions can lead to lipid segregation and cause global reorganisation. Cardiotoxin II, a cationic peptide, was previously shown to segregate anionic from zwitterionic lipids. Additionally changes in the quadrupolar splitting of headgroup deuterated POPC (^{2}H NMR) indicated altered electrostatics at the interface [52]. Similar changes of obscured electrostatics were observed in the membrane interaction of melittin, a peptide found in bee venom, and showed altered macroscopic lipid phases [53]. Headgroups of phosphatidylcholine and phosphatidylserine adapt their conformation upon melittin interactions most likely due to changes in the overall surface charge upon cationic peptide binding [54]. Alike observations have been made for a dissimilar cationic model peptide (K-2GL-20K-2A), suggesting that the lipid head-group moieties adopt to the altered electrostatics at the bilayer surface [55; 56].

1.2 Membrane proteins and peptides

Membrane associated proteins are an essential part of every membrane that account for specific characteristics and specifically designed function. Membrane proteins are responsible for cell-cell communication, environment sensing, exchange of solutes and chemicals as well as energy conversion. In order to fulfil these versatile tasks membrane proteins exist in various forms and classes. It is known that ca. 30% of all genes known encode membrane proteins, yet our knowledge of their structures at atomic resolution remains poor [57; 58]. An overview of all classes of membrane proteins and peptides is beyond the scope of this thesis and a limited introduction to the membrane protein and peptide classes concerned in this thesis will be given.

1.2.1 Viral ion channels

Movement of most hydrophilic substances across a membrane comes with an energetic barrier and thus is aided by special transporters. Some transporters require chemical or physical energy to facilitate transport against a chemical gradient (e.g. ATP or an electro-chemical gradient) and are known as active transporters. Proteins that facilitate chemical transport in the absence of a direct energy source (passive transport) are classified as channels.

Viral ion channels, often referred to as viroporins, are a class of proteins that form functional channels in host cell membranes. Viroporins tend to be small proteins of 60-120 amino acids and contain at least one hydrophobic transmembrane domain [59; 60]. Oligomersiation of individual monomeric subunits results in the formation of hydrophilic channnels that allow for selective transport of ions down their electro-chemical gradient. The relatively small size and high degree of hydrophobicity are common features across all viroporins.

Due to the intrinsic small size of a monomer, oligomerisation of individual protomers is a necessity for the formation of a functional channel architecture. Up to 18 α-helix transmembrane domains have been reported in the channel-forming unit of viroporins (the hexameric form of E5 found in the human papillioma-virus type 16 with three predicted transmembrane domains per monomer [61]). The first viral protein with reported ion channel activity was the M2 protein found in influenza virus A [62]. Since this discovery many other viroporins encoded by a variety of viruses have been reported (representative viroporins shown

in Figure 1.8). It is noteworthy that viral ion channels posses only a low sequence homology when compared to eukaryotic or prokaryotic channels [63]. Viroporins differ in function from classic cellular channels: they often show only very low specificity for a distinct set of ions and only possess a limited gating mechanism. This is attributed to their simplistic architecture which in turn is caused by the restricted coding capacity of the viral genome.

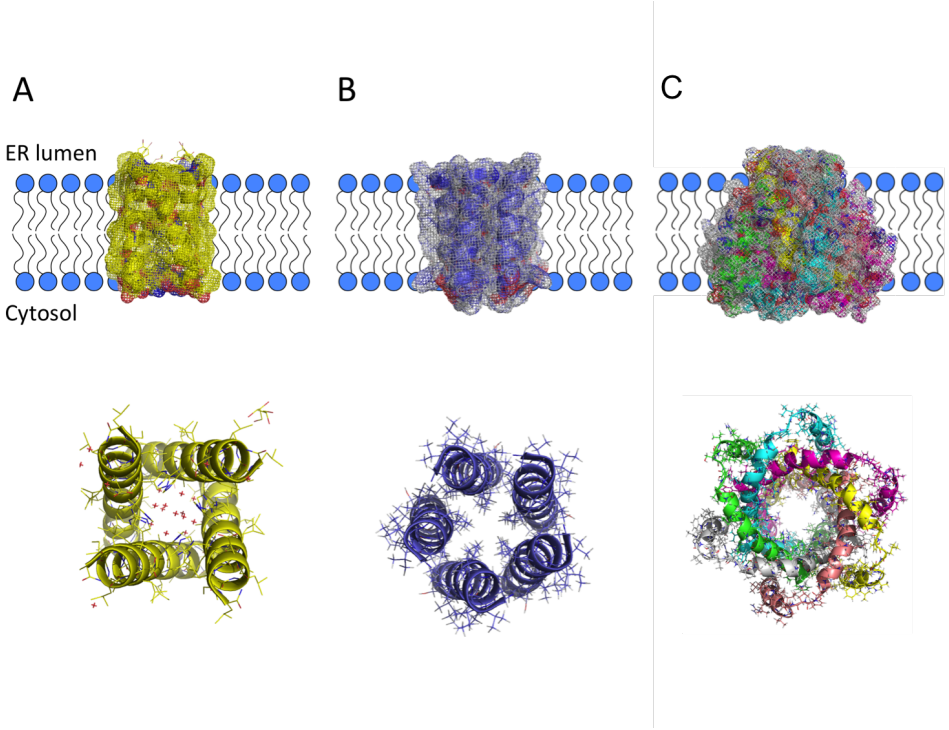

Figure 1.8: Viroporins are shown schematically in a membrane (top) as well as from a top down perspective (bottom). (A) High resolution structure of the oligomeric form of the hydrophobic transmembrane segment (residues 25-46) of M2 (matrix protein 2) from the influenza A virus (diffracted to 1.65 Angstrom, Class IA) [64]. (B) Solid-state NMR structure of the transmembrane segment (residues 2-30) of the Class IA viroporin VpU (viral protein unique) found in HIV-1 [65]. (C) Hexameric structure of the class IIA viroporin p7 found in the Hepatits C Virus. Structure was obtained by solution NMR supported by EM [66].

Viroporins show different behaviours ranging from distinct channels (M2) showing clear single channel opening events in bilayers [67] to more abrupt short lived behaviours (p7; found in Hepatitis C Virus (HCV)). However, p7 has also been shown to conduct by longer lived single-channel events under certain conditions postulating the importance of lipid environment and genotype for distinct functional behaviour patterns [68; 69; 70; 71; 72]. These observations stimulated a debate as to whether viral ion channels are distinct channels or form unspecific pores across a membrane, although the ion conductance of viroporins can be selectively inhibited in most cases, broadly suggesting discretely organised membrane

channels. This complexity is further enhanced by the possible coexistence of multiple oligomeric states in a lipid environment, which might depend on environmental differences and experimental conditions [68; 73; 74].

With an increasing rate of discovery of new viroporins, a classification system based on their topology has been proposed: Viroporins with one transmembrane domain are classified as Class I and viroporins with two transmembrane domains are classified as Class II [75]. These classes are further subdivided where Class IA has a short N-terminal domain facing the the ER lumen and Class IB has its N-terminus projecting towards the cytosol; the same applies for Class II. Viroporins with predicted three transmembrane domains are yet to be included in the classification system. It is also noteworthy that structurally related viroporins often perform very different functions in the affected host cell (Figure 1.9). Initially, viroporins were discovered in RNA viruses, however they have also been identified in DNA viruses [76; 77].

The exact functional mechanism of viroporins remains poorly understood. Viroporins have been found to be involved in infection, viral replication, viral assembly and viral release (Figure 1.9). The best understood viroporin to date is the proton-selective M2 channel, which depolarises the viral membrane post endocytosis, which in turn causes release of the viral RNA genome [78; 79]. M2 has been shown to equilibrate the pH gradient of the Golgi membrane post viral entry, which maintains the pre-fusion form of the glycoprotein hemagglutin during viral maturation [80; 81]. The precise function of other viroporins is less well established. However, viroporins might posses the possibility to act in multiple functionalities (Figure 1.9); the viroporin p7 has been previously shown to alter the pH gradient across the secretory pathway [82], but it is also known to interact with other non-structural proteins of HCV at the plasma membrane (e.g. NS2) [83; 84; 85; 86; 87]. In general viroporins show an ability to depolarise cellular membranes, having an impact on cellular homeostasis, which can affect cellular and viral processes like induction of apoptosis and viral release [75; 88]. Further to this, general cation leakage has been attributed to viroporins which is linked to apoptosis [89]. Thus viroporins affect a range of relevant cellular processes of host cells, most of which lead to disruption of physiological relevant cellular systems (Figure 1.9), including cellular trafficking and signalling. A common characteristic of viroporins is that they are nearly universally essential to the viral life cycle [59]; it is yet to be shown if this is attributed to their channel function or alternative functions in the viral life cycle that viroporins may perform [90]. Viroporins are therefore an attractive therapeutical target.

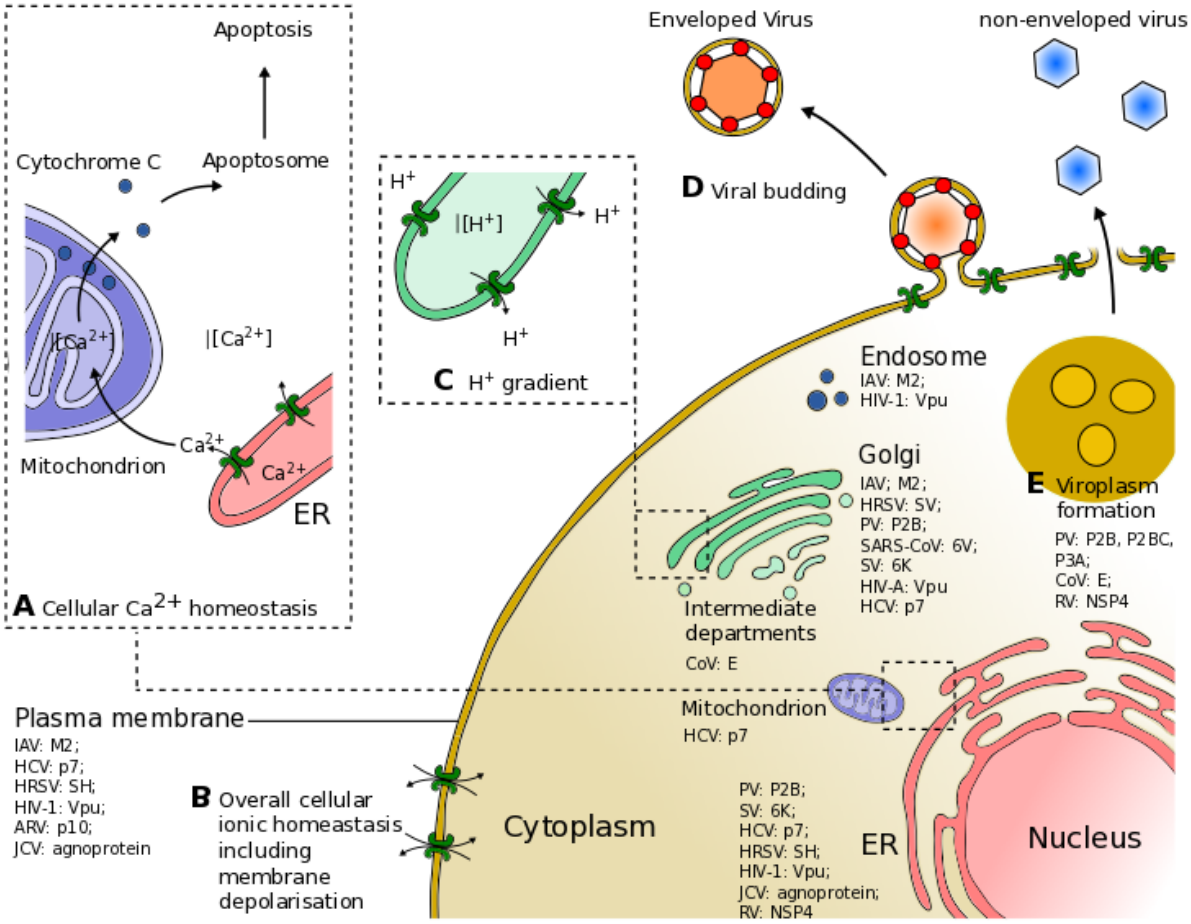

Figure 1.9: Schematic illustrating the different cellular processes that have been shown to be affected by various viroporins. It has been shown that viruses with malfunctioning or absent viroporins are not able to reproduce functional viruses within the host cell. As illustrated all main organelles are targeted by viroporins, which mostly translates into altered host homeostasis. The viruses and corresponding viroporin affecting the specific organelle are listed. (A) Viroporins associated with Ca^{2+} homeostasis. Release of Ca^{2+} from the ER via viroporins can lead to Ca^{2+} uptake by the mitochondria altering the membrane potential, which in turn triggers the release of cytochome c, which in the cytosol is associated with apoptotic mechanism. (B) Viroporins affecting the plasma membrane potential. (C) Viroporins have been shown to alter the proton gradient in different cellular compartments including the trans-Golgi network. Proton release lowers acidity and has an effect on glycoprotein trafficking. (D) Viroporins have been reported to be involved with viral budding and (E) also cause remodelling of the viral membrane during virus maturation. IAV: influenza virus A; HRSV: human respiratory syncytial virus; PV: poliovirus; SV: Sindbis virus; JCV: JC polyomavirus; CoV: coronavirus; RV: rotavirus; ARV: avian reovirus; SARS CoV: severe acute respiratory syndrome CoV. Figure adapted from [75]

1.2.1.1 Pharmacological relevance of viroporins

The M2 viroporin has been a drug target for a prolonged time. Amantadine was the first drug to be licensed for the treatment of influenza A virus (IAV) in the 1960s [91; 92; 93; 94; 95; 96], although its exact target was not know and only later it was discovered to be the M2 protein [97] with its channel-forming activity being discovered even later [62].

The transmembrane domains of the M2 viroporin have been extensively characterised in membrane mimetic and membrane environments (solution, solid-sate NMR and crystallography). The transmembrane domain forms in all cases a left handed tetrameric helix bundle. The channel lumen contains well defined His37 and Trp41 tetrads. Despite extensive structural information, at different pH levels and with bound inhibitors (amantidine, remantidine and others), the distinct drug binding site is controversial. A solution NMR structure of the transmembrane domain in detergent placed rimantidine to a peripheral membrane phasing site, suggesting allosteric inhibition [98], whereas a solid-state NMR structure in DMPC showed amantidine bound to the channel lumen [99; 100]. Similarly a crystal structure of the transmembrane domain also showed amantidine bound to the channel lumen [101]. Recently, progress has been made to elucidating the full length M2 structure in a bilayer [102].

In spite of an extensive structural characterisation of adamantine inhibition, its use as a drug came to a halt due to increasing cases of resistance. It is noteworthy that most resistance mutations are located at the channel lumen, consistent with an amantidine binding site in this region [99; 103; 104; 105; 106; 107]. The most prominent examples of resistance-carrying influenza strains included isolates from H1N1, H5N1 and H7N9 [108], often referred informally to as 'swine' and 'avian' flu influenza. These pandemics also stimulated high interest in finding novel M2 inhibitors, most of these "new" compounds are derivatives of amantidine.

VpU, a class I viroporin found in HIV-1, has been demonstrated to be inhibited by hexamethylene amiloride (HMA). HMA has been shown to inhibit the cation selective channel activity *in vitro* and also inhibit viral particle formation in cell culture *in vivo* [109; 110; 111; 112]. There are several solution NMR structures of both the cytosolic and the transmembrane domain of VpU available (Cytosolic: [113; 114]; Transmembrane domain: [65; 115; 116; 116]). The two separate domains were modelled to gain insight into the full length VpU structure

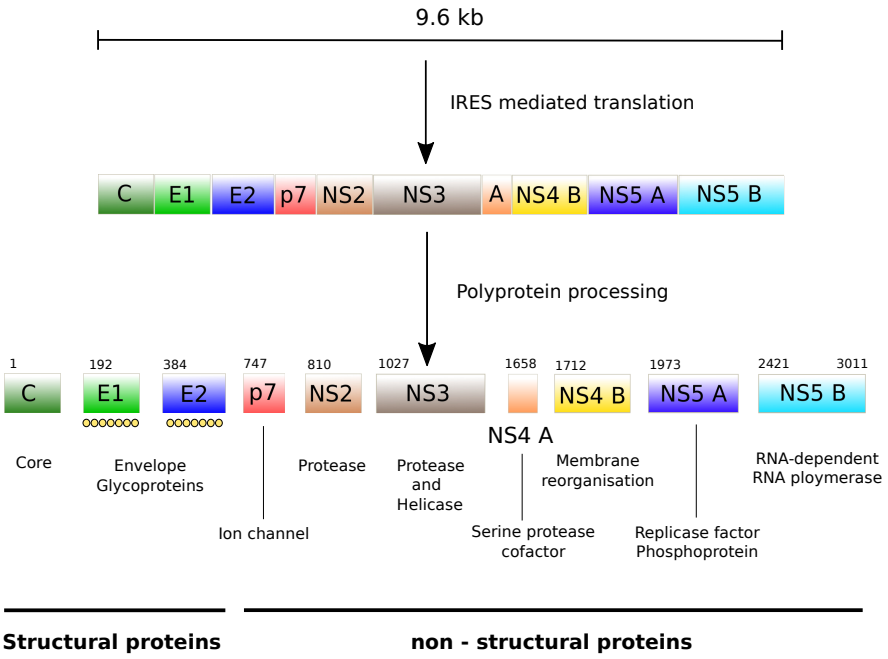

Figure 1.10: Schematic illustrating the HCV genome (positive RNA genome shown on top) and polyprotein processing. The positive RNA genome is translated via an IRES into a polyprotein. Individual components are depicted and the amino acid sequence position is displayed above each. The processed polyprotein yields three structural proteins and six non-structural proteins plus one cofactor as shown. It is noteworthy that the non-structural proteins are processed by the viral proteases NS2-3 and NS3-4A. The structural proteins and p7 are cleaved by the endoplasmic reticulum signal peptidase. Figure adapted [121].

[117]. Interestingly an introduced His residue at position 18 (Ala18His) generated a VpU mutant that is sensitive to amantidine. A His residue at position 18 completes the H[x x x]W motif found in M2 and reinforces the hypothesis that VpU has a channel like behaviour and an amantidine interaction with the His and Trp tetrads in M2 [118; 119; 120]. The lack of mechanistic insight and complete structural information makes it difficult to place inhibition by HMA into context. There are no resistance mutations to HMA reported and thus the HMA binding site remains elusive. Docking studies predict HMA binding to the channel lumen neighbouring serine at position 23 [112].

The viroporin p7, located between the structural and non-structural proteins within the polyprotein (Figure 1.10), has two transmembrane domains and thus is classified as class II. p7 primarily localises to the endoplasmic reticulum (ER) membrane and has been shown to be sensitive to amantadine, nonylated imino-iminosugars and HMA [70; 71; 122]. HCV studies on chimpanzees showed p7 to be essential for viral replication and established its

potential as a therapeutic target [123]. With the availability of HCV culture methods, based around HCV genotype 2a isolate "JFH-1" , its importance during the viral life cycle was confirmed [124; 125]. The channel function, shown to be a dualism between single channel events and more pore like bursts, is dependent on protomer oligomerisation where precise channel behaviour depends on the lipid environment [72]. p7 is known to have additional functions that rely on protein-protein interactions most likely with the viral protease NS2, NS5A, core and E2 (Figure 1.10), but here the stoichiometry remains unknown [83; 126]. p7 interaction with NS2 has been characterised in part and it is postulated that p7 acts as a mediator in viral particle assembly. p7 and NS2 control sub-cellular compartmentalisation within infected host cells coordinating the location of core between the ER and lipid droplets [127; 128; 129; 130; 131]. Its interaction with core, E1, E2 and NS2 complements evidence of a role during viral assembly in the late stages of the viral live cycle [132; 133].

The large genetic variance within the viroporin p7 (see Chapter 7 and Figure 7.1) led to speculation that common inhibitors such as amantadine will not have a broad enough spectrum of activity and p7 was often portrayed as an unqualified therapeutic target. Indeed various sensitivity profiles of drugs were observed across different genotypes [134; 135]. Nevertheless, two candidates showed sufficiently broad sensitivity profiles to further pursue p7 as drug target: rimantadine and *N*-nonyl deoxynjirimycin (*N*N-DNJ), an imino-sugar [134; 135]. Amantadine showed conflicting results in *in vitro* and *in vivo* studies, showing inhibition of p7 channel function *in vitro* (p7 gt1b J4) but no affect on viral release in cell culture (Gt1b Con1) [70; 134; 135]. Strikingly, amantidine resistance was shown to be residue independent of *N*N-DNJ resistance. Amantadine has been expected to interact with the peripheral region where two conserved leucine residues are located, mutation of which affects drug sensitivity [136; 137]. Later amantadine was indeed found to be located close to the peripheral region of a hexameric channel obtained by solution NMR [138]. A peripheral binding site is also supported in a heptameric model despite clear structural differences in both models [139]. In both cases the resistance inducing polymorphism at residue 20 is shown to be in close proximity [140]. A peripheral binding site broadly suggests an allosteric mode of action stabilising a closed channel formation, similar to the proposed allosteric inhibition of M2 [98].

The binding site of *N*N-DNJ is still unknown. Initial docking studies suggested a potential drug interface between the individual monomers and a possible interaction with Phe25

[137]. This is also consistent with known resistant polymorphisms from genotypes 3a which contains Ala25, transferring this mutation into other genotypes induced resistance to *N*N-DNJ. Following this it was proposed that *N*N-DNJ acts by hindering oligomerisation.

Overall viroporins represent attractive therapeutic targets and numerous new members to the family are still being discovered in a range of different viruses. Yet, it remains still a rather unexplored area of virology. Despite the broad range of viroporins rimantadine and amantadine remain the only licensed therapeutics suggesting that with up-to-date drug discovery methodology there is still high potential for novel and more effective compounds. An example being BIT225, currently in phase II clinical trials against HIV-1 and HCV (Gt 1) and inhibits both p7 and VpU channel activities [141]. It is however evident that the lack of meaningful high-resolution structural data is currently impeding the identification of new improved drug candidates as well as biophysical characterisation of their binding sites.

1.2.2 Membrane-active peptides

Peptides fulfil a range of different functions in Biology. Peptides are involved in cellular signalling, form part of large assemblies on membranes and often show membrane activity as bilayer-disrupting agents or as biological agents that successfully pass through a membrane. A particular interest has been devoted to antimicrobial peptides (AMPs) also known as host defence peptides, a primarily membrane lytic class of peptides that forms part of the innate immune system [142; 143; 144; 145]. More recently it was also shown that AMPs might possess a function as signal transducting peptides affecting the cellular machinery. The precise molecular mechanisms by which these peptides act are complex and depend on many parameters.

1.2.2.1 Antimicrobial peptides (AMPs)

AMPs are highly versatile and come in different forms that have attracted recent focus due to their potential as novel antibiotics. Generally most AMPs are short amino acid strains ranging from 10-50 amino acids in length (Figure 1.11A) and can adopt an alpha helix or a disulphide bridge stabilised beta sheet. Unstructured loop regions are also found. In the AMP sequences discovered to date (ca. 2700), it is not possible to identify a general sequence motif that is responsible for membrane activity, however, most peptides have a

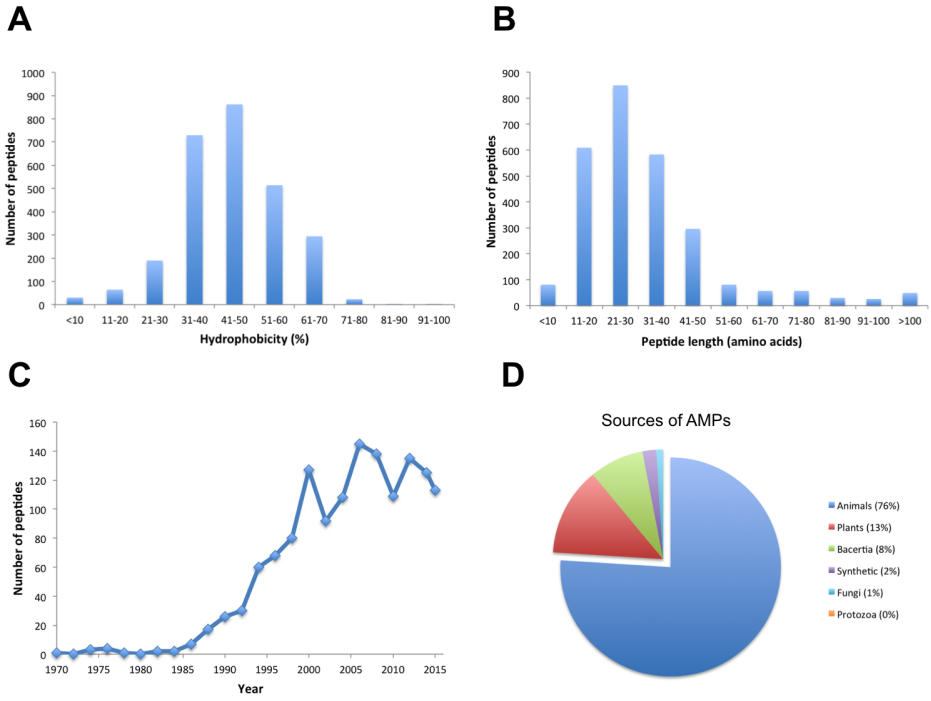

Figure 1.11: General statistical information on the nature of AMPs. (A)The percentage hydrophobicity and (B) the average peptide length is plotted against number of peptides in the database. (C)The number of new peptide discoveries is plotted as function of time with the last datapoint being 2015. (D) The relative sources of the to date discovered AMPs is plotted in percentiles. Statistics obtained from the antimicrobial peptide database in July 2016 [146; 147]. Data for figure part "D" taken from [148].

net positive charge and a spatial separation between charged and hydrophobic residues (amphipathicity). This basic architecture is thought to allow peptide interaction with charged lipid headgroup moieties and simultaneous infiltration of the hydrophobic core region resulting in a destabilisation of the bilayer.

Most AMPs are thought to act by compromising the bilayer integrity by distinct mechanisms that eventually cause cell lysis. However, more recent studies suggest that below lethal concentrations peptides can also act as signal transducing agents that pass a membrane [149]. Cecropin A has been shown to alter transcription levels of multiple genes when added to *E. coli* in culture. Whether this is a specific response or a generic stress response remains elusive, yet the up-regulated genes are distinct from other stress responses (thermal, oxidative, osmotic or nutritional origin; [150]).

Similarly some AMPs have been shown to inhibit specific cellular functions post membrane permeabilisation. It has been postulated that this secondary inhibition might be the actual

lethal event. This hypothesis was formulated based on a temporal and functional separation between membrane interference and cellular death [151; 152; 153; 154]. Pyrrhocoricin, drosocin and apidaepicin, all originating from insect cells, were shown to inhibit the intracellular heat shock protein DnaK, which in turn prevents chaperone-assisted protein folding and leads to cell death. Other AMPs have been shown to inhibit the biosynthesis of the cell wall by interacting with lipid II (e.g. Class I bacteriocins nisin; [155]). Others inhibit the biosynthesis of nucleic acids and proteins; buforin II, sharing a sequence identity with the N-terminal domain of histone H2A, is known to bind to DNA and RNA post membrane penetration without causing membrane lesion [156]. It is possible that AMPs act by a combinatorial approach of multiple distinct mechanisms including membrane activity. This theorem has been referred to as "multi-hit process" [157]. Yet such a process may depend on local factors such as pH, temperature and osmolarity [23].

Despite other cellular targets, most AMPs were shown to have a certain degree of membrane activity and primarily act by causing membrane lesion. The structural properties of AMPs often relate to their mode of action, yet a precise structure-function relationship is mostly unknown. It has become increasingly evident that the action of AMPs depends on the structural elements of inherent charge, peptide conformation, polar angle, relative hydrophobicity and amphipathicity (summarised in Table 1.4). It is the interplay between these factors, which are dictated by the precise amino acid sequence, that determines the fate of AMP function.

The first contact of AMPs with a biological membrane is most often mediated by electrostatic interactions. Most evident is the electrostatic attraction between the anionic lipid headgroups and the cationic residues of the peptide, which most likely attributes for the conservation of positive charged residues across all AMPs. It has been proposed that at first contact with a Gram-negative bacterial membrane, AMPs displace the divalent cations found in the LPS layer, destabilising the outer membrane. Gram-positive bacteria that lack the outer membrane contain additional negatively charged teichoic and teichuronic acid, which enhances AMP-membrane interactions. The comparably large electrochemical gradient across the bacterial membrane further drives the AMP-pathogen interaction. Indeed early studies showed an increased membrane activity correlating to a larger electrochemical gradient (melittin and tachyplesin I; [159]).

Table 1.4: Biophysical properties of AMPs

Biophysical characterisitcs of AMPs	
1. Conformation	Despite the vast sequence variety of AMPs most peptides display an alpha helical or beta sheet secondary structure. Mixed alpha helical and beta sheet secondary structure (defensins) or non-structured (indolicidis) AMPs have also been reported. Alpha helical peptides most commonly exist in unstructured extended conformations in solution and adopt their secondary structure upon membrane interaction.
2. Charge	Most AMPs possess an intrinsic net positive charge ranging from +2 - +9. The charged residues often form defined patches and are thought to be critical for an interaction with the anionic membrane of most microorganisms (PG, PS and CL). The membrane electrostatics differ by up to 50% between microbial targets and most mammalian cells, thus this interaction was proposed to be key for AMP selectivity.
3. Amphipathicity	Many different forms of amphipathicity exist, however the most common structural motif is the amphipathic alpha helix; an amphipathic helix is normally based on 3 to 4 residue periodicity and forms an optimal cluster for membrane insertion. Beta sheets form amphipathicity by alternating strands of high hydrophobic and low hydrophobic contents, most often in an antiparallel manner. While being important for antimicrobial activity, hydrophobicity has also been attributed to peptide interaction with zwitterioninc membranes and thus the toxic effect of hemolysis. Amphipathicity is generally measured by the hydrophobic moment of a peptide.
4. Hydrophobicity	Most AMPs have a relative hydrophobicity (abundance of hydrophobic residues) of ca. 50% (Figure1.11A). Hydrophobicity is important for membrane activity yet it can result in a high degree of cytotoxicity and an interplay with the positive charged residues is important to achieve selectivity, which depends on the exact characteristics of the targeted membrane eg. lipid composition.
5. Polar Angle	The polar angle is a relative measurement of polar and non-polar segregation around a helix. If one half along the longitude axis of the cylinder-like helix is composed of polar residues and the opposite side entirely of hydrophobic residues this would correspond to a polar angle of 180°. It is suggested that a smaller polar angle corresponds to greater membrane permeabilising abilities and forms pore structures more readily, yet the stability of these pores is also considerably less when compared to peptides with a large polar angle. Eg. PGLa ($\theta = 100°$) has a higher permeabilising ability then magainin 2 ($\theta = 180°$) [158].

Summery of key biophysical properties of AMPs. The precise mode of action of an individual AMP depends on the interplay of all or a subset of these features [23].

Initial membrane contact triggers folding of the peptide, which is unstructured in solution. This is thought to be followed by one of three distinct mechanisms that disrupt membrane integrity (Figure 1.12): by forming a barrel-stave pore (A), a toroidal pore (B) or a less organised carpet mechanism (C). The mechanistics of each are outlined below.

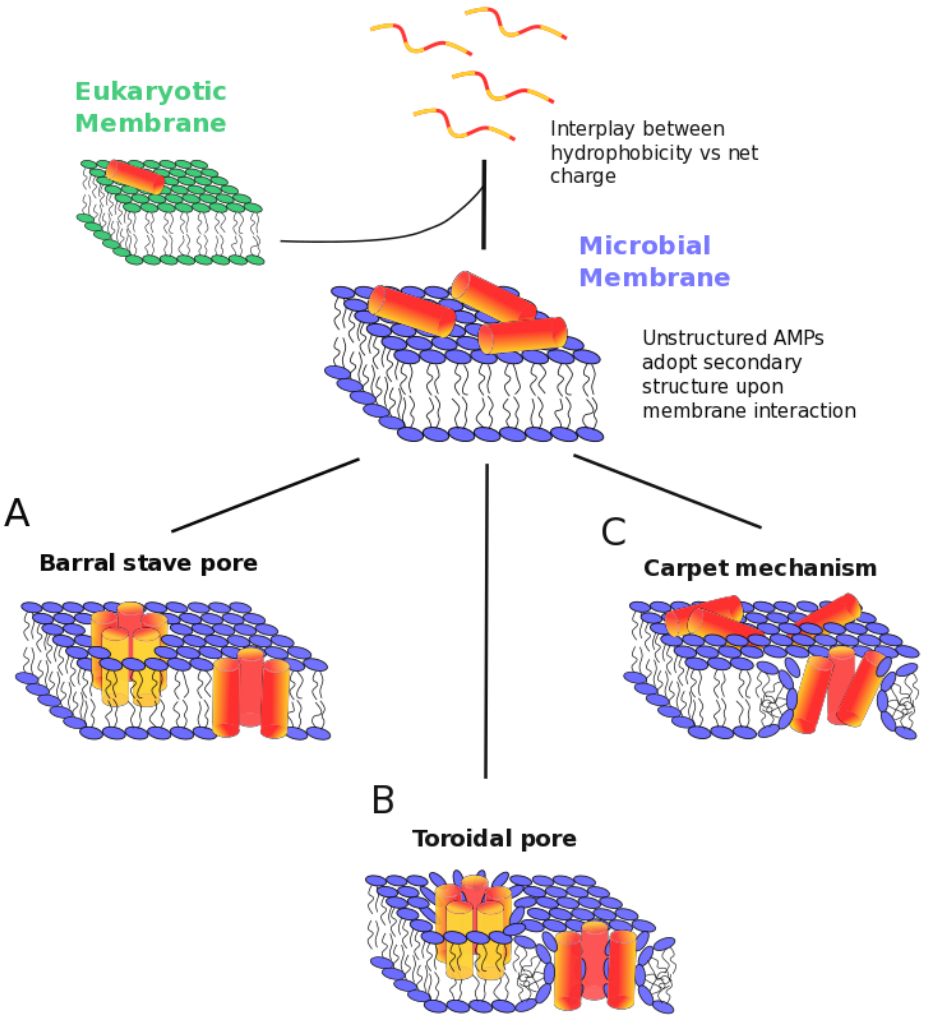

Figure 1.12: Schematic illustrating the most commonly cited modes of actions of AMPs. AMPs tend to be unstructured in solution and adopt their secondary structure upon membrane interaction, most commonly folding into their characteristic amphipathic arrangement (hydrophobic regions (yellow) and charged regions (red) are spatially separated). The membrane selectivity of AMPs is mainly dependent on an interplay between the overall charge and hydrophobicity (Table 1.4). Commonly AMPs are thought to compromise membrane integrity by one of three ways: (A) Barrel-Stave pore, (B) Toroidal pore and (C) a less organised carpet mechanisms. Note that sometimes an additional detergent-like mechanism is also quoted, which in principal is similar to the here illustrated carpet mechanism. All depicted mechanisms induce membrane lesion.

1. Barrel-Stave pore:

In a barrel-stave mechanism individual peptides come together to form the classical architecture of a membrane pore structure: a ring-like peptide structure that shields the aqueous pore interior from the hydrophobic membrane core. The amphipathicity of the peptide is exploited and the hydrophobic residues point to the bilayer core whereas the charged peptide side lines the aqueous pore. The pore forming process is dependent on the local peptide concentration. At an initial membrane binding event a conformational change opens up the headgroup region of the membrane and allows peptide translocation towards the membrane interior. It is thought that, subject to a critical local peptide concentration, peptides continue to aggregate and force the assembly structure further into the membrane until a complete pore is established. This process may be assisted by local membrane thinning and curvature. The initial peptide aggregation is most likely driven by hydrophobic interactions where aggregation is thermodynamically favourable as it shields the charged amino acids from the bilayer core. In general a minimum peptide length of ∼20 amino acids is required in order to span the full bilayer in an alpha helix. Recent studies have also indicated that pores might be prone to expansion up on additional peptide addition [160; 161].

2. Toroidal pore:

In a toroidal pore peptides bend into the bilayer and line the pore together with the lipid headgroups that also bend in away from the bilayer normal, forming a lipid connection between both membrane leaflets. The polar lipid headgroups associate together with the polar peptide phase, which most likely masks the cationic peptide charge and lines the aqueous pore [161]. The main difference to the barrel-stave model is that the peptide interacts with lipid headgroup moieties along the entire span of the pore.

Similar to the barrel-stave pore, a toroidal pore is preceded by an initial membrane binding event with peptides oriented perpendicularly to the membrane normal, triggering a minor disruption in the phospholipid bilayer. Lipid displacement by the hydrophobic peptide side triggers positive lipid curvature that, with increasing local peptide concentration, develops into a toroidal pore.

Magainin and mellitin are toroidal pore forming peptides [25; 161]. Novicidin has also been shown to form toroidal pores, yet novicidin orientation is not parallel to the membrane normal and is close to a near perpendicular orientation, suggesting that complete bending of the peptide is not needed to induce a complete toroidal pore [162].

3. Carpet mechanism:

The carpet mechanism does not require specific interactions between peptide monomers for membrane solubilisation. Peptides initially bind to the membrane and cause rupture in a detergent-like manner, which causes extreme membrane destabilisation. Prior to this a critical threshold level needs to be reached at which non-specific quaternary structures containing both peptide and lipid form. Following this slightly stochastic process the thermodynamic barrier of the peptide clustered membrane is passed and it disintegrates. It has also been suggested that the peptide inserts in the headgroup region in a cone like manner, which cause strong lipid curvature. Formation of micellar structures has been reported [163; 164].

More recently, imaging of almethicin pores (barrel-stave) revealed a dynamic pore that may posses multiple conducting states, if this behaviour originates from a single pore or an assembly of multiple pores at the same spot remains to be seen [165]. Furthermore, a distorted toroidal pore was observed in the case of melittin and a magainin analog where lipids are curved, yet these models show a more stochastic peptide distribution [166; 167; 168]. Similarly the toroidal pore has been proposed to be an artefact due to relatively high peptide concentration *in vitro* and might portray the end state of membrane lesion caused otherwise by a carpet mechanism [169]. The relative live time of toroidal pores varies [164]. Furthermore, AMPs can act in synergy, which was successfully shown for PGLa and megainin 2. Individually these peptides are either near-parallel to the bilayer plane or slightly tilted, however at equimolar ratio PGLa changes to a fully inserted transmembrane peptide. Magainin on the other hand does not change its orientation [170; 171]. PGLa is highly susceptible to the local environment and different topological states have been observed [170]. This synergistic behaviour translates into increased antimicrobial activity and resulted in excess of 20-fold increased carboxyfluoresein leakage from vesicles treated by a combination of magainin-2 and PGLa [172].

Hence, it becomes increasingly evident that AMPs might not simply act by distinct individual mechanism as previously thought, but instead develop their potency via multiple dynamic intermediate states that might possess a certain degree of disorder. It is plausible that the three described mechanisms of action are related and might even portray a continuum [169]. Such a versatile scenario may explain the low degree of resistance to AMPs, as no single conserved mechanism is established.

1.2.2.2 Therapeutic potential of AMPs and resistance

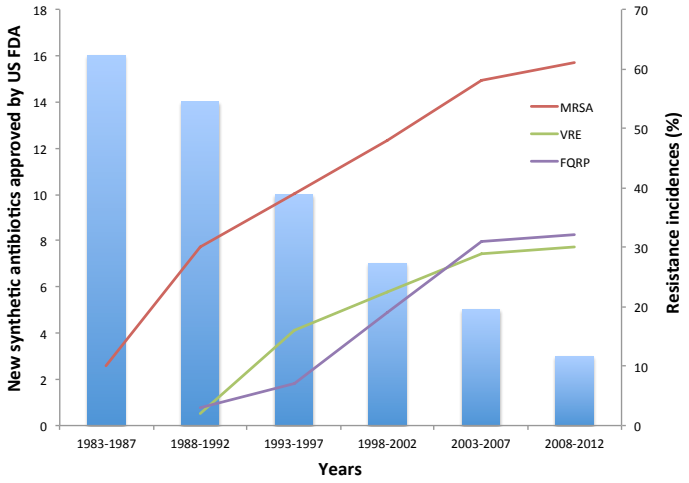

Figure 1.13: The approval of new synthetic antibiotics by the US FDA is plotted as a bar chart. The occurrence rate of three common resistant infections is plotted for comparison. Methicillin-resistant *Staphylococcus aureus* (MRSA), vancomycin-resistant *enterococci* (VRE) and fluoroquinolone-resistant *Pseudomonas aeruginosa* (FQRP) all show an increase in relative occurrence whereas the development of new antibiotics is lacking. This development creates a toxic environment for modern health care. (The data is based on estimates based around intensive care units of hospitals that participate in the CDC National Nosocomial Infections Suveillance System.) Figure adapted from [173].

The recent spread of antimicrobial resistance drives the search for alternative means to combat microbial infection. The first conventional antibiotic, penicillin, was introduced to the market in the 1940s. This triggered a flood of new small-molecule antibiotics, which peaked in the 1960s and has been on a decline since. The affordability and ready availability of antibiotics triggered heavy overuse and in turn the development of resistance (Figure 1.13). Sir Alexander Fleming was already sceptical when giving his Nobel Lecture in 1945: "The time may come when penicillin can be bought by anyone in the shops. Then there is the danger that the ignorant man may easily under-dose himself and by exposing his microbes to non-lethal quantities of the drug make them resistant." The rise of antibiotic resistance and

the lack of novel antibiotics creates a critical challenge for the modern healthcare systems, stimulating the urgent search for novel antibiotics.

Understanding of AMP-lipid interactions is key in order to further develop AMPs as potential drug candidates. Despite their ubiquity in higher organisms, not many cases of resistance to AMPs are known, since unlike most conventional antibiotics, AMPs lack a specific protein target. Instead AMPs interact with a broad range of hydrophobic and anionic targets, hence development of a single resistance mechanism becomes more difficult. In order to exploit the potential drug reservoir of AMPs, a detailed understanding of the structure-function relationship is needed in order to design of more selective and more potent peptide sequences.

Different approaches have been applied for the development of new peptide sequences. First-generation peptides typically relied on naturally occurring templates. Pexiganan, a derivative of megainin, is currently in phase III trials for treatment of diabetic foot ulcers. Omiganan, similarly template based, has also reached phase III clinical trials and shows promise to combat catheter infections [174]. The field has now progressed to more elaborate design principles based on biophysical fundamentals in combination with computer-assisted molecular design. Recently machine learning and genetic algorithms mimicking evolution have been added to the toolbox [175; 176; 177; 178]. Despite initial success, AMP based therapeutics still have challenges to meet: peptide manufacturing is still comparably expensive, peptides are inherently prone to proteolytic degradation and still have an unknown toxicology profile, as data on systematic AMP administration is scarce.

An alternative strategy for therapy is the selective stimulation of native AMP production by the innate immune system, where AMPs play a crucial role for inflammation. Studies have shown that Vitamin D can stimulate the production of AMPs. Calcitriol, a metabolite of Vitamin D, was shown to enhance the production of cathelicidin and hBD-2 in cell culture of keratinocytes. This resulted in an increased cytotoxic effect against *S. aureus* [179; 180]. In addition to the antibacterial effects, cathelicidin peptide LL-37 showed increased antiviral effects in human specifically against the herpes simplex virus (HSV), vaccinia virus and also more generally against retroviral replication [179; 181].

Despite the great therapeutic potential of AMPs, some common resistance mechanisms have been observed. Most commonly these involve the shielding of the membrane potential, thus inhibiting initial charge-driven AMP binding. *B. thetaiotaomicron*, a Gram-negative bacterium residing in the gut microbiota, was shown to be more sensitive to AMPs during an inflammation response when the *lpxF* encoding gene was deleted. *LpxF* is responsible for dephosphorylation of lipid A and when active neutralises the surface charge [182]. Similar behaviour is induced in the response to AMPs by the PhoP-PhoQ and OmrA-PmrB regulatory systems. PhoQ triggers a gene regulatory response in *Salmonella enterica* Typhimurium that results in the addition of a positively charged 4-amino-4-deoxy-L-arabinose (Ara4N) moiety to LPS [183]. *Burkholderia capacia* is known to be resistant to AMPs, and similarly this is believed to be caused by continuous production of Ara4N containing LPS. Gram-positive bacteria have similar resistance mechanisms that mainly focus on D-alanylation of teichoic acid to reduce the net membrane charge [184]. Many of these processes are facilitated by specific target gene regulations.

Biofilms cause many persistent infections, which are resistant to many antimicrobial compounds and also show reduced susceptibility to AMPs. Extracellular DNA, which is needed to stabilise the architecture of a biofilm environment [185], is known to be able to chelate cations and was recently reported to also reduce AMP activity. Note that DNA at high concentrations possesses an antimicrobial activity itself by chelating the divalent cations of LPS. However, at sub-lethal concentrations external DNA was shown to create a divalent cation depleted environment, which in turn is sensed by the PhoP-PhoQ pathway and triggers a genetic response that reduces AMP efficiency by LPS modification [186].

Peptides are prone to proteolytic degradation, which is exploited by many pathogens that produce specific proteases and peptidases. AMPs are unstructured in solution and thus present easily accessible proteolytic cleavage sites. The proteolytic susceptibility of LL-37 has been extensively studied and many human pathogens have been identified that facilitate LL-37 degradation. Early degradation products produced by *P. aeruginosa* elastase showed some antimicrobial potency that was lost by the final products. Remarkably elastase was shown to preferentially cleave regions that are responsible for antimicrobial activity [187].

Similar to conventional multi-drug resistances, efflux pumps have been shown to have an effect on AMP activity. The energy-dependent Mtr efflux pump found in *Meiseria*

gonorrhoeae was shown to be involved in resistance to LL-37 and PG-1, among other AMPs. Interestingly, LL-37 is an alpha helical peptide whereas PG-1 adopts a beta sheet secondary structure, which illustrates the broad spectrum of substrates of Mtr. Similar transporter systems like ABC transporters can also contribute to AMP resistance, implying a broad and general mechanism for AMP resistance [188].

More recently the possibility of specific AMP inhibiting peptides was demonstrated. These peptides form stable coiled-coil interactions with AMPs, successfully inhibiting their activity, although this has not yet been observed in nature and remains an intellectual exercise [189]. Nonetheless, no widespread resistance to AMP action is observed to date, and reported examples are specific scenarios, thus illustrating the potential of AMPs as new antimicrobial compounds for therapy.

1.2.2.3 Cell-penetrating peptides (CPPs)

The hydrophobic core of membranes is an effective barrier to the passage of hydrophilic substances, critical to the biological concept of compartmentalisation. Peptides that are capable of penetrating the biological membrane, in contrast to insertion followed by membrane lysis for AMPs, are useful tools to deliver cargo (nucleic acids, drugs or imaging agents). CPPs are known to be able to enter the cell by direct membrane penetration, receptor-mediated uptake or by the energy-dependent process of endocytosis [190; 191; 192]. Examples of naturally derived CPPs are the common TAT and penetratin peptide sequences, which are both truncated versions of the corresponding full length protein [193; 194; 195].

Similar to AMPs, CPPs are generally positively charged and possess a high degree of lysine and arginine residues. CPPs are proposed to primarily interact with anionic lipids like PS and PG most likely via the guanidine group found in arginine that allows extensive hydrogen bonding. Lysine has the same net charge, yet lacks the guanidine group and has weaker penetrating properties when acting on its own [196]. It is evident that these characteristics are similar to many general features of AMPs; hence CPPs might indeed possess some intrinsic antimicrobial activity too and conversely AMPs might serve as templates for future development of CPPs.

CPPs have been used to deliver covalently and non-covalently attached cargo to the cellular interior and thus play also a role in the development of nanocarriers that deliver larger cargo to cells *in vivo* and *in vitro*. CPPs tend to be active against a broad range of cells and often lack distinct specificity, which led to the idea of "smart" platforms: nanocarriers that trigger release based on local tissue-dependent characteristics. The distinct hypoxic microenvironment of tumours shows high potential to be susceptible to one of these systems.

1.3 Aims of this thesis

The aim of this thesis is the structural investigation of the versatility of alpha-helical membrane-active peptides and proteins in a native-like model environment. The work is supported by a BBSRC-CASE studentship with the National Physical Laboratory (NPL) and collaborative work is acknowledged where it is included to aid understanding. Two distinct membrane-active systems are biophysically characterised, each with a different mode of membrane activity allowing for selective functions, ranging from destructive membrane assemblies to defined channel structures. The individual membrane active systems studied require different strategies for characterisation due to significant differences in the respective modes of membrane interaction. Principles of magnetic resonance based on single structural constraints are used in order to gain molecular understanding, supplemented by a range of biophysical methods in order to achieve a more holistic understanding. On the one hand, short antimicrobial peptide sequences (AMPs; 21 amino acids) are characterised in an anionic membrane environment, mimicking the bacterial cytosolic membrane. On the other hand, a larger system of the viroporin p7 (HCV, 63 amino acids) is investigated regarding helix orientation and protein oligomerisation in membrane environments mimicking the native endoplasmic reticulum (ER) membrane, where p7 is expected to localise. The systems differ in the fact that the studied AMPs were designed to develop their antimicrobial potency in the membrane interface; whereas p7, naturally expressed as part of HCV viral genome, is expected to span the membrane in a near-perpendicular orientation relative to the membrane surface with two transmembrane domains in a monomeric form and is prone to oligomerisation. Thus the versatility of membrane-active alpha helical peptides and domains together with their associated importance for function are explored.

(I) AMPs: An engineering approach, with the aim of altering the peptide-membrane insertion mechanism, is used in order to evaluate structure-function relationships of AMPs. The dynamics and membrane insertion motif of the resulting peptide sequence is characterised using EPR and solid-state NMR approaches. The molecular understanding of the membrane activity from magnetic resonance studies is combined with biophysical methods including microscopy, circular dichroism (CD) and minimal inhibitory concentration (MICs) assays, in order to present data of different timescales and resolutions, reporting a model describing the observed antimicrobial activity. It is aimed to illustrate that synthetic AMP design principles, based on this case study, can be used in order to create new bactericidal peptides, that are much needed in the fight against antimicrobial resistance.

(II) p7: The HCV viroporin p7 has been extensively characterised in detergents and solvents by solution NMR. The work described in this thesis aims to add to the existing models by examining their plausibility in a model membrane environment. Solid-state NMR approaches are used to investigate helical tilt of the transmembrane domains, and are combined with single distance constraints obtained by pulsed EPR (DEER) yielding information on both inter- and intramonomer distance distributions. The individual experimental constraints are used in order to compare previously published structures of p7 in a ER-like model membrane. The oligomeric state in a membrane and the associated dynamics, which remain a major challenge for the field, are discussed.

In summary, structure-function relationships of a range of alpha-helical membrane-active peptides with direct relevance to infection are investigated. The therapeutical scope of these systems significantly differs in the fact that AMPs are peptide-based therapeutics with the broad-spectrum activity targeting bacterial membranes, whereas p7 from HCV is a drug target that can be inhibited by small molecules. The versatility of membrane activity found in the greater context of Biology is explored.

2

Experimental Principles

Contents

2.1 Solid-state Nuclear Magnetic Resonance (ssNMR) 35
2.1.1 NMR experiments of I = 1/2 nuclei used in this thesis 40
2.1.2 NMR experiments of quadrupolar nuclei nuclei used in this thesis . . 44
2.2 EPR 45
2.2.1 Continuous wave EPR (cwEPR) 46
2.2.2 Pulsed EPR (DEER) 50
2.3 Fluorescence 57
2.3.1 Tryptophan fluorescence 58
2.3.2 Förster Resonance Energy Transfer (FRET) 58

2.1 Solid-state Nuclear Magnetic Resonance (ssNMR)

A nucleus needs to possess a spin greater then 0 in order to be NMR active. The spin of a nucleus is characterised by the spin quantum number I. If a single nucleus with I=1/2 is placed into a large external magnetic field it will populate one of two possible energetic states: (I) parallel or (II) antiparallel; giving rise to the Zeemann splitting. A NMR active nucleus processes a small intrinsic magnetic moment and thus the alignment with the external magnetic field is not perfect and the nucleic magnetic moment possesses around the longitudinal axis of the large external magnetic field at a given frequency, the Larmor frequency (which depends on the external magnetic field strength).

The Larmor frequency (ω_{Lar}) is given by:

$$\omega_{Lar} = -\gamma B_0 \tag{2.1}$$

where γ is the gyromagnetic ratio, intrinsic to each individual nucleus and B_0 is the applied external magnetic field.

At equilibrium, the bulk magnetisation is described as being aligned along B_0, which is placed along the z-axis in the rotary frame. Upon a strong radio-frequency (rf) pulse the magnetisation flips into the x-y plane. This is described by the flip angle of a certain pulse and varies depending on the NMR application. Over a certain period of time the equilibrium magnetisation relaxes back to its initial alignment along the z-axis. The spin relaxation process depends on the *longitudinal relaxation* (T_1) and the *transverse relaxation* (T_2), where T_1 leads to a relaxation along the z-axis and T_2 causes the loss of phase coherence in the x/y - plane. The relaxation times are an important consideration for NMR experiments as the line width depends on $1/T_2$ and thus slowly tumbling molecules with a long T_2 tend to give rise to broad NMR signals.

In solution molecules tumble fast on the NMR correlation time scale ($\tau_1 = 10^{-6}$), which creates an isotropic average, meaning that each spin active nuclei in an identical molecule experiences the same external magnetic field and the Larmor frequency becomes averaged. In other words sample orientation is irrelevant for NMR in solution. The restricted tumbling of membrane associated proteins and peptides does not allow for orientational averaging and anisotropic interaction are possessed in the spin system.

These anisotropic interactions in a certain spin system are best described by a quantum mechanical model, where the spin system describes the ensemble average of individual spins in the sample in a given environment (e.g. B_0 along the z-axis). The interactions in a given spin system are summarised by the energy operator of the spin system: the Hamiltonian ($\hat{H}$):

$$\hat{H}_{total} = \hat{H}_Z + \hat{H}_{CS} + \hat{H}_D + \hat{H}_J + \hat{H}_Q \tag{2.2}$$

The Zeeman effect ($\hat{H}_Z$) describes the interaction between the nuclear spin and the external magnetic field (B_0), $\hat{H}_{CS}$ the chemical shift and relates to the electronic distribution around a nucleus, $\hat{H}_D$ the dipolar couplings relating to direct dipolar nuclear spin interactions, $\hat{H}_J$ the J-couplings that arise from indirect electron mediated nuclear spins and $\hat{H}_Q$ the quadrupolar interactions in the spin system, which arise from nuclear spin interactions with electrical field gradients. A brief description of the individual terms of the Hamiltonian are provided below.

Table 2.1: The different magnetic interactions in NMR

Interaction	Liquids (Hz)	Solids (Hz)	Averaging Methods
chemical shift anisotropy (σ or CSA)	10-10^4	10-10^4	Magic angle spinning (MAS)
J-coupling (J)	10^2	10^2	Decoupling
dipolar coupling (D)	0	10^4	Decoupling, MAS
quadrupolar interaction (Q)	0	10^5-10^6	MAS

information taken from Watts, A; lecture notes.

The Hamiltonian ($\hat{H}_Z$) of a single isolated spin in an external magnetic field (B_0) depends on the nuclear spin interaction with the magnetic field. If B_0 is applied along the z-axis then such a system is described by:

$$\hat{H}_Z = -\gamma\hbar\hat{I}_z B_0 \tag{2.3}$$

where γ is the gyromagnetic ratio, $\hbar$ is the reduced Planck's constant, $\hat{I}_Z$ is the nuclear spin operator along the z-axis and B_0 the external magnetic field.

The chemical shift anisotropy ($\hat{H}_{CS}$) describes the relative electronic distributions around a nuclear spin. The interaction can be described by a second rank tensor and related to an axial system with principal elements σ_{11}, σ_{22} and σ_{33}.

$$\hat{H}_{CS} = -\gamma\hbar(\sigma_{11}sin^2\theta cos^2\phi + \sigma_{22}sin^2\theta sin^2\phi + \sigma_{33}cos^2\theta)B_0\hat{I}_z \tag{2.4}$$

The angles θ and ϕ relate the the principal axis system to the external magnetic field.

The dipolar interaction ($\hat{H}_D$) is described by:

$$\hat{H}_D = 2\pi \sum_{k<l}^{N} I_k D_{kl} I_l \tag{2.5}$$

where D_{kl} describes the direct coupling tensor. Under the high field approximation this can be approximated to:

$$H_D = \frac{\hbar \gamma_k \gamma_l}{4\pi^2 r^3_{I_k I_I}} (1 - 3cos^2\theta)(3I_k I_l - \overrightarrow{I_k}\overrightarrow{I_l}) \tag{2.6}$$

where γ_k and γ_l describe the gyromagnetic ratios of nuclei k and I, r_{lk} is relating to the inter-spin distance, θ refers to the angle between the inter spin vector and the external magnetic field, $\overrightarrow{I_k}$ and $\overrightarrow{I_I}$ are the spin operators of spins l and k.

The electron mediated scaler couplings ($\hat{H}_J$) between spins I_k and I_I are described by:

$$\hat{H}_J = 2\pi \sum_{k<l}^{N} I_k J_{kl} I_l \tag{2.7}$$

which is characterised by the indirect coupling tensor J_{kl}.

The quadrupolar interaction ($\hat{H}_Q$) component is described by:

$$\hat{H}_Q = 2\pi \sum_{k<l}^{N} I_k Q_k I_k \tag{2.8}$$

which can be written within the principle axis system of the electrical field gradient into:

$$\hat{H}_Q = \frac{e^2 q Q}{4I(2I-1)} [3I_Z^2 - I(I+1) + \frac{1}{2}\eta(I_+^2 + I_-^2)] \tag{2.9}$$

where Q is the quadrupolar moment, e is the elementary charge, $\eta = \frac{V_{xx}-V_{yy}}{V_{zz}}$ and describes the electrical field gradient; $eq = V_{zz}$. $I_{\pm}$ relates to the principle axis system as follows: $I_{\pm} = I_x \pm iI_y$

where Q_k describes the quadrupolar moment of nucleus k and can be written in terms of the electrical field gradient:

$$Q_k = \frac{eQ_k}{2I_k(2I_k-1)\hbar}V_k \tag{2.10}$$

Q_k describes the quadrupolar moment of the nucleus.

In complex spin system involving multiple separate spins that are coupled to each other the Hamiltonian can described in very general terms by:

$$\hat{H}_{total} = \hat{H}_{external} + \hat{H}_{internal} \tag{2.11}$$

where the total energy of the spin system $\hat{H}_{total}$ is the sum of the external and internal interactions of the spin system (equation 2.11). $\hat{H}_{external}$ includes the nuclear interaction with the magnetic field resulting in the Zeeman effect and local interactions with applied rf fields. $\hat{H}_{internal}$ summarises local internal electronic interactions (chemical shift), inter-spin interaction (dipolar coupling) and field gradients (quadrupolar coupling) as described above. $\hat{H}_{internal}$ is the component exploited by NMR experiments to obtain nuclear information on the biological samples [197]. Most of the internal magnetic interactions described by the Hamiltonian (2.2) are anisotropic and thus depend on the sample orientation, which for most biological samples is a powder describing a sum of all possible orientations. Yet under specific condition these become very useful to obtain orientational information. Uniformly aligned samples (mechanically between glass slides) are presented in this thesis using different nuclei to obtain orientational constraints relative to the bilayer normal, which in the experiments presented here is aligned with B_0. The following section describes how the $\hat{H}_{internal}$ component is used for different nuclei in this thesis in order to obtain structural and dynamical information.

2.1.1 NMR experiments of I = 1/2 nuclei used in this thesis

In ssNMR most biologically relevant information is obtained from relatively low γ spin $I = 1/2$ nuclei, which have a low natural abundance (e.g. ^{13}C, ^{15}N). Thus isotope enrichment is needed to increase the inherently low abundance. Nevertheless, spin $I = 1/2$ nuclei have the advantage of resulting in comparably narrow lines. Important nuclei to be considered in Biology are summarised in table 2.2.

Table 2.2: Characteristics of biologically relevant nuclei

Nucleus	Spin Quantum number (I)	Gyromagnetic ratio γ	Natural abundance (%)	Quadrupolar moment (Q, $e \cdot 10^{28} m^2$)	relative sensitivity
^{1}H	1/2	2.79	99.99		1.00
^{2}H	1	0.41	0.015	0.003	0.0096
^{13}C	1/2	0.70	1.1		0.016
^{14}N	1	0.40	99.6	0.02	0.001
^{15}N	1/2	-0.28	0.37		0.001
^{17}O	5/2	-1.89	0.04	-0.004	0.029
^{19}F	1/2	2.62	100		1.00
^{31}P	1/2	1.31	100		1.00

Biologically relevant nuclei are listed including their relative abundance, gyromagetic ratio γ, inherent sensitivity and quadrupolar moment [198].

2.1.1.1 Phosphorus (^{31}P)

^{31}P possesses an intrinsic spin *I=1/2*. Its large abundance of close to 100% in biological samples and especially in phospholipids makes ^{31}P an important nucleus for biological sample characterisation, which renders isotopical labelling unnecessary. CSA dependance of ^{31}P (outlined below) is largely exploited to investigate lipid structure, distinct macromolecular lipid phases, which give rise to specific ^{31}P line shapes or to investigate more local lipid perturbations in bilayers upon protein/peptide interaction [199]. In the past ^{31}P NMR has been extensively used to characterise peptide-lipid interactions; for example the phase dependent lipid binding of melittin to phospholipid bilayers has been elucidated by ^{31}P NMR

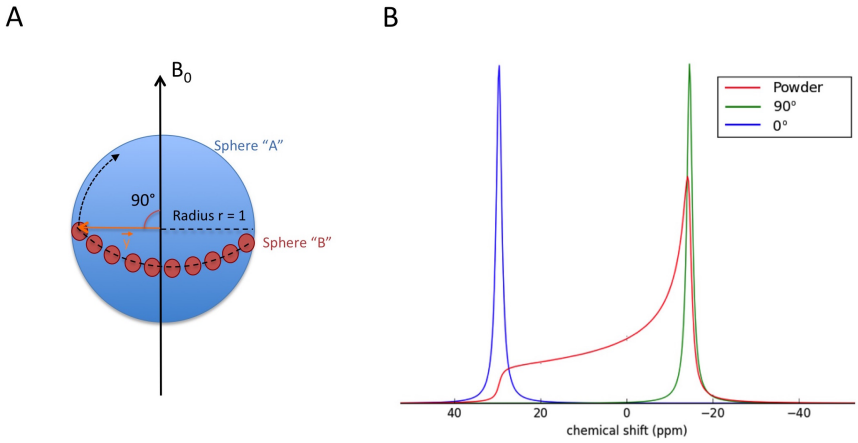

Figure 2.1: (A) Illustration of a ^{31}P powder pattern as observed for lipid vesicles. (B) Simulated static ^{31}P NMR spectra: for an anisotropic powder (red), a uniform alignment at 90 ° (green) and at 0 ° (blue). A chemical shift anisotropy of 44 ppm was assumed roughly corresponding to DOPC, lines were broadened by 250 Hz and an external magnetic field of 400 MHz was used [202]. The powder component was rescaled by a factor of four for plotting. Simulations were performed using Simpson [203; 204]

[200; 201]. ^{31}P is also important to evaluate lipid alignment for macroscopically aligned samples as quality control for sample preparation.

The characteristic orientation-selective powder pattern exploited by most ^{31}P ssNMR applications (Figure 2.1) is best explained by assuming a sphere "A" with a vertical $z-axis$ passing through the centre of mass and a radius $r = 1$. The sphere "A" is covered in lipid headgroups, each represented by small spheres "B" themselves, and a vector $\vec{y}$ connecting the centres of mass of "A" and "B". If the centre of mass of "A" is centred to the $xy-plane$, then the radius of the circle describing the sphere relative to the $xy-plane$ is largest at $z = 0$, in other words at a 90° orientation of the vector $\vec{y}$ relative to the $z-axis$. This radius approaches 0 at increasing $|z|$; $\vec{y}$ and z only align at $z = 1$ and the angle between $\vec{y}$ and z is 0°, in an ideal scenario this is only the case for a single sphere "B". Hence, the observed powder pattern is a function of the radius of the sphere "A" in terms of the $xy-plane$, when moving it along the $z-axis$, and thus the 90° orientation is populated the most (see figure 2.1). Note that this is only true for a large molecular assembly tumbling slowly on the NMR timescale, for fast tumbling samples, a single isotropic resonance at 0 ppm is observed.

2.1.1.2 Nitrogen (^{15}N)

^{15}N has a spin spin quantum number of *I = 1/2* and is an inherently insensitive nucleus with a relative sensitivity of 0.001 subject to its low gyromagnetic ratio (γ) and natural abundance (Table 2.2). Both the narrow line widths achieved for spins with *I=1/2* and the absence of a quadrupolar moment are advantageous compared to the much more abundant ^{14}N nucleus. ^{15}N is a biologically relevant nucleus that can be isotopically incorporated into biological systems with relative ease and thus report on structural features such as backbone orientation and ligand binding sites.

Dipolar coupling

A spin property that is commonly exploited, or at least needs consideration, is dipolar coupling between the individual magnetic moments of two individual spins. Homonuclear and heteronuclear spins can be coupled to each other. These interactions are anisotropic and thus are important for solid samples. The Hamiltonian describing the dipolar interaction of a heteronuclear system can be given in tensor form by:

$$\hat{H}_{dd} = -2\hat{I} \cdot D \cdot \hat{S} \tag{2.12}$$

where $\hat{I}$ and $\hat{S}$ represent the angular moments of spins S and *I*. S is the cause of the local field observed by *I*. D represents the dipolar coupling tensor, which depends on the internuclear vector on spins I and S in B_0. The coupling constant (d) is related to inter-spin distance (r) is given in angular frequency units (rad s^{-1}) by:

$$d = \hbar(\frac{\mu_0}{4\pi})\frac{1}{r^3}\gamma_I\gamma_S \tag{2.13}$$

The angular moments of S and I are quantised with respect to B_0 and thus directly depend on the relative orientation with respect to B_0. The strength of the experienced local field at I due to close proximity to S depends on the angular orientation of the internuclear vector relative to B_0 and thus can yield structural information on the system of interest [205]. This effect exists both as *homonuclear dipolar coupling* and as *heteronuclear dipolar*

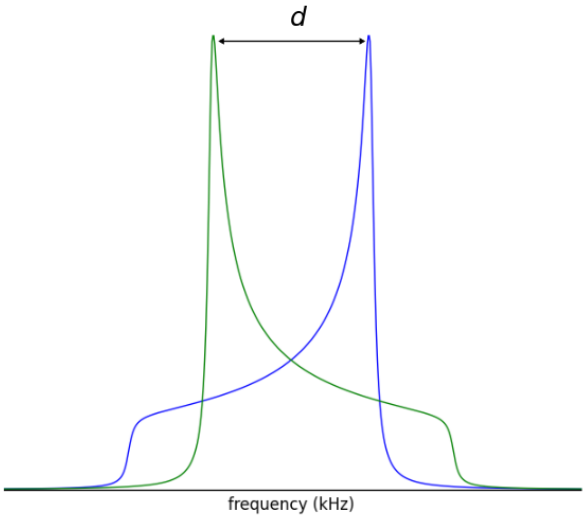

Figure 2.2: The heteronuclear dipolar coupling of two spins I and S is illustrated and gives rise to a Pake doublet due to the $(3\cos^2\Theta - 1)$ dependancy [205]. Note that for homonuclear dipolar coupling $H_{II} = \frac{3}{4}d$ and for heteronuclear dipolar coupling $H_{IS} = \frac{1}{2}d$

coupling. In this thesis the heteronuclear coupling between ^{1}H and ^{15}N will be utilised for structural characterisation as part of PISEMA experiments.

For a powder sample of two heteronuclear spins S and I, this can be visualised by the typical Pake doublet (Figure 2.2). Each spin system allows for one energy transition and has a $(3\cos^2\Theta - 1)$ dependence. However, one spin system will have a $+(3\cos^2\Theta - 1)$ and the other a $-(3\cos^2\Theta - 1)$ dependence and hence this gives rise to a doublet, where the dipolar coupling constant d is related to distance between the observed "horns".

Cross-polarisation (CP)

For low sensitivity nuclei, cross-polarisation (CP) is a common technique to enhance sensitivity of dilute spins [206]. CP is now commonly as a building-block in most ssNMR pulse sequences. During a basic CP experiment magnetisation is transferred from a nucleus with a high gyromagnetic ratio (eg. ^{1}H) to a nucleus with a low gyromagnetic ratio (eg. ^{15}N). As a result the total magnetisation and thus the sensitivity of the nucleus with a low gyromagnetic ratio is enhanced by the ratio of the individual gyromagnetic ratios. In order for magnetisation transfer to be effective, the two nuclei must be spin locked at the same field and fulfil the Hartman-Hahn condition:

$$|\gamma_I B_{rf}^I| = |\gamma_S B_{rf}^S| \tag{2.14}$$

where the radio-frequency (rf) pulses applied to the I and S nuclei are represented by B_{rf}^I and B_{rf}^S respectively. γ_I and γ_S are the gyromagnetic ratios of the individual nuclei. If one considers a graphical representation of spin energy levels, then this would correspond to a matching of energy levels.

This enhancement can be further amplified when using an adiabatic sweep through the Hartmann-Hahn condition. Here the rf pulse on the I nucleus is varied and a ramp is applied. A further advantage of this method is that CP conditions require less careful rf matching [207; 208].

2.1.2 NMR experiments of quadrupolar nuclei nuclei used in this thesis

Quadrupolar nuclei possess a non-spherical charge distribution and thus can be affected by electric field gradients. In general nuclei with *I>1/2* possess an intrinsic imbalanced charge distribution, which results in asymmetric electric fields intrinsic to the nucleus. This is known as a quadrupole moment and is in addition to the common dipole moment. A quadrupole moment interacts with local electric field gradients and perturbs the individual spin energy levels accordingly, which becomes detectable in a quadrupolar echo experiment, consisting of two consecutive 90° pulses.

For nuclei with *I = +/-1*, two single quantum energy transitions need to be considered and the quadrupolar splitting can be measured as the absolute separation between the two resonance frequencies (Figure 2.3). The same $(3\cos^2\Theta - 1)$ relationship as for dipolar coupling and CSA applies, and in a powder a similar line shape to the one illustrated in Figure 2.2 is therefore observed. The quadrupolar moment depends on the relative orientation to B_0, which can be exploited in uniformly aligned samples to obtain orientational constraints of selectively deuterated peptides relative to the bilayer normal (aligned parallel or antiparallel to B_0). The quadrupolar splitting is dependent on both the relative orientation and the dynamics of the nucleus on the NMR timescale (in the range of μs). Consequently the motional averaging of the carbon-deuterium vector in deuterated lipid samples relative to

the axis of reference becomes evident and can be measured. Generally this is expressed as an effective order parameter (S_{eff}) related to measured quadrupolar splitting of the labelled site. The quadrupolar splitting becomes averaged in isotropic liquids.

In this thesis ^{2}H solid-state NMR is used in order to obtain orientational constraints relative to B_0 in mechanically aligned samples with the bilayer normal being aligned to B_0, as well as calculation of order parameters of acyl chain deuterated lipids.

2.2 EPR

Electron paramagnetic resonance (EPR), also known electron spin resonance (ESR), is a technique that exploits the high sensitivity of electron spins. However, unlike for nuclear spins, site directed spin-labels of unpaired electrons need to be incorporated in protein samples, mostly in the form of nitroxide radicals (except for non-silent metals as contained for example in haem groups). Continuous wave EPR (cwEPR), where a continuous wave radio frequency is applied under a varied magnetic field, allows for the detection of dynamics on the timescale of *ns* at the site of the spin label. More similar to NMR, pulsed EPR techniques apply short

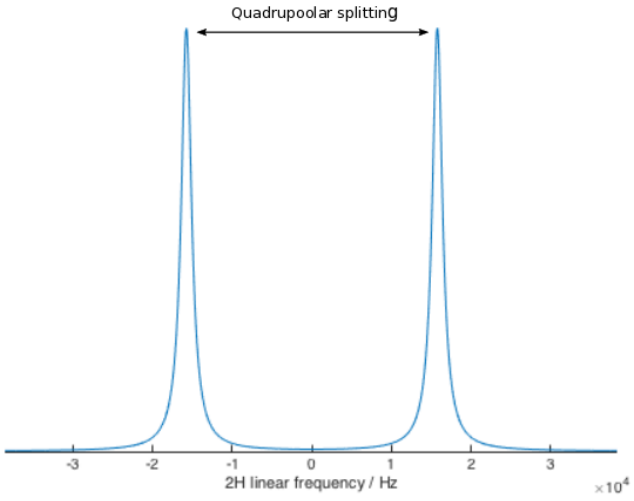

Figure 2.3: Oriented ^{2}H spectrum at a relative tilt of 45_o to B_0; simulated at relative field strength of 900 MHz and 100 Hz apodization was applied. The characteristic two energy transitions are observed, giving rise to a quadrupolar splitting of 38 kHz. The simulation was run using the software library *spinach* [209]

ns pulses that can, for instance, resolve the dipolar coupling between two individual electron spins. Pulsed double-electron-electron-resonance (DEER) resolves the distance dependancy of the dipolar coupling of up to 6 nm for membrane proteins and hence is a powerful technique to measure precise distances between localised spins [210].

2.2.1 Continuous wave EPR (cwEPR)

cwEPR measures the energy transitions of electron spin states ($I = 1/2$) when in a magnetic field. The Zeeman splitting of electrons can be described, analogous to the NMR methodologies, by a Zeeman spin Hamiltonian ($\hat{H}_z$):

$$\hat{H}_z = \mu_B \cdot \vec{B} \cdot g \cdot \hat{S} \tag{2.15}$$

where $\hat{S}$ is the spin operator of the electron with g-tensor g; μ_B represents the Bohr magneton and $\vec{B}$ is the magnetic field tensor. If B is taken to be the length of the Bohr magneton, which in turn describes the *z-axis* of the spin system and the g-tensor is isotropic, $\hat{H}_z$ can be written as:

$$\hat{H}_z = g \cdot \mu_B \cdot B \cdot S_z \tag{2.16}$$

with corresponding eigenvalues:

$$E = g\mu_B m_S B = \pm\frac{1}{2} g\mu_B B \tag{2.17}$$

and under the application of the correct microwave frequency this will lead to energy transitions between the two spin states (ΔE):

$$\text{if } hv = g\mu_B B_0 \tag{2.18}$$

where h is the Planck's constant and v is the microwave frequency. If this condition is met, this will lead to a net absorption of energy and transition of spin from the low energy level to the high energy level as described by the Boltzmann distribution (Figure 2.4).

However, in a characteristic nitroxide radical, additional energy splittings due to the hyperfine interaction with the local ^{14}N are observed. The hyperfine interaction arises due to a partial localisation of the unpaired electron in the p_z orbital of the ^{14}N nucleus with spin $I = 1$, which results in three hyperfine energy splittings of the *+1/2* and *-1/2* Zeeman energy splittings respectively (spin states m = 1, 0 and -1; Figure 2.4). Under a constant application of microwave frequency and a magnetic field sweep, each transition becomes possible at the specific magnetic field strength that renders equation 2.18 true for this specific energy transition. A total of three energy transitions are seen.

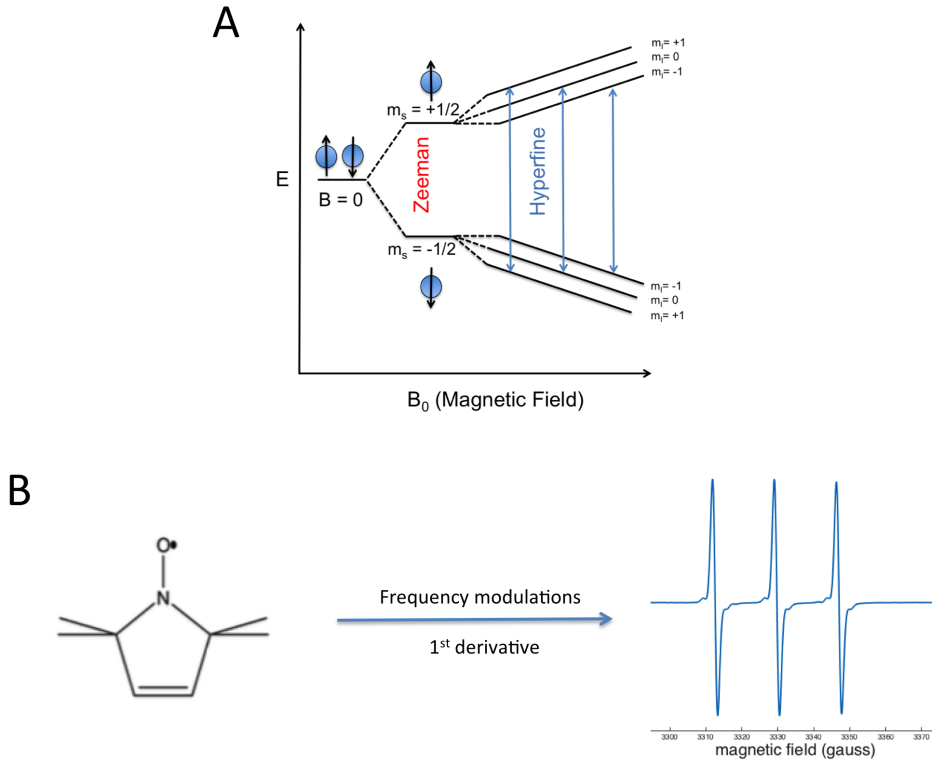

Figure 2.4: The characteristic energy landscape of a nitroxide spin resulting from the Zeeman splitting of the $I = 1/2$ of an electron and the hyperfine interaction with the local ^{14}N with $I = 1$ that results into an additional splitting into three sub levels (A). Due to the quantum mechanical selection rules this results in three possible energy transitions. The chemical structure of a nitroxide radical highlighting the unpaired electron is shown (B) A typical cwEPR spectrum 1st derivative is shown, clearly illustrating the three energy transitions during a magnetic field sweep at a constant microwave frequency.

This can be described by the following hamiltonian $\hat{H}$:

$$\hat{H} = \mu_B \cdot \vec{B} \cdot g \cdot \hat{S} + \hat{I} \cdot A \cdot \hat{S} \tag{2.19}$$

where $\hat{I}$ represents the nuclear spin operator and A stands for the hyperfine tensor. The hyperfine splitting can be used to probe local polarity of the spin label environment. In a more polar environment the unpaired electron will populate the p_z orbital on the ^{14}N to a larger extend then the p_z orbital of ^{16}O, which leads to an increased hyperfine splitting [211]. For a more complete description of the spin Hamiltonian describing nitroxide radicals in a magnetic field, additional interactions need to be considered:

$$\hat{H} = \hat{H}_z + \hat{H}_{ZFS} + \hat{H}_{HF} + \hat{H}_{NZ} + \hat{H}_{NQ} + \hat{H}_{NN} \tag{2.20}$$

where $\hat{H}_z$ describes the Zeemann effect; $\hat{H}_{ZFS}$ the zero field splitting; $\hat{H}_{HF}$ the hyperfine interaction; $\hat{H}_{NZ}$ the nuclear Zeeman effect; $\hat{H}_{NQ}$ the angular quadrupolar interaction and $\hat{H}_{NN}$ the nuclear nuclear interaction. However, most of these energetic descriptions are only required for relatively high spin-density samples; sufficiently spin diluted samples can be accurately described by equation (2.19).

Taking equation (2.19) to describe a dilute spin system the interactions of the electron interactions are defined by two parameters: (I) the *g-tensors* that describe the interaction with B_0 and (II) the *A-tensors* describing the electron hyperfine interactions. The *p-orbital* that accommodates the free electron has an intrinsic directionality and thus the hyperfine interaction as well as the magnetic interaction are associated with a degree of axial anisotropy [212].

The relative anisotropies can be described by the following matrices where the *x-axis* is aligned with the N-O bond vector [213]:

$$g = \begin{Bmatrix} g_{xx} & g_{xy} & g_{xz} \\ g_{yx} & g_{yy} & g_{yz} \\ g_{zx} & g_{zy} & g_{zz} \end{Bmatrix} \quad A = \begin{Bmatrix} A_{xx} & A_{xy} & A_{xz} \\ A_{yx} & A_{yy} & A_{yz} \\ A_{zx} & A_{zy} & A_{zz} \end{Bmatrix} \tag{2.21}$$

The diagonal of the anisotropy matrices are the principal values for g - and A-tensors.

Due to the intrinsic anisotropy of the spin Hamiltonian describing nitroxide spins, the partial averaging of the anisotropies can be measured and report on local dynamics at the spin label environment. Both isotropic and anisotropic motions will lead to partial averaging of the spin anisotropy. In fast isotropic motional scheme the cwEPR spectrum consists of three

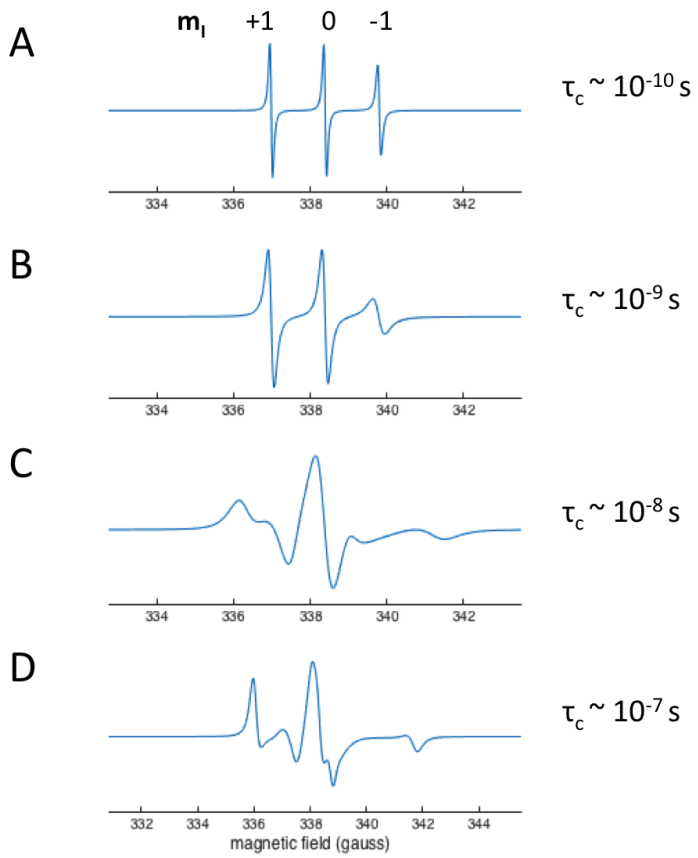

Figure 2.5: Simulated cwEPR spectra of a single nitroxide spin at different correlation times (τ_R): $10^{-10}s$ (A), $10^{-9}s$ (B), $10^{-8}s$ (C) and $10^{-7}s$ (D). A clear line broadening can be observed when moving to shorter correlation times to a near static environment reaching the rigid motion limit on the EPR timescale. Spectra were simulated at X-band and a experimental temperature of 298 K. The nitroxide radical was described by principal hyperfine g-value tensors $g_{xx} = 2.0085$; $g_{yy} = 2.0063$ and $g_{zz} = 2.0025$. The principal axial anisotropy was set to $a_{xx} = 5.8$; $a_{yy} = 5.8$ and $a_{zz} = 30.8$ Gauss. Simulations were performed using *EasySpin* [214].

sharp lines (Figure 2.5A). Slower motions will change the line shape of the EPR spectrum accordingly. Axial anisotropic motions are often measured in order to probe the angular amplitude of motion of spin labels attached to phospholipid acyl chains [215; 216; 217].

For spin labels attached to proteins the relative mobility of the spin label is determined by three main components: (I) The relative motion of the spin label compared to the motions of the protein backbone; (II) the overall motions of the secondary structure of the protein, which might be influenced by amino acid location and packing as well as secondary, tertiary and quaternary protein structure; and (III) the overall motion of the protein containing environment. For large proteins (>15 kDA) and proteins embedded into a bilayer; component (III) can be neglected as the correlation times are slow enough for these environments to be

experienced as "static" on the EPR timescale. In this case the line shape is dominated by local effects [218]. This motional sensitivity can be used to probe protein secondary, tertiary and quaternary structure as well as more localised conformational changes.

The influence of dynamics on cwEPR line shape is visualised by simulation in Figure 2.5, where line broadening due to slow correlation times is seen, compared to the isotropic fast moving environment. This broadening effect is due to the A_{zz} component being more pronounced at slow dynamics.

2.2.2 Pulsed EPR (DEER)

Pulsed EPR is analogous to NMR where under a constant magnetic field nitroxide spins are excited by high power microwave pulses at a given frequency. DEER, also known as Pulsed Electron-Electron Double Resonance (PELDOR), experiments are based around a simple Hahn echo pulse sequence (Figure 2.6) at a constant magnetic field, where the spin population is puled at two separate frequencies. A Hahn echo experiment creates a spin echo by two consecutive pulses: a $\pi/2$ or 90° pulse followed by a π or 180° pulse (Figure 2.6 A). In the rotary frame representation with an equilibrium setting of the bulk magnetisation (B_1 being aligned with the *z-axis*), a $\pi/2$ pulse flips the magnetisation into the *xy-plane*. This is followed by dephasing of the individual spins. A π-pulse then flips all individual spins by 180^0 to rephase the spins, which then relax back to their initial alignment along z and generate the measured spin echo (Figure 2.6 B; [219; 220]).

The simple Hahn echo pulse sequence used for DEER is applied at a given frequency, the observer frequency (v_{obs}). An additional π pulse is applied at a frequency offset, selectively exciting a separate sub-population of spins in the same sample, the pump frequency (v_{pump}). The frequency offset between v_{obs} and v_{pump} needs to be large enough to avoid overlap of the two excitation windows. If the two separately pulsed spin populations are coupled, the pulse applied at v_{pump} will affect the local field of the observer spins and thus affect the phase of the spins during the Hahn echo sequence. By varying t, the offset time at which the pump pulse is applied, the dipolar coupling of the two stimulated spin populations can be resolved (Figure 2.7 and 2.8 A). The basic experiment described above is known as a *3-pulse* (3p) DEER experiment [221].

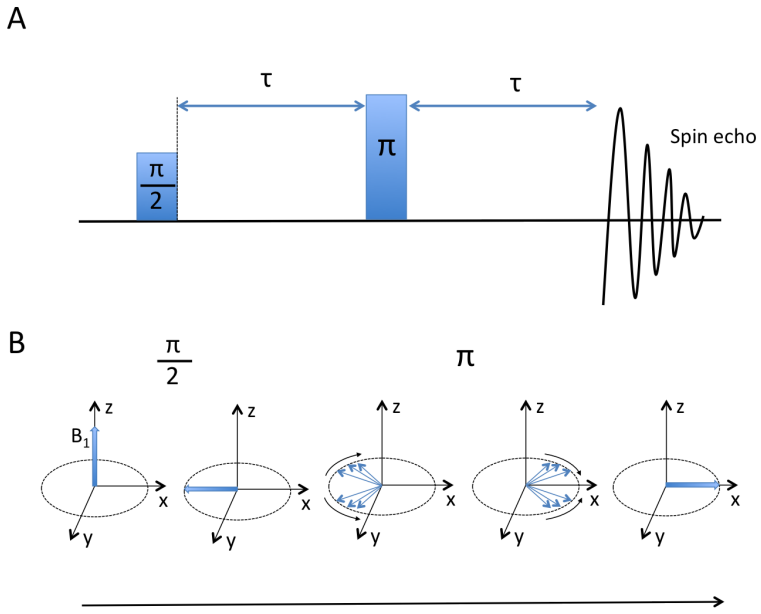

Figure 2.6: The pulse sequence of a Hahn echo is illustrated (A). The corresponding effect on the magnetisation B_0 is illustarted in the rotary frame representation (B). In short a *pi*/2 pulse causes the magnetisation to flip into the *xy - plane*, which is followed by dephasing; a π pulse flips the spins over and causes them to rephase. The rephased spins relax back to their equilibrium position aligned along *z*.

The relative spin populations separated by Δv are illustrated at their relative positions in a nitroxide absorption spectra at Q-band (microwave frequency 34 GHz and a magnetic field strength of 12000 Gauss). The pump pulse is applied at the centre of the absorption spectrum, which allows for short *ns* pump pulses that are efficient at flipping a large proportion of spins.

The *3-pulse* (3p) experiment has the inherent problem that at short offset times of t the $\pi/2$ pulse at v_{obs} and the π pulse at v_{pump} have a temporal overlap, which distorts the initial data points of the recorded DEER time trace. This is referred to as *"dead time"* and for the 3p experiment this is in the range of 30-100 ns. However, short distances are resolved in the initial data collected at short t times and hence it is important that this region is undistorted. The more recently developed *4-pulse* (4p) DEER experiment overcomes this problem (Figure 2.8 B [222]).

In a 4p DEER experiment an additional π is applied at v_{obs} following the last π of the Hahn echo sequence. This creates a transient echo as part of the pulse train. The pump pulse applied at v_{pump} can now be applied at t=0, at the refocused echo, without pulse

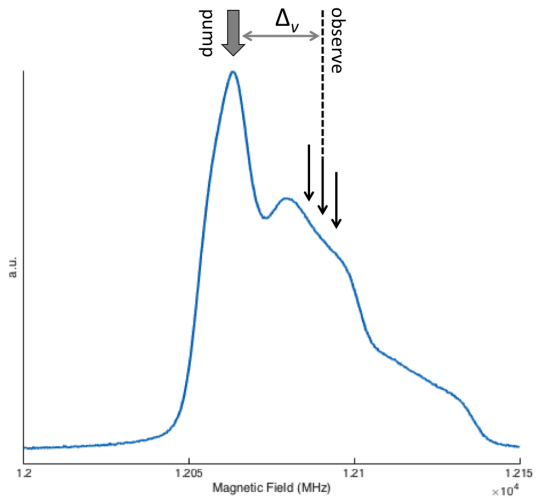

Figure 2.7: An absorption spectrum of a nitroxide radical covalently attached to a protein via disulphide bond, recorded at Q-band and 30 K, is shown. The relative position of the pump and observing frequencies, and the corresponding frequency offset are illustrated by arrows.

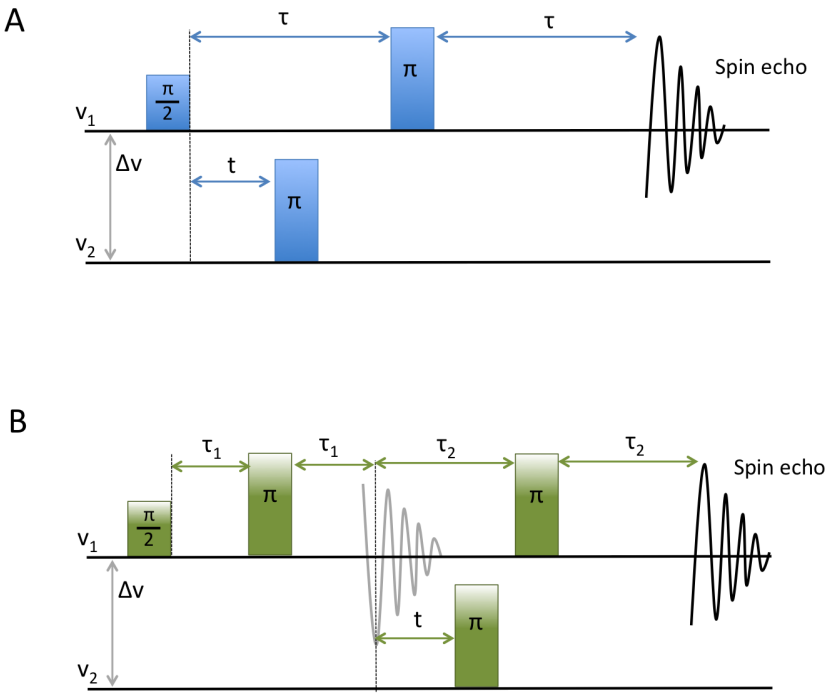

Figure 2.8: The pulse sequence of a 3p DEER (A) and a 4p DEER experiment (B) are illustrated. The top pulse train is applied at the v_{obs} and the bottom pulse sequence is applied at v_{pump}.

overlap with any pulses applied at v_{obs}. This allows for accurate data collection at short t-times at the cost of a slightly reduced signal amplitude.

A combination approach of acquiring a 3p and 4p DEER has been proposed [223], where by post-experimental processing, the early data points of the 3p time trace are cut and replaced by the shorter 4p experiments. This approach has the advantage that long time traces become possible as the long and higher signal to noise ratio 3p DEER trace can be used.

The time trace recorded by the DEER experiment, is the echo intensity as a function of t, and is referred to as the dipolar evolution function $D(t)$. $D(t)$ is a combination of the background signal ($B(t)$) and the form factor ($F(t)$). The background signal is due to spin interactions of the spin of interest with other spins in the bulk environment. The form factor is the signal of coupled spins within the nano-object of interest.

$$D(t) = B(t)F(t) \tag{2.22}$$

where $F(t)$ is defined as:

$$F(t) = 1 - \lambda + \lambda \int_0^{\pi/2} ((3\cos^2\theta - 1)\omega_{dd}t) \sin\theta d\theta \tag{2.23}$$

where the angular frequency dependency is given by ω_{dd} and λ represents the modulation depth. The modulation depth describes the relative proportion of pumped spins in a sample. It is advantageous to have a large modulation depth that allows for a good separation of $(B(t))$ and $(F(t))$.

ω_{dd} is described by:

$$\omega_{dd} = \frac{g_1 g_2 \mu_B^2 \mu_0}{4\pi r^3} \tag{2.24}$$

This establishes a relationship between the inter-spin distance in a nano-object of coupled spins 'r' and the dipolar frequency, that is obtained from the experimental trace.

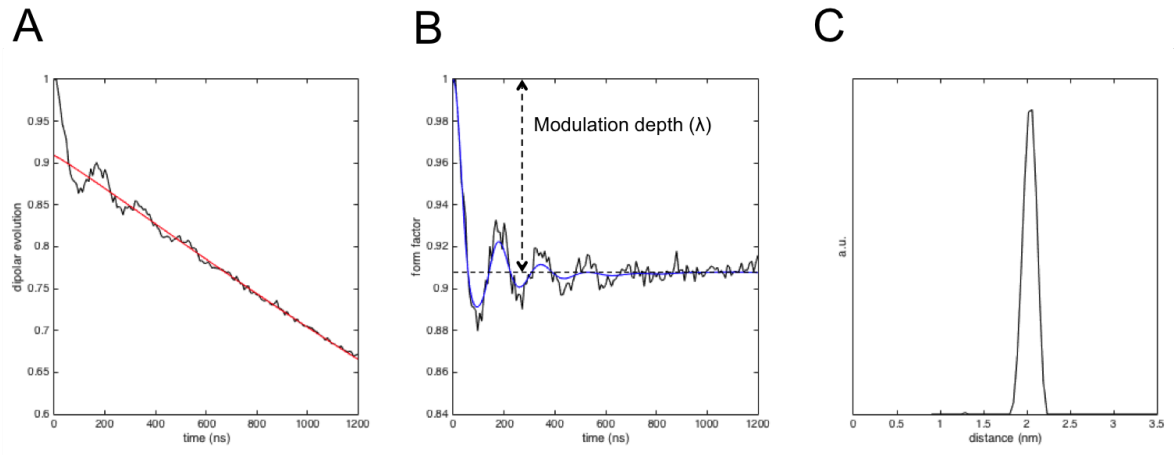

Figure 2.9: Background correction and distance normalisation are illustrated using a Bruker supplied standard for DEER measurements. The dipolar evolution function was acquired at Q-band at a temperature of 50K. (A) The experimental time dependent dipolar evolution function is shown. The background correction is shown in red. (B) The background corrected form factor is plotted. The modulation depth corresponding to $1 - \lambda$ is graphically illustrated. (C) The corresponding distance distribution shows a single distance of 2 nm. The distance distribution was obtained by Tikhonov regularisation.

$B(t)$ depends on the overall distribution of spins in the bulk of the sample, which should be homogenous and large compared to the inter-nano-object spin distribution. The background contribution can be estimated using a stretched exponential:

$$B(t) = exp - (kt^{d/3}) \tag{2.25}$$

where k relates to the overall spin concentration in the sample of interest and d is the background dimension. In a theoretical case the background dimension for a membrane protein in detergent should be ca. 3 and a protein contained in a bilayer can be approximated to a dimension of ca. 2. However, it is common that in biological settings the background dimension deviates from the theoretical case.

Background correction of an experimental dipolar evolution function is illustrated in Figure 2.9.

Practical DEER considerations

The obtained signal intensity in DEER greatly depends on spin relaxation rates. Generally the relaxation can be divided in two separate processes *spin-spin* (T_2) relaxation and *spin-lattice* relaxation (T_1). Both need to be considered for experimental DEER.

DEER experiments are acquired in the frozen state for three main reasons (I) restricted mobility of the spin label in the sample results in increased modulation of the dipolar evolution function and narrow distance distributions; (II) the relative population of the spin states in the Boltzmann distribution differs; and (III) T_1 and T_2 increase at low temerpatures. At low temperatures T_2 is large, which results in an increased spin coherence and thus enables long t_2 times, that allow for the collection of long dipolar evolution traces (Figure 2.8). This allows for the measurement of weaker dipolar interactions and also longer distances, which are increasingly resolved with long dipolar evolution functions. The set-up temperature is a compromise between all three parameters [224]; the here described DEER experiments were recorded at a sample temperature of 30 K.

In order to suppress magnetisation relaxation due to *spin-spin* interaction with protons, the sample matrix is enriched with deuterium (D_2O) which has a lower gyromagnetic ratio and thus causes only limited spin relaxation. This greatly lengthens the T_2 times. However, in dipolar experiments this causes small spin echo envelope modulations in the sample. The phase of the nuclear modulations depends on the inter pulse delay in the 4p DEER pulse train, thus by varying the pulse delay between the $\pi/2$ and π pulse at v_{obs} the nuclear modulations can be averaged. At Q-band this can be efficiently achieved with a 8-step averaging cycle, each with a 16 ns increment (Figure 2.10, [225]).

The shot repetition time (SRT) depends on spin relaxation rates. For a short SRT time more DEER pulse trains can be acquired in a set amount of time and a better signal-to-noise ratio can be achieved. However, after the last π-pulse in the DEER pulse train sufficient time should remain for the magnetisation to fully relax back to the equilibrium state along the *z-axis* and the signal to be acquired. Typically equilibrium magnetisation is reached after 3-5 times the T_1 time (which is typically in the low μs regime).

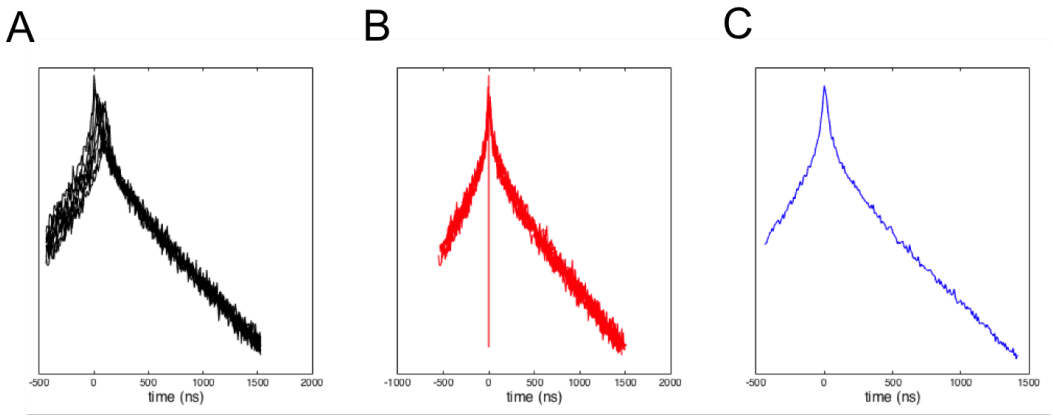

Figure 2.10: The dipolar evolution function with varying interpulse delays (tau 1). (A) Dipolar evolutions function collected each with 16ns different interpulse delay. Note that the initial echo start is shifted accordingly. (B) A rotation matrix is applied to align all individual dipolar evolution function in the incremented tau 1 avaraging cycle. (C) The individual traces are added and a dipolar evolution function with averaged nuclear modulations is achieved (Matlab script written by W Myers).

In a 4p DEER experiment the signal intensity depends on a combination of the T_1 and T_2 times, that can be experimentally determined.

Signal intensity relates to [224]:

$$S_0 = kC(1 - e^{-SR/T_1})e^{-T_e/T_2} \tag{2.26}$$

where C relates to the spin concentration in the sample, T_e is the time between the $\pi/2$ pulse and the start of echo detection and k is a constant intrinsic to the instrument. The total signal intensity S_{total} across the experiment can then be described by the following and depends on SRT and time (T):

$$S_{total} = S_0 \cdot (T/SRT) \tag{2.27}$$

where the signal-to-noise (S/N) ratio is described by:

$$S/N = S_0 \cdot \sqrt{T/SRT} \tag{2.28}$$

2.3 Fluorescence

Fluorescence is a form of luminescence that is emitted from a compound post absorption of energy in the form of light or other electromagnetic irradiation. During energy absorption a fluorophore transitions from its ground state (S_0) to an excited singlet state (S_1) via absorption of a photon. Each energy level contains multiple sub vibrational states. The energy possessed by a distinct photon can be described by the Planck-Einstein relationship:

$$E_e = h \cdot f \tag{2.29}$$

where h is the Planck's constant the f describes the light frequency.

Similarly a photon is emitted during the relaxation process of the orbital electron back to its ground state. However, an excited state can also relax by other competing pathways, like vibration resulting in the generation of heat. The emitted light (fluorescence) has a longer wavelength as some energy is lost during the process. This is known as the Stokes shift. This is due to non radiative relaxation from a higher vibrational state to the lowest vibrational state within an energy level described by the Franck-Condon principle.

This intrinsic property of a fluorophore is quantified by the quantum yield that describes the relationship between the number of photons absorbed per emitted photon. Generally this parameter is viewed as how well a fluorophore of choice will perform. Other parameters to consider are the excited state lifetime, a measure of the lag period between the excitations by absorption and the emission of fluorescence. This is an ensemble measure and does not allow for accurate prediction of single emission events.

Similarly to nitroxide spin labels fluorescence emission can be asymmetric, and thus be related to the laboratory frame at the time of excitation. This is an important parameter to consider for dynamical information of the local fluorophore during the excited state lifetime.

2.3.1 Tryptophan fluorescence

The intrinsic fluorescence of amino acids (Tryptophan and Tyrosine) are commonly used to report on the electrostatic environment of proteins. Local electrostatics can be probed using chromophores that are wavelength sensitive to electric fields. Tryptophan is commonly used to probe the polarity of the local environment [226; 227].

One of the most common applications is to monitor δ_{max}, the wavelength at the maximum emission intensity of tryptophan fluorescence as this reports directly on the local polarity. The local polarity has an effect on the excited energy state. A higher solvent polarity leads to a reduced solvent-relaxed excited state and thus affects the Stokes shift. Generally the Tryptophan side chain is buried in a non-polar environment if δ_{max} is shorter then 330 nm and the emission spectrum is "blue-shifted". For polar environments δ_{max} tends to be larger then 330 nm [228] due to a partial system relaxation upon excitation due to reorientation of the solvent envelope in a polar environment.

2.3.2 Förster Resonance Energy Transfer (FRET)

FRET is a powerful biophysical technique that is built around the wavelength (λ) deviation between the absorption and emission spectra of fluorophores. FRET is the successful energy transfer from fluorophore A (donor) to fluorophore B (acceptor) due to spectral overlap, which occurs without direct molecular contact. Two fluorophores with spectral overlap that allow for FRET are referred to as a donor/acceptor pair. This distance-dependent phenomena has been used to investigate protein interaction and conformational change as well as oligomeric state. FRET is also a naturally occurring phenomena that can occur between two flourescently active proteins. The green colour of the jellyfish *Aequorea victoria* is produced by the Green Fluorescence Protein (GFP), which in turn accepts energy from aequorin, which in isolation emits blue light itself [229; 230].

The energy transfer from donor to acceptor results in a decreased emission intensity of the donor as well as a decreased lifetime of donor fluorescence and in turn increases the fluorescence emission of the acceptor fluorophore (Figure 2.11).

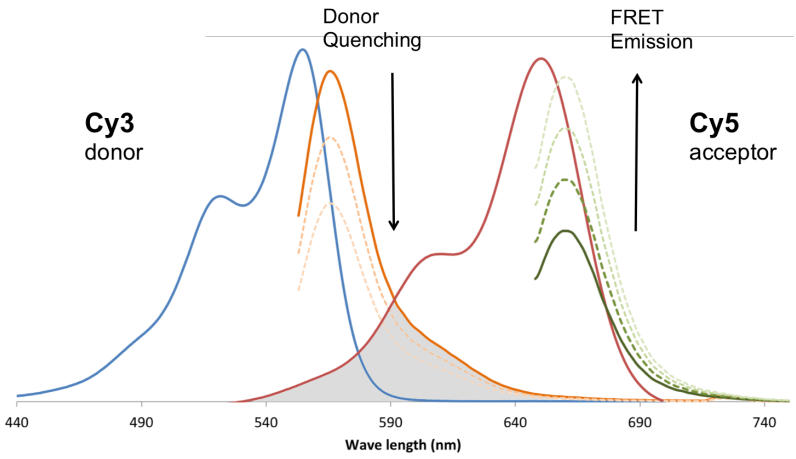

Figure 2.11: The physical phenomenon of FRET is illustrated using the FRET pair of Cy3 and Cy5. The excitation of Cy5 (blue) triggers fluorescence emission (orange), part of the emitted fluoresce is absorbed due to spectral overlap (grey) by the acceptor Cy5, which in turn trigger the emission of FRET fluorescence (green). Note that upon increased energy transferred the observed donor fluorescence intensity decreases.

The physical principle of FRET can be best explained by means of the Jablonski diagram, that illustrates the energy transitions during electron excitation and relaxation (Figure 2.12). Where an electron becomes excited to a higher energy state due to light absorption, and in the absence of a FRET acceptor, the electron would relax back to the ground state (S_0) and thereby release energy in the form of light - fluorescence. Strictly speaking energy can also be released as other forms like heat or energy transfer to non-fluorescent molecules in close proximity. If the excited electron of the donor molecule is in close proximity to an acceptor it is possible for energy to be transferred via an electromagnetic field to a FRET acceptor, that in turn causes electron excitation within the acceptor fluorophore. Note that this is a non-radiative process where no emitted photons are involved. The excited electrons of the acceptor will relax back to their ground state and emit fluorescence - the FRET signal. Energy is lost in the process and thus the observed FRET emission is at a longer λ.

FRET is distance dependent and thus has been used extensively to characterise intra- and intermolecular distances between conjugated fluorophores in biological samples. Most FRET applications rely on the measurement of FRET efficiency, that is related to the acceptor to donor distance:

$$E = \frac{R_0^6}{R^6 + R_0^6} \tag{2.30}$$

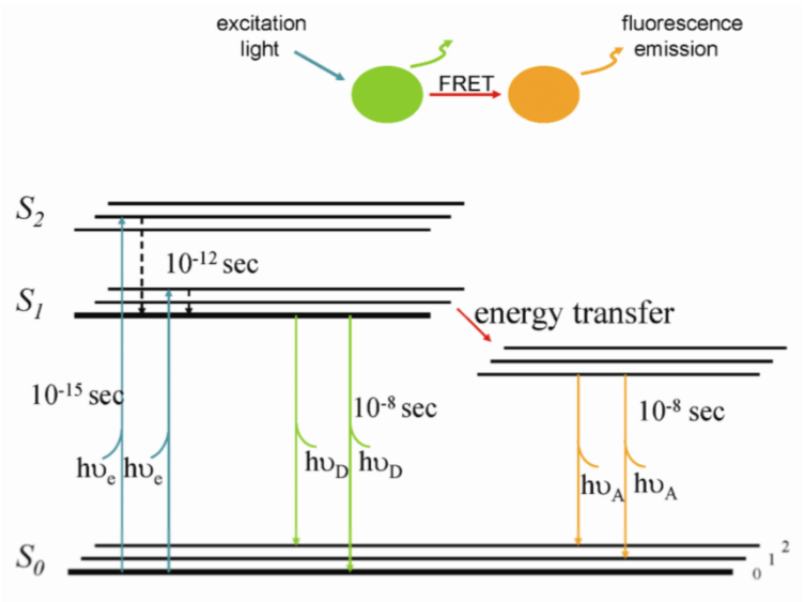

Figure 2.12: The electron transitions observed during the FRET process are described. S_0 depicts the ground state whereas S_1 and S_2 illustrate exited electron states. The vibrational sub energy levels are shown as additional minor energy levels. Energy transition upon photon (hv) acceptance of emission (fluorescence) are illustrated by arrows: acceptance of initial excitation light (blue), emittance of donor fluorescence (green) and emittance of acceptor fluorescence (orange). The timescales of the individual transition steps are shown. Figure taken from [231]

where R is the distance between the two involved fluorophores and R_0 is the Förster radius, which describes the distance at which the FRET efficiency E is 50%. The Förster radius is intrinsic to each specific acceptor/donor pair and typically lies in the range of 30 - 80 Å. R_0 depends on the integrated spectral overlap between the donor and acceptor spectra (J), as well as the relative orientations of the dipole moments of the donor/acceptor pair (κ), the refractive index of the media (n) and the donor quantum yield (Φ_0). If all these parameters are known R_0 can be calculated:

$$R_0^6 = \frac{9000\Phi_0(ln10)\kappa^2 J}{128\pi^5 n^4 N_A} \tag{2.31}$$

where N_A is the Avogadro's constant.

Experimentally, FRET can be measured by selective donor quenching ($E_{app,dq}$) or the sensitised FRET emission ($E_{app,se}$), also referred to as apparent FRET intensity.

$$E_{app,dq} = \frac{I_D - I_{DQ}}{I_D} \tag{2.32}$$

$$E_{(app,se)} = \frac{\epsilon_A}{\epsilon_D} \cdot \frac{F_{AD} - F_A}{F_A} \tag{2.33}$$

where I_D is the donor fluorescence intensity in the absence of an acceptor, I_{DQ} the donor intensity in the presence of an acceptor. Measurement of I_D is challenging as it would require complete photobleaching of the acceptor fluorophore in the sample and thus I_D is often approximated from a separate sample. F_{AD} is the acceptor fluorescence in the presence of a donor, and F_A is the acceptor fluorescence in the absence of a donor, which can easily be measured by exciting at the acceptor excitation wavelength. ϵ_A and ϵ_D are the molar extinction coefficients of the acceptor and donor respectively. When measuring $E_{app,se}$ the FRET signal needs to be carefully corrected for "bleed-through" intensities from fluorescence emitted by the donor in the wavelength range of the acceptor emission spectra and for "cross talk" of acceptor excited by the excitation light at the excitation wavelength of the donor.

Part I

Antimicrobial peptides

3

Peptide design, synthesis and activity

Contents

3.1 Introduction 63
3.2 Peptide sequence design 64
3.2.1 Sequence design principles of tilamin 64
3.2.2 Sequence design principles of ChoM 68
3.2.3 Solid phase peptide synthesis of antimicrobial peptides 70
3.3 Activity of tilamin 73
3.3.1 Minimum Inhibitory Concentration (MIC) 73
3.3.2 Confocal Microscopy 74
3.3.3 Atomic Force Microscopy (AFM) 77
3.3.4 Circular Dichroism (CD) 79
3.4 Activity of ChoM 81
3.4.1 Minimum Inhibitory Concentration (MIC) 81
3.4.2 Confocal Microscopy 82
3.5 Conclusion 84

3.1 Introduction

De novo peptide are designed based on principles that link primary and secondary peptide structures. For alpha helical structures these typically use heptad repeat sequence motifs in order to build secondary and super-secondary structures (coiled coils). *De novo* designed synthetic AMPs are characterised in this thesis in order to investigate the relationships between amino acid sequence, structure and function. The design principles are based around

autonomously folding naturally occurring structural motifs, which produce an amphipathic alpha helical secondary structure upon binding to an anionic membrane surface. The design principles will be outlined, with the main aim being to create novel broad-spectrum AMPs. All peptides are designed to primarily develop their antimicrobial potency via membrane lytic mechanisms. The AMP sequences used are predicted to be alpha helical when folded and are 21 amino acids in length, which corresponds to six helical turns and a total peptide length of ca. 30 Å when folded.

The predicted membrane activity of the designed sequences is characterised using spectroscopic and biophysical methods: (I) cwEPR (II) ssNMR (both outlined in Chapter 4) and (III) microscopy (Fluorescence confocal and Atomic force complemented by minimum inhibitory concentration (MIC) assays and circular dichroism (CD)). For this purpose different variants of the individual peptide sequences have been manufactured; for example including isotopic enrichments or the addition of a fluorophore, needed for NMR and microscopy studies respectively. The interplay of different biophysical methods on various timescales should allow for characterisation of a holistic picture of the precise function of the peptide of interest. The experimental methods are aided by computational simulation and verification wherever possible.

In this chapter the individual design principles and motifs will be outlined together with initial characterisation of the bactericidal potency of the designed peptide using microscopy, MIC assays, and CD. EPR and solid-state NMR studies are outlined in Chapter 4.

3.2 Peptide sequence design

3.2.1 Sequence design principles of tilamin

Tilamin is based around a previously *de novo* designed peptide sequence (amhelin), which forms expanding transmembrane pores [160]. Both peptides amhelin and tilamin are 21 amino acids long and contain neutral or small (N), polar cationic (C) and hydrophobic (H) residues that in an alpha helix cluster to create the characteristic spatial charge separation (Figure

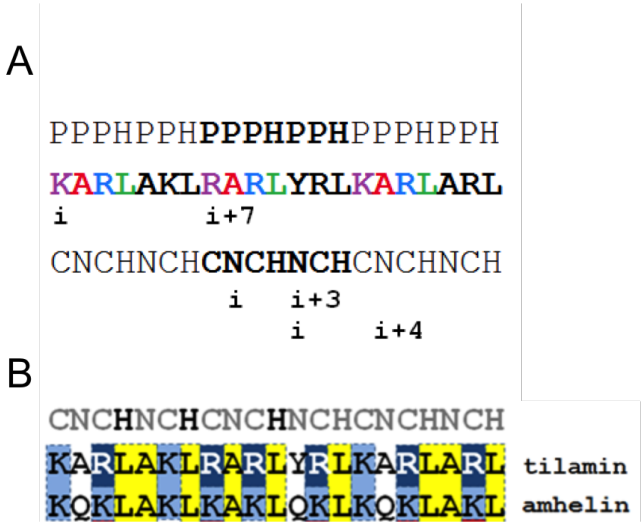

Figure 3.1: The design principles of tilamin, which is based on a repeat pattern of "hydrophobic", "cationic" and "neutral" residues. (A) The peptide sequence is based around two heptad repeat sequences ensuring amphipathicity and peptide folding upon membrane interaction. The tilamin sequence is shown in the middle whereas the heptad repeat sequences are placed above and below the amino acid sequence respectively. (B) Sequence alignment of tilamin and amhelin is illustrated. Note that amhelin is based around the same heptad repeat. Conserved cationic residues are shown in blue (lysines) and dark blue (arginines); conserved hydrophobic residues (yellow). (P = polar; H = hydrophobic; C = cationic; and N = neutral polar; Figure supplied by MG Ryadnov (NPL)).

3.1). The most basic underlying principle of peptide design are heptad repeat sequences with the identity $(PPPHPPH)_n$. This generic repeat motif averages a 3.5 residues spacing between individual hydrophobic residues and thus allows for the segregation of specific side chain characteristics and allows for peptide amphipathicity. Heptad repeats result in vertically "stacked" amino acid side chains in an ideal alpha helix with 3.6 amino acids per turn. This is exploited in separating the helix into individual flanks of helical spacings *i*, *i+3* and *i+7*. The repeat sequence of *CNCHNCH* is applied in order to generate cationic (C), hydrophobic (H) and neutral (N) helical segments (Figure 3.1). This geometry allows for adaptation of an amphipathic alpha helix in a membrane environment [232].

The overall length of the helical peptide is ∼3.15 nm (assuming 0.54 nm height per complete helical turn [160]), which is a typical length of AMPs when compared to native sequences (Figure 1.11) comprising a total of 6 helical turns. The aim of the tilamin sequence is to generate a potent peptide sequence that does not function by complete bilayer poration and acts on the interface region with a broad activity spectrum.

The peptide-membrane interaction consists mostly of ionic interactions between positively charged amino acids and the anionic microbial membrane, mainly via interactions of lysine and arginine residues. The precise chemistry of each individual amino acid is an important consideration, since for example, the free energy of hydration is dependent on side chain structure. Both lysine and arginine have to overcome an energy penalty when crossing the bilayer in a protonated form due to the hydrophobic effect. However the energetic penalty of arginine is higher then for lysine, which can be deprotonated within a membrane [233]. The guanidine group of arginine favours extensive hydrogen bonding, which supports peptide interaction at the membrane interface region. Each guanidine group allows for five hydrogen bonds preferentially locating the side chain to the phosphate cluster at the interface, and thus promoting membrane interaction. For this reason six lysine residues of amhelin were replaced by arginine residues in the design of tilamin limiting the propensity to cross the membrane as would be required for the formation of a pore.

Further to this, the ratio of hydrophobic to polar residues needs to be considered for peptide design. A large hydrophobic contribution will favour haemolytic and cytotoxic peptide action [23]. Charged amino acids will direct the peptide to the microbial membrane, and the hydrophobic component will allow for membrane perturbation. Tilamin was designed with a polar to hydrophobic ratio of 1.5:1 [160], achieved by splitting of the charged cluster into two faces separated by a weakly hydrophobic alanine cluster. Splitting the charged cluster in two faces allows for extensive electrostatic interactions on two peptide faces. The charge interplay of the two arginine/lysine clusters is predicted to anchor tilamin to the membrane interface, where the membrane lytic activity should primarily develop [233].

The alanine cluster is separated into two faces by a bulky tyrosine, which allows for some flexibility along the otherwise predicted straight alpha helix, allowing the peptide to adapt to membrane curvature. Further to this the tyrosine side chain is expected to be located in the aromatic belt region close to the glycerol backbones of the bilayer [234]. A complementary property of this design feature is the intrinsic tyrosine fluorescence and A_{280} absorbance that allows for easy monitoring during peptide purification and initial membrane binding studies.

A highly hydrophobic leucine cluster is placed opposite the alanine cluster, separated by the cationic peptide flanks. Leucine possess a high intrinsic hydrophobic index, which

results in strong lipid binding via hydrophobic interactions. In general leucines and isoleucine residues are the most common hydrophobic component to AMPs [146]. These residues are smaller than other bulky hydrophobic residues like phenylalanine or tryptophans and thus have also a higher aqueous solubility.

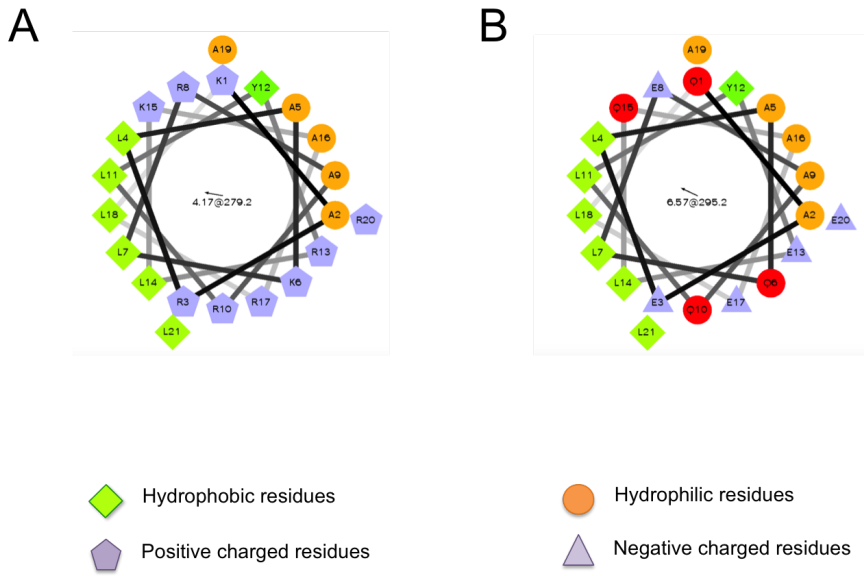

Figure 3.2: Helical wheel representation of designed AMP sequences are shown. (A) 21 amino acid long sequence of tilamin is shown. (B) The 21 amino acid long QAELA, the negatively charged counter part to tilamin is depicted. The colour intensity codes for the relative strength of hydrophobicity, where hydrophobic residues are green and less hydrophobic residues are shown as yellow. Similarly the most hydrophilic residues are depicted in red and less hydrophilic residues are coded as orange. Residues carrying a charge are shown in light blue. Helical wheel representations were generated using the tool available at http://rzlab.ucr.edu/scripts/wheel/wheel.cgi.

Peptide oligomerisation is promoted by exploiting the characteristic helical spacing of i and i+7, using a neutral residue spacing of i, $i + 3$ and $i + 4$ which promotes peptide-peptide interactions (Figure 3.1 B). This pattern is often referred to as the 3,4 hydrophobicity pattern and promotes oligomerisation in a cooperative manner [160]. For this reason leucine residues are placed around the helix in spacings of +7, creating motifs similar to leucine zippers. This is further enhanced by the high hydrophobicity index of leucine bringing individual peptides together [160].

A control peptide was also synthesised ((QAELA), Figure 3.2), which was based around the same design rationale, yet the cationic residues were replaced by anionic residues in order to abregate membrane-lytic activity.

All amino acids used in the peptide design have a high helical propensity, which accounts for the projection of tilamin to fold into an alpha helix once it interacts with an anionic phospholipid bilayer.

3.2.2 Sequence design principles of ChoM

The peptide ChoM is designed based on the sequence of cecropin B (CecB), which is a member of the ceropin family found as part of the innate immune system of insects. Cecropins were first isolated from *H. cecropia* in 1980, but they have also been identified in other insects [235; 236]. These peptides are typically 31-39 amino acids that fold into an alpha helix [237]. They have been shown to possess antimicrobial activity against Gram-positive and Gram-negative bacteria and fungi [237]. The C-terminus is capped with an amide group for most cecropins, which might be crucial for a charge driven insertion into the pathogen membrane [238; 239]. In addition to the characteristic antimicrobial activity, cecropins have also been shown to be active against parasitic infection, to inhibit viral replication in the case of HIV-1 and have a potential anti-cancer activity [240; 241; 242; 243; 244]. Cecropins are unstructured in solution and fold into an amphipathic alpha helix upon membrane binding.

Cecropin B is 35 amino acids in length and active against Gram-positive and Gram-negative bacteria. The folded form of cecropin B contains two alpha helical domains [245; 246]. The N-terminal domain shows an amphipathic character, whereas the the C-terminal domain has a strong overall hydrophobicity. This results in an overall peptide length of 5 nm in the folded state. The N-terminal domain, having a net positive charge, is the driving force for pathogenic membrane interaction, whereas the C-terminal domain might promote membrane insertion and possibly even pore formation. However, the whole length structure of cecropin B is believed to act primarily by a carpet like mechanism [247].

Here the two alpha-helical cecropin domains have been separated and a 21 amino acid long peptide comprising the amphipathic N-terminal domain has been created (ChoC). Preliminary results indicated that the N-terminal domain possesses the ability to fully insert into a bilayer followed by the formation of clear pores (AFM (NPL), not shown). Following these results

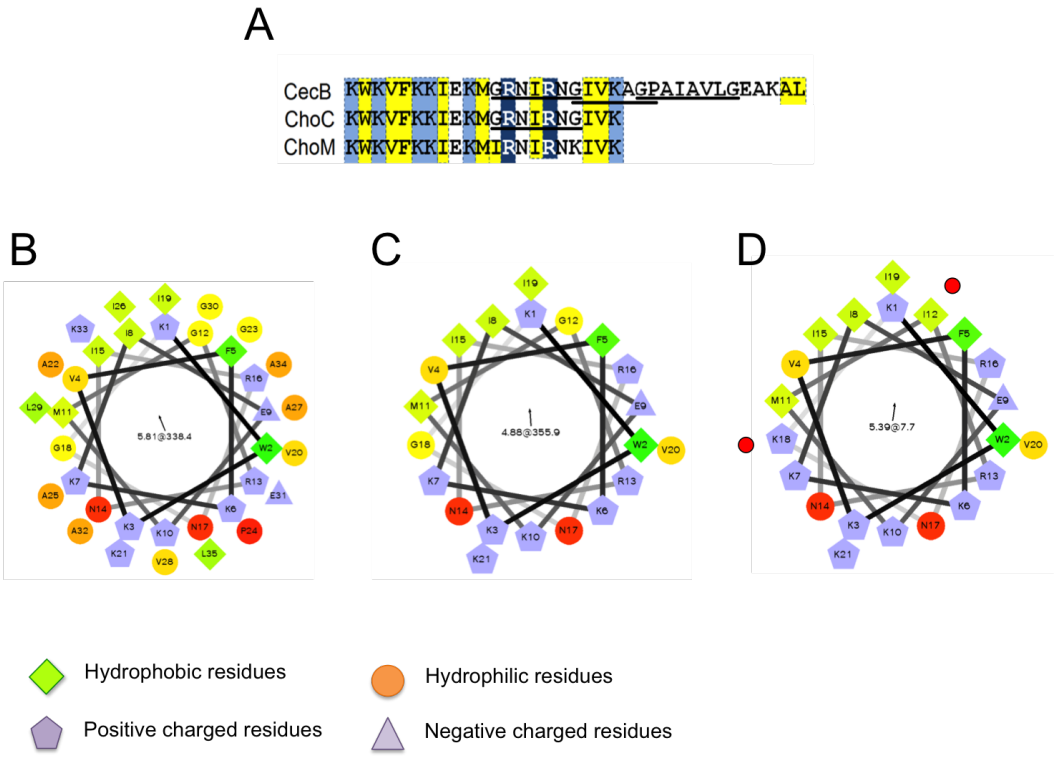

Figure 3.3: The sequence design principles of ChoM are illustrated. (A) The native sequence of CecB is shown. The N-terminal isolated amphipathic helical domain is shown (ChoC) and the slightly altered version thereof (ChoM). Conserved cationic residues are shown in blue (lysines) and dark blue (arginines); conserved hydrophobic residues (yellow) and glycine zipper motifs are underlined (Figure taken from MG Ryadnov). (B) Helical wheel reprsenation of CecB; (C) helical wheel representation of ChoC and (D) helical wheel representaion of ChoM, where altered amino acid residues are highlighted by a red point (compared to ChoC). Helical wheel representations were generated using the tool available at http://rzlab.ucr.edu/scripts/wheel/wheel.cgi .

two amino acids have been replaced: glycine at position 12 is replaced by an isoleucine and glycine at position 19 is replaced by a lysine, leaving no glycine residues in the sequence (Figure 3.3). Glycine residues allow for peptide deformations along the alpha helix and thus the peptide can adopt to membrane curvature and thinning. The introduction of the additionally charged lysine residue at position 19 not only limits the hydrophobic face of the peptide but should additionally place a thermodynamic barrier to full transmembrane peptide insertion via a charge-driven interface interaction, possibly involving a snorkelling lysine side chain interacting directly with the lipid head groups or phosphate. A similar membrane-lytic potency to tilamin developed at the membrane interface is expected.

3.2.3 Solid phase peptide synthesis of antimicrobial peptides

A range of different peptides were synthesised for use in biophysical characterisation methods presented in this thesis. Both isotopically labelled and fluoresecently labelled peptides have been manufactured. All peptides were synthesised by solid-phase synthesis using Rink amide MBHA resin and thus an amide cap is located at the carboxyl terminus. The individual peptide sequences are summarised in table 3.1.

Table 3.1: Summary of all synthesised peptide sequences

Peptide name	Amino acid sequence
tilamin	KARLAKLRARLYRLKARLARL
tilamin - (5) - Ala_{d3}	KARLA_{d3}KLRARLYRLKARLARL
tilamin - (9) - Ala_{d3}	KARLAKLRA_{d3}RLYRLKARLARL
tilamin - (16) - Ala_{d3}	KARLAKLRARLYRLKA_{d3}RLARL
tilamin - (19) - Ala_{d3}	KARLAKLRARLYRLKARLA_{d3}RL
tilamin - (12) - Tyr_{15N}	KARLAKLRARLY_{15N}RLKARLARL
tilamin - fluorescein	KARLAKLRARLYRLKARLARL -β - Ala - fluorescein
tilamin - Cys	KARLAKLRARLYRLKARLARL - β - Ala - Cys
QAELA	QAELAQLEAQLYELQAELAEL
QAELA - fluorescein	QAELAQLEAQLYELQAELAEL -β - Ala - fluorescein
ChoM	KWKVFKKIEKMIRNIRNKIVK
ChoM - (4) - Ala_{d3}	KWKA_{d3}FKKIEKMIRNIRNKIVK
ChoM - (8) - Ala_{d3}	KWKVFKKA_{d3}EKMIRNIRNKIVK
ChoM - (12) - Ala_{d3}	KWKVFKKIEKMIRNA_{d3}RNKIVK
ChoM - (20) - Ala_{d3}	KWKVFKKIEKMIRNIRNKIA_{d3}K

Peptides were synthesised using a microwave-catalysed synthesis method (CEM Inc., Matthews, NC, USA) using a 100 μmol scale, dictated by the resin substitution factor. Amino acids were Fmoc protected and othogonal protection was used for reactive side chains (see

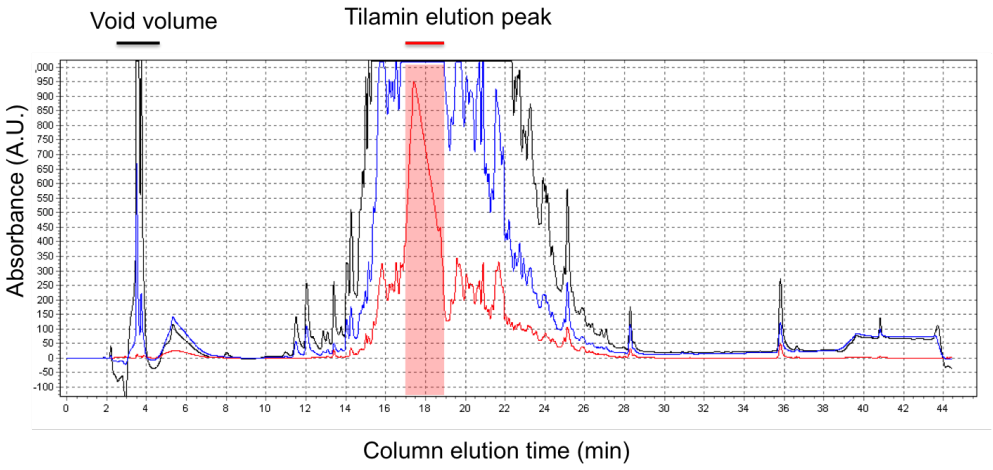

Figure 3.4: A representative semi-prep HPLC trace is shown. Sample was injected in 5% acetonitrile in the presence of 0.1% TFA. The void volume of unbound material is indicated (black line above the graph) and the elution of tilamin is highlighted in red. The elution profile was monitored by absorbance at 280 nm (red), 230 nm (blue)and 214 nm (black). Note that the absorbance at 214nm and 230nm are out of range for the main elution peak, yet they are a good indicator for minor peptide fractions coming off.

Appendix A.2.1.1). All peptide sequences were cleaved from the resin using 95% TFA, this was followed by lyophilisation to remove the remaining acid. The peptide was solubilised in 5% acetonitrile and 0.1% TFA for purification by HPLC.

A characteristic HPLC trace illustrating peptide purification is shown in Figure 3.4, using reverse phase chromatography on an immobilised hydrophobic phase that allows for peptide binding in aqueous conditions. The bound peptide is eluted by a gradient elution of varying organic solvent water composition (here acetonitrile was used). An example elution trace of a C18 column (for tilamin) is shown in Figure 3.4 where the elution peak is central ($\sim$ 18 min) to the trace and highlighted.

The peptide identity was confirmed by mass spectrometry (MALDI TOF) and peptide purity was analysed by analytical HPLC: all traces are shown in Figure 3.5. The corresponding MALDI TOF MS profiles are shown in the appendix to this chapter (see Appendix A.2.1.2).

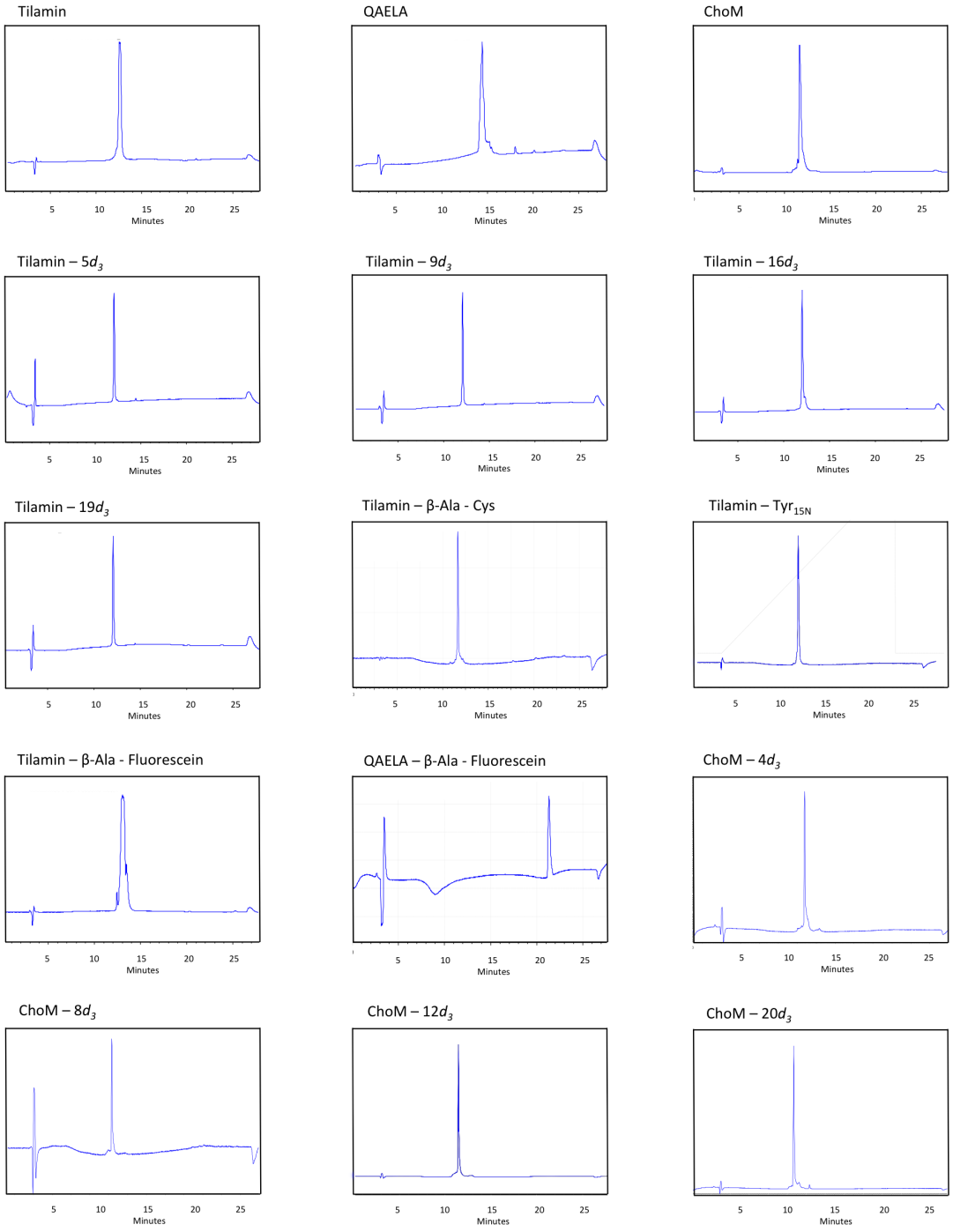

Figure 3.5: Analytical HPLC traces of purified peptides are shown. In all cases a high purity represented by a single and sharp elution peak was achieved. The samples were run on reverse phase columns with an elution gradient from 5% acetonitrile to 95% acetronitrile in presence of 0.1% TFA and absorbance at 214 nm was monitored. All tilamin constructs were analysed on C18 columns; QAELA on a C8 column; QAELA-fluorescein on a C18 column and ChoM constructs on a C18 column.

3.3 Activity of tilamin[1]

3.3.1 Minimum Inhibitory Concentration (MIC)

Tilamin activity across a range of bacteria was tested and does not show a strong preference to Gram-positive or Gram-negative bacterial species (Table 3.2). As predicted the anionic control peptide QAELA is non-active, confirming that a electrostatic membrane interaction is important for tilamin activity. Furthermore, neither peptide shows hemolytic activity against human erythrocytes.

Tilamin showed high bactericidal potency measured by MIC, the lowest peptide concentration at which pathogenic growth is inhibited, in the μM range against a broad range of Gram-positive and Gram-negative bacteria (Table 3.2). Low μM activity profiles are consistent with the potency of naturally occurring AMPs: melittin (9 - 18μM); magainin - 2 (40 - 50μM); cecropin-P1 (0.3 - 17μM) or omiganan (4 - 8μM) [248; 249; 250; 251; 252; 253; 254].

The variation in peptide potency across the tested bacteria is not systematic and the relative lower potency to some bacteria might be due to limited resistance phenotypes that vary across different species [255; 256]. The obtained MICs vary from as low as 0.5 μM for *Micrococcus luteus* to 12 μM for *Pseudomonas aeroginosa*. In general tilamin shows a slightly higher activity against Gram-positive bacteria compared to Gram-negative, which might possibly be explained by differences in the cell wall of the two bacterial classes. Overall the MICs for tilamin are more consistent across all tested bacteria when compared to the template AMP amhelin, which showed MICs as high as the 50 μM against *Staphylococcus aureus*. The MICs of amhelin against Gram-negative bacteria are in a similar range when compared to tilamin [160]. MIC experiments give a guideline to antibiotic effectiveness of the compound tested. They rely on the observation of macroscopic changes eg. loss of cellular growth and do not give microscopic detail on peptide action. It is noteworthy to point out the timescale of MIC experiments, which normally run for 24 h and thus give little information on the timescale of peptide activity or molecular changes on the cellular level, nevertheless they are a valuable initial starting point for peptide characterisation. The reported MIC concentrations determine the onset of a macroscopically detectable threshold-like cell death and thus does

[1]Note that experimental details for this section are given in appendix A.1.1

Table 3.2: MICs for tilamin against Gram-positive and Gram-negative bacteria

Bacterium	tilamin (μM)	QAELA (μM)
Gram-negative		
Escherichia coli (K12)	10	>250
Pseudomonas aeroginosa (ATCC 27853)	12	>250
Salmonella enterica (ATCC700720)	3	>250
Gram-positive		
Staphylococcus aureus (ATCC 6538)	9	>250
Micrococcus luteus (ATCC 7468)	0.5	>250
Bacillus Subtilis (ATCC 6633)	1	>250
Human erythrocytes	>250	>250

MIC values reported for antimicrobial tilmain activity. Experiments were done in triplicates starting with a two-fold serial dilution in peptide concentration and refined MIC values were obtained for a linear series with stepwise increase (step size 1μM) in peptide concentration in the region of interest. Low μM values are observed across all bacterial strains tested. QAELA, the anionic control peptide, is not active against the bacteria tested. Neither peptide interacts with human erythrocytes (MIC experiments in collaboration with B Lamarre (NPL); additional information found in section A.1.1).

not fully represent the onset or pre-stages of peptide function, which might occur already at an earlier time point or lower peptide concentration. The observed activity profiles initially confirm the underlying peptide design principles and a broad spectrum of bactericidal activity.

3.3.2 Confocal Microscopy

Most AMPs primarily act on membranes, yet the bacterial cell envelope is complex and alternative target sites within the cellular envelope as well as intracellular targets exist. Confocal microscopy experiments of fluorescein-labelled tilamin on giant unilamellar vesicles

(GUVs) and bacteria were performed to visualise peptide activity and potential membrane localisation together with peptide induced deformations. The GUVs were composed of POPC:POPG (3:1, molar ratio) in order to mimic the overall charge distribution of the bacterial cytosolic membrane (based on *E. coli*).

GUVs were stable over the time range of the microscopy (Figure 3.6 A). Upon addition of fluorescein-tagged tilamin peptide, localisation to the membrane is clearly observed; as illustrated by overlap of the fluorescein tag (green) and the CellMask^{TM} stained membrane (blue) (Figure 3.6 B). After a short incubation time this leads to membrane deformations (5 min), which is followed by membrane disintegration and vesicle leakage as observed by mixing of sulforhodamine B, CellMask^{TM} and fluorescein (Figure 3.6 B). Similar effects were also observed for tilamin in the absence of fluorescein, suggesting that the fluorescein addition (separated from the native peptide sequence by a β-Alanine residue) did not quench or drastically alter peptide activity (Figure 3.6 C). Drastic membrane deformations and vesicle disintegration are visible in the late stages illustrated by high intensity local concentrations of CellMask^{TM} stained membrane (Figure 3.6 C; 10 and 20min; orange arrow). These deformation occur prior to vesicle leakage as the sulforhodamine is still relatively contained (red). Interestingly, distinct membrane fractions are observed after long incubation times, illustrated by the CellMask^{TM}-stained islets (highlighted by an orange arrow Figure 3.6 C), which could be indicative of removed membrane fractions or formation of micellar lipid structures as late stage of membrane and vesicle rupture. The resulting membrane deformation could arise due to tilamin induced lipid curvature upon membrane interaction. A distinct channel-like behaviour would possibly result in more defined vesicle leakage compared to complete disintegration, also this remains plausible as a late stage. Fluorescein-tagged tilamin was also incubated in the presence of *S. aureus* and *E. coli* to represent both Gram-positive and Gram-negative bacteria (Figure 3.6 D). *E. coli* show their characteristic rod-like appearance and *S. aureus* their more spherical morphology. In both cases peptide localisation to the bacterium was observed, however, it is not possible to determine the precise peptide location. Qualitatively, no deformation of the overall bacterial morphology can be observed, possibly due to the increased overall stability in presence of an intact cell wall. It is suggested that, based on the GUV observations, tilamin localises to the membrane and cellular envelope (Figure 3.6 B,C). Nevertheless, peptide translocation to the cytoplasm cannot be excluded for bacterial images, where substantial peptide coverage was observed.

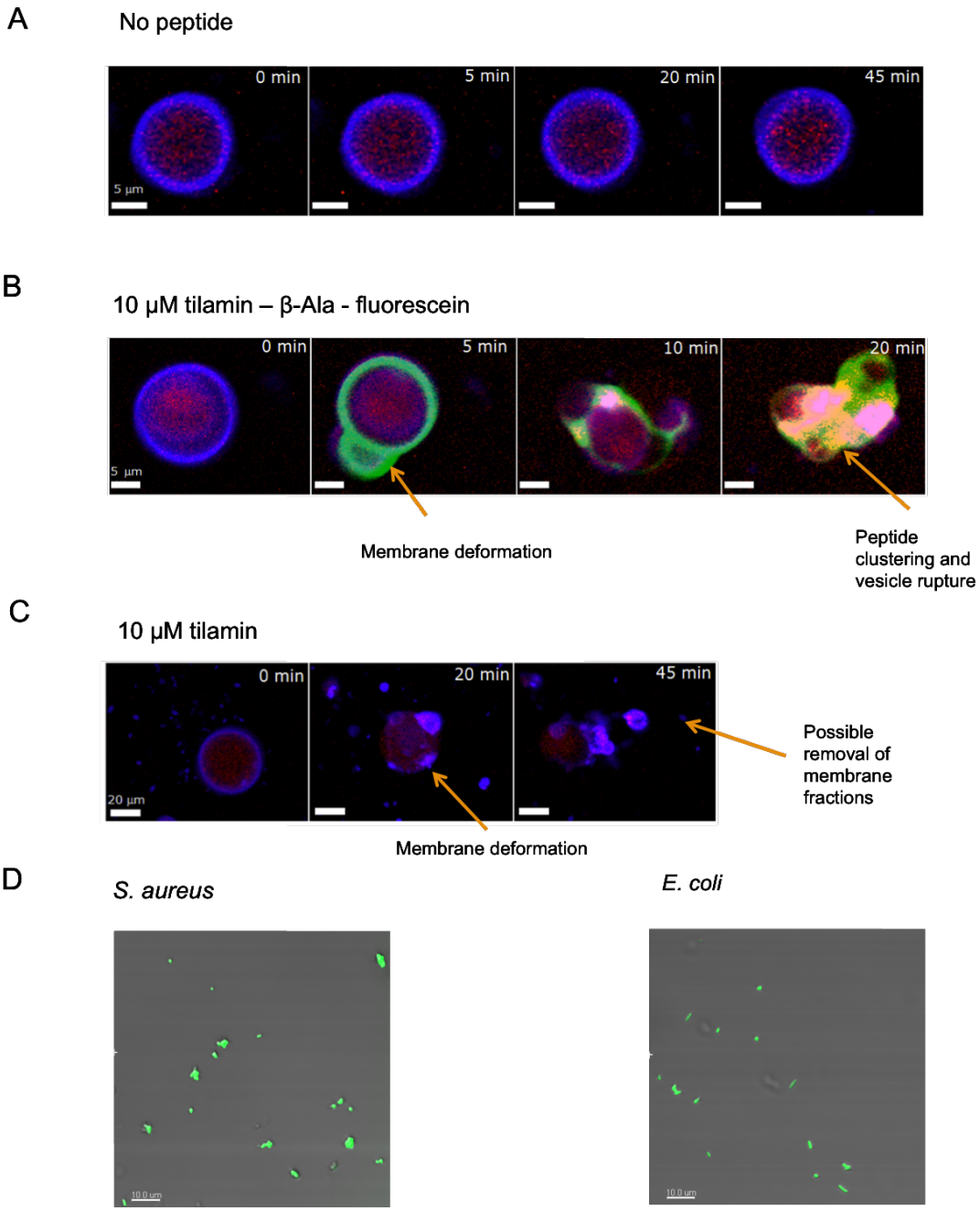

Figure 3.6: Confocal microscopy images of tilamin and tilamin conjugated to fluorescein are shown. GUVs are prepared of POPC:POPG (3:1, molar ratio). The interior of GUVs contains sulforhodamine B (red) and the membrane is stained by CellMask^{TM} Deep Red staining (blue), the fluorescein-tagged tilamin is shown in green. (A) GUV staining in the absence of AMPs. (B) GUVs upon fluorescein-tagged tilamin addition. The peptide seems to cluster at the membrane causing bilayer deformation (highlighted by an orange arrow) and eventually lysis and peptide segregation (highlighted by an orange arrow). (C) GUVs are incubated with untagged tilamin and similar bilayer effects when compared to fluorescein-tagged tilamin are observed. (D) Fluorescein-tagged tilamin is incubated with *S. aureus* and *E. coli* at $10\mu M$, clear peptide association with the bacterium is seen, the precise peptide location is difficult to determine (GUV preparation by Dr. A Bella (NPL) and microscopy in collaboration with B Lamarre (NPL)).

The results are indicative of qualitative membrane activity of tilamin. The peptide has the ability to deform a phospholipid bilayer and cause leakage. No peptide translocation across the bilayer could be observed for the tilamin-fluorescein construct in GUVs (Figure 3.6 B), which evidently bound to the bilayer prior to membrane rupture. The importance of the bacterial envelope is difficult to assess, and peptide might interact with negatively charged LPS and the peptidoglycan layer. The high density peptide coverage of *S. aureus* and *E. coli* is in agreement with similar activity profiles against Gram-positive and Gram-negative bacteria (MICs, Table 3.2), despite different cell envelope compositions.

3.3.3 Atomic Force Microscopy (AFM)

In order to observe topography changes induced by tilamin upon bacterial interaction, AFM experiments have been performed on intact *E. coli* and spheroplasts, cells that lack the outer membrane. Both intact cells and spheroplasts were immbolised on gelatine (0.5 %) coated Mica substrates for imaging [257]. *E. coli* in the absence of tilamin showed the expected rod like shape and a smooth surface (Figure 3.7 A). Upon stripping off the outer membrane, the rod like appearance is lost and spheroplasts are depicted with a smooth membrane showing a marbling pattern. (Figure 3.7C). A destabilising of the membrane was clearly evident in both scenarios when tilamin was added. In the case of intact *E. coli*, overall morphological changes were observed (Figure 3.7 B) possibly resembling cell envelope deformations. For spheroplasts clear destruction of the membrane was observed, no clear membrane morphology could be observed anymore, and additional cellular leakage occurred. It is unclear if the observed cellular leakage contains micellar membrane fragments due to lipid removal, which might be expected for peptide behaviour by a carpet or toroidal-like mechanism.

The corresponding cross sectional profiles are shown in Figure 3.8 for intact *E. coli* cells and post 5 min treatment with tilamin. For intact *E. coli* smooth height profiles are observed for the longitudinal and latitudinal axis (Figure 3.8 A). The qualitatively observed deformations caused upon tilamin interaction translate in a uneven cellular morphology with "crater"-like structures present (Figure 3.8 B). The height profile varies as much as 150 nm between the lowest and highest points of the cross sectional profiles. These changes in morphology

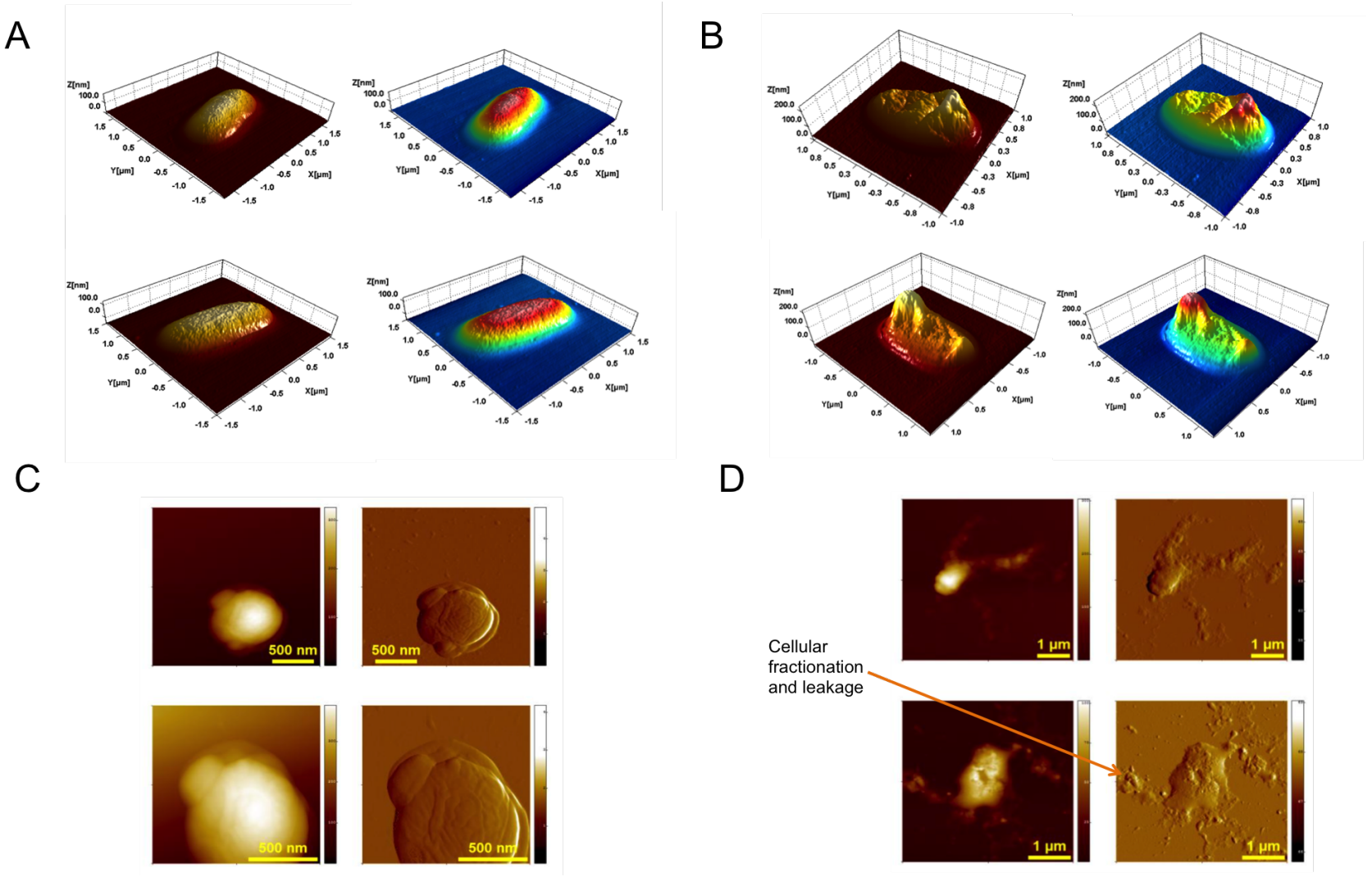

Figure 3.7: Representative AFM topographies of *E. coli* and *E. coli* derived spheroplasts in absence and upon 5 min tilamin incubation (10 μM). (A) 3D topologies of individual *E. coli* cells in the absence of peptide. (B) 3D topologies of individual *E. coli* cells upon peptide interaction. (C) Topography (left panels) and amplitude (right panel) of spheroplasts in the absence of peptide. (D) Topography (left panels) and amplitude (right panel) of spheroplasts in the presence of peptide. All images and tomographies are representative of scenarios found across the multiple samples investigated (Sample prepartion in collaboration with B Lamarre and AFM images taken together with Dr S Ray (NPL)).

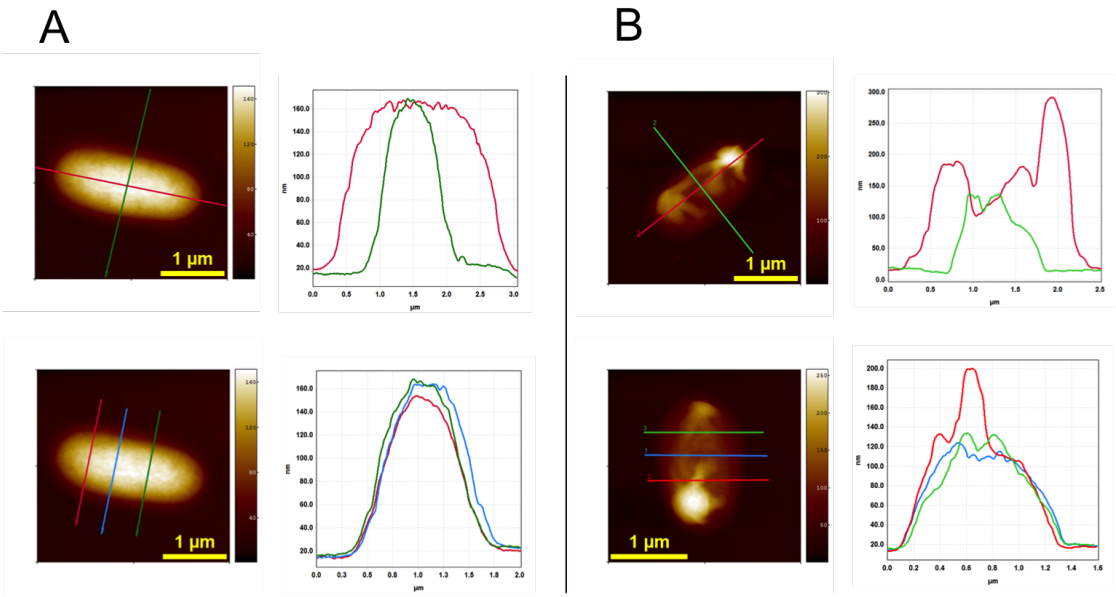

Figure 3.8: Representative cellular cross section of *E. coli* in the absence and presence of tilamin (10 μM, 5 min incubation). (A) Rod-shaped *E. coli* in the absence of tilamin. (B) Rod-shaped *E. coli* post tilamin treatment. (Experiments performed in collaboration with B Lamarre and Dr S Ray (NPL)).

are in agreement with the membrane restructuring events seen using confocal microscopy. The seemingly explosive-like leakage seen for spheroplasts is not seen for intact *E. coli* cells, suggesting that the outer membrane and the associated LPS are important for the overall stability of the cell. It should be noted that observed morphological changes are large when compared to *E. coli* treated with amhelin (10μM, 30 min), which possibly indicates tilamin mechanistics that are distinct from amhelin ([160], Figure S2 A and B). The results reported here qualitatively suggest that tilamin interacts with the plasma membrane of spheroplasts, which is also a likely for intact *E. coli* causing membrane deformations (Figure 3.7 D).

3.3.4 Circular Dichroism (CD)

Further to the membrane activity observed by confocal microscopy and AFM, the secondary structure of tilamin within a model membrane was confirmed using CD. The peptide is unstructured in solution and becomes alpha-helical upon contact with POPC:POPG (3:1, molar ratio) bilayers (Figure 3.9). The anionic PG component seems to be important for full peptide folding, since only a partial fold is observed in a POPC only environment (Figure 3.9).

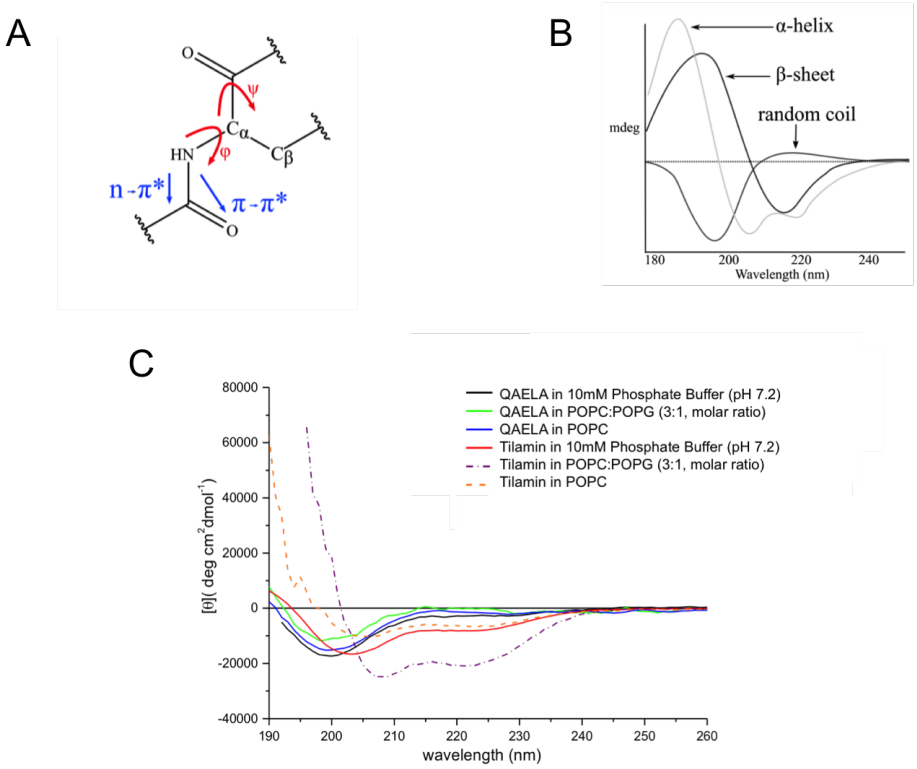

Figure 3.9: CD spectra of tilamin in the presence and absence of vesicles. (A) The amide bond transitions giving rise to the characteristic absorbance at in the UV region are illustrated ($n \rightarrow \pi^*$ and $\pi \rightarrow \pi^*$ result in UV absorption at 190 and 220 nm respectively). The exact absorption depends on the bond angles Ψ and φ and thus report directly on secondary structure. (B) The characteristic CD line shapes for an α-helix, β-sheet and random coil are shown. (C) The recorded CD spectra for tilamin and QAELA in different environments are displayed. The peptide concentration of 30 μM at all samples and the peptide to lipid molar ratio was 1:100. Exact sample conditions are found labelled in the figure legend. In collaboration with NPL; Parts A and B kindly obtained from D Yin (Oxford).

Full alpha-helical peptide folding is important for tilamin action via the designed principles. The characteristic and crucial amphipathic peptide character is only present in an alpha helical confirmation. The CD data (Figure 3.9) suggests that such a conformation only arises in net anionic membranes mimicking the pathogenic membrane. This also emphasises the importance of electrostatic interactions for tilamin folding and function, that are present in an anionic membrane environment. The control sequence of QAELA does not change its secondary structure upon membrane presence (Figure 3.9), most likely not interacting with the bilayer.

A full alpha helical configuration is essential for tilamin in order to develop its bactericidal potential and to translate the mechanistics predicted by the outlined design principles (section 3.2) into biological function, since the peptide design is based around repeating heptads. The

model lipid composition used in this study and for peptide-lipid interaction characterisations hereafter is POPC:POPG (3:1, molar ratio) unless otherwise stated. The relative acyl chains are palmitoyl and oleoyl chains with respective length of C16:0 and C18:1, are major components (but not exclusively) of *E. coli* and other bacterial membranes [258].The PC:PG (3:1, molar ratio) is a generic anionic composition that broadly resembles the charge distribution of zwitterionic and anionic lipids in the bacterial membrane. However, this can only be seen as an approximation as lipid species and the precise distribution varies across different bacterial species (Table 1.2). Note that depending on the organism, the main zwitterionic lipid component varies between PE and PC, e.g *E. coli* contains a large proportion of PE, whereas it is absent for *S. aureus*. This however, did not affect tilamin activity, which shows broad potency against the tested bacterial species (MICs, Table 3.2).

3.4 Activity of ChoM

3.4.1 Minimum Inhibitory Concentration (MIC)

Similar to tilamin, the activity of ChoM variants were tested for antimicrobial activity against bacteria (Table 3.3). In contrast to tilamin, which contains alanine residues as part of the designed sequence, ChoM had to be chemically changed for incorporation of deuterated methyl groups, which are exploited for structural investigation using oriented solid-state NMR.

ChoM shows high antimicrobial activity with MICs <10 μM, across all bacteria tested, which is a similar potency to tilamin. The chemical alterations (V4A, I8A, I12A and V20A) did not alter the antimicrobial activity, with MIC values in a similar range. ChoM - (8) - Ala_{d3} is the only peptide variant that shows slightly lower activity against *S. aureus* with an MIC of 25 μM compared to the other peptide sequences. Similarly the probed activity against *P. aeroginosa* and *K. pneumoniae* are also reduced by a factor of two but still remains in the μ M range. Residue eight is central to the hydrophobic peptide phase (Figure 3.3), which might be important for peptide activity. The other mutated residues are placed towards the edges of this hydrophobic face. None of the peptide variants induced high hemolysis rates suggesting that the intended antimicrobial character is retained.

Table 3.3: MICs for ChoM against Gram-positive and Gram-negative bacteria

Bacterial species	ChoM (μM)	ChoM - (4) - Alad_3 (μM)	ChoM - (8) - Alad_3 (μM)	ChoM - (12) - Alad_3 (μM)	ChoM - (20) - Alad_3 (μM)
Gram-negative					
Escherichia coli (K12)	1.56	3.12	3.21	6.25	3.12
Pseudomonas aeroginosa (ATCC 27853)	3.12	3.12	6.25	3.12	3.12
Klebsiella pneumoniae (NCTC 5055)	6.25	6.25	12.5	6.25	6.25
Gram-positive					
Staphylococcus aureus (ATCC 6538)	6.25	12.5	25	12.5	6.25

Hemolysis (at 250 μM peptide)	ChoM - (4) - Alad_3 (%)	ChoM - (8) - Alad_3 (%)	ChoM - (12) - Alad_3 (%)	ChoM - (20) - Alad_3 (%)
Bovine erythrocytes	1.2	1.2	2.0	1.7

MIC values reporting on the antimicrobial activity of ChoM and ChoM. All peptides tested show MICs in the low μM range and are active against all bacterial strains tested. Neither peptide induced hemolysis when tested with bovine erythrocytes. All experiments were done in triplicates and the lowest value of a two-fold dilution series at which no bacterial growth was detected is reported (experiments in collaboration with B Lamarre (NPL)).

3.4.2 Confocal Microscopy

The prepared GUVs were stable across the experimental time, which is illustrated by the sulforhodamine B (red) contained within the vesicle stained with CellMask^{TM} (blue, Figure 3.10 B). GUV incubation with ChoM led to membrane deformations, illustrated by non uniform staining by CellMask^{TM} and non spherical membrane appearances (examples of deformations are highlighted in Figure 3.10, orange arrow). Incubation with ChoM and mutants caused dye leakage of the GUVs after 10-20 min for all constructs. Furthermore, qualitatively the vesicle sizes seem to decrease after extended incubation times with ChoM. No distinct differences could be observed between the individual peptide constructs, all showing membrane activity in agreement with MIC experiments (Table 3.3). The overall morphological changes are less drastic compared to tilamin, which showed complete mixing of lipids, peptide and sulforhodamine B.

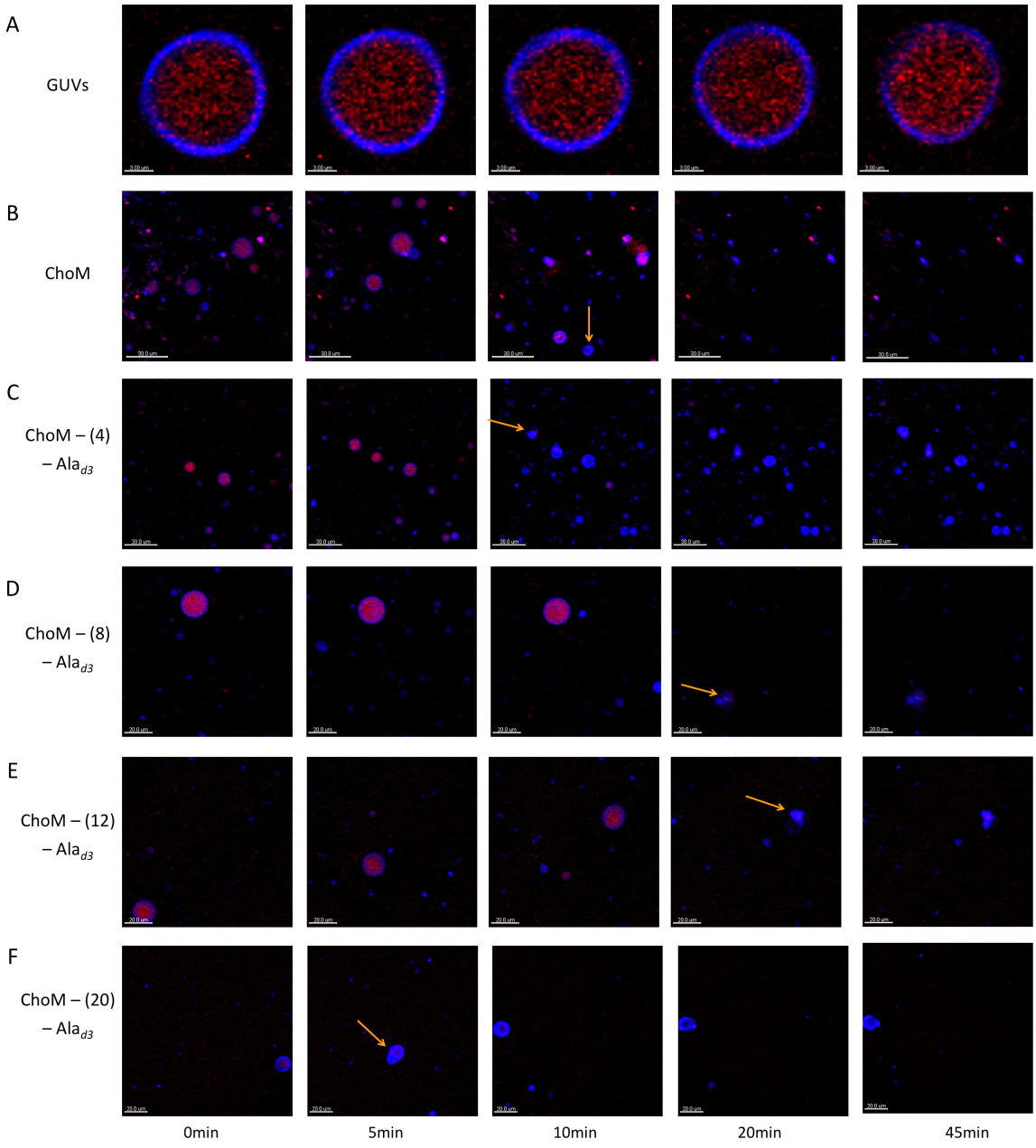

Figure 3.10: Confocal microscopy images of ChoM and ChoM variants in the presence of GUVs. The colours indicate staining by CellMask^{TM} (blue) and sulforhodamine B (red). Pictures were taken at different time points to monitor GUV leakage and membrane deformations. (A) GUVs in absence of ChoM (10 μM), (B) ChoM (C) ChoM - (4) - Alad_3 (10 μM), (D) ChoM - (8) - Alad_3 (10 μM), (E) ChoM - (12) - Alad_3 (10 μM), (F) ChoM - (20) - Alad_3 (10 μM). Vesicle deformation are highlighted by arrows (orange). Experiments in collaboration with B Lamarre (NPL).

3.5 Conclusion

The biophysical characterisation of peptide interaction is broadly consistent with the peptide design principles outlined in section 3.2. Tilamin is a potent antibiotic showing activity against a range of bacterial species both Gram-positive and Gram-negative (Table 3.2). The peptide is structured upon interaction with a bacterial membrane mimetic (Figure 3.9) and develops its high antibiotic potency by membrane disruption (Figure 3.6 and Figure 3.7). The further aim of this thesis is to characterise the tilamin - membrane interaction in detail investigating its effect on lipid dynamics and structure as well as to gain insight into the peptide membrane insertion mode. A microscopic understanding of tilamin behaviour will contribute to the validation of common design principles and aid the understanding of peptide-function relationships.

The shortened CecB construct consisting of the amphipathic N-terminal alpha helical segment (ChoM) shows antimicrobial activity despite lacking the hydrophobic C-terminal peptide domain. It was previously suggested that the N-terminal domain is responsible for the cytotoxic activity whereas the C-terminal domain is not important in this regard and might serve other purposes like membrane insertion [164]. This hypothesis is supported by observation that cecropin B3, consisting of two hydrophobic domains, could not induce currents upon treatment of a stomach carcinoma cell line, which is in contrast to cecropin B, which contains an amphiphathic and a hydrophobic domain [259]. Further to this, cecropin B1, consists of two amphipathic helices and shows potency against leukemia cell lines [164; 260]. A similar behaviour is plausible for antimicrobial activity. The N-terminal amphipathic helical domain (ChoM) will be further characterised to investigate if a carpet-forming peptide sequence (CecB, full length) can acquire the ability to form transmembrane pores if the hydrophobic mismatch is reduced and a peptide of 21 amino acids is created.

4

Peptide - membrane interaction by magnetic resonance

Contents

4.1 Tilamin - lipid interaction investigated by cwEPR 85
4.1.1 Introduction to cwEPR techniques 85
4.1.2 Results 90
4.2 Tilamin - lipid interaction investigated by solid-state NMR . . . 99
4.2.1 Introduction to experimental solid-state NMR techniques (^{2}H and ^{15}N) 99
4.2.2 Results 106
4.3 ChoM - lipid interaction investigated by ssNMR 128
4.3.1 Acyl - chain perturbation probed by ^{2}H NMR 128
4.3.2 Peptide orientation probed by ^{2}H NMR 129
4.4 Discussion 133
4.4.1 Tilamin - lipid interaction based on cwEPR 134
4.4.2 Tilamin - lipid interaction based on ^{2}H and ^{15}N ssNMR 135
4.4.3 Membrane perturbation upon tilamin interaction by ^{2}H NMR 137
4.4.4 ChoM - lipid interaction 139
4.5 Conclusion 139

4.1 Tilamin - lipid interaction investigated by cwEPR

4.1.1 Introduction to cwEPR techniques

The structural effects on lipid dynamics of peptide-membrane interactions are investigated using selectively spin-labelled lipids at different acyl chain positions, which act as specific

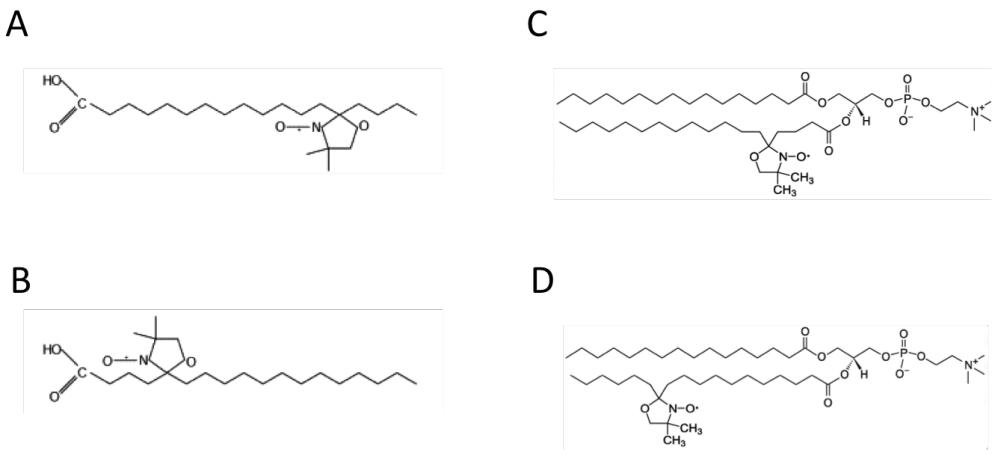

Figure 4.1: Different nitroxide spin probes used here to investigate membrane dynamics. (A) Stearic acid labelled at acyl chain segment 14 (14-SASL). (B) Stearic acid labelled at acyl chain segment 5 (5-SASL). (C) Phosphatidylcholine labelled at acyl chain segment 5 (5-PCSL) and (D) phosphatidylcholine labelled at acyl chain segment 12 (12-PCSL)

probes for lipid perturbations at different regions of the bilayer. It should be noted that for EPR studies the precise lipid morphology is not important as vesicles of small and large sizes tumble slow on the EPR timescale ($\sim 10^{-8}s$).

The first derivative of the nitroxide absorbance spectrum yields information on lipid conformation and dynamics. Here it is important to separate the bulk environment from lipids interacting directly with membrane-associated peptides or integral membrane proteins [261; 262]. A peptide- or protein-membrane interaction causes restrictions to lipid dynamics, which become visible in the line shape, linewidth or hyperfine splitting of the recorded EPR spectrum. Restricted lipid motion due to peptide interaction may give rise to a second broadened spectral component within the composite EPR spectrum [43; 263], if the peptide complex is large enough (ca. four monomers) and is diffusing sufficiently slowly. This can also be an indication for domain formation on the EPR timescale (ns) [264].

Selectively labelled lipids and stearic acids have been used to probe different lipid environments. Three different acyl chain label positions are used: (I) Position 5; (II) Position 12 and (III) Position 14. This allows for the comparison of dynamic changes at different bilayer levels and thus will allow to determine a peptide-bilayer penetration profile. Spin-labelled phosphatidylcholine lipids at acyl chain segment 5 and 12 are used in combination

with less restrained stearic acid that has been selectively labelled with nitroxide radicals at acyl chain positions 5 or 14 (Figure 4.1).[1]

4.1.1.1 Segmental order and dynamics probed by cwEPR

4.1.1.1.1 Amplitude of segmental acyl chain motion

The hyperfine splittings, $A_{//}$ and $A_{\perp}$, of the nitroxide spin-labelled stearic acid and phosphatidylcholine relate to the anisotropic averaging of the spin label motion at its segmental position of the acyl chain, and thus can be used to calculate an order parameter (S_{eff}) for the spin label at its local position relating to $S = \frac{1}{2}(3 \cdot \cos^2 \Theta - 1)$, where Θ is the amplitude of chain motion at the label position, assuming a fast motional rate in fluid bilayers ($\tau_c^{-1} > \sim 10^8 Hz$) (A. Watts in [265]). S_{eff} is a measure of the experimentally determined spectral anisotropy.

The order parameters were calculated as described by D. Marsh and A. Watts [266], where the molecular axes of the spin label are represented by the principal hyperfine splittings A_{zz}, A_{yy} and A_{xx}. The effective order parameter (S_{eff}) is calculated according to:

$$S_{eff} = \frac{A_{II} - A_{\perp}}{A_{zz} - 1/2(A_{xx} + A_{yy})} \cdot \frac{a_0^{'}}{a_0} \tag{4.1}$$

with line positions for $A_{\perp}$ and A_{II} shown in Figure 4.2; $a_0^{'}$ and a_0, the polarity parameters are given by:

$$a_0^{'} = \frac{1}{3} \cdot (A_{zz} + A_{yy} + A_{xx}) \tag{4.2}$$

$$a_0 = \frac{1}{3}(A_{II} + 2 \cdot A_{\perp}) \tag{4.3}$$

The principal hyperfine splittings A_{zz}, A_{yy} and A_{xx} for the spin label were previously characterised in oriented crystals, with principle hyperfine couplings found to be 5.9, 5.4 and 32.9 gauss [267]. The polarity normalization term of $a_0^{'}/a_0$ is introduced in the

[1] All cwEPR experiments described in this chapter are single experiments recorded in three scans and average spectra are depicted. For further experimental detail see section A.1.2.

calculations of S_{eff} to compensate for the different polarities at the specific membrane environments of the spin label [268].

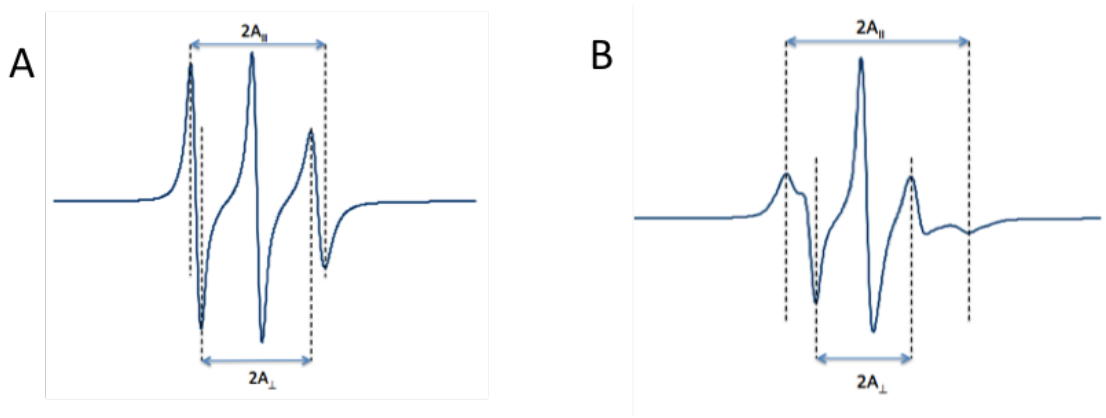

Figure 4.2: Hyperfine splitting as observed in the EPR spectrum of SASL. (A) EPR spectra obtained from SASL-14 indicating the two hyperfine splitting (A_{II} and $A_{\perp}$). (B) Same two hyperfine splittings in an EPR spectrum obtained from SASL-5. Both spectra are obtained from DPPC vesicle dispersions at 20 °C.

4.1.1.1.2 Dynamics of segmental acyl chain motion

The central linewidth (ΔH_0) provides dynamic information on the nitroxide spin label's correlation time. The central linewidth is a peak-to-peak measure of the central energy transition reported in the first derivative of the absorption spectrum. Unlike the hyperfine splitting of the spectrum, the central linewidth reports on the frequency of the segmental acyl chain motion and thus reports on relative correlation times rather then overall segmental order [269]. A spectral broadening that indicates restricted spin label motion typically results in an increased central linewidth. The nitroxide spin-label rotational correlation time can be related to the central line widths and low field line intensity:

$$\tau_r = 6.5 \cdot 10^{-10} \Delta H_0 \cdot (\sqrt{\frac{h(0)}{h(-1)}} - 1) \tag{4.4}$$

where ΔH_0 is the peak-to-peak width of the central line and $h(0)$ and $h(-1)$ are the height of the lines at the central and high field transition [269].

4.1.1.1.3 Heisenberg spin-spin interaction observed by cwEPR

The interaction of two spins in close proximity can be observed in the cwEPR spectrum. Heisenberg exchange is the phenomenon of spin exchange of close unpaired electrons via partial orbital overlap. The upper distance limitation for Heisenberg exchange is 1.5 nm in most solids, however this can be larger for highly delocalised spin systems. In liquid samples, Heisenberg exchange is strongly dependent on paramagnetic centre collisions that cause strong orbital overlap for a limited amount of time.

Heisenberg coupling is a combination of isotropic and anisotropic contributions, that are described by the exchange coupling tensor (J). Heisenberg exchange leads to line broadening that can be useful to obtain structural information on the spin system [270].

$$\hat{H} = S_1 J S_2 \tag{4.5}$$

where S_1 and S_2 are the individual spins.

An alternative method to obtain distance constraints by cwEPR is by analysis of dipolar broadening between two spins, for spins that are 0.7 - 2.0 nm apart. Spin interaction in this regime results in a distance-dependent broadening of the EPR spectrum by a Pake pattern [271]. The distance dependancy can be analysed by simulation of well described spin systems, Fourier based de-convolution or by de-convolution with broadening functions [272; 273; 274].

The ratio between the relative line amplitudes can be used as a quantitative estimate of inter-spin distance due to broadening. Spectral line broadening depends on the inter-spin distance and by careful analysis a distance resolution of 0.1 - 0.2 nm can be theoretically achieved. The line amplitudes of the frozen cwEPR spectrum can be used to determine if dipolar broadening is present in the spin system.

The peak-to-peak amplitude ratio is given by [271; 275]:

$$k = \frac{d_1}{d} \tag{4.6}$$

where, d_1 and d are defined in Figure 4.3.

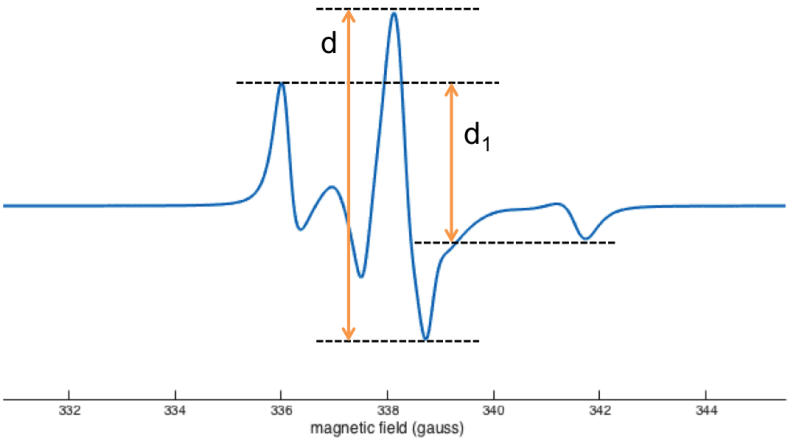

Figure 4.3: The relative line amplitudes used to quantify dipolar broadening are illustrated d_1 and d. The frozen spectrum was simulated using *EasySpin* using principal hyperfine g-value tensors g_{xx} = 2.0085; g_{yy} = 2.0063 and g_{zz} = 2.0025. The principal axial anisotropy was set to a_{xx} = 5.8; a_{yy} = 5.8 and a_{zz} = 30.8 Gauss and a correlation time τ_c of $10^{-7.5}$ s.

In the absence of spin-spin interaction, $k_0 = 0.32 - 0.35$ for a nitroxide radical (MTSL), that contains 12 surrounding methyl protons [275].

4.1.2 Results

4.1.2.1 Lipid acyl chain perturbation upon tilamin interaction probed by 5-SASL and 14-SASL

Spectral changes of the hyperfine splittings of 5-SASL in bilayers of POPC:POPG (3:1, molar ratio) can be observed upon peptide interaction (Figure 4.4A). In addition, the peptide interaction introduces multiple components to the EPR spectrum leading to a composite spectrum. These effects are seen to a lesser extent for 14-SASL, possibly due to the faster dynamics at a lower region of the acyl chain lead to averaging of these effects on the EPR timescale (Figure 4.4 B).

Calculated order parameters (S_{eff}) for the slow mobility component (Equ. 4.1) illustrate a reduction in the segmental motional freedom of the probed segments upon tilamin interaction, reported by 5-SASL, which is not observed at the 14-position (Figure 4.5). Furthermore, the reduced amplitude of motion at the 5-position correlates with peptide concentration, and a higher peptide concentration leads to a larger S_{eff} at the probed segment. The anionic

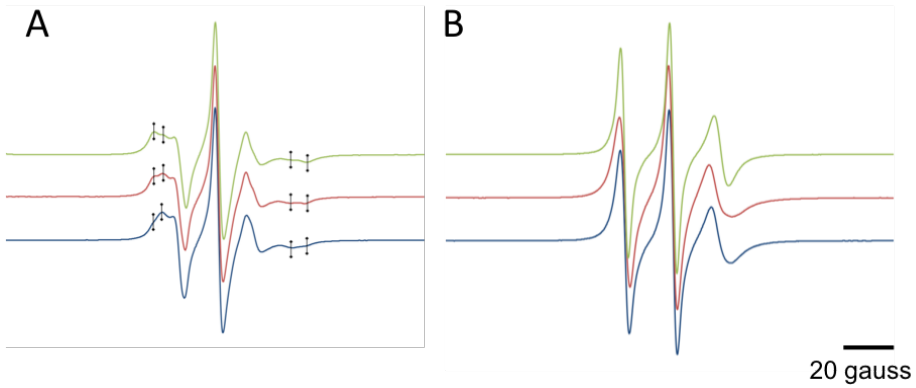

Figure 4.4: cwEPR spectra of SASL incorporated into bilayers are shown. the tilamin-lipid interaction is probed at different peptide to lipid ratios as well as different acyl chain segments. (A) cwEPR spectrum as probed by 5-SASL at different peptide (tilamin) to lipid molar ratios: no peptide (blue), 1:100 (red), 1:25 (green). Areas of overlapping multiple components are highlighted (black errors). (B) cwEPR spectra as probed by 14-SASL at different peptide (tilamin) to lipid molar ratios: no peptide (blue), 1:100 (red), 1:25 (green).

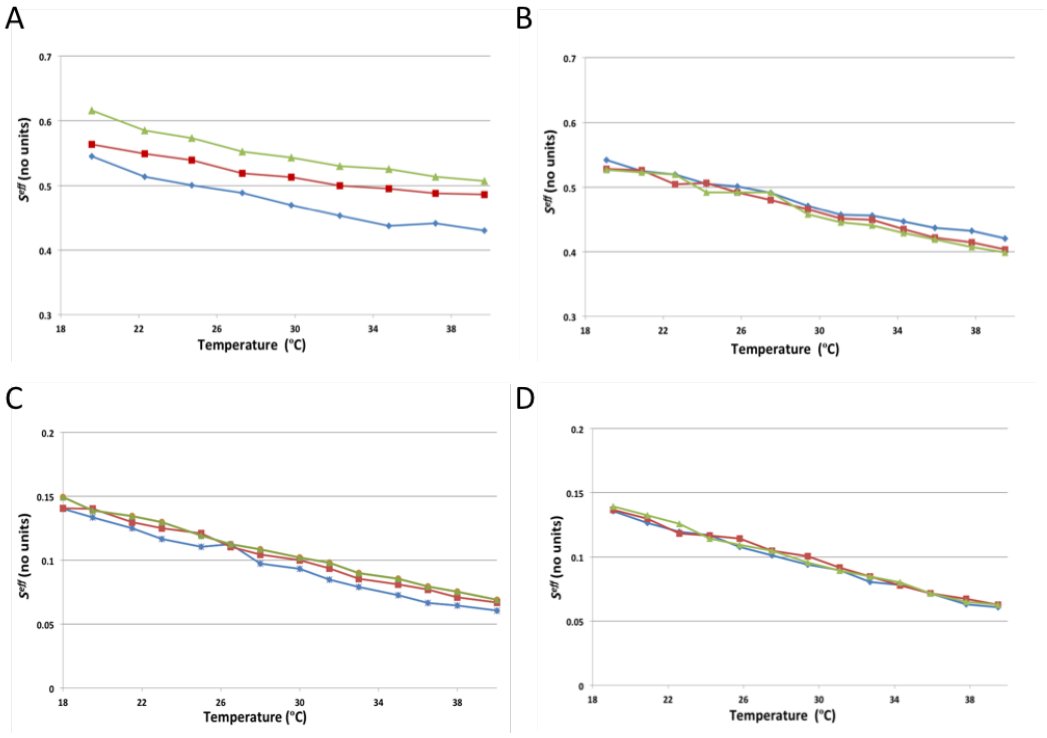

Figure 4.5: Segmental order parameters S_{eff} calculated from cwEPR spectra are plotted at different temperatures. (A) S_{eff} as calculated from the slow mobility component hyperfine splittings of 5-SASL upon tilamin interaction. (B) S_{eff} calculated for 5-SASL upon QAELA interaction. (C) S_{eff} calculated for 14-SASL in the presence of tilamin. (D) S_{eff} calculated for 14-SASL in the presence of QAELA. All S_{eff} are shown in the absence of peptide and at 1:100 and 1:25 peptide to lipid molar ratios (blue: absence of peptide; red: 1:100 peptide to lipid molar ratio; green: 1:25 peptide to lipid molar ratio).

peptide counterpart QAELA, does not show any influence on the amplitude of segmental lipid motion on the EPR timescale (Figure 4.5 C and D).

The EPR spectrum of 5-SASL comprises multiple components upon tilamin interaction, consistent with a degree of lipid-peptide interaction mediated lipid separation into a slow and fast moving lipid component (Figure 4.4 A, most evident at 1:25 lipid:tilamin molar ratio). This results in a composite EPR spectrum and thus the exchange between the two environments is slow on the EPR timescale. De-convolution of a composite spectrum by subtracting the normalized EPR spectrum for bulk lipid allows the approximation of relative proportions of the individual phases that are present.

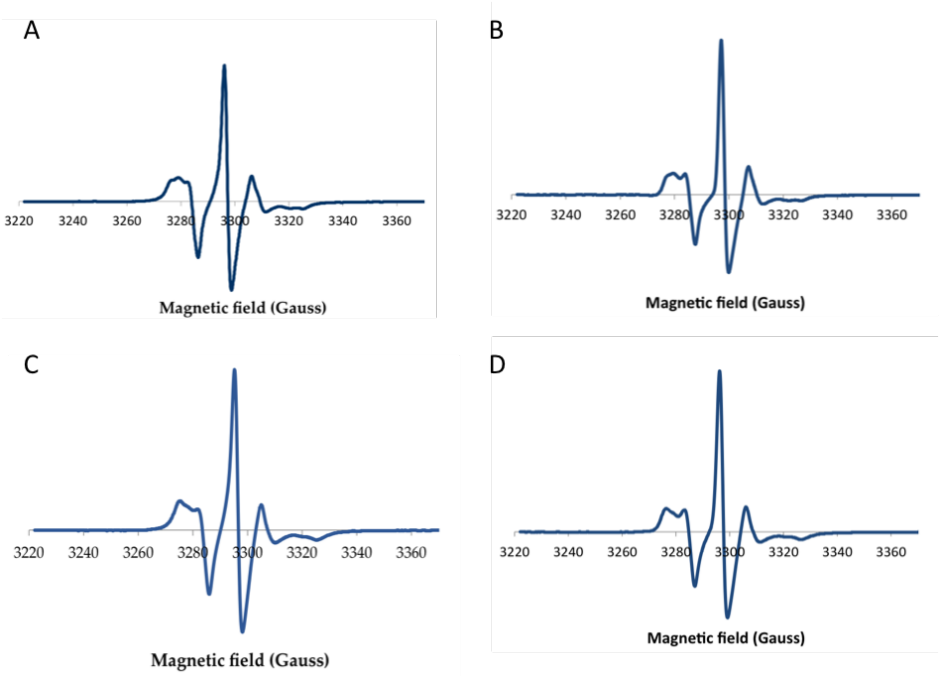

Figure 4.6: Multicomponent cwEPR pre and post spectral de-convolution are shown. (A) Composite spectrum as probed for 5-SASL at tilamin:lipid (1:100 molar ratio). (B) Composite spectrum at tilamin:lipid (1:100 molar ratio) after subtracting 60% of the 5-SASL spectrum as probed in bulk lipid. (C) Composite spectrum as probed for 5-SASL at tilamin:lipid (1:25 molar ratio). (D) Composite spectrum at tilamin:lipid after subtracting 40% of the 5-SASL spectrum as probed in bulk lipid. See appendix A.1.1 for detail on deconvolution precedure.

The qualitatively best fit for the de-convolution of the 5-SASL spectrum at a 1:100 tilamin to lipid molar ratio was achieved when subtracting a proportion of 60% of mobile component (Figure 4.6 A and B). De-convoluting the EPR spectrum of 5-SASL at a 1:25 peptide to lipid ratio was fitted best to the subtraction of 40% mobile lipid phase (Figure 4.6 C and

D, error estimate 10%). Hence, at a 1:25 peptide to lipid ratio a disproportionally higher fraction of lipid is involved in the peptide interaction. This suggests a localized peptide distribution rather then a uniformly random peptide distribution across the bilayer. Multiple lipid environments may be induced through direct lipid-peptide interaction or through peptide clustering most likely due to peptide oligomerisation.

Figure 4.6 (C and D) show the fitted EPR spectrum after de-convolution of two motionally distinct lipid domains. It is evident that additional components might be present (Figure 4.6 C and D), suggesting that the binding mode of tilamin is complex. The lower peptide to lipid molar ratio complex may correspond to a mixed initial peptide binding interaction whereas the full potent peptide configuration is formed at a molar ratio of 1:25.

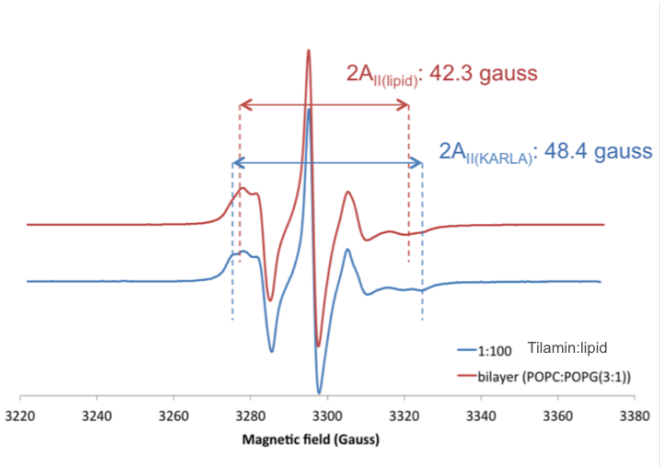

Figure 4.7: Comparison of $2A_{II}$ of 5-SASL in bulk lipid and 5-SASL in 1:100 tilamin to lipid molar ratio. The direct observed difference (in gauss) was converted to Hertz, which allows for an estimation of the limit of slow exchange between the distinct dynamically domains. The spectral difference of 6.8 gauss translates to a limit of slow exchange of $< 2 \cdot 10^7 s^{-1}$.

A direct comparison between the hyperfine splittings ($2A_{II}$) of the bulk lipid spectrum and the more anisotropic component of the composite spectrum (upon tilamin interaction) allows for an estimate of the limit of slow exchange between the distinct lipid domains (Figure 4.7). The upper limit of slow exchange is represented by the difference of the hyperfine interaction between the two observed environments ($A_{//}$) The lower limit of slow exchange between the individual lipid domains present here is estimated to be $2 \cdot 10^{-7} s$.

The spectral splitting was converted according to:

$$v_{ex} < \frac{\Delta A}{h} = \frac{A^I_{//} - A^S_{//}}{h} \tag{4.7}$$

where, $A_{//}$ is the hyperfine interaction in Tesla for each spectrum and h is the Plancks constant (A. Watts in [265]). Roughly a difference of 0.1 mT corresponds to an exchange rate of 2.8 MHz.

In summary, de-convolution of the spectra assumed a simple two-component system comprised of the mobile bulk lipid population and a less mobile component, possibly representing the population of the lipid interacting with the peptide. The two defined lipid populations are in slow exchange with each other (ns) on the EPR anisotropy averaging timescale (Figure 4.7). However, this is a simplified model, and a more complex environment, including additional less populated components with a distinct dynamic behaviour that are not resolved, may be present. It should be noted that the possibility of peptide-probe interaction can also explain the observed spectral components. The stearic acid possesses a negative charge, yet it is only present at 0.5% of the total lipid quantity and thus the anionic PG component should be dominant, if interacting with the peptide. In this scenario the free spin-probe diffusion would be hindered, yet two distinctly probed environments remain where the spin-probe would most likely resemble the interaction characteristics of anionic PG.

4.1.2.2 Lipid acyl chain perturbation upon tilamin interaction probed by 5-PCSL and 12-PCSL

Native-like zwitterionic phosphotidylcholine lipids spin-labelled with a single nitroxide radical are used to probe segmental ordering. The aim is to gain a better understanding of lateral lipid segregation upon tilamin interaction, which was observed when probed with SASL, a charged fatty acid not resembling phospholipids that contain a glycerol backbone and a headgroup moiety. Similar to the above studies PCSL labelled at two different segments were probed: (I) acyl chain segment 5 and (II) acyl chain segment 12.

Figure 4.8 shows the characteristic cwEPR line shape for 5-PCSL in a pure POPC:POPG (3:1, molar ratio) bilayer across a temperature range. The phase transition temperatures (T_m) for POPC and POPG are -2 °C at pH 7.0 and thus all presented spectra are above the

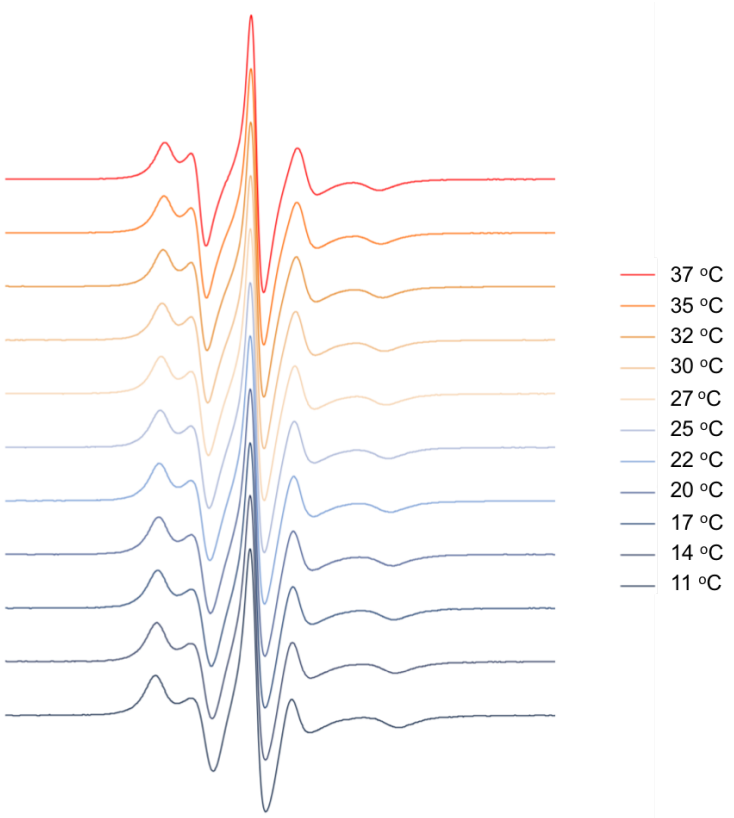

Figure 4.8: 5-PCSL spectra of pure POPC:POPG (3:1, molar ratio) spectra. A temperature range from 11 °C to 37 °C are shown. The line broadening due to less dynamic bilayers at lower temperatures becomes visible, which illustrates the sensitivity of nitroxide spin labels to segmental acyl chain order, the amplitude of segmental motion. The corresponding order parameter are plotted in Figure 4.10 (blue data set).

phase transition in the fluid phase. Nevertheless, changes in lipid dynamics with temperature variation are evident as the lines become narrower at higher temperatures, demonstrating the sensitivity of axial anisotropy averaging to local dynamics on the EPR time scale of $\sim 10^{-8}$ s.

The EPR spectrum of 5-PCSL and 12-PCSL, recorded at 37 °C, are shown in Figure 4.9 in the absence of tilamin and at two peptide to lipid molar ratios (1:100 and 1:25). The line shape observed at position 12 is sharper and narrower agreeing with the expected higher mobility of the acyl chain closer to the bilayer centre. No obvious changes of the line shapes upon peptide interaction are visible for 12-PCSL, in contrast to spectra recorded in the presence of 5-SASL (Figure 4.9). All spectra show clear single component line shapes, unlike for the same peptide-lipid interaction probed using spin-labelled stearic acid.

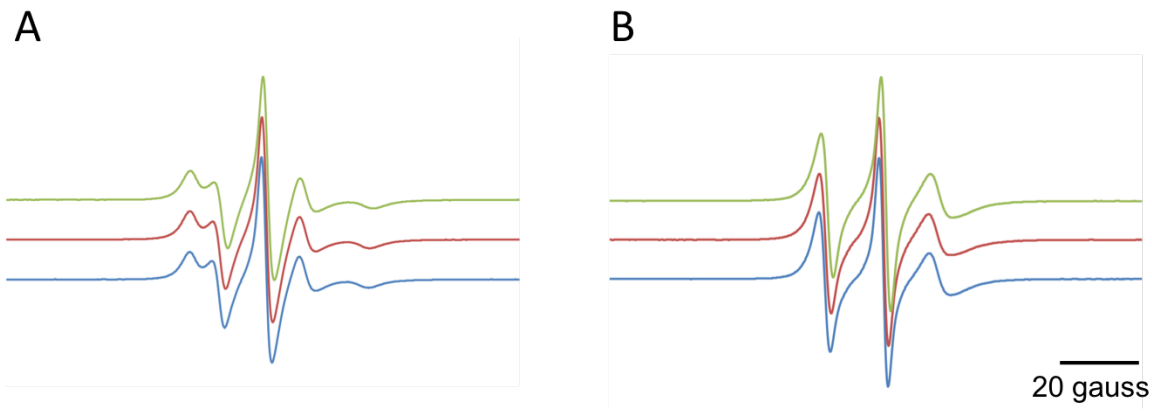

Figure 4.9: cwEPR spectra of 5-PCSL upon peptide addition. All spectra acquired at 37 °C. (A) 5-PCSL. (B) 12-PCSL. In a bilayer (blue); upon addition of 1:100 tilamin to lipid molar ratio (red) and upon addition of 1:25 tilamin to lipid molar ratio (green). Separate parameters plotted in Figure 4.10 and 4.11

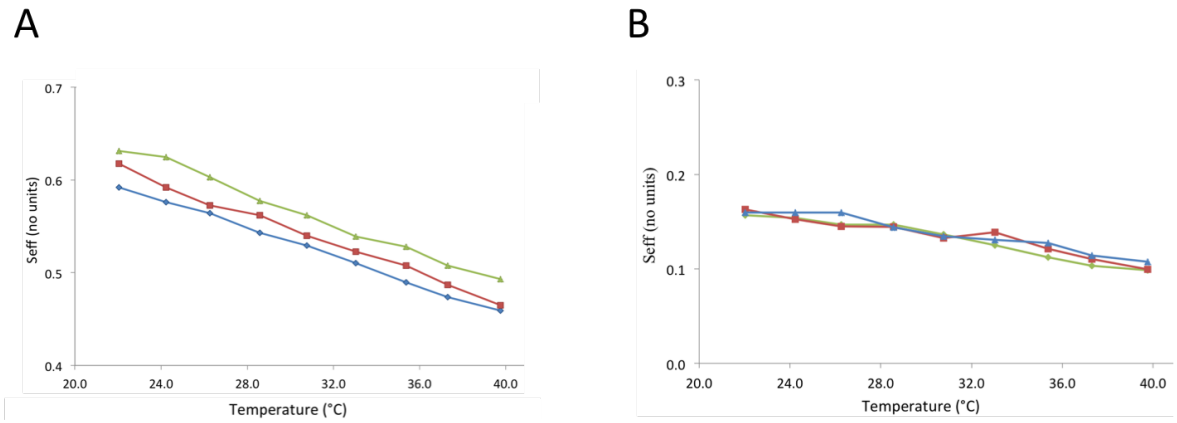

Figure 4.10: Segmental order parameters S_{eff} calculated from cwEPR spectra are plotted at different temperatures. (A) S_{eff} as calculated from the hyperfine splittings of 5-PCSL. (B) S_{eff} as calculated from the hyperfine splittings of 12-PCSL. The spin label segmental motion was probed at two separate tilamin to lipid molar ratios (blue: absence of peptide; red: 1:100 peptide to lipid molar ratio; green: 1:25 peptide to lipid molar ratio).

The calculated order parameters S_{eff} (Figure 4.10) illustrate a reduction in the amplitude of motion at the higher 5th segment, which is not seen for the acyl segment 12. This is broadly in agreement with the observed behaviour when probed by SASL (Figure 4.5), suggesting restricted lipid motion close to bilayer interface. The rate of lipid motion has also been investigated for the PCSL spin labels. The spin label correlation time at the labelled acyl chain segment is described by the linewidth of the central EPR transitions (Equation 4.4). In agreement with the reduction in chain amplitude, an increased motional frequency was also

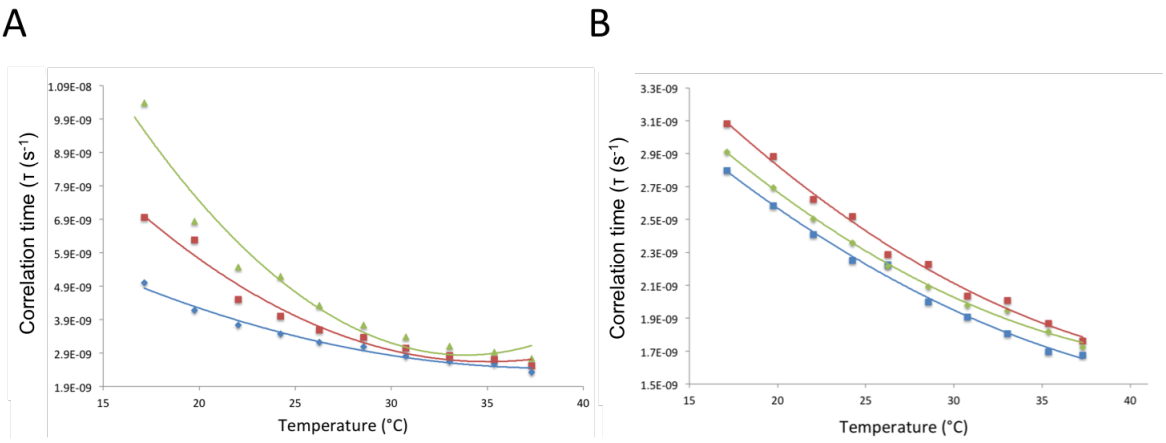

Figure 4.11: Spin-label correlation times of the two probed segments are plotted at different temperatures. (A) τ_{corr} as calculated from the central linewidths of 5-PCSL. (B) τ_{corr} as calculated from the central linewidths of 12-PCSL. Correlation times were probed at two separate tilamin to lipid molar ratios (blue: absence of peptide; red: 1:100 peptide to lipid molar ratio; green: 1:25 peptide to lipid molar ratio). Note the different scales.

observed at segment 5 at low temperatures: up to half a magnitude of difference is observed at 17 °C between a pure bilayer and a tilamin peptide molar ratio of 1:25 (Figure 4.11 A). The difference in dynamic behaviour seems to be averaged at higher temperatures probably due to an overall higher membrane fluidity allowing for more motional freedom. Only small deviation can be observed for the correlation times at segment 12 (Figure 4.11), suggesting that the main impact on bilayer dynamics due to tilamin interaction occurs in the interface region, possibly causing minor rearrangements of the individual phospholipids that cause an increased lateral pressure that reduces overall freedom of motion and in turn an increased correlation time in this lower region. The fact that the correlation times at segment 12 are also altered suggests that a dynamical change at the interface region is translated along the acyl chain, whereas the overall order was not altered at this segment. Interestingly the correlation time at segment 12 of PCSL increases slightly across the whole temperature range ($\sim 0.2 \cdot 10^{-9}$ s) at a tilamin to lipid molar ratio of 1:100. This is followed by a decrease at the higher tilamin molar ratio of 1:25, possibly indicating a more global rearrangement of tilamin organisation at the membrane (e.g oligomerisation at the interface).

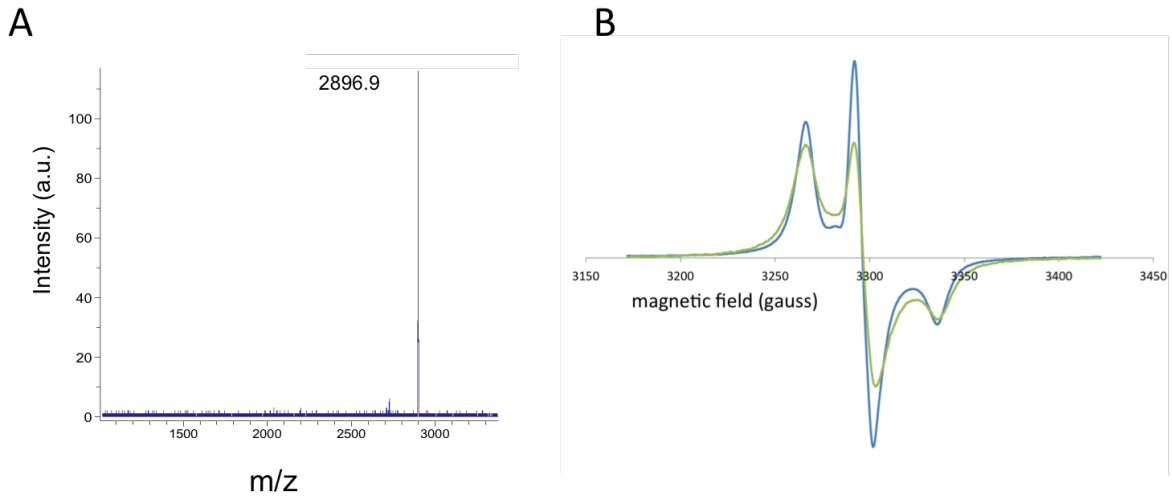

Figure 4.12: Mass spectrometry and cwEPR of MTSL-labelled tilamin are shown. (A) MALDI-TOF mass spectrometry results of MTSL labelled tilamin post HPLC purification showing a clear peak at m/z 2896.9. The expected mass is 2895.4. (B) cwEPR spectra of MTSL-labelled tilamin in a POPC:POPG (3:1, molar ratio) membrane at 1:25 peptide to lipid molar ratio. 100% spin-labelled tilamin is shown in green and 1:10 spin diluted tilamin is shown in blue.

4.1.2.2.1 Peptide - peptide interaction by cwEPR

A tilamin sequence containing a C-terminal cysteine residue has been used for side-directed spin labelling of the peptide. The cysteine residue is separated from the native peptide sequence by a β-alanine to ensure that peptide activity of tilamin remains unaltered (Table 3.1). The reduced peptide was reacted with S-(1-oxyl-2,2,5,5-tetramethyl-2,5-dihydro-1H-pyrrol-3-yl)methyl methanesulfonothioate (MTSL) and afterwards HPLC purified to remove free unreacted MTSL. The purity was determined by MALDI TOF mass spectrometry (Figure 4.12 A).

The frozen spectrum of tilamin added to a POPC:POPG (3:1, molar ratio) has been recorded (Figure 4.12 B). The dipolar broadening was estimated by calculation of k (Section 3.1.1). A clear broadening can be observed for both 100% spin labelled and 10% spin labelled samples giving $k = 0.7$ and $k = 0.5$ respectively. A spin-dilution using unlabelled peptide to a total of 10% of spin-labelled peptide should lead to reduced spectral broadening due to spin-spin interactions. Both values are above the expected 0.3 in the absence of broadening, and the baseline does not reach zero in between the individual lines, which is indicative of Heisenberg exchange and spins in very close proximity causing orbital overlap. The spin interactions could not be eliminated by spin dilution to only 10%, nevertheless a slight reduction in spin coupling was achieved. This might indicate a stochastic peptide

aggregation on the membrane rather then well defined pores comprised of a specific number "n" peptides or at least in ensemble $n > 10$ as otherwise the spin-spin interaction should have been significantly lowered or completely removed by spin dilution.

Taken together this suggests that individual peptides interact with each other on a bilayer. Heisenberg exchange is observed, suggesting a stochastic peptide-lipid interaction across the entire bilayer. It remains elusive is whether these are transient dynamic interactions or defined oligomers. The seemingly stochastic peptide behaviour is hardly surprising for chaotic AMP systems. These findings are broadly in agreement with the de-convoluted SASL cwEPR spectra that also suggested a non-uniform peptide distribution on the membrane.

4.2 Tilamin - lipid interaction investigated by solid-state NMR

4.2.1 Introduction to experimental solid-state NMR techniques (^{2}H and ^{15}N)

Besides the common MAS solid-state NMR experiments, uniaxially aligned samples have become a complementary NMR technique to resolve anisotropic and thus orientation selective interactions. Angular constraints can be elucidated and related relative to the external magnetic field. Most commonly these methodologies resolve the quadrupolar interaction of spins *I>1/2* or the orientation-selective chemical shift anisotropy (CSA) together with dipolar coupling, which allow for orientational and structural approximations to be derived. This approach requires peptides to be reconstituted into uniaxially oriented bilayers achieved by controlled rehydration of lipid mixtures on microscope cover slides. This allows for structural characterisation in a hydrated liquid-crystalline disordered membrane environment at elevated temperatures - resembling a native-like environment.

Uniaxially aligned NMR approaches have been developed around antimicrobial peptides from the beginning of the methodology onwards. Gramacidin A and megainins were first characterised using oriented NMR [44; 276; 277]. More recently the methodology has also been proven useful for larger integral membrane proteins and membrane spanning sequences such as the transmembrane domain of VpU or bacteriorhodopsin [65; 278]. For larger integral membrane proteins the two dimensional Polarisation Inversion Spin Exchange at the Magic

Angle (PISEMA) is commonly used. For smaller AMP systems a combination of multiple one dimensional experiments can equally be applied [44; 51; 279]. For structural insight, deuterated methyl groups as part of the alanine side chain are used to resolve direct angular peptide constraints. This is possible since the side chain undergoes fast rotation on the NMR timescale and the methyl group itself is directly referenced to the helical axis via a well characterised angle. A secondary approach is used in order to investigate lipid perturbation upon peptide interaction, here the hydrocarbon segments of a single acyl chain are perdeuterated and report on orientational lipid order and peptide-induced disorder.

The structural peptide analysis presented uses four separate quadrupolar constraints of deuterated alanine side chains located across the peptide, together with the orientational selective CSA of a single labelled amide ^{15}N to sample the conformational space of tilamin and further understand its membrane interaction [280].

4.2.1.1 Lipid order and orientation dependence of ^{2}H & ^{15}N

4.2.1.1.1 Deuterium (^{2}H)

Segmental acyl chain order parameter (^{2}H)

The deuterium spectrum of mechanically oriented samples of lipids with perdeuteraded acyl chains is a superposition of individual Pake doublets, each corresponding to a deuterated segment of the acyl chain [281; 282]. The axis of motional symmetry of lipids in a bilayer is perpendicular to the bilayer plane. The C-D bond reorients itself rapidly at a near perpendicular orientation relative to B_0 and thus results in relatively well resolved peaks. The quadrupolar splitting ($\Delta\nu_Q$) of the carbon deuterium bond is described by [283]:

$$\Delta\nu_Q = 3/4\frac{e^2qQ}{h} \cdot S_{CD} \tag{4.8}$$

where e^2qQ is the quadrupolar coupling constant and segmental acyl chain order parameter is given by S_{CD}:

$$S_{CD} = 1/2 \cdot (3\cos^2\Theta_{CD} - 1) \tag{4.9}$$

In the NMR spectrum an average of equation 4.8 is observed, where Θ_{CD} is the relative orientation between the carbon-deuterium bond vector and the external magnetic field.

The Pake doublets corresponding to the more dynamic acyl segments, located close to the bilayer centre, are well resolved as narrow doublets of small absolute quadrupolar splittings in the centre of the recorded spectrum. The less dynamic segments located close to the interface region are less well resolved and often show significant overlap. Smoothened order parameters assume a monochromatic decay of dynamics in this region as information on individual acyl positions is lost, nevertheless the dynamics of the acyl chain as a whole can be characterised [284; 285].

It is noteworthy to point out the difference in the experimental timescale when compared to the segmental order parameters calculated from cwEPR spectra, which are on the regime of *ns*. The order parameters obtained by segmental quadrupolar splittings give information on the dynamic timescale of μs (quadrupolar coupling constant $\sim$ 167 kHz for aliphatic C-H^2 bonds [286]), and thus report highly complementary structural information to lipid order probed by cwEPR. Note that reorientations and changes in the chemical environment will also be reported by a quadrupolar nucleus.

Relative peptide orientation (^{2}H)

Distinct quadrupole splittings, resolved for each of the labelled alanine positions, were referenced to B_0 to give a bond vector with relative orientation of the $C_\alpha - C_\beta$ side-chain vector to the bilayer normal that is aligned with B_0. Note that C_α forms part of the peptide backbone and thus the quadrupolar splitting is directly related to the longitude peptide orientation (Figure 4.13). The relative theoretical sensitivity profile of the quadrupolar splitting relative to tilt and peptide rotation is shown in Figure 4.14. Accordingly, the quadrupolar splittings were fitted to an overall tilt and rotational peptide angle using previously described relationships, where the 0° rotation was defined as the location opposite, the central leucine residue in the hydrophobic cluster [279; 287]:

$$\Delta v_Q = 3/4 \Delta v_{Q,Theoretical} \; [3\cos^2\beta(\cos\tau - \sin\tau\cos\delta\tan\beta)^2 - 1] \tag{4.10}$$

where $\Delta v_{Q,Theoretical}$ is defined as:

$$\Delta\nu_{Q,Theoretical} = (e^2qQ/h)S \tag{4.11}$$

where (e^2qQ/h) is the quadrupolar coupling constant and S refers to a structural order parameter that resembles intrinsic motion that can cause averaging of the quadrupolar interaction [51]. δ and τ correspond to the helical rotation angle and overall tilt angle repsectively. β is the angle between the side-chain orientation defined by $C_\alpha - C_\beta$ and the helix axis (for graphical illustration see Figure 4.13). For a carbon deuterium bond the quadrupolar splitting constant is 167 kHz, which in methyl groups (as contained in the alanine side chain) was initially thought to be averaged due to fast rotation around the C - ^{2}H bond [288]. It was suggested that for peptides 84 kHz is a more accurate description of the quadrupolar coupling constant of an alanine side chain in a static environment, yet in hydrated system the quadrupolar coupling constant tends to be <80 kHz due to motional averaging [289; 290]. A maximum quadrupolar splitting of 74 kHz was observed for dry peptide powder (PGLa) and for [C-^{2}H$_3$] - labelled Plexiglas, showing some intrinsic peptide motions leading to partial averaging in a powder form [279; 286]. Additional motions can cause further reduction of the quadrupolar splitting constant and are described by S. The

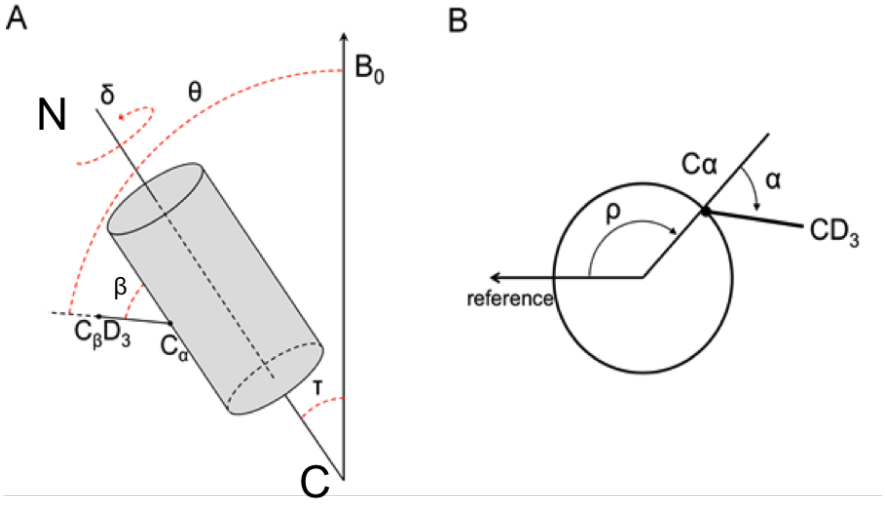

Figure 4.13: The relative angles that relate the helix orientation to the external magnetic field (B_0) are illustrated. (A) A side view of an alpha helix illustrated (cylinder). The overall side chain tilt is shown by Θ, the rotational pitch by δ, the side chain tilt by β and the helical tilt by τ. (B) A top view of a model alpha helix is shown. The relative rotational pitch angle is described to a defined reference. ρ is the overall helical pitch angle where α describes the additional pitch due to the intrinsic side chain tilt, which needs consideration. Figure adapted from [51].

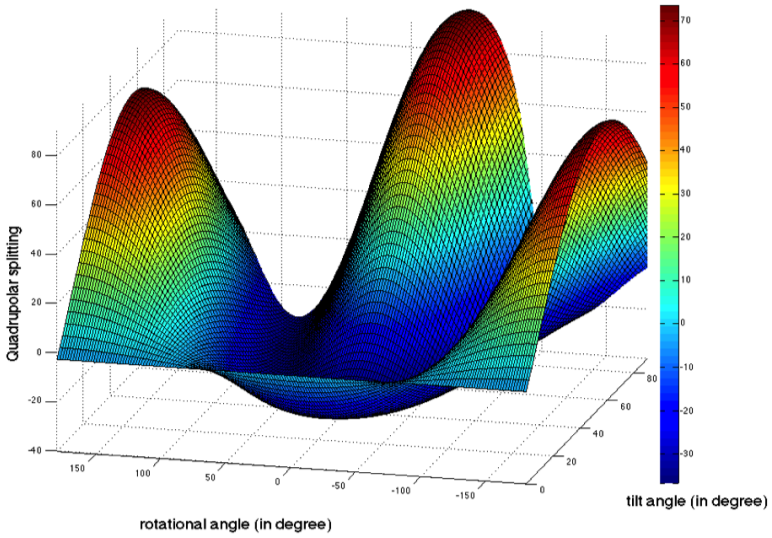

Figure 4.14: The theoretical quadrupolar splitting is plotted as a function of rotational and helical tilt angles. The quadrupolar splitting (Δv_Q) is plotted on the z-axis, tilt and rotational angles are plotted as x - and y - values respectively. The graphical surface representation was generated using Matlab.

experimentally measured quadrupolar splitting is reported as an absolute value since the sign cannot be determined from a simple deuterium spectrum.

The observed quadrupolar splittings (measured between the two maxima of the observed resonances) were fitted to theoretical calculated splittings (equation 4.10) using RMSD analysis. The following equation was minimised to obtain peptide orientation:

$$RMSD = \sqrt{\frac{\sum((data) - (expected))^2}{n}} \tag{4.12}$$

The geometric relationship between side chain tilt, rotational pitch and overall peptide orientation in a hypothetical straight alpha helix, as assumed for this study, are shown in Figure 4.13. Note that the assumed relationships does not compensate for mosaic spread which might be represented in the lineshape only the absolute quadrupolar splittings for a single labelled site are considered for RMSD analysis. Note that this approach does not account for mosaic spread.

4.2.1.1.2 Nitrogen (^{15}N)

Similarly to the quadrupolar interaction the orientational selectivity of ^{15}N CSA can be exploited to obtain angular dependent constraints. In a peptide that contains a single ^{15}N nucleus, the inter nucleus distances are large enough to be ignored and an uncoupled spin can be assumed. In addition, the surrounding protons are decoupled by high field irradiation at the ^{1}H frequency. If such a spin system is placed into a large magnetic field under static and unoriented conditions, a typical powder pattern of ca. 160 ppm CSA is observed [289]; the CSA relates to the static main tensor elements that are described by the discontinuities within the ^{15}N powder lineshape.

The CSA interaction of ^{15}N can be described by a principal axis system, where the orthogonal elements of the second rank tensor persist and accurately describe the chemical shift interaction. σ_{11}, σ_{22} and σ_{33} describe the static main tensor elements (Figure 4.15) and can be determined from the discontinuities within a ^{15}N powder line shape. The tensor elements are molecule- and nucleus- specific and relate the internal molecular arrangements to the external magnetic field. The tensor elements can be related to the coordinate frame dictated by the external magnetic field via the Euler angles (Φ, Θ, Ψ, [289]):

$$\sigma_{zz} = \sigma_{11} \sin^2 \Theta \cos^2 \Phi + \sigma_{22} \sin^2 \Theta \sin^2 \Phi + \sigma_{33} \cos^2 \Theta \tag{4.13}$$

where σ_{zz} is the measured chemical shift in an uniformly oriented system (Figure 4.15 B).

The main tensor elements vary between amino acids and also depend on secondary structural elements. The best characterised tensor elements are for glycine and alanine residues [292; 293; 294]. The main tensor elements for ^{15}N-Tyr are: $\sigma_{11} = 52.1 ppm$, $\sigma_{22} = 77.1 ppm$ and $\sigma_{33} = 209.3 ppm$ [295].

When considering the molecular frame of an alpha helix it becomes evident that the CSA tensors of the ^{15}N - ^{1}H bond vector are oriented only within a few degrees relative to the helix axis and thus able to report on the helix axes (Figure 4.15 A).

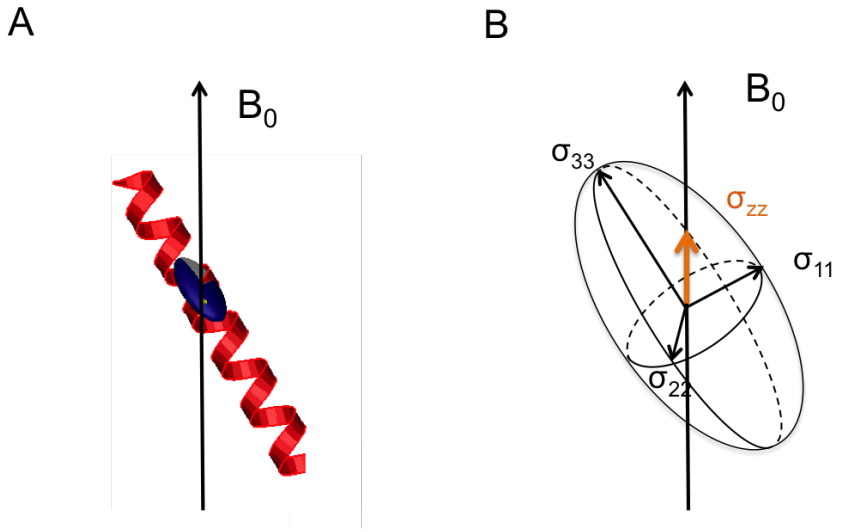

Figure 4.15: (A) Graphical representation of the ^{15}N amide of CSA of residue 11 in a straight alpha helix at a relative tilt of 30° to B_0. The representation was created using SIMMOL [291]. (B) A schematic of the ^{15}N CSA illustrating the main tensor elements σ_{11},σ_{22} and σ_{33} and the orientation selective σ_{zz}.

As previously described, different peptide versions were synthesised (Chapter 3) each containing a single label (deuterium or ^{15}N; Figure 4.16). Oriented solid-state NMR is used to relate each labelled position individually to the external magnetic field, which is oriented parallel to the bilayer normal. Using multiple single constraints, the overall peptide orientation relative to the bilayer normal is characterised. Note that the observed line shape corresponds to a motional average of all orientations present in the near uniformly aligned sample. For dynamic systems this can lead to line broadening. Single constraints can limit possible solutions, but often yield multiple possibilities and ambiguity. This problem is further enhanced by the sign ambiguity of quadrupolar splittings. In the analysis presented here absolute values are considered for all reported quadrupolar splittings. Some of the potential solutions can be eliminated using multiple constraints and/or chemical and thermodynamical consideration [280; 296]. This will be complemented with lipid acyl chain order parameters obtained for POPC and POPG respectively as well as simple MD analysis.

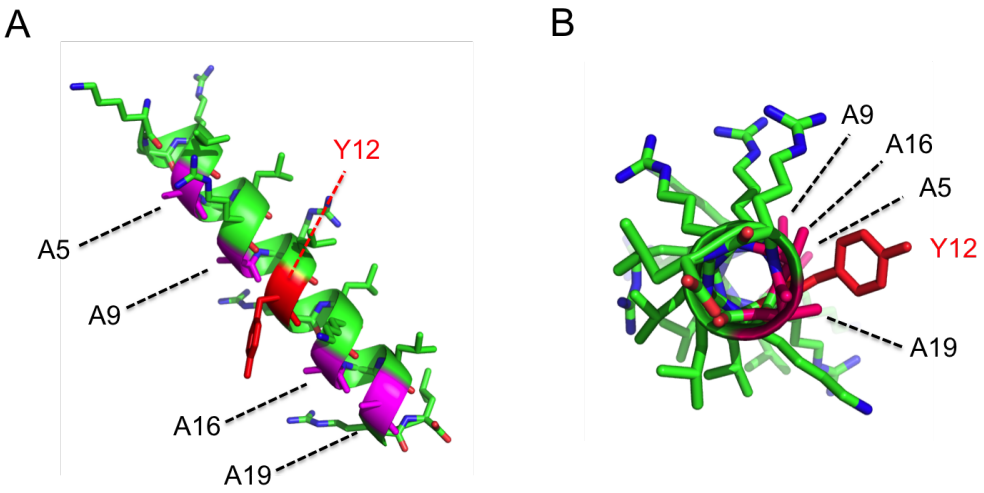

Figure 4.16: Orientational constraints used for the ssNMR characterisation of peptide orientation are shown. (A) Side view of tilamin represented as a straight alpha helix. Position for selective labelling with Ala - d_3 are shown in magenta. Residues for selective labelling with ^{15}N are shown in red.

4.2.2 Results

4.2.2.1 Acyl - chain perturbation probed by ^{2}H NMR

Tilamin induced membrane perturbations were probed by acyl-chain deuterated PC and PG as part of a POPC:POPG (3:1, molar ratio) bilayer respectively and each at different peptide to lipid ratios. The characteristic overall wing-like distribution of the individual Pake doublets is best observed in the absence of tilamin (Figure 4.17). The central doublet corresponds to the fast moving acyl chain methyl group and the broader doublets follow the motional profile along the acyl chain [281]. The wing shape arises due to spectral overlap of the slow moving acyl chain segments closest to the rigid glycerol backbone. The largest splitting observed for POPC-d_{31} in the absence of peptide corresponds to the CD_2 group located closest to the glycerol backbone, which is relatively rigid. Following this logic the smallest quadrupolar splitting of 3.5 kHz is assigned to the fast moving methyl group at the end of the hydrocarbon chain (Figure 4.17 and 4.18).

Qualitatively an overall narrower spectral width is observed upon peptide addition for both PC and PG components. In both scenarios this seems to be peptide concentration dependent. Additionally the distinct resonance frequencies are less well resolved in high peptide to lipid ratios, suggesting an overall disruption of the bilayer. Smoothened segmental order parameters

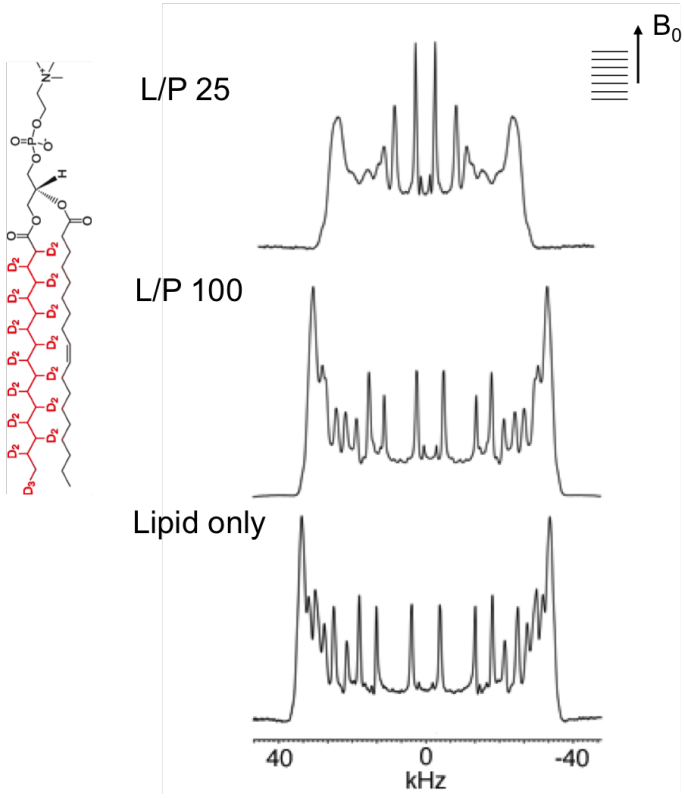

Figure 4.17: ^{2}H spectra of chain-deuteratated POPC probe. Note that the last deuterated acyl chain segment is a CD_3 methyl group. A ^{2}H spectrum of POPC:POPG (3:1, molar ratio) in the absence of tilamin is shown (bottom), where clearly resolved resonances are seen. tilamin interaction is probed at two molar ratios and less distinct deuterium resonance are observed, indicating bilayer perturbation. All samples are uniformly aligned with the bilayer normal parallel to B_0. Spectra are recorded at 20 °C and a deuterium frequency of 122.78 MHz

have been calculated for the individual segments of the PC and PG acyl chains respectively (Figure 4.19). In both cases the qualitative observation of narrower overall frequency profiles is confirmed by lower order parameters. For the PG-component this is a concentration dependent reduction. The order profile of the acyl chains at the PC component is also affected, but to a lesser extent than the PG component, again pointing towards a preferred PG-tilamin interaction. A slight reduction in acyl chain order is observed at a peptide to lipid molar ratio of 1:100. The bilayer becomes much more disordered at the high peptide to lipid molar ratio of 1:25, possibly due to a more global membrane reorganisation at this peptide to lipid molar ratio. The larger disordering of the PG component is consistent with a charge-driven membrane interaction by tilamin (also consistent with order probed by EPR; Figure 4.10).

Disordering of the bilayer due to peptide interaction can be related to membrane thinning, mainly due to increased flexibility and freedom of movement in the acyl chain region caused by

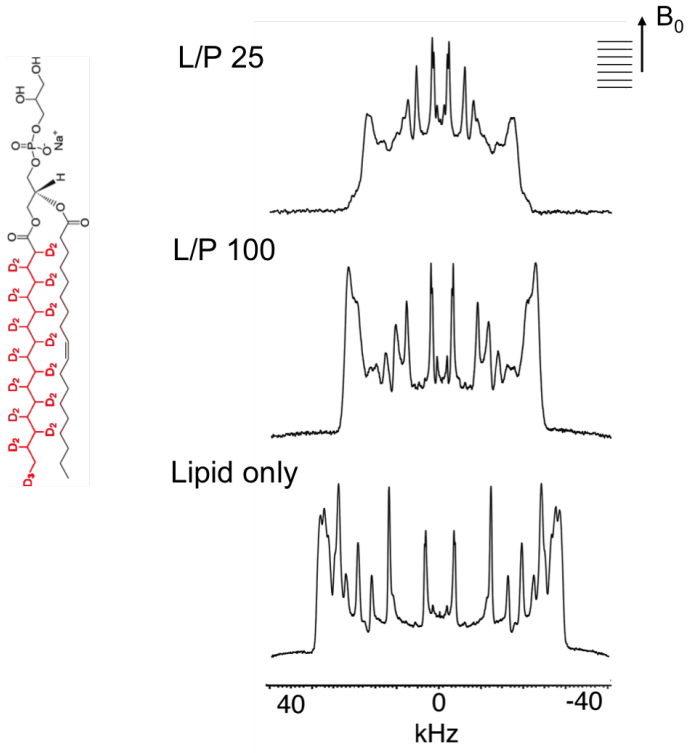

Figure 4.18: ^{2}H spectra of chain-deuteratated POPG probe. Note that the last deuterated acyl chain segment is a CD_3 methyl group. A ^{2}H spectrum of POPC:POPG (3:1, molar ratio) in the absence of tilamin is shown (bottom), where clearly resolved resonances are seen. tilamin interaction is probed at two molar ratios and less distinct deuterium resonance are observed, indicating bilayer perturbation. All samples are uniformly aligned with the bilayer normal parallel to B_0. Spectra are recorded at 20 ^{o}C and a deuterium frequency of 122.78 MHz

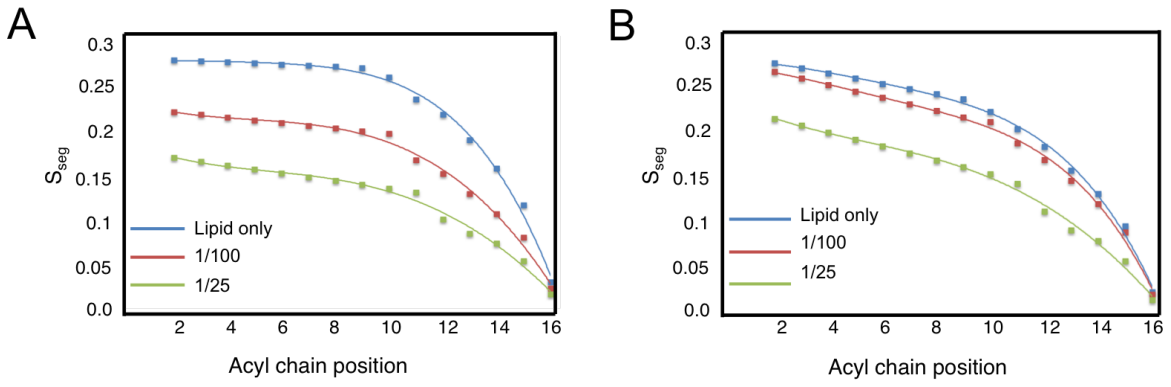

Figure 4.19: The calculated segmental order parameters as probed by chain-deuterated POPC and POPG. The order parameters are smoothened for the six positions closest to the glycerol backbone, where a linear decay has been assumed. (A) The acyl chain order profiles probed for POPG at different tilamin to lipid ratios are shown. (B) The acyl chain order profiles probed for POPC at different tilamin to lipid ratios are shown.

peptides in the bilayer interface region. This in turn causes lipid deformations, trans-gauche isomerisation or inter-leaflet interdigitation in order to fill possible "voids" in the hydrophobic core region. This effect has been investigated and different relationships have been established between the structural order parameter and absolute membrane thickness. Most of these are based on a set of assumptions, that are discussed elsewhere [281; 297; 298]. The net change of the bilayer thickness is most reliably described by [299]:

$$\Delta d = 2L_0 \Delta \langle |S| \rangle \tag{4.14}$$

where L_0 is the the length of the all-trans acyl chain and $\langle |S| \rangle$ is the average change in the order parameter across the bilayer. Note that this can only be seen as an approximation of the mean change in bilayer thickness and localised effects might be plausible.The hydrophobic thickness of a POPC bilayer is 26 - 27 Å [300]. Thus a membrane thinning of maximum 3 Å of the POPC component at a peptide lipid molar ratio of 1:25 was estimated, whereas for the POPG component at the same molar ratio an overall membrane thinning of 5.5 Å could be estimated; purely based on the observed membrane perturbations. The total bilayer thickness for a pure POPC membrane was previously determined to be ∼40 Å [301] and hence an average thinning of 4.25 Å between the proposed two lipid phases would bring the bilayer thickness to 35.75 Å or if only the change of the POPG component, is considered to 34.5 Å. The 21 amino acid long peptide tilamin is predicted to fold into an alpha helix with a total length of ca. 31.5 Å . Thus a thinning of the membrane could partially compensate for hydrophobic mismatch of fully inserted tilamin. However, the changes in lipid order and membrane morphology are only an indirect measure of peptide action and thus do not allow for distinct characterisation of an AMP insertion mode.

The relative effects on PC and PG components are consistent with the effects observed by EPR, where a larger ordering was observed for the PG component. cwEPR probes acyl chain order on the regime of ns, in contrast the segmental order parameters calculated from quadrupolar splittings are in the regime of μs. Additionally, quadrupolar splittings also reflect a possible reorientation of the lipids due to membrane thinning or selective lipid curvature, which are only observed indirectly by cwEPR. A reorientation or an overall disordering on the μs time scale can indeed lead to a more dense acyl chain environment due to clustering and reduced amplitude of motion on the ns time scale probed by cwEPR.

4.2.2.2 Peptide orientation probed by ^{2}H & ^{15}N NMR

4.2.2.2.1 Orientation probed by Deuterium ^{2}H NMR

Orientational constraints based on individual peptides deuterated at a single alanine residues were obtained. A total of four different label positions were considered (Figure 4.20). All labelled residues are "native" alanine residues and thus no chemical changes needed to be incorporated to the designed peptide sequence. The bilayer normal is aligned parallel with the external B_0, in which case lateral diffusion as well as rotational diffusion of the membrane-associated peptides as a whole do not change the relative orientation to B_0 (Figure 4.26 A). However, if these dynamics are fast they will scale the observed quadrupolar splitting. Other sample alignments can be advantageous if other parameters peptide dynamics are studied [302].

A typical deuterium spectrum for a well aligned sample is shown in Figure 4.21. As illustrated the spectra have been de-convoluted (by fitting Lorentzians to the individual spectral components) to obtain information on linewidth and relative proportions of the observed quadrupolar splittings for each labelled residue (See Appendix A.1.1 for detail).

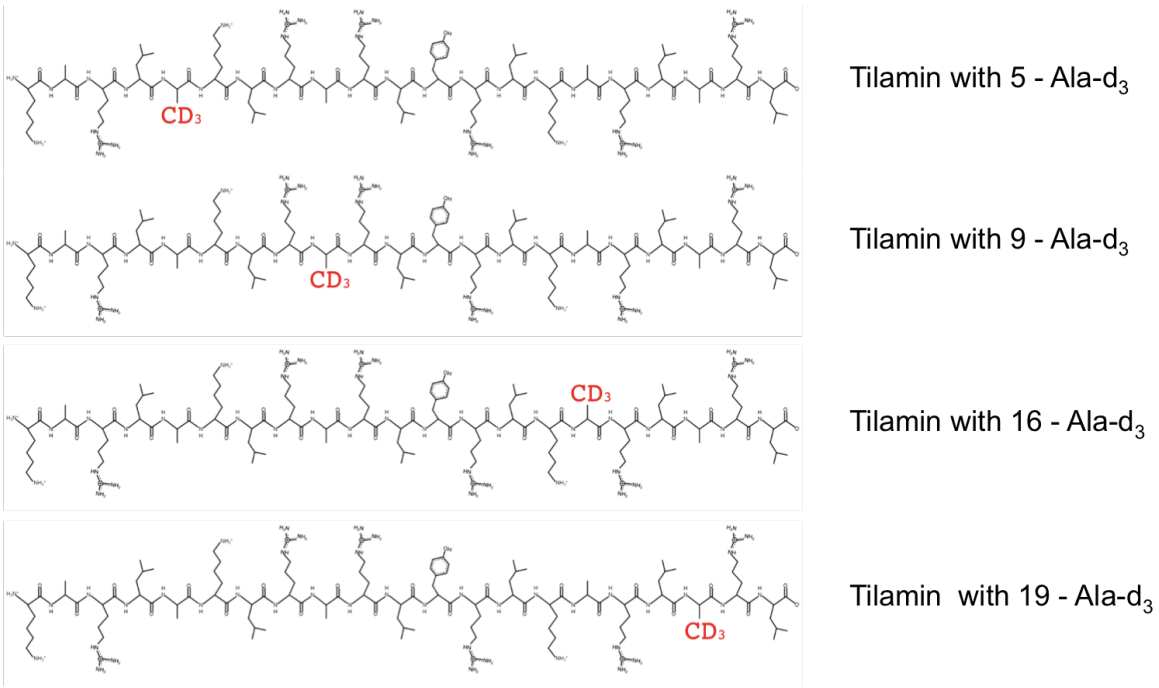

Figure 4.20: A linear representation of the locations of Ala-d_3 used for the NMR characterisation are illustrated. The deuterated alanine side chains are highlighted in red. please note that only a single position is labelled per peptide variant.

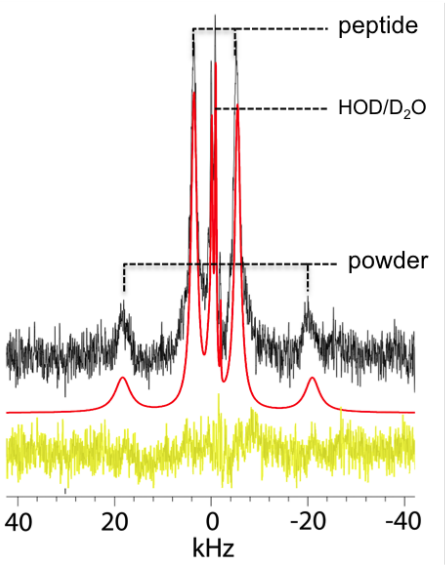

Figure 4.21: A ^{2}H spectrum is shown illustrating the individual components that are expected for a deuterated peptide in a uniformly aligned sample. The spectrum is analysed by fitting Lorentzians to the individual components (see appendix A.1.1 for detail) . The de-convolution process used in order to extract relative proportions of the individual components, as well as line width, is illustrated. Note that to fully de-convolute a powder component with all its orientations a Pake doublet including the 0° edges should be used. The original spectrum is shown in black, the de-convoluted spectrum in red and the residuals in yellow. Spectrum is recorded at 20 ^{o}C and a deuterium frequency of 122.78 MHz

The large doublet seen in the example in Figure 4.21 corresponds to a powder component that normally gives rise to resonances with a splitting of ∼38 kHz [296]. The quadrupolar splitting at ∼10 kHz originates from the deuterated alanine side chain position of tilamin. The central resonance around 0 kHz is the naturally abundant D_2O and HDO that tumble fast on the NMR timescale and hence average to a central doublet. However, the central line may also have other causes. Unbound deuterated peptide is expected to tumble fast on the NMR timescale and thus would most likely average to central resonance [303]. Equally any orientation at the exact magic angle (54.7^o), would render the $(3\cos^2\theta - 1)$ relationship equal to zero and thus result in a central line, however statistically such a uniform orientation with only a very narrow conformer distribution is unlikely. Note that the central resonances are split into clear doublets for aligned membranes in the absence of peptide, due to molecular water alignment along the membrane interface introducing a degree of anisotropy (Figure 4.22).

The net charge of the model membrane used is negative (POPC:POPG (3:1, molar ratio)), which promotes electrostatic interaction with water, and the intensity of the central peak correlates with tilamin to lipid ratio (Figure 4.23): at lower peptide to lipid molar ratios (eg

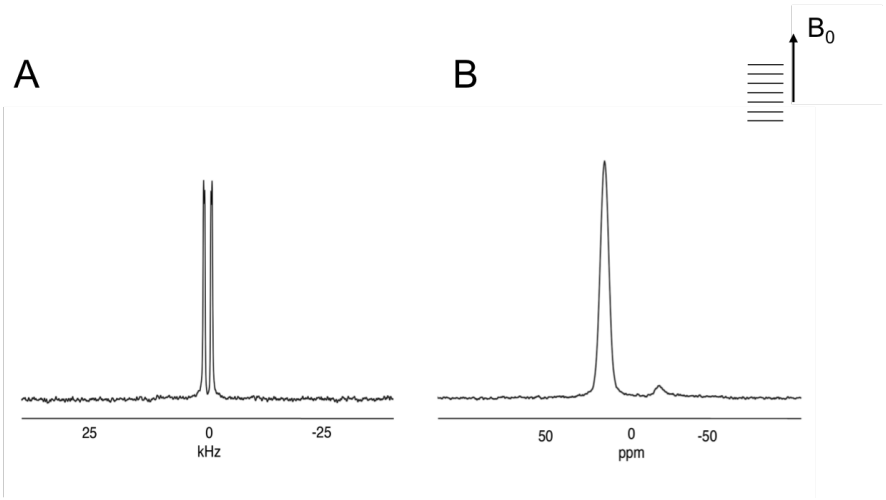

Figure 4.22: Spectra for an oriented POPC:POPG (3:1, molar ratio) membrane is shown in the absence of a deuterium probe or peptide. (A) The arising central resonance is due to naturally abundant deuterium that orients at the bilayer interface. (B) A ^{31}P NMR spectrum of the same sample is shown to confirm sample alignment. Good lipid alignment is shown at 0°, with a minor underlying powder component likely due to lipids that curve around the edges of the oriented bilayer. Spectra are recorded at 20 °C and a deuterium frequency of 122.78 MHz

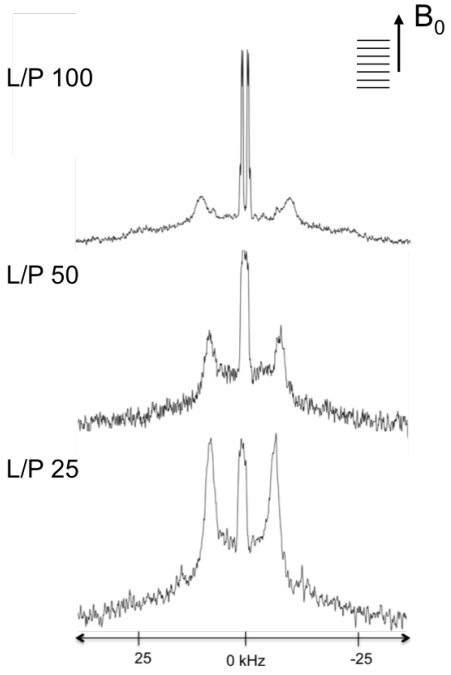

Figure 4.23: The ^{2}H spectra of deuterated tilamin (9 - Alad_3) at different peptide to lipid molar ratios are probed. At low peptide to lipid ratios (1:100) a slightly larger quadrupolar splitting is observed when compared to high ratios. Also note the change in relative intensities between the central resonance and the larger splitting. The resolution of the central resonance doublet also changes. Spectra are recorded at 20 °C and a deuterium frequency of 122.78 MHz

1:100), the central resonances are large compared to the doublet corresponding to the peptide splitting, which is in agreement with the larger "free" membrane area that does not interact with peptide and allows for orientation of free water. Further to this the central resonance is a clear doublet at a peptide to lipid ratio of 1:100. At higher peptide ratios the doublet is replaced by a single broad resonance; this is consistent with tilamin perturbing the oriented water layer upon membrane interaction. It is plausible that some water is pulled into the bilayer, facilitated by positively charged arginine and lysine residues and thus contribute to the disruption of the electrostatic charge network at the bilayer interface [233; 304].

Further to this a slight decrease in the observed quadrupolar splitting was observed upon tilamin addition at different peptide to lipid molar ratios (Figure 4.23). The absolute quadrupolar splitting decreased from from 23.1 kHz at a peptide to lipid ratio of 1:100 to 19.1 kHz at a peptide to lipid ratio of 1:25. Similar reductions could be observed across all deuterated positions measured and are summarised in table 4.1.

Table 4.1: Relative proportion of de-convoluted lipid domains

Sequence position of deuterated alanine with tilamin	Quadrupolar splitting ($\Delta\nu_Q$ in kHz)	
	Peptide to lipid 1:100	Peptide to lipid 1:25
-5d_3	48.1	46.3
-9d_3	23.1	19.1
-16d_3	40.8	38.5
-19d_3	10.8	8.7

All reported quadrupolar splittings are in a POPC:POPG(3:1, molar ratio) bilayer and were acquired at a B_1 field of 122.78 MHz.

The consistent reduction in quadrupolar splittings across all probed positions suggest a change due to a different dynamic membrane profile at a higher peptide to lipid ratio; which might be facilitated by an overall less organised bilayer as suggested by the order profiles from chain-deuterated lipid acyl chains, where a peptide-dependent decrease was observed (Figure 4.19). Such an effect would lead to a slightly increased overall motional averaging

of the observed quadrupolar interaction. A small reorientation of the ensemble peptide confirmation could lead to similar results, however in such a case increased quadrupolar splittings for some residues could also be possible.

The quadrupolar splittings were analysed by the relationships described earlier (equation 4.10), where a straight alpha helix was assumed for the intrinsic geometry relating the distinctly labelled position in respect to each other. A side chain tilt of 55.2° and a side chain rotational tilt of 44.7 ° were assumed (Figure 4.13, [305]). All labelled positions gave rise to clear distinct quadrupolar splittings (Figure 4.24 A). The sharp resonances with line width in the range of 2 kHz are indicative for well aligned samples with the bilayer normal parallel to B_0. The spectral components are summarised in table 4.2. The lipid alignment was monitored using ^{31}P NMR and also showed well aligned samples with a minor underlying powder component (Figure 4.24 B).

Table 4.2: Relative proportion of de-convoluted spectral components of ^{2}H NMR spectra of tilamin (See Appendix A.1.1 for detail)

Sequence position of deuterated alanine with tilamin	Spectral component	Line width (kHz)	Proportion (%)
tilamin-5d_3	Peptide splitting	2.2	90.4
	Powder	-	-
	Isotropic	0.3	9.6
tilamin-9d_3	Peptide splitting	2.3	77.9
	Powder	2.7	8.2
	Isotropic	0.5	13.8
tilamin-16d_3	Peptide splitting	2.0	78
	Powder	1.6	7.8
	Isotropic	0.2	13.2
tilamin-19d_3	Peptide splitting	2.1	78.6
	Powder	2.4	10.0
	Isotropic	0.4	11.4

de-convolution process outlined in Figure 4.21. Corresponding ^{2}H spectra are shown in Figure 4.24 A. See appendix A.1.1 for details on deconvolution.

AMPs are relatively small molecules compared to polytopic proteins like GPCRs for instance, and are expected to be intrinsically dynamic. In addition to that, their often

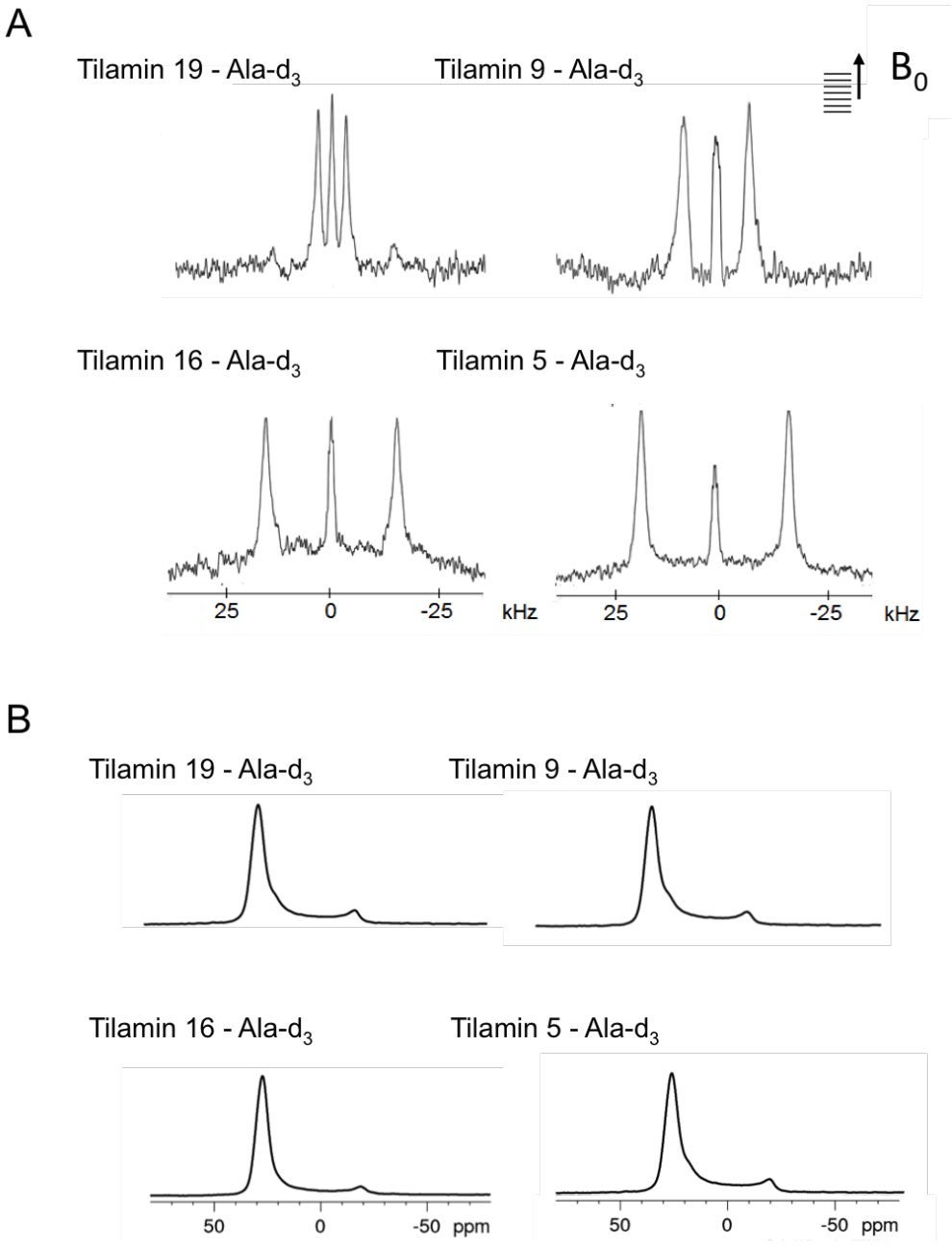

Figure 4.24: (A) The quadrupolar splittings of different labelling positions around the peptide structure are shown. All spectra are recorded at a peptide to lipid molar ratio of 1:25. The samples are uniformly aligned with the bilayer normal parallel to B_0. The individual positions of the labels depicted by the individual spectra are marked. Spectra are recorded at 20 °C and a deuterium frequency of 122.78 MHz. (B) Corresponding ^{31}P NMR spectra are show confirming lipid alignemt with a minor underlying powder pattern. Spectra are recorded at 20 °C and a deuterium frequency of 161.98 MHz.

unspecific and only partial membrane insertion in an initial binding stage add to their mobility. Peptide motions observed in a bilayer are fast and range from 10^{-5} to 10^{-8} s^{-1} for axial and off-axial peptide reorientations as a whole. Peptide plane motions tend to be even faster up to 10^{-9} s^{-1}. A typical ssNMR acquisition window is in the range of μs for deuterium NMR and thus partial motional averaging of the otherwise anisotropic quadrupolar interaction is expected [171; 302; 306]. The theoretical static quadrupolar splitting of 84 kHz was observed to be reduced to 74 kHz for deuterated peptides (PGLa) in the powder form, which is attributed to internal motional averaging [279]. It is very likely that the peptide in an aqueous environment is at least as mobile as in powder form, and additional averaging of the quadrupolar interaction due larger mobility profiles in an membrane environment are likely [279; 302]. In order to compensate for motional averaging the structural order parameter "S" is employed in order to scale the quadrupolar coupling constant, this is a linear approximation for all labelled positions that has been used extensively [44; 51; 279]. Recently more variable approximations for a dynamic profile have also been reported. Here, RMSD plots of different linear structural scalars have been calculated in order to find good RMSD fits, where in previous publications "S" varied considerably between $S =$ 0.5 to a complete static model of S = 1. The tilt and rotational angle can vary slightly based on the dynamic profile applied [279]. Here, S was varied between 1 and 0.4 in steps of 0.12 and the results are presented in Figure 4.25. Distinct individual local minima in the RMSD analysis were observed using a structural scalar of 0.76 corresponding to a maximum quadrupolar splitting of 64 kHz (Figure 4.25). Note that the overall RMSD landscape remained fairly stable across the probed dynamic scalars.

The dynamical characteristics of membrane associated peptides are essential for their function, yet in solid state NMR investigations access to the conformational and configurational states associated with dynamic equilibria are often limited. Especially the precise aggregation/oligomerisation state often relies on approximations that mostly don't allow for distributions. The peptide dynamical behaviour can give initial insights into a potential aggregation state within the framework of the NMR timescale yet does not allow to give a precise aggregation number "n". The dynamical behaviour of tilamin was probed using parallel and orthogonally aligned membrane samples. In the parallel aligned membrane samples lateral and rotational diffusion patterns will not alter the relative peptide tilt to B_0, yet fast motions like peptide "wobbling" or rotations around the molecular axis can lead to partial averaging of

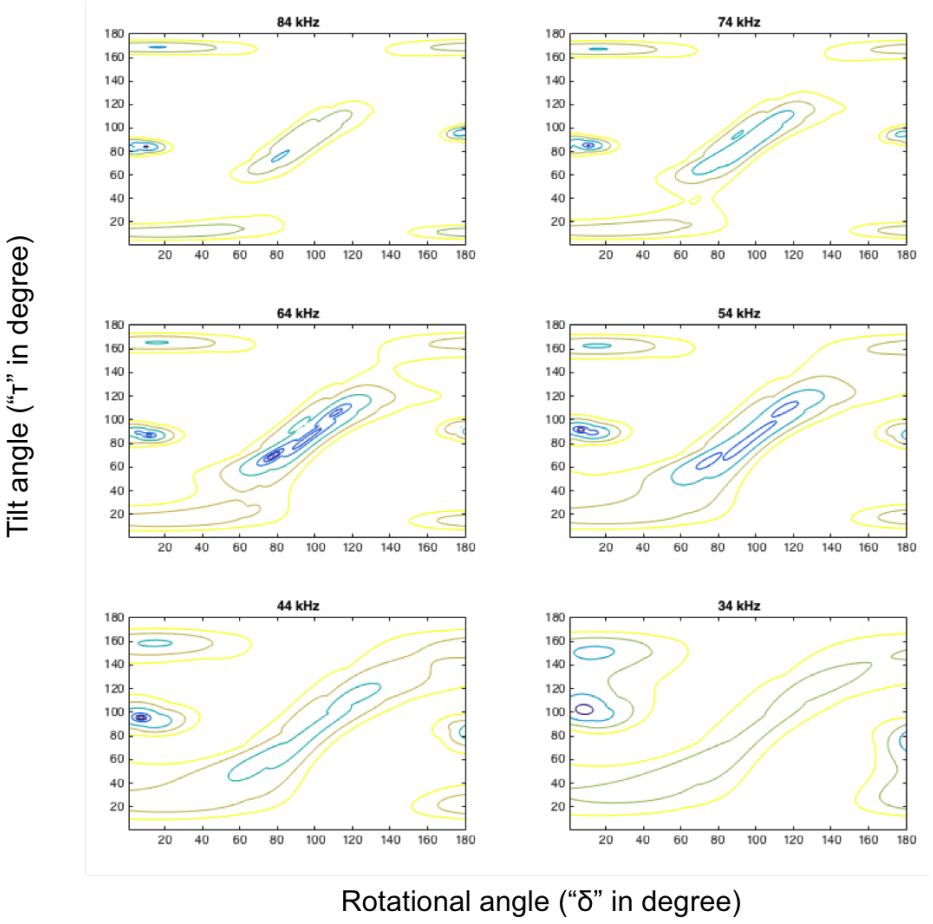

Figure 4.25: RMSD plots of tilt (τ) and rotational (δ) angle are plotted taking into account the individually measured quadrupolar splittings as absolute values due to the sign ambiguity of quadrupolar splittings. The data vector is related to theoretically calculated quadrupolar splittings by equation 4.10. Different theoretical maximum quadupolar splittings are plotted to account for different dynamical models. The overall profile of the RMSD plot remains similar yet the distinct RMSD levels change in accordance with the dynamical model applied. Good fit and distinct solutions are found for a maximum quadrupolar splitting of 64 kHz, which corresponds to ca. 25% averaging due to peptide motion.

the investigated anisotropies and need to be considered for precise analysis. In the orthogonally aligned configuration the peptide orientation relative to B_0 changes upon rotational diffusion around the bilayer normal. The angular diffusion patterns of either sample orientation are illustrated in Figure 4.26 A and B respectively. The orientation selective diffusion of an orthogonally aligned sample is illustrated by two separate angles α and β (Figure 4.26 B). For fast motions this orientation-selective movement becomes an averaged ensemble and for large aggregates tumbling slower than the NMR timescale, distinct orientations based on the rotational pattern would be expected, each resulting in a distinct quadrupolar splitting. Indeed fast motional averaging was observed for tilamin in a bilayer as a clear narrow line quadrupolar

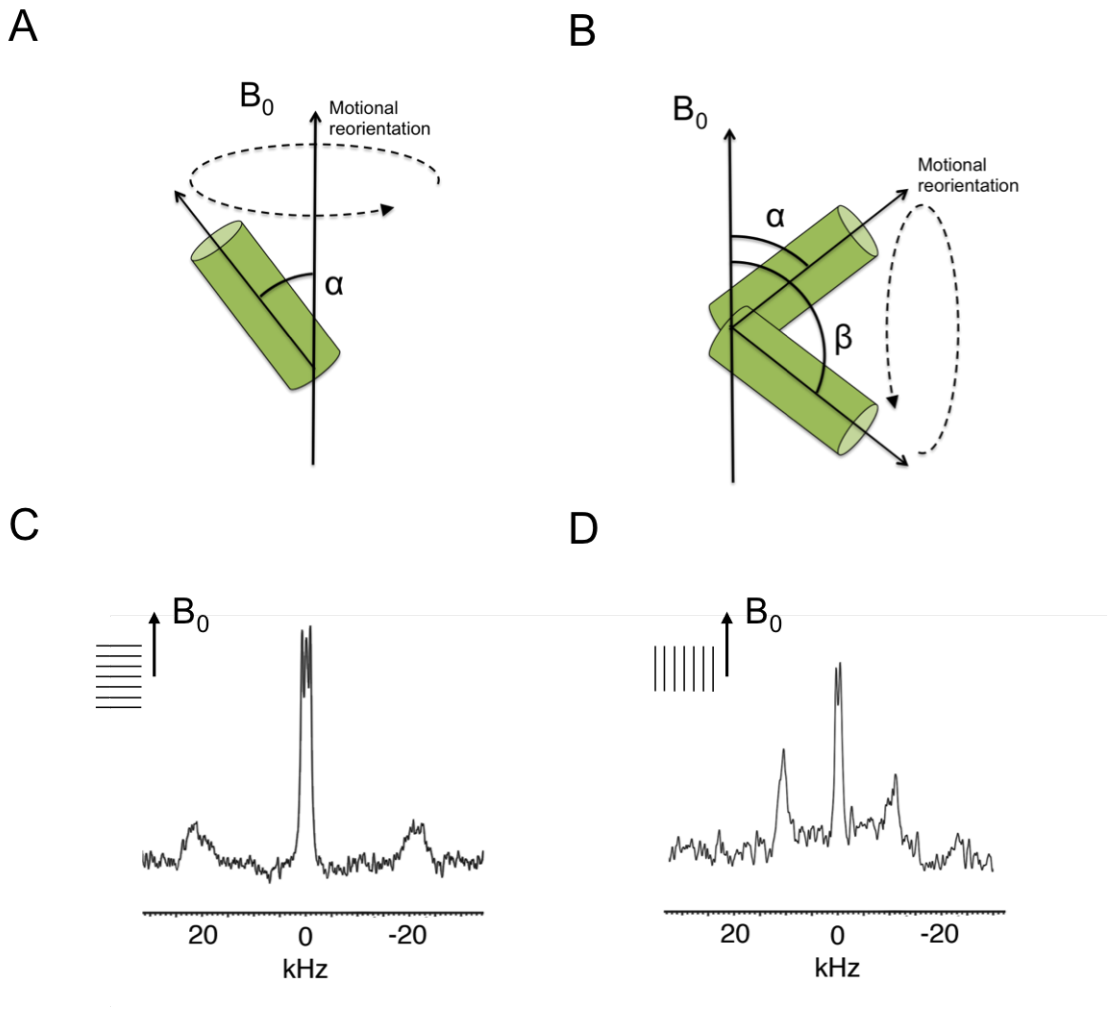

Figure 4.26: Deuterium spectra of tilamin selectively deuterated at position 16 at a peptide to lipid molar ratio of 1:100 are shown. (A) The expected motional peptide regime expected for a sample alignment with membrane normal parallel to B_0 and (B) the bilayer normal perpendicular to B_0 are illustrated. (C) ^{2}H NMR spectrum with bilayer normal oriented parallel to B_0 and (D) with the bilayer normal perpendicular to B_0. Spectra are recorded at 20 °C and a deuterium frequency of 122.78 MHz and 61.39 MHz respectively.

splitting is observed (ca. 21 kHz; Figure 4.26), suggesting rotational averaging faster then 10^{-5} s [296]. However, due to a comparably low signal to noise ratio it remains unclear whether additional components or a cylindrical peptide distribution might be present. Under this consideration temporary and reversible oligomerisation becomes plausible, if however this occurs fast on the NMR timescale it would not be detected. The minor contribution of a larger splitting around 48 kHz might correspond to aggregated peptide that has restricted rotational diffusion and does not allow for significant averaging of the quadrupolar interaction. In a stable larger peptide complex no single distinct quadrupolar splitting would be resolved

as motional averaging would not occur fast on the NMR timescale and a distribution of angles would be observed, hence if membrane poration by tilamin occurs the pores are predicted to be dynamic. Overall, the quadrupolar splitting halved within experimental error, when tilted to an orientation of the normal perpendicular to B_0, indicating fast correlation times [296; 302]:

$$D_{pep} = \frac{1}{4} \cdot \frac{k_B T F}{4 S \eta h} \tag{4.15}$$

where F is describing the overall shape and thus to the size of the aggregate, k_B is the Boltzmann factor, T the temperature, η is a viscosity constant, S the relative surface of the object and h is the relative object thickness in a bilayer.

In summary, multiple distinct local minima were observed based on four individual quadrupolar constraints and using a motionally averaged quadrupolar splitting for RMSD plot analysis (Figure 4.25). In order to limit the possible orientational solutions further, a ^{15}N constraint was included that more directly reports on the absolute helix tilt due to the near alignment of the amide bond CSA tensor with the longitude axis of an alpha helix. This approach is complementary to the deuterium based analysis.

4.2.2.2.2 Orientation probed by ^{15}N NMR

^{15}N static oriented ssNMR in POPC:POPG (3:1, molar ratio) of tilamin containing a single ^{15}N label (Tyr-12) were recorded at 400 MHz in order to deduce the amide bond orientation of the spin of interest by evaluation of the CSA. The amide bond of the central tyrosine residue was chosen for labelling and alignment with the bilayer normal oriented parallel to B_0.

The CSA was recorded in two different lipid environments: (I) POPC:POPG (3:1, molar ratio) and (II) DLPC:DLPG (3:1, molar ratio) (Figure 4.27). Similar chemical shifts were obtained for both lipid environments at 72 ppm and 75 ppm respectively. The line widths were 14 ppm and 15 ppm respectively, which are in good agreement with literature values. Line widths of of 20 ppm for selectively labelled M2 in oriented bilayers and line widths of 10 ppm for magainin are reported [307; 308].

The CSA reported in both lipid environments is broadly consistent with an in-plane peptide orientation, whereas a fully transmembrane configuration would be expected to yield a CSA of ca. 200 ppm. The comparable line width between the two tested lipid environments is striking as ^{2}H NMR spectra in DLPC:DLPG (3:1, molar ratio) showed an underlying powder component, while giving similar absolute quadrupolar splittings. Thus it appears that the peptide is more disorganised in saturated lipids based on the ^{2}H NMR spectra (see appendix A.5). For this reason the peptide to lipid ratio in DLPC:DLPG (3:1, molar ratio) is at a molar ratio of 1:50 double the peptide to lipid ratio used in POPC:POPG (3:1), at higher peptide to lipid ratios no well aligned samples could be prepared suggesting a higher destructive potency for saturated lipids. The bilayer thickness of DL lipids is less and thus the overall hydrophobic mismatch is reduced, possibly facilitating transient pore structures that lead to membrane disruption. Structures of this type are not present in the ^{15}N probed spectrum, or at least not stable, on the NMR timescale as no resonances in the region of 200 ppm were observed.

The comparable narrow line width and absence of a powder probed by ^{15}N spectra in both lipid environments suggest a relatively well aligned sample. It also possibly indicates that the labelled tyrosine residue is anchored to the electrostatic interface network and restricted in reorientation. A conformationally restricted tyrosine residue will give rise to a single line, yet

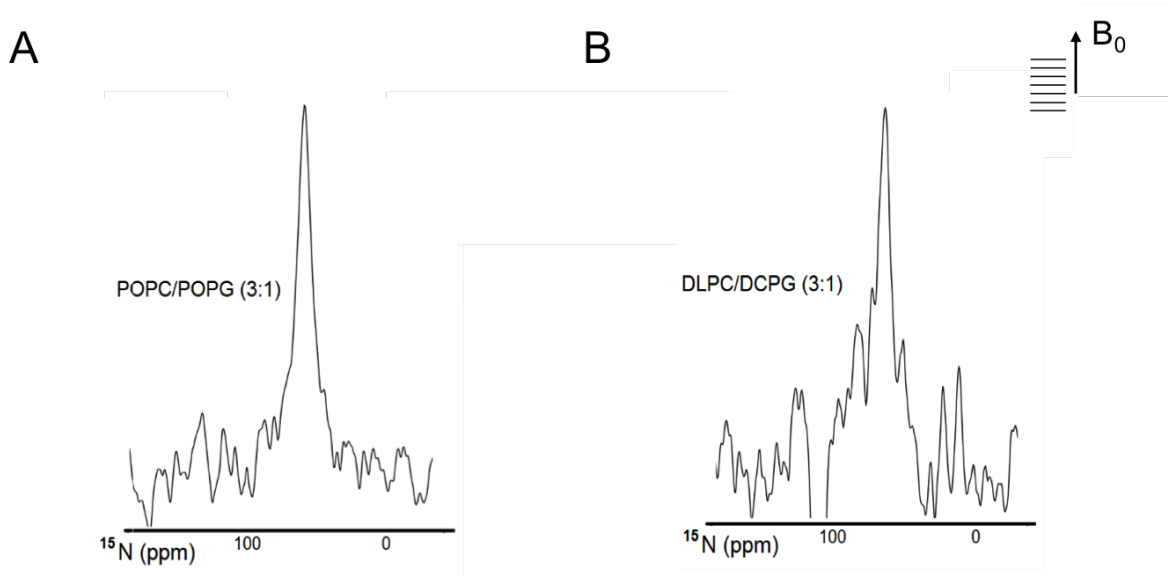

Figure 4.27: ^{15}N spectra of uniformly aligned samples labelled at residue 12-Tyrosine. (A) Single line observed in POPC:POPG (3:1, molar ratio) at a peptide to lipid ratio of 1:25. (B) Single line observed in DLPC:DLPG (3:1, molar ratio) at a peptide to lipid ratio of 1:50.

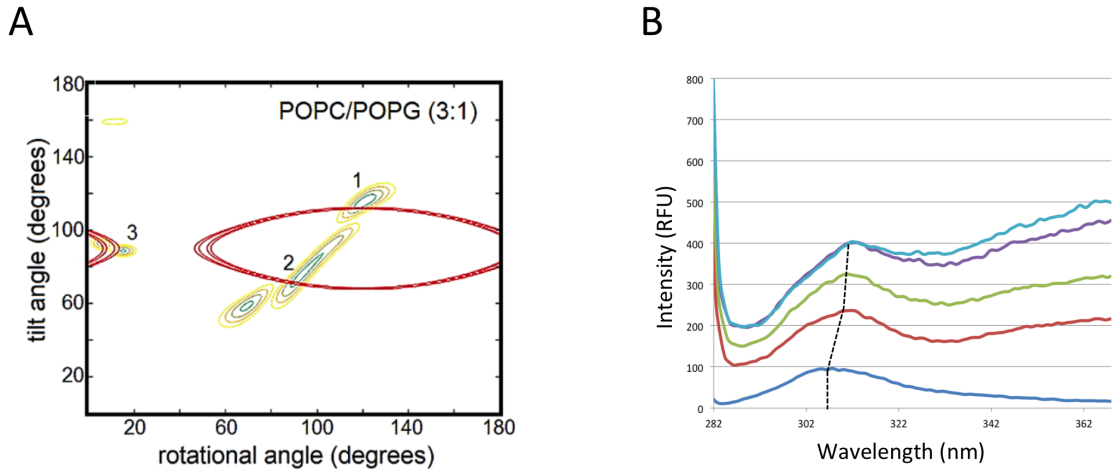

Figure 4.28: (A) A combined RMSD analysis plot is shown including a contour plot based on the ^{2}H constraints shown by contour lines for 7 kHz (yellow), 6 kHz (orange), 5 kHz (brown) and 4 kHz (green) and the calculated ^{15}N constraints (red). Intersections are numbered illustrating three consistent solutions with all NMR constraints. (B) Intrinsic tyrosine fluorescence is measured upon vesicle titration (POPC:POPG(3:1, molar ratio)). An increased fluorescence and a red shift is observed. In the absence of lipid (blue), 1 mM lipid (red), 2.5 mM lipid (green), 5 mM lipid (purple) and 7.5 mM (cyan).

Table 4.3: Relative solutions from combine ^{2}H and ^{15}N constraints

	Tilt and rotational angles	
	Tilt	Rotation
solution 1	110°	115°
solution 2	70°	90°
solution 3	90°	15°

Note that solution 3 is only a partial overlap with the local ^{2}H minimum, yet it is in close proximity and thus reported here.

a more disorganised behaviour of the alanine cluster in saturated lipids would still allow for a significant underlying powder pattern. Such a scenario is also consistent with a red-shift of the intrinsic tyrosine fluorescence upon bilayer interaction, suggesting a charge-driven interplay within the electrostatic interface network (Figure 4.28 B). Further to this, tyrosine (like tryptophan) is known to preferentially interact and locate at the membrane interface which might encourage a conserved, preferred orientation within the probed ensemble [234].

This interaction might possibly restrict the peptide from full transmembrane configurations as the tyrosine residue is located central to the peptide sequence.

Taking into account the CSA constraint measured, the RMSD plot was refined (Figure 4.28 A) and intersections between solutions supported by ^{2}H and the ^{15}N constraints are highlighted and reported. A total of three possible peptide orientations are found to be consistent with the reported NMR data (Table 4.3), consistent with tilamin location in the interface at an acute angle to the planar membrane orientation.

4.2.2.3 Simulation of ^{2}H spectra

In order to confirm the structural geometric analysis performed, the corresponding deuterium spectra of a model alpha helix described by basic Euler angles, labelled at corresponding positions with a single deuterium nucleus, were simulated using the software library *Spinach* [209]. Note that a single nucleus is used to describe the side chain orientation due to the fast motional averaging of the CD_3 side chain of alanine, which will yield a single constraint represented by a single quadrupolar splitting.

The orientational dependence of a single nucleus in an ideal alpha helix is illustrated by rotating the helix in a stepwise manner by 45° (Figure 4.29). The initial alpha helix was described by Euler angles [0.0, 55.2, 0.0] aligning the longitudinal helix axis with B_0 [305]. This basic axial configuration of a single ^{2}H spin, a system temperature of 293 K and an external magnetic field of 18.8 T were used to describe the spin system. Furthermore an inter coupling matrix describing the quadrupolar interaction was generated to set the initial Hamiltonian. An additional orientational constraint was added to the principal spin Hamiltonian corresponding to the specific helical tilt and rotation of interest allowing to simulate spectra for all relative peptide orientations.

The *Spinach* software library is Matlab based and designed to handle large spin system (>20 spins), which is not the case for the problem presented here. Yet its Matlab interface and broad applicability are advantages for large simulations. The simulated RMSD plot shown here uses a step size of three in each dimension and each data point is the sum of four individually simulated spectra (one for each label position), hence a total of 14400 spectra were simulated (Figure 4.30 A, for simulation parameters see section A.1.2).

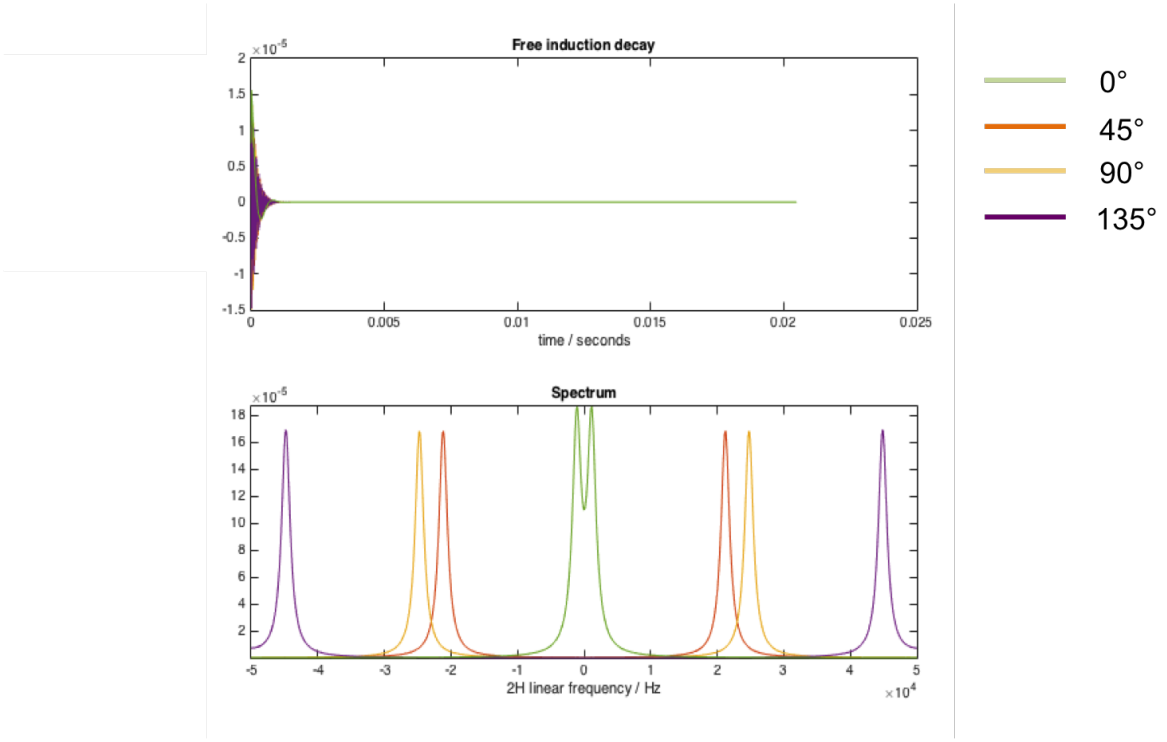

Figure 4.29: Quadrupolar splittings of a single nucleus defined by Euler angles describing a alanine side cain within an alpha helix. The FID of the individual trace is plotted and overlaid (above) and the individual quadrupolar splittings for each configuration are shown (below). Note the central peak at an initial helix tilt of 0° (due to the side chain tilt) is close to the magic angle at which the quadrupolar splitting collapses due to the averaging of the anisotropic dependence of $(3\cos^2\Theta - 1)$ to 0. Full simulation parameters are provide in section A.1.2.

The RMSD plot obtained from spectral simulation is in good agreement with the RMSD analysis based on geometric relationships (Figure 4.30), the small variation might be an attribute to the larger step size used in each dimension due to limitations in computational power or due to spectral processing. The absolute quadrupolar splittings obtained for the best fit by simulation are compared to the experimental values in Table 4.4 and are in relativly good agreement within the experimental error of 2 kHz. Note that the deuterium spin at position 16 of tilamin indeed gave a simulated quadrupolar splitting of 37.9 kHz, which is close to the peak-to-peak splitting of a powder (ca. 38 kHz), yet here simulation confirmed a uniformly aligned sample configuration and not a powder, further to this the 0° degree edges would be expected for a powder pattern.

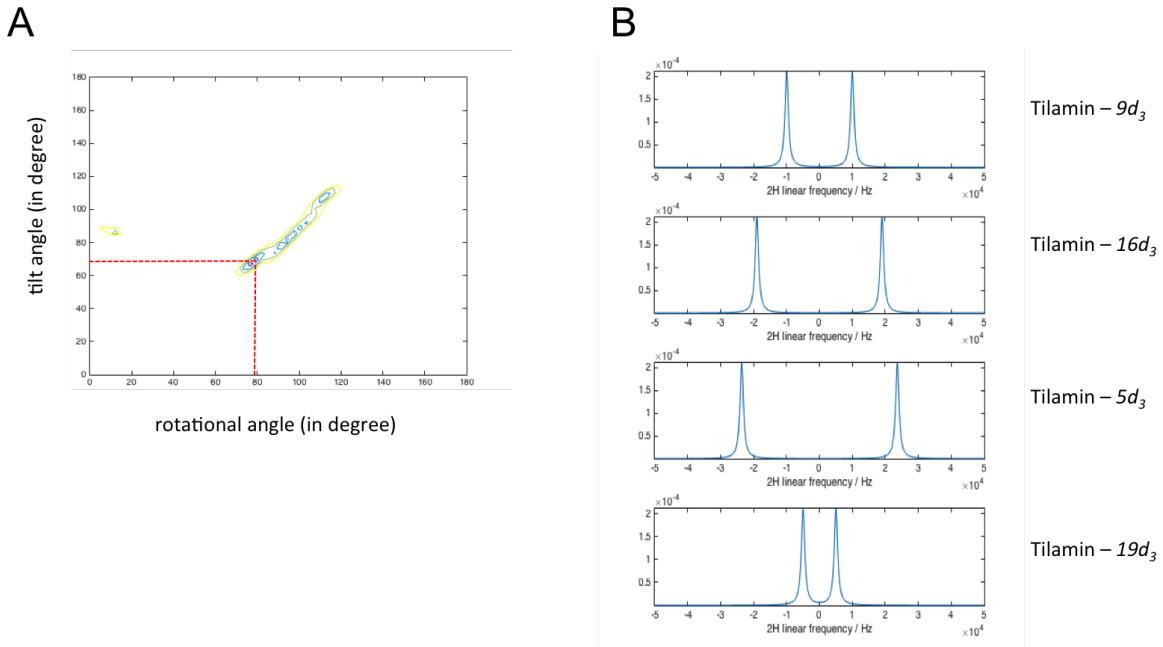

Figure 4.30: Simulation based analysis of deuterium constraints are illustrated. (A) RMSD plot based on individually simulated ^{2}H are shown. The contour lines plotted are 2, 3, 4, and 5 kHz respectively. The best of an RMSD of 1.1 kHz is illustrated with a red line. (B) The individual ^{2}H composing the best fit illustrated in part A are plotted for comparison to the experimental data. The absolute quadrupolar splittings as determined by simulation are shown in table 4.2

Table 4.4: Quadrupolar splittings of experimental and simulated spectra

^{2}H constraint	Simulated $\Delta\nu_Q$ (kHz)	Experimental $\Delta\nu_Q$
tilamin - $9d_3$	18.8	19.1
tilamin - $16d_3$	37.9	38.5
tilamin - $5d_3$	47.1	46.3
tilamin - $19d_3$	9.9	8.7

4.2.2.4 Molecular dynamics (MD) simulation of probed interaction

MD analysis of both monomeric and oligomeric peptide assemblies were performed in order to gain better insight into the tilamin mode of action and relate to the experimental data. An initial simulation of an individual alpha helical tilamin was run in order to analyse peptide lipid interactions. Tilamin was found to locate at the membrane interface in a near planar orientation. Normalised rotational distribution functions were calculated for the charged residues relating their relative proximity to the lipid phosphate group. The tyrosine residue at position 12 shows significant interaction with the PG and PC head group suggesting an electrostatic intercalating interaction as previously reported by intrinsic fluorescence and ^{15}N NMR. Similar to the ^{2}H NMR data, a preferred charge-driven interaction with the anionic lipids was confirmed (Figure 4.31 A) showing a preferred PG interaction for residues Lys 1, Lys 6, Arg 8 and Lys 15, where residues 1, 8 and 15 form part of the same peptide phase, suggesting a preferred interaction between the bilayer interface and this part of the peptide. Looking at the lateral distribution of these amino acids it becomes evident that, apart from Lys 15, they form part of the first half of the sequence possibly indicating that the N-terminal half is favourably anchored in the interface region and allowing the C-terminal half to penetrate further into the bilayer.

Indeed, a slight tilting of the peptide into the bilayer is observed across the simulation frame (Figure 4.31 B), which is consistent with the insertion mode and the preferred charge-driven interaction determined by NMR. The long side chain of Lys 15 possibly anchors the C-terminal domain to the interface region via a snorkelling motif thus preventing complete peptide insertion.

Complete peptide insertion was probed using an octameric peptide bundle (other oligomeric states were also considered, further information in appendix section A.1.2, Figure A.7 and Figure A.8) and placing the pore structure into the bilayer. Coarse-grain simulation (Figure 4.32 A,B) did render this configuration unstable and the structure disintegrated. It should be noted that coarse grain simulations for a small system like an AMP might lead to minor changes in peptide characteristics due to averaging approximations. Interestingly the peptide bundle opened into a flower shape, which was converted back to an atomistic model for further analysis and its plausibility as an intermediate transient state. The

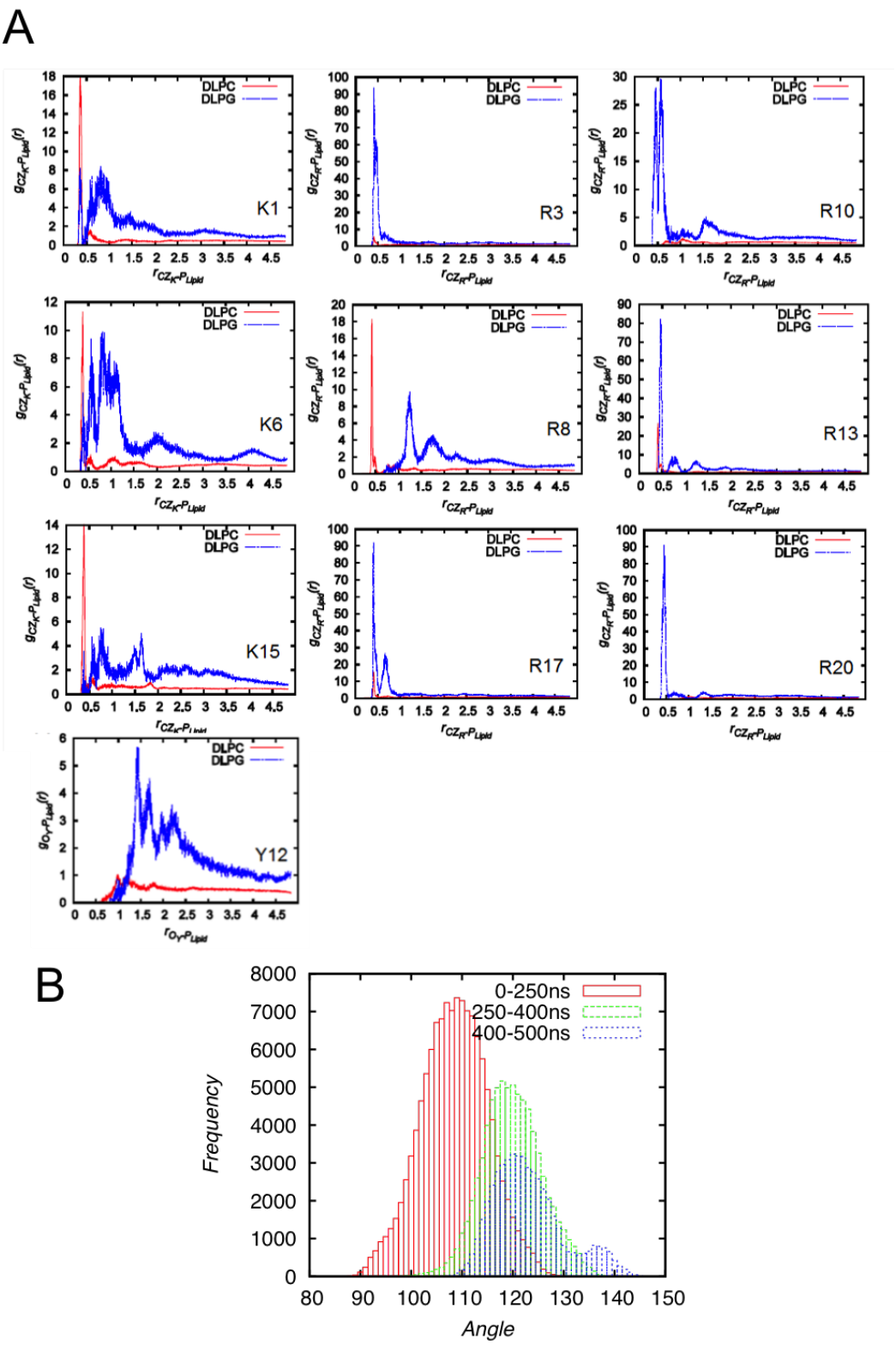

Figure 4.31: Atomistic MD simulations of a single helical tilamin peptide over 500ns. (A) The electrostatic charge driven peptide interaction was analysed by normalised rotational distribution functions for the charged amino acid residues. (B) Broadly an in planar peptide configuration with respect to the membrane was observed with some tilting into the bilayer across the entire time frame. Some more pronounced tilting could be observed in the later simulation frames. Note that the data is based on the simulation of a single helical peptide in DLPC:DLPG (3:1, molar ratio). Simulation parameters and information on data analysis can be found in section A.1.2. Simulation run by B Little (Edinburgh); data analysis and figure by P Judge (Oxford).

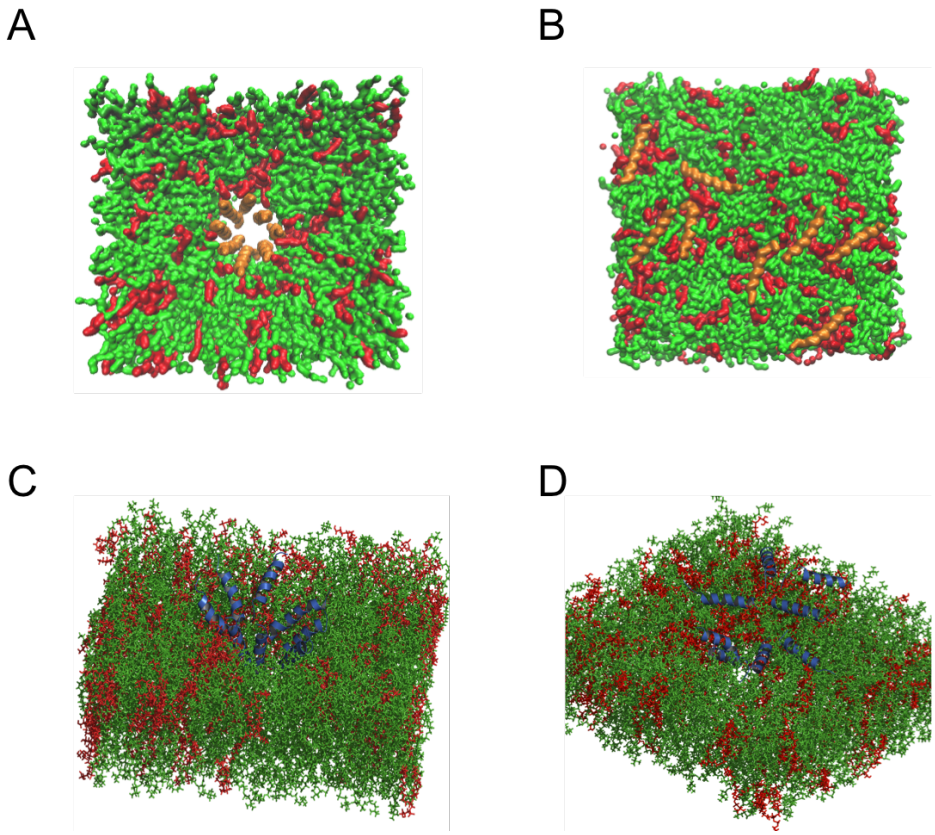

Figure 4.32: The potential of tilamin to form a pore in an oligomeric form was investigated. (A) A coarse-grain simulation of tilamin pore in POPC:POPG (3:1, molar ratio). The starting point is an octameric tilamin assembly spanning the entire bilayer. This conformation was not stable over the simulation and dissociated (B). (C) An intermediate conformation showing an open pore structure was taken and converted to an atomistic model and simulated for 70 ns showing a metastable conformation on this time scale (D). (green: POPC; red: POPG; Simulation parameters and strategy are described in section section A.1.2. Figures and simulation by Juan M Garcia (Oxford))

"flower" confirmation was partially stable in an atomistic MD simulation on the time scale of 70 ns. A conserved peptide aggregation mechanism could not be identified, suggesting that if peptide oligomers are present they will most likely only be of a transient nature or aggregates of no clear set oligomerisation state.

MD simulation of dynamic small peptides remain challenging and results often depend on the forcefield used. Combined coarse grain and atomistic simulation analysis are also readily used to gain different resolution levels [309]. The results here seem to exclude complete poration as a mode of action for tilamin, which leads to the question of the importance of transient states that might only be seen as part of large experimental systems allowing for selective local environments and global effects in an ensemble.

4.3 ChoM - lipid interaction investigated by ssNMR

4.3.1 Acyl - chain perturbation probed by ^{2}H NMR

Lipid perturbation upon peptide interaction were investigated using acyl chain deuterated POPC and POPG (Figure 4.33). ^{2}H NMR spectra in the absence and presence of ChoC and ChoM are shown, with two peptide to lipid molar ratios tested. Qualitatively, peptide interaction in both cases introduced disorder, resulting in less well resolved Pake doublets and a reduced overall spectral width. The individual Pake doublets were assigned where possible (typically 6 - 9 position could be identified) and smoothed order parameters were calculated across the acyl chain (Figure 4.34).

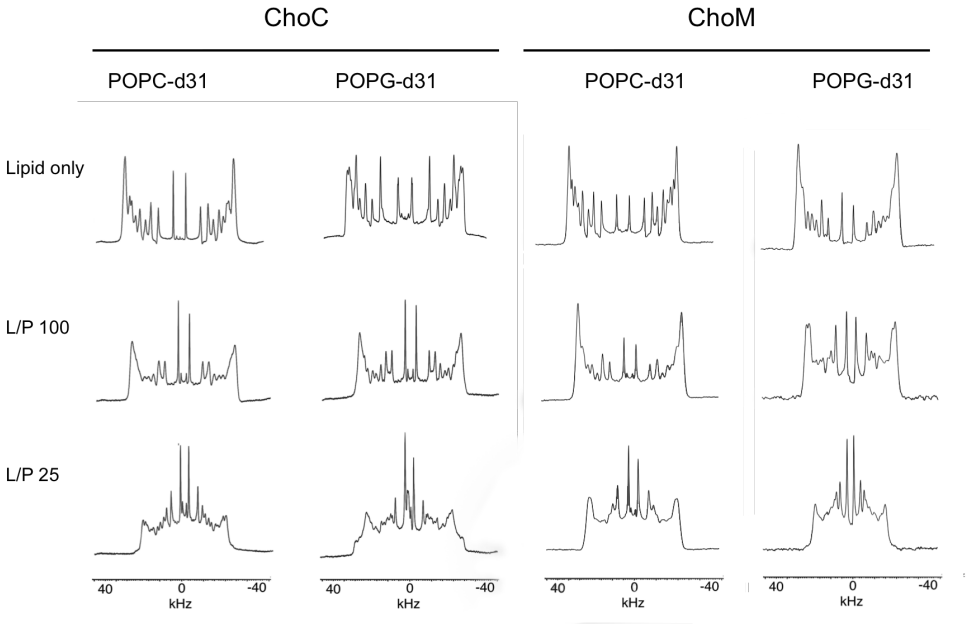

Figure 4.33: ^{2}H NMR spectra of acyl chain deuterated POPC and POPG in the presence of ChoC and ChoM. Acyl chain perturbations were probed at two peptide to lipid molar ratios: (I) 1:100 and (II) 1:25. The spectra were acquired with the membrane normal aligned parallel to B_0 and at a ^{2}H frequency of 122.78 MHz.

For both peptides a large disordering for both POPC and POPG was observed, whereas the POPG component is slightly more affected upon peptide interaction compared to POPC. This is comparable to the changes observed for tilamin, and possibly indicates a preferred charge driven interaction of ChoC and ChoM with the anionic POPG component. Similarly this can lead to membrane thinning, local curvature destabilising the bilayer and trans

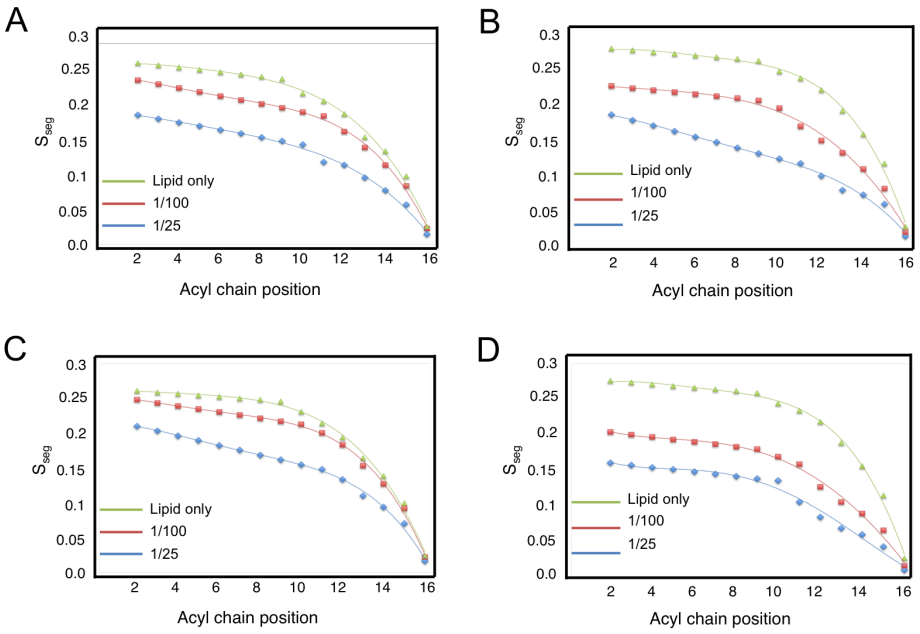

Figure 4.34: The smoothened segmental order parameters for acyl chain deuterated POPC and POPG are plotted. (A) POPC-d_{31} perturbations upon ChoC interaction, (B) POPG-d_{31} perturbations upon ChoC interaction, (C) POPC-d_{31} perturbations upon ChoM and (D) POPG-d_{31} perturbations upon ChoM interaction. Lipid order was probed at two peptide to lipid molar ratios as indicated in the graph: (I) 1:100 and (II) 1:25.

gauche isomerisations. No clear difference between ChoC and ChoM could be identified, suggesting that in an ensemble both peptides show a similar membrane activity. The large changes are consistent with peptide intercalating at the interface introducing a large degree of motional freedom in the acyl chain region.

4.3.2 Peptide orientation probed by ^{2}H NMR

Selectively side chain deuterated (alanine) peptides were investigated using oriented NMR in order to obtain angular constraints on peptide orientation with respect to the bilayer normal. Unlike for tilamin, chemical changes were incorporated into the peptide sequence in order to accommodate the alanine residues (Figure 4.35). All peptide constructs were tested for antimicrobial activity and were shown to be potent (Figure 3.10 and Table 3.3).

The individual ^{2}H NMR spectra are shown in Figure 4.36. Most peptide sequences resolved in large quadrupolar splittings indicating a non-transmembrane peptide orientation (Table 4.5). For two labelled positions (ChoM - (12) - Ala-d_3 and ChoM - (12) - Ala-d_{20})

Table 4.5: Quadrupolar splittings of alanine side-chain deuterated ChoM

Peptide	Quadrupolar splitting ($\Delta\nu_Q$)	
	Component 1	Component 2
ChoM - (4) - Ala-d_3	43.4	-
ChoM - (8) - Ala-d_3	31.7	-
ChoM - (12) - Ala-d_3	21.1	28.5
ChoM - (20) - Ala-d_3	10.5	12.5

two component spectra were observed, suggesting the existence of two sub populations that exchange slow on the NMR timescale and thus are resolved.

Interestingly, the two components are only observed at the positions of the C-terminal half of ChoM possibly indicating structural flexibility of this peptide half. Alternatively this can reflect and orientational peptide distribution within the sample. This scenario can be further investigated by simulating the exact spectral lineshape for the observed average conformation, which will give information on relative populations sizes as well as dynamics and orientational distributions within the observed spectral components. Simulations can also

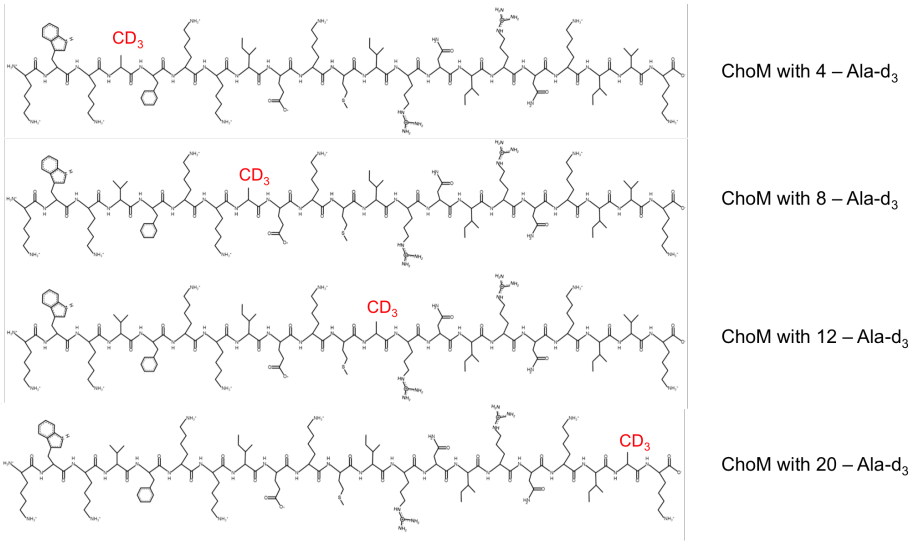

Figure 4.35: Mutated ChoM sequences in order to incorporate side-chain deuterated alanines. The mutations are V4A, I8A, I12A and V20A spanning the whole length of the peptide sequence. Deuterated positions are highlighted (CD_3, in red).

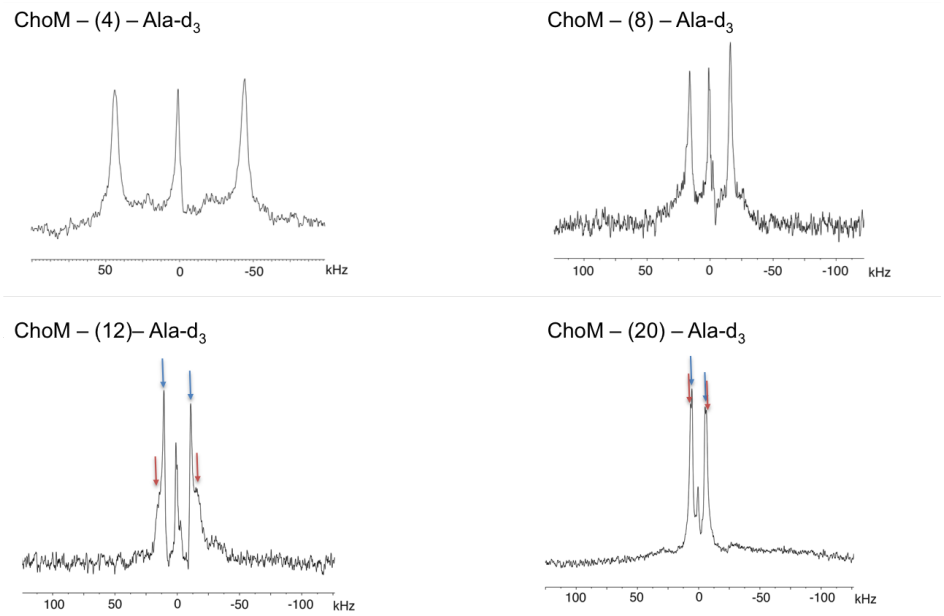

Figure 4.36: ^{2}H NMR spectra of peptide incorporated deuterated alanine side chains. Two components for a distinct labelled position are highlighted by arrows, if seen. The spectra were recorded in POPC:POPG (3:1, molar ratio) at 20 ^{o}C and a ^{2}H frequency of 122.78 MHz.

be used in order to describe the angular dependence of the quadrupolar splitting for spectra recorded at different orientations relative to B_0. Further to this, orientational distributions due to mosaic spread can be compensated for and analysed accurately by line shape simulations. In general increased mosaic spread leads to broadening of the observed resonances. Similarly, simulation of the line shape of the aligned ^{31}P spectrum can provide meaningful insight into the overall mosaic spread within the sample alignment; note that the mosaic spread of the lipid alignment does not necessarily reflect the spread for protein or peptide alignment in the same sample, which might differ significantly.

The individual constraints (in case of a two-component spectrum, the more pronounced component) were fitted to relationships described earlier in order to gain initial insight into peptide orientation (equation 4.10, Figure 4.37), using a varied structural parameter "S" in order to compensate for motional averaging of the quadrupolar interaction.

For a structural parameter of 0.74 (same as for tilamin), two local minima were observed both at an overall orientation nearly parallel to the membrane plane (+/- 10°). Based on these preliminary results ChoM is expected to act in a mainly planar orientation at the membrane

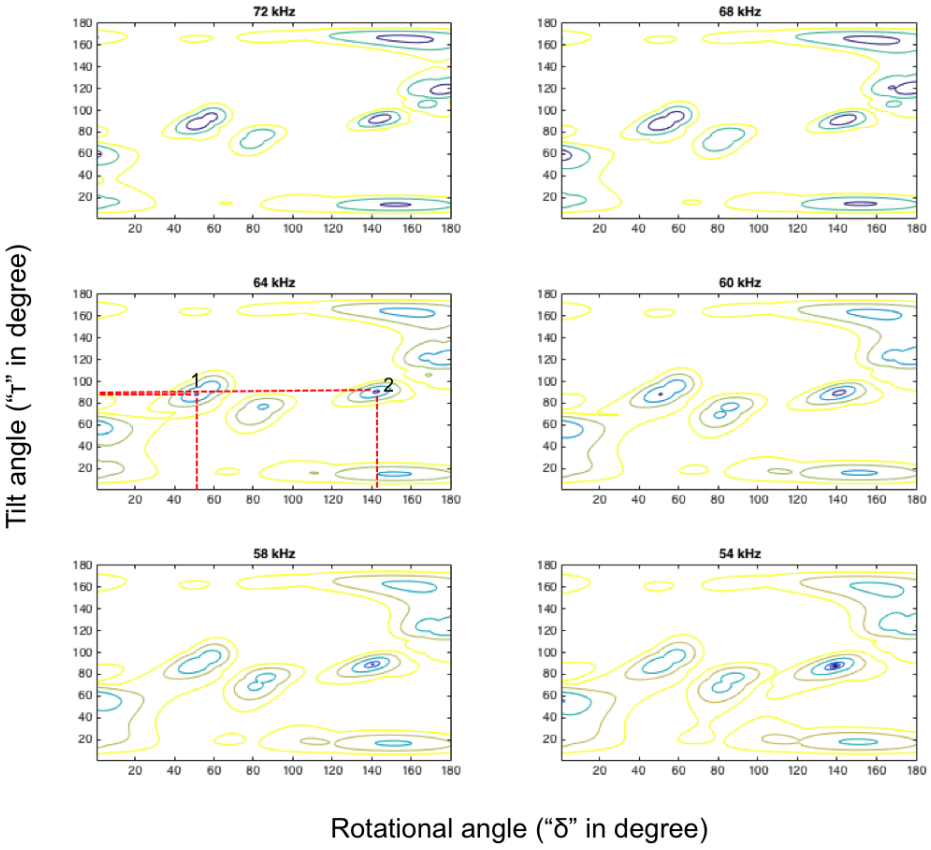

Figure 4.37: RMSD plots at different maximum quadrupolar splittings based on the individual deuterium constraints. Constraints spanning the entire helix are included under the assumption of a straight alpha helix. The structural parameter "S" was varied from 0.86 - 0.64 in steps of 0.05, based on previous results obtained for tilamin. Local minima for an structural parameter S = 0.76 are highlighted and numbered.

interface by a carpet-like mechanism on a similar dynamical scale compared to tilamin, causing large membrane perturbations that possibly lead to larger membrane reorganisation as observed by microscopy (Figure 3.10). The molecular behaviour of ChoC and ChoM is expected to be similar, based on segmental order parameters despite preliminary data (AFM, data not shown) showing local membrane pores for ChoC. However the removal of two glycine residues might affect peptide flexibility and a more thorough characterisation is required in order to obtain a detailed insight into the antimicrobial activity mediated by ChoM. The C-terminal domain of cecropin B does not seem to be needed for antimicrobial activity and,

similar to the cecropins B activity towards tumour cells, might serve a different purpose.

4.4 Discussion

Antimicrobial peptides exploit a large conformational space [302]. They are unstructured in solution and adopt regular secondary structures upon membrane interaction. The membrane interaction itself can be highly versatile and multifaceted. The combinational approach of NMR, EPR, AFM, MIC, CD and fluorescence microscopy presented here might shine light on the antimicrobial mode of action by combining different timescales and resolution levels (Figure 4.38). However the analysis is simplified and based on assumptions, like a perfect alpha helix (a general alpha helical character was confirmed by CD; Figure 3.9). Structural characterisation of inherently dynamic AMP systems remains challenging, mainly due to low synthesis yields and difficulty generating solubilisation conditions that resemble a native environment [302].

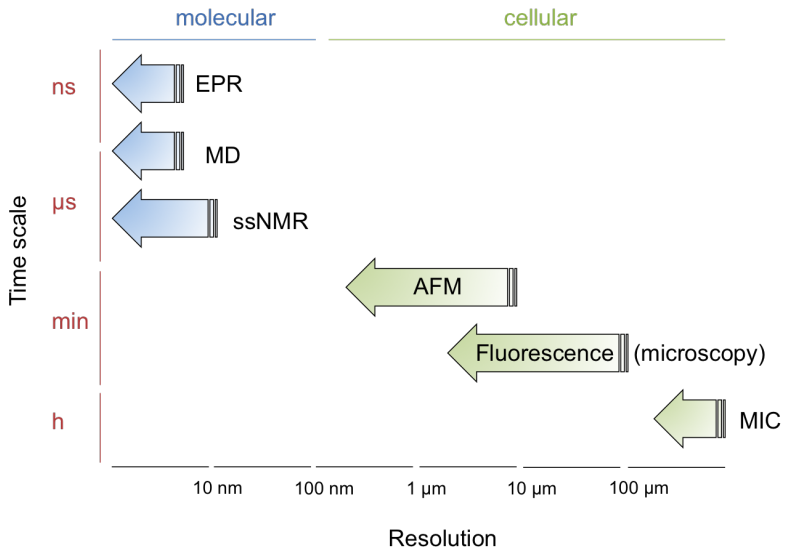

Figure 4.38: An illustration of the techniques used to study tilamin's mode of action. The individual timescale and approximated resolution ranges for the specific technique is illustrated. Note that MIC experiments are included for completion and do not have an associated resolution.

4.4.1 Tilamin - lipid interaction based on cwEPR

The EPR data shows a lipid interaction of the cationic antimicrobial peptide tilamin, whereas no interaction of the anionic counterpart QAELA was observed. This interaction may be electrostatic in origin; tilamin may induce lipid lateral phase separation, and SASL samples the different domains. The calculated order parameters show an increased effect on lipid dynamics at the probed position of 5-SASL compared to that at the position of 14-SASL. This reinforces a charge-driven interaction of tilamin with the lipid headgroup, leading to reduced motional freedom within this region. The SASL concentration is rather low at 0.5% and hence should not considerably alter bilayer characteristics.

The SASL-probed EPR spectra recorded in the presence of tilamin are composed of multiple components, consistent with lipid lateral phase separation. De-convolution of the composite spectra led to the identification of two main lipid phases, with a rough fractional distribution of 40:60 at a molar peptide to lipid ratio of 1:100. This distribution changes disproportionally at increased peptide concentrations, thus indicating a localized peptide distribution. The estimated limit of slow exchange of the two distinct lipid environments is $2 \cdot 10^7 s^{-1}$, which is within the expected exchange rates for phospholipids in unperturbed bilayers. This environmental exchange is in the range of previously reported lipid-lipid diffusion in pure phosphatidylcholine bilayers of 0.8 μs [310; 311]. The comparably small molecular structure of SASL compared to a phosphoglycerolipid might attribute to the slightly faster exchange rate observed here. Yet this scenario is a simplification and it is likely that additional dynamic environments are present. It should be noted that SASL is charged, similar to PG, and thus a the multicomponent spectra may arise due to spin-probe peptide interactions. The apparent pKa for the carboxylic group of SASL was shown to be 6.3 in a membrane environment [312]. Multiple components could not be confirmed when probed with PCSL spin labels, despite similar increases in lipid order upon tilamin interaction (5-PCSL). This broadly suggests that if multiple lipid environments are present in the membrane, PCSL only samples one of them whereas SASL can more freely diffuse between the individual environments.

The segmental ordering observed at position 5 (5-PCSL) could not be confirmed at position 12 (12-PCSL), which agrees with the lipid order profile probed by SASL. The spin-label correlation time represented by the central linewidth was altered upon tilamin interaction at the

5-PCSL position. Small changes in spin-label correlation times were also observed for 12-PCSL suggesting that the altered dynamical behaviour might be translated along the acyl chain.

In summary, the peptide may induce a segregated lipid environment, caused by a charge-driven interaction of the peptide with the phospholipid headgroup region leading to reduced motional freedom in the upper region of the bilayer. In light of the established modes of AMP action (section 1.2.2.1) these results are consistent with a toroidal-like or carpet mechanism of interfacial peptide location, intercalating between the headgroup moieties creating toroidal-like features (Figure 4.41 A and B). The peptide location at the head-group region of the bilayer most likely causes lipid deformations that can result in increased lateral pressure and reduced motional freedom at the bilayer interface region, which is reported by lipid order probed by cwEPR. It is likely that the interfacial peptide location causes lateral lipid segregation resulting in lipid domains and curvature, which would be followed by membrane thinning and an overall bilayer destabilisation.

4.4.2 Tilamin - lipid interaction based on ^{2}H and ^{15}N ssNMR

The intersecting ^{2}H and ^{15}N constraints resulted in a total of three possible solutions for the conformational space of tilamin orientation. The solutions are summarised in Table 4.3.

All three solutions are broadly consistent with a peptide orientation at the bilayer interface at an acute angle to the bilayer plane. However, the structural parameters obtained (Figure 4.28) represent the ensemble of peptide orientations and at a single molecular level minor populations at different peptide orientations or transient states together with a specific set of peptide-lipid interactions are plausible. Based on thermodynamical logic, solution 1 (Table 4.3), despite being consistent across all different structural scalar factors (Figure 4.25), seems unlikely. A tilt angle of $\sim 90^{o}$ at this rotational pitch ($\sim 15^{o}$) would place the alanine cluster towards the hydrophobic membrane core, which at first might seem plausible, however, this in turn places the hydrophobic leucine cluster facing the aqueous phase, which would impose a large thermodynamic penalty. The remaining two solutions both, at least partially, orient the hydrophobic peptide moment with the bilayer normal and show a mainly planar peptide orientation at slightly tilted conformations. The imperfect alignment of the peptide hydrophobic moment and the bilayer normal could be an indication that part of

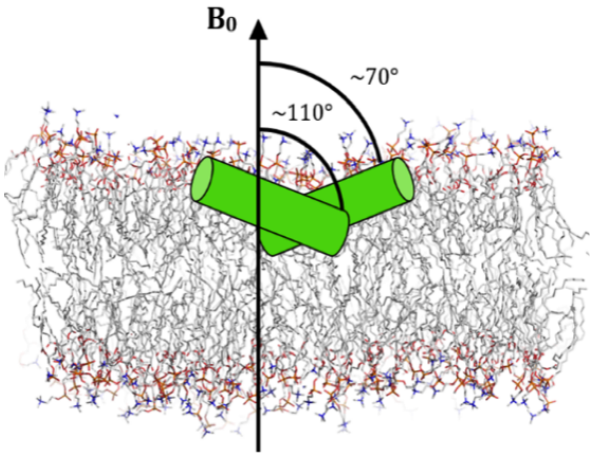

Figure 4.39: The two most plausible orientational solutions based on individual solid-sate NMR constraints are shown. The tilt angles are drawn to scale and placed on an equilibrated POPC membrane for illustration. Note that the overall tilt of both solutions is near identical, yet the inserted terminus differs between the two depicted solutions.

the peptide is aggregated, possibly facilitated by shielding of the hydrophobic phase and thus yielding an altered rotational pitch affecting the ensemble. However, they differ in their mode of action by opposing termini pointing towards the bilayer interior (Figure 4.39). The C-terminus is capped with an amide group and thus does not possess an intrinsic charge and might be more likely to penetrate into the bilayer core, which was also observed by MD simulation an a single peptide (Figure 4.31 B).

It is noteworthy that recently it was also demonstrated that a full transmembrane peptide orientation is not needed for transmembrane poration. Novicidin showed a ^{15}N chemical shift indicative of a planar peptide orientation despite forming toroidal pores [162]. A similar phenomenon was modelled for magainin where pores were formed in the bilayer despite no transmembrane peptide orientation. Here, a planar-oriented magainin peptide stabilises the pore by binding to the pore rim and remains in a parallel orientation to the bilayer plane [168; 313]. The ensemble information presented in this thesis is a good indication, but generally peptide orientation does not allow for an immediate conclusion on a distinct peptide functionality.

Additionally, it is increasingly evident that un-specific peptide fluctuations in peptide structure and behaviour as well as localised modulations in the bilayer phase properties need consideration in order to fully understand peptide behaviour. The low peptide-lipid

ratios used for biophysical characterisation (here 1:25 peptide to lipid molar ratio) as low as 1:6, peptide to lipid molar ratio for Omiganan, often questions the physiological relevance [314]. A recent intellectual exercise demonstrated that the relative high partition constants and MIC values in the μM range can indeed translate to local membrane concentrations that are about 10 000 times higher than in solution, yielding scenarios similar to complete membrane coverage. This is striking and indeed might result in localised and un-specific peptide environments on the pathogenic membrane, which itself is already highly complex. Such a scenario is difficult to biophysically characterise. In light of a hypothetical complete peptide membrane coverage, transient non-cooperative peptide-peptide interactions are highly likely and can result in spontaneous pore formation. These phenomena are in the absence of well characterised peptide-peptide interactions and thus challenging to be observed or quantified in an experimental setting or in small scale MD simulation that assume underlying biophysical principles [28]. Such a seemingly stochastic local peptide behaviour might be an advantage and might be the underlying principle to the often multistep mutation processes needed to develop resistance [315]. Nevertheless, better adapted biological model systems are still scarce and thus makes the interpretation of these microscopic biophysical and structural results in light of a macroscopic biological settings difficult.

These results are specific to the sample conditions used here. Based on previous data on similar antimicrobial peptides (e.g PGLa [170; 316]) alike results were shown to vary based on peptide to lipid ratio, precise membrane composition, sample hydration, temperature and buffer compositions and thus care should be taken when interpreting results based on different methodologies requiring a different set of experimental conditions. The simple model membranes used here and bilayers supported by glass slides are simplistic and should be considered with care.

4.4.3 Membrane perturbation upon tilamin interaction by ^{2}H NMR

The suggested in-planar peptide orientation at the bilayer interface region results in large membrane disorganisation on the ^{2}H μs timescale. Generally the bilayer disordering is expected to be less for fully transmembrane peptides compared to peptides that form in

plane conformations, which is consistent with the large membrane disordering observed here [299]. A transmembrane peptide spans the bilayer more evenly and does not allow for the introduction of "space". Peptides that preferentially sit at the interface or the glycerol backbone region allow for additional space in the acyl chain region. In a graphical illustration peptides interacting with the interface region are often portrayed as "spacers" between the individual head groups leading to motional freedom of the acyl chains and disorganisation. These effects are often partially compensated by head group tilting, acyl chain interdigitation and trans-gauche isomerisations usually seen in disordered bilayers in an attempt to fill "voids" leading to membrane thinning [199]. The volume and hydrophobic moment of the distinct peptide affect the extent of these deformations [299; 317].

The disordering effect is more pronounced in the hydrocarbon acyl chain of POPG rather then POPC (that also shows some disordering), which suggests a preferred interaction between the cationic peptide interaction and the negatively charged lipid headgroups. Such a peptide interaction could lead to lateral segregation of the individual lipid species in the model bilayer. Similarly preferential lipid interactions have also been observed for other cationic peptide systems, an example being pleurocidin which also showed preferential interaction with the anionic PG component in mixed lipid systems [318]. It was suggested that generally cationic AMPs are capable of causing lateral phase separation and domain formation with effects on localised lipid order and deformations at the lipid phase boundaries [319]. Additionally, it was shown for a magainin analogue (MSI-78) that localised membrane thinning can be the result of lipid segregation, which was later confirmed by atomic force microscopy (AFM) [320].

Some peptides have also been identified, which promote ordering upon peptide interaction, an example being cateslytin [321]. Strikingly this peptide lacks a large hydrophobic face that allows for peptide penetration into the hydrophobic core and the observed bilayer ordering might be due to only partial peptide penetration into the bilayer [322]. This might imply that the hydrophobic moment and associated membrane partitioning relates to the extent of membrane order perturbation.

The membrane thinning effect due to acyl chain disorder was estimated to be ca. 3 Å and ca. 5.5Å for the POPC and POPG component respectively. Broadly suggesting a larger thinning effect within a PG-enriched lipid domain due to a larger overall disordering. Membrane

thinning will eventually result in local membrane curvature at the domain edges, which in turn causes additional constraints on the membrane most likely adding to destabilisation, possibly leading to membrane budding as observed for GUVs (confocal microscopy, Figure 3.10). The tyrosine residue might introduce the necessary flexibility for tilamin to adopt to local curvature.

4.4.4 ChoM - lipid interaction

The limited data presented on ChoM indicates that the N-terminal alpha helical domain of cecropin B possesses a high degree of antimicrobial activity facilitated by interaction with the membrane (Table 3.3 and Figure 3.10). Structural analysis showed that ChoM orients in a planar orientations causing a large degree of membrane disorganisation. This broadly consistent with a carpet-like mechanism as previously observed for cecropin B and the hydrophobic C-terminal domain seems not to be crucial for antimicrobial activity. Further to this the replacement of two glycine residues did not compensate antimicrobial potential, however a more detailed structural analysis is required in order to depict the precise importance for these residues. It should be noted that previously a similar peptide to ChoC (residues 1-20 of CecB) was suggested to insert perpendicular to the membrane plane [323], thus removal of the glycine residues would reverse this effect at no cost to the antimicrobial activity. It can be suggested that replacing the glycine residues by isoleucine and lysine reduces the overall flexibility of the peptide.

4.5 Conclusion

In summary the presented biophysical and magnetic resonance characterisation of the antimicrobial activity of tilamin are consistent with the proposed peptide design that is membrane active and causes membrane rupture. The peptide design successfully transitioned a pore-forming transmembrane peptide (amhelin) into a sequence that develops its antimicrobial activity solely by insertion into the interface region, which allows for broad activity as confirmed by MICs. The spectrum of activity (MICs) suggests a mechanism that is largely independent of precise lipid composition as the precise membrane compositions varies across species. Most species contain a certain degree of anionic PG in their membrane that is

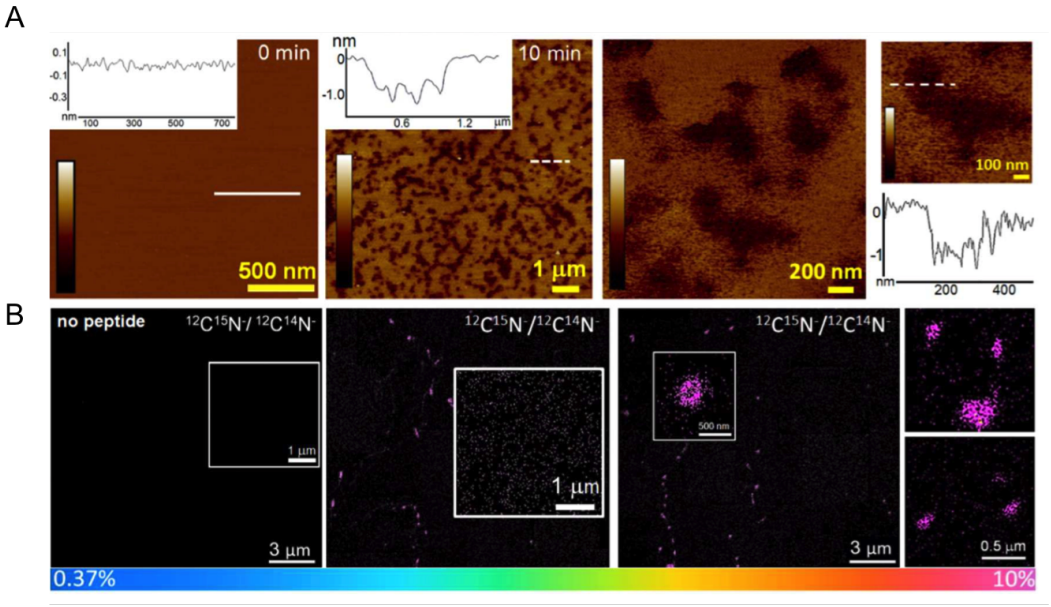

Figure 4.40: Tilamin-lipid interaction with supported bilayers (DLPC:DLPG (3:1, molar ratio). (A) Topological AFM of supported bilayers upon Tilmain interaction (1.8 μM, pH 7.4). Images at time point 0 min and 10 min are shown. Topological profiles of the bilayer deformation are shown; no complete bilayer poration is observed. (B) SIMS images of isotope enriched tilamin in absence of peptide (left) and in presence of tilamin (right, 10 μM, pH 7.4). Multiple sequential images are overlaid and the colour scale range form natural isotope abundance (blue) to 10% (pink). Peptide clustering into pore-like assemblies is observed. Figure taken from [325].

balanced to zwitterionic lipids. For instance PE lipid are the dominant zwitterionic component in *E. coli* wheras *S. aureus* lacks the species. Resistant bacterial species also show altered membrane compositions including unusual lipids in an attempt for resistance development [324]. Further to this, the thick pepditoglycan layer of Gram-positive bacteria, proposed to induced partial peptide folding [23], did not have an effect on peptide activity.

The most plausible mechanistic explanation within the framework of reported modes of action falls in the category of toroidal-like mechanisms of intercalating peptide-lipid complexes. Based on the here presented data together with complementary studies on supported bilayers (Figure 4.40), a tilted in-plane peptide orientation is proposed that causes membrane thinning. Nano-sims experiments confirmed peptide clustering in an experimental setting (Figure 4.40 B), which could not be reproduced in the MD studies, most probably due to limitations of the force field and restriction in the simulation size (a larger sample might be needed to allow for localised peptide effects in simulation). The slightly tilted planar membrane insertion possibly causes quaternary assemblies like a peptide lined membrane "crater" that attracts the PG

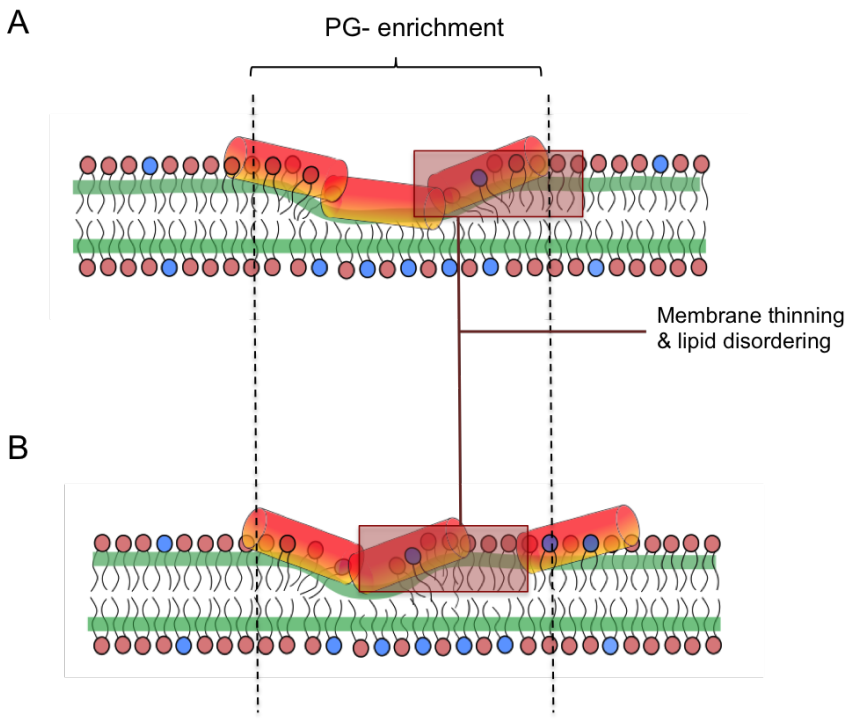

Figure 4.41: Proposed tilamin insertion is illustrated: (A) Aggregated peptides forming separated intercalated domains that result in membrane craters and (B) An aggregate crate-like membrane deformation combined with carpet/detergent-like peptide behaviour. The presented scenarios result in local peptide enrichment followed by preferred PG localisation and membrane thinning.

component of the model bilayer and leads to thinning, indicated by the AFM topography profile (Figure 4.40 and Figure 4.41 A and B). The lateral separation of the PG component and peptide interaction leads to an overall charge neutralisation of the membrane, which will have an effect on the membrane asymmetry. Additionally the peptide interaction disrupts the membrane hydration layer and might pull water into the interface region possibly facilitated by the Arg and Lys residues of tilamin causing additional destabilisation. It should be noted that a full transmembrane pore can be viewed as two monolayer motifs coming together to form a pore or at least facilitate the formation thereof, which could not be confirmed by AFM (Figure 4.40 A; [326]). The degree of specificity involved in this process remains elusive and hence two possible scenarios are presented in Figure 4.41: (I) Distinct individual peptide "craters" formed in one leaflet and (II) A hybrid method of peptide facilitated membrane "craters" leading to thinning and a detergent-like peptide behaviour. It is likely that in the late stage of such a mechanism, in conjunction with a high membrane coverage, toroidal-like micelles will be formed leading to disintegration of the bilayer. It should be noted that

supported bilayers and monolayers are expected to be more stable then similar environments found in nature, monolayers can be stable in water for a few days [327], which allows for characterisation of such peptide phenomena; in a biological setting however a similar impact on membrane integrity will most likely lead to fast membrane disintegration. Nonetheless, studies on model membranes are important to understand peptide behaviour and can yield functional insight, which might help to design peptide based antibiotics. It seems laborious to argue for a single distinct "correct model" as depending on precise sample conditions and methodologies different peptide states might be observed individually or even in coexistence.

Part II

The viroporin p7

5

*N*N-DNJ-membrane interaction probed by ^{2}H ssNMR

Contents

5.1 Introduction 144
5.1.1 ^{2}H NMR of headgroup deuterated lipids 147
5.2 Results 148
5.3 Discussion 152

5.1 Introduction

Hepatitis C Virus (HCV), a member of the *Flaviviridae*, is the major cause for chronic hepatitis. It causes severe liver cirrhosis as well as liver carcinomas [328]. Until recently HCV was primarily treated by a combinational therapy using pegylated interferon α and ribavirin (PEG-IFN-α and RBV), which was only poorly tolerated by some patients and additionally showed varied responses across different genotypes. New drugs against HCV, mainly targeting the nonstructural proteases and viral replication machinery are in the development pipeline. Recently approved drugs are Telaprevir (*Incivek*) and Boceprevir (*Victrellis*), both targeting NS3 protease and are effective against viral infections by HCV genotype 1 [329; 330]. In contrast to the previous treatment of PEG-IFN-α and RBV, these newer therapies are direct

acting antivirals (DAA), which is a significant advancement that avoid the secondary effects by PEG-IFN-α and RBV. Telaprevir and Boceprevir are first generation DAAs. Other second generation protease inhibitors are now available too (e.g. Grazoprevir, effective against various genotypes). This wave of new drugs are focused on three viral proteins, and there is an interest in broadening the spectrum of DAA targets. The high cost of new treatments has restricted their access to patients and more affordable drugs are required [331]. Additionally, the high mutation rate of HCV has already resulted in the appearance of resistance variants to some of the new treatments [330], so that new drug targets will likely be necessary in the long term. The p7 viroporin is essential for the assembly and release of infectious viral particles in cell culture [123; 124] and amongst others, iminosugar derivatives inhibiting p7 channel activity have been shown to clear HCV from cell culture, which makes p7 a potential drug target [135].

The glucose and galactose derivatives deoxynojirimycin (DNJ) and deoxygalactonojirimycin (DGJ) in conjugation with long-alkyl chains have shown potential as antiviral compounds. The glucose derived iminosugars (long chain; nonyl (*N*N-DNJ, Figure 5.1) and short chain, butyl *N*B-DNJ) were first tested against bovine viral diarrhea virus (BVDV) due to the lack of a suitable HCV cell culture model [332]. Treatment by either derivatives showed misfolding of viral envelope glycoproteins. This is most likely caused by the inhibition of the ER α-glucosidase I and II [333; 334], which results in hyperglucosylated envelope proteins and prevents interaction with calnexin and calreticulin, leading to misfolding. Further to this the glucose derived iminosugars were compared to the non glucosidase inhibiting galactose derivative (*N*N-DGJ and *N*B-DGJ). The long-chain derivative (*N*N-DGJ) showed reduced viral infectivity, indicating a secondary inhibition mechanism independent from glucosidase I and II inhibition [334]. Moreover, the relative length of the alkyl chain seems to affect the inhibitory potential as the short-chain *N*B-DGJ does not affect viral activity, the long-alkyl chain derivative *N*N-DGJ shows potential for antiviral activity [334].

Leading on from these initial observations, p7 was postulated as a potential drug target for long-alkyl chain iminosugars, given that *N*N-DGJ has activity against both pesti- and hepaciviruses, but not other flaviviruses like dengue virus or Japanese encephalitis virus [335], that both lack p7. Pest- and hepaciviruses both contain p7, which is absent in other flaviviruses. p7 of pestiviruses (BVDV) is very similar to p7 found in HCV; BVDV p7 is a 70 amino acid long peptide that was shown to be necessary for the production of infectious

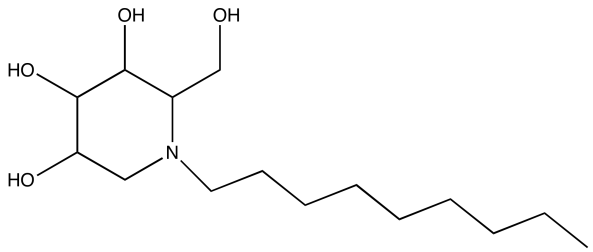

Figure 5.1: The chemical structure of the iminosugar *N*N-DNJ.

viral particles [336]. This hypothesis was confirmed by inhibition of HCV p7 ion channel activity in black lipid membranes (BLM; [71]). Notably the short alkyl chain iminosugars (*N*B-DGJ and *N*B-DNJ) were ineffective in inhibiting channel function in this assay [71]. Experiments were performed in a POPC:POPE (4:1, wt:wt) bilayer, broadly resembling a minimalistic model for the ER lipid composition. The PE and PC components contribute a total of ca. 75% to the overall ER membrane structure [337]. PS, PI, cholesterol and sphingomyelin are other constituents of the hepatocyte ER membrane [338].

The iminosugars *N*N-DNJ and *N*B-DNJ were tested in cell culture based assays for potential HCV treatment, and indeed reduced the production of infectious viral particles in a dose-dependent manner. The viral genotype 2a JFH1 was used for transfection of Huh7-Lunet cells [135]. The *N*N-DNJ derivative was more active in the case of JFH1 transfected cells, however small variations across genotypes were observed. Furthermore *N*N-DNJ and *N*N-DGJ were also reported to moderately reduce viral entry, but the cause of such effect remains unknown. p7 has not been detected in virus particles [83] and so it is unlikely that the reduction in viral entry is due to p7 inhibition in viral particles. In contrast to the iminosugars, an effect of the common antiviral drug amantidine on viral replication or infectivity could not be confirmed [135]. However, there are some early reports of amantidine that describe an effect on p7, which might be due to a variation across genotypes or experimental settings [70; 136; 137].

Following on from these initial reports of p7 as a potential DAA target, p7 function as an ion channel was investigated across a set of different membrane environments mainly consisting of PC, PE or a combination of both. p7 was confirmed to be active in mixtures of PC and PE, with behavioural differences observed in different membrane compositions [72]. p7 showed a high activity of short and burst-like channel openings in the lipid composition of DOPC:POPE (4:1, wt:wt), which is also the lipid composition used in this chapter.

The aim of this study is to complement the initial observations of p7 inhibition by *N*N-DNJ by investigating a potential interaction of the detergent-like drug (Figure 5.1) and a model lipid bilayer in which p7 was previously shown to be active. Such an interaction might be of importance in a potential inhibition mechanism of p7.

5.1.1 ^{2}H NMR of headgroup deuterated lipids

The basic underlying principles of quadrupolar nuclei is outlined in section 2.1.2. Headgroup-deuterated lipids have been used extensively to characterise peptide-lipid as well as drug-lipid interactions in the membrane interface region, reporting on orientation, local dielectric environment and dynamical changes at the labelled position [339; 340; 341]. The lipid headgroups build the interface between the hydrophobic bilayer core and the aqueous surroundings. The headgroups are known to align with the bilayer plane (within 30°; [342]) and are likely to show evidence of perturbation if the iminosugars are present.

The "Choline-tilt" - model describes the responsiveness of the choline headgroup to local variations of surface charge. It has been shown by similar NMR studies that the headgroup (described by the P-N vector) can adapt to the introduction of charge by a conformational response. Previous studies of bilayer interactions with divalent cations or peptides showed that the electric dipole moment of the $P^- - N^+$ zwitterionic choline group is responsible for the orientational adjustments [343; 344; 345]. This dipole responsiveness has been referred to as the "molecular voltmeter" [346]. Deposition of a positive charge causes the choline headgroup to tilt towards the bilayer normal. In contrast, a negative charge will force the dipole orientation towards the hydrophobic core [346]. For the deposition of a positive surface charge, a decrease of the observed quadrupolar splitting at the α-position and an increase in the observed quadrupolar splitting at the β-position is reported (Figure 5.3 and 5.2). This relationship is reversed for the surface deposition of negative surface charges [342]. This effect is illustrated for selectively deuterated POPC at the α-position in Figure 5.2.

It should be noted that changes in the local charge distribution at the interface can also be due to internal membrane interaction with anionic lipids, which cause electrostaticly induced and conformational changes in the headgroup region [347].

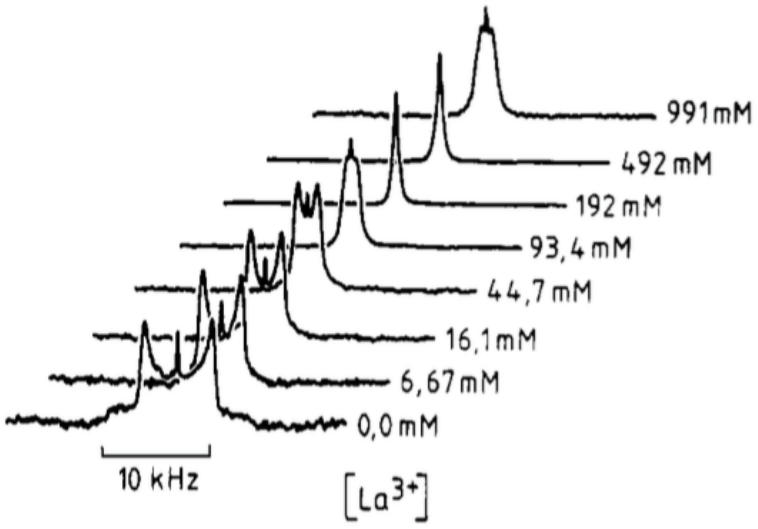

Figure 5.2: Changes in the quadrupolar splitting of α-deuterated POPC are shown upon addition of La^{3+} ions to the membrane. At high La^{3+} concentration the quadrupolar splittings passes through zero and increases again. Note that the quadrupolar splitting is absolute and the sign cannot be determined. Figure taken from [342].

The interaction of *N*N-DNJ and a model bilayer (DOPC-d_4:POPE (4:1, wt:wt)) was studied by static solid-state NMR. The "molecular voltmeter" effect was exploited in order to detect different protonation states of *N*N-DNJ in a bilayer, which allows determination of the pK_a of the drug directly in a membrane environment. Headgroup-deuterated DOPC-d_4 (Figure 5.3) was used and samples were analysed at a magnetic field strength of 500 MHz and in vesicle dispersions. The resulting spectra were post-experimentally dePaked using a weighted Fourier transformation in order to simulate the spectrum for uniformly aligned samples with the bilayer normal parallel to B_0 [348].

5.2 Results

Titrating *N*N-DNJ into the model bilayer showed only minor changes in the $\Delta\nu_Q$ (Figure 5.4). The absolute $\Delta\nu_Q$ of the β positions seems to decrease slightly, whereas a slight increase in the $\Delta\nu_Q$ in the α position is observed as a function of *N*N-DNJ concentration. This would be consistent with an iminosugar placement in the interfacial region possibly facilitated by an interaction of the *N*N-DNJ nitrogen and the negatively charged phosphate group. At the highest *N*N-DNJ concentration (200 μM) an additional shoulder seems to be present

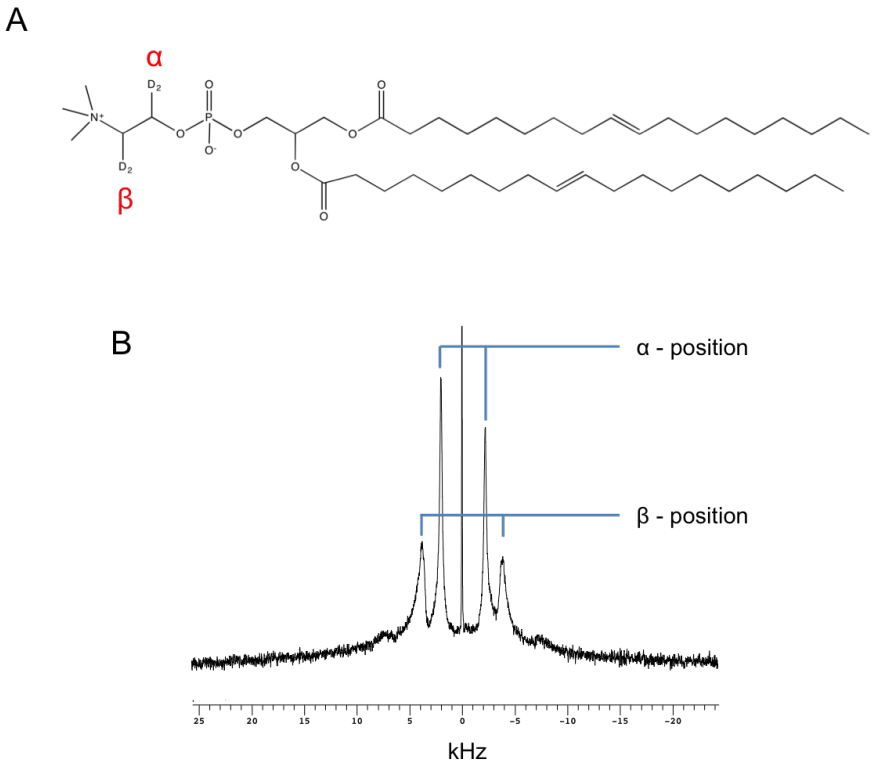

Figure 5.3: (A) The chemical structure of the DOPC-d_4. The headgroup deuterated positions are shown as D_2 groups for illustration and labelled as the α and β positions respectively. (B) A corresponding ^{2}H - NMR spectrum is shown illustrating the quadrupolar splittings corresponding to the α and β positions.

at the β-splitting, indicative of a separate environment within the bilayer as a whole, and exchange between the environment to be slow on the timescale v_{ex} <10kHz (Figure 5.4). The ^{2}H NMR spectrum up to a presence of 150 μM *N*N-DNJ does not show multiple environments suggesting that *N*N-DNJ is dynamic in the membrane with v_{ex} > 10kHz [340].

The observed minor changes suggest that the iminosugar does not induce a large interaction with the bilayer interface, and does not carry a charge at this pH level (7.2), which would otherwise lead to changes in the electrostatic network at the bilayer interface upon membrane localisation (Figure 5.4). It should be noted that this is an indirect methods of measurement and the direct protonation state can be investigated by solution NMR methodaologies.

A pH titration was performed in order to detect changes in the ionisation state of the iminosugar, which should lead to larger headgroup deformations and thus a plausible interface location should become detectable. Similar studies were previously performed to detect the

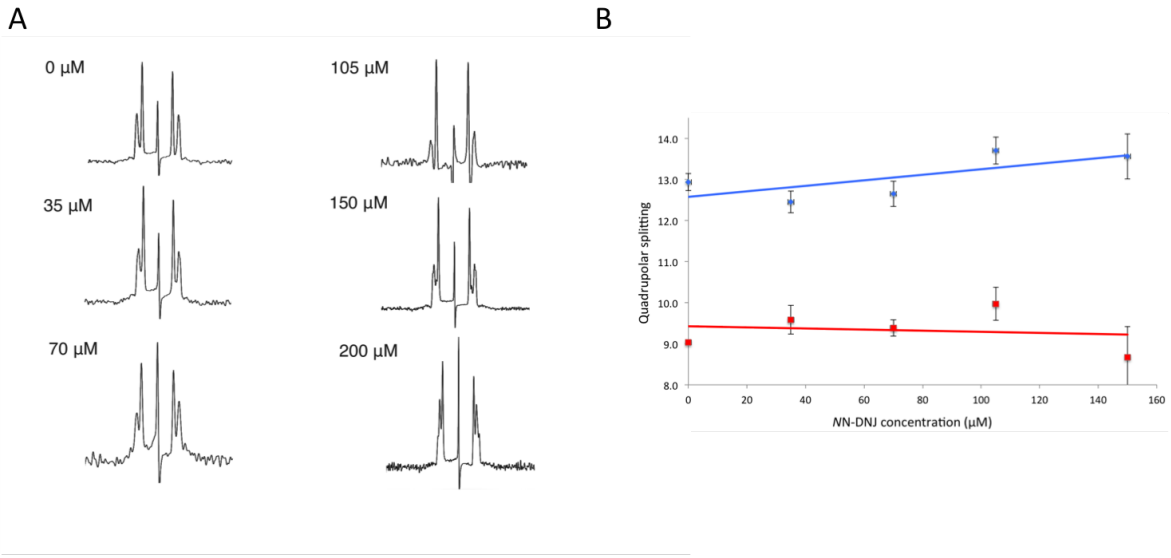

Figure 5.4: (A) ^{2}H NMR spectra of headgroup deuterated DOPC in DOPC:POPE (4:1, wt:wt) are shown at different *N*N-DNJ concentrations. (B) The absolute quadrupolar splittings observed for the α and β positions are plotted as a function of *N*N-DNJ concentration. Note that the values reported are an average of duplicates, the deviation is reported as error bars (alpha position in red and beta position in blue).

ionisation state of tetracaine in a membrane environment [339]. Additionally this allows for insight into the ionisation behaviour of *N*N-DNJ directly in a bilayer environment, which might stabilise a specific protonation state.

Changes in pH affected the $\Delta\nu_Q$s of both labelled positions. This is most apparent in the pH 5 - 7 region (Figure 5.5 B), where the corresponding $\Delta\nu_Q$ values for the α-CD_2 and β-CD_2 position start to overlap in the presence of *N*N-DNJ. The characteristic overlap is indicative for the deposition of a positive charge at the membrane, which results in opposing trends of the α and β labelled positions, causing spectral overlap [342]. Large changes in the $\Delta\nu_Q$ of all samples are seen above pH 8. This reflects the change in the ionisation state of the primary amine group of the PE-headgroup, which dramatically changes the hydrogen bonding network at the headgroup region leading to conformational changes (pK_a ca. 9.6 determined for DMPE:DMPC dispersions [339]).

A significant difference is seen between samples containing *N*N-DNJ and samples without *N*N-DNJ at the pH range of 5 - 7 (Figure 5.5) for both labelled positions. The $\Delta\nu_Q$s for samples including *N*N-DNJ change over this pH range (pH 5 - 7), whereas in the absence of drug $\Delta\nu_Q$s are constant. This change in headgroup conformation is caused by a change in the

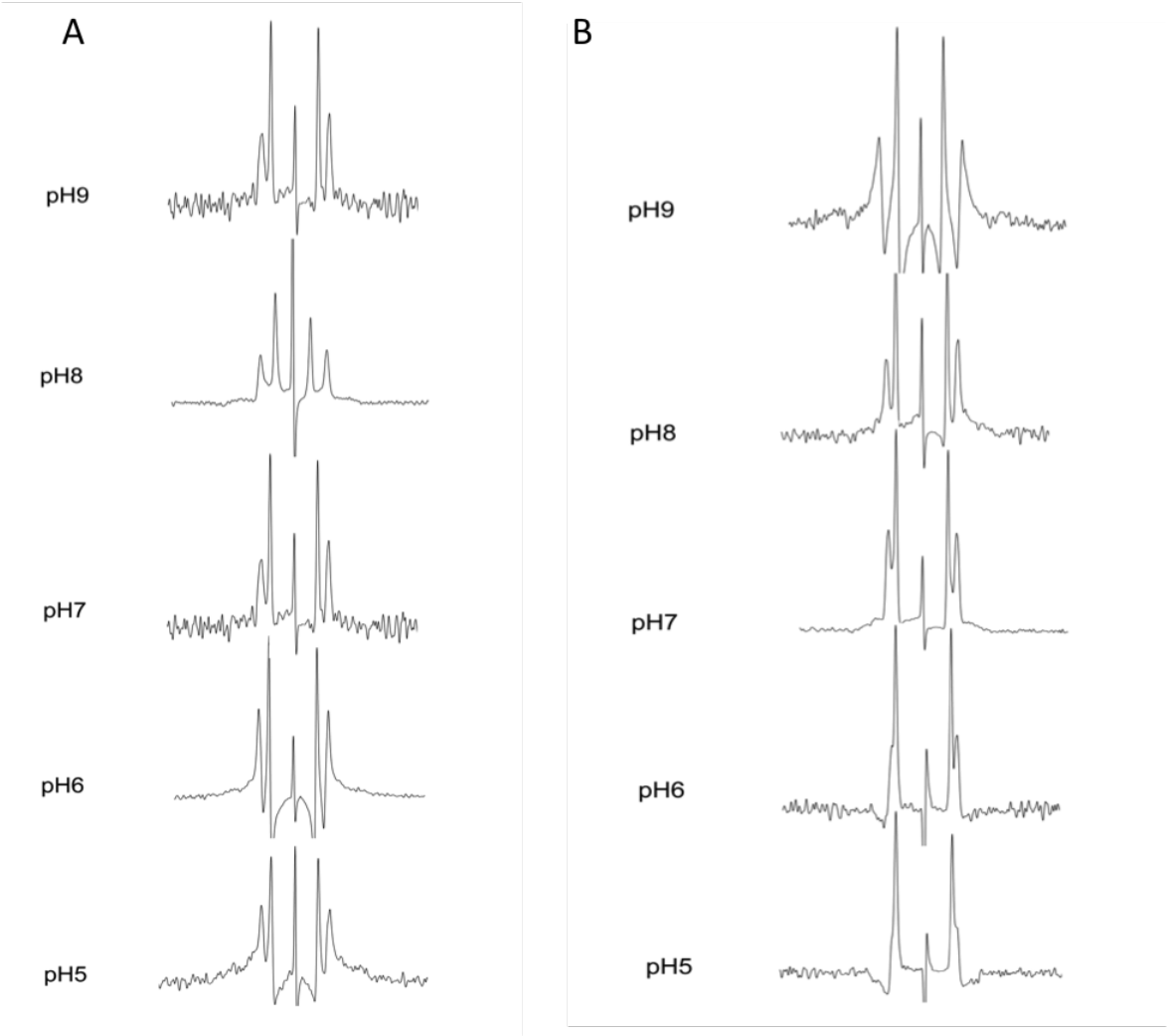

Figure 5.5: ^{2}H-NMR spectra of headgroup deuterated DOPC in a DOPC:POPE (4:1, wt:wt) membrane are shown at different pH levels in absence (A) and presence (B) of 150 μM *N*N-DNJ. The following buffer conditions were used: 10 mM acetate (pH 5), 10 mM potassium phosphate (pH 6), 20 mM HEPES (pH 7), 20 mM HEPES (pH 8), 10 mM Bicine (pH 9). Spectra are only shown for single integer pH level, whereas half integer steps were chosen. Note that the negative central intensity is most likely an artefact due the dePaking procedure.

ionisation state of the iminosugar and thus can be directly related to the pK_a of *N*N-DNJ. The $\Delta\nu_Q$s of the β and the α positions suggest an estimated pK_a of 6.3 of the ionisable nitrogen in *N*N-DNJ (Figure 5.6). Both labelled positions are affected concomitantly, which indicates that the spectral changes are consistent, and show that iminosugars have a marked effect over the headgroup region of the lipid. Nevertheless, a change in the ionisation state could also have an effect on the partitioning constant of *N*N-DNJ, which in turn could affect headgroup orientation and thus the measured pK_a. In such a scenario the observed changes might be a combination of changes in the iminosugar localisation and changes in the overall carried charge.

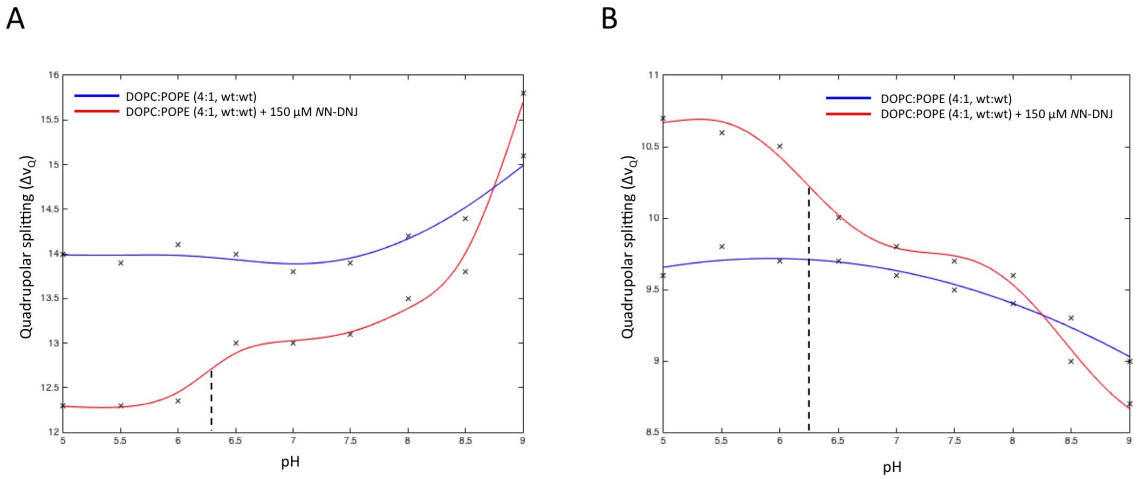

Figure 5.6: The absolute quadrupolar splittings at different pH levels in the absence (blue) and presence (red) of 150 μM *N*N-DNJ. The quadrupolar response of the α position is shown in part (A) and for the β position in part (B). The approximate position of the pK_a of *N*N-DNJ is illustrated by a black dashed line.

The pK_a value of 6.3 for *N*N-DNJ is in good agreement with the pK_a of the related *N*B-DNJ of 6.6, which was determined by a pH titration in solution (solution NMR analysis; [349]). This agreement suggests that the ionisable group of the *N*N-DNJ remains relatively unaffected by the electrostatic environment of the interface region of the bilayer.

5.3 Discussion

The reported results (Figure 5.5 and 5.6) illustrate a drug-membrane interaction of *N*N-DNJ in the membrane interface region. This is most probably facilitated by an electrostatic interaction between the headgroup moiety of *N*N-DNJ and the lipid headgroups, whereas the long-alkyl chain is probably projecting towards the hydrophobic membrane core. The protonatable nitrogen in the *N*N-DNJ head moiety changes its ionisation state, despite being in a membrane environment, and this change in the local electric environment is reported in a non-perturbing way by the quadrupolar splittings (Figure 5.5). The deposition of a positive charge at the membrane most likely results in a reorientation of the headgroup itself as described by the "Choline-tilt" model. Additionally, the presence of *N*N-DNJ can have a potential impact on phases and membrane dynamics. Similar effects have been observed for salicylic acid, an anti-inflammatory drug, that localises at the glycerol moiety causing

increased headgroup dynamics [350; 351]. Similarly doxorubicin, an anti-cancer drug , affects the micro-fluidity of membranes [352]. Nevertheless, here the overall partition constant of *N*N-DNJ to the bilayer and the local concentration at the bilayer remain elusive. Similar non-perturbing characterisation of the ionisation state of tetracaine in a membrane environment was reported in the literature, and similar to *N*N-DNJ, the pK_a of portioned drug was in a similar range for tetracaine in solution [339; 340].

It should be noted that other methods for determining accurate pK_a values exist. Instead of the static solid-state NMR approach presented here MAS methods employing ^{31}P and ^{14}N have been proposed to monitor changes to the surface charge upon peptide or drug interaction. This method directly probes the negatively charged phosphate group and the positive moiety of the choline group, thus presenting an attractive noninvasive solid-state NMR method on naturally abundant nuclei [353]. This method also allows for approximation of the net surface potential using isotropic chemical shifts whereas orientational changes of the headgroup are reported by the anisotropic CSA of ^{31}P and the quadrupolar moment of ^{14}N. Further to this pK_a values can be effectively measured using solution NMR by monitoring chemical shift changes in solution or for a membrane interacting compound ROESY experiments can be used to investigate the drug-lipid contacts [354; 355]. Computational methods also exist yet here it is more difficult to predict the effect of the bilayer environment on the pK_a, however this becomes increasingly more successful in the combination with MD methodologies. Other methods for pK_a determination, depending on the characteristics of the compound of interest, include fluorometry, chromatography, potentiometry and spectrometry like UV. Yet the here presented method yields information on the pK_a in a native-like bilayer environment.

*N*N-DNJ has been proposed to inhibit p7 channel function by breaking the oligomeric form apart into individual monomers ([137]; personal communication with N Zitzmann). Additionally p7 function has been reported to be sensitive to the membrane environment [72]. Thus, this raises the question as to whether a *N*N-DNJ-membrane interaction leads to changes in the bilayer environment as a whole and whether this is a plausible explanation for an altered p7 behaviour in the presence of *N*N-DNJ. Consideration of the *N*N-DNJ-membrane interaction is important when investigating potential drug binding sites located at the protein. Since the iminosugar is localised at the membrane interface, any first contact with p7 will most likely be also in this region of the bilayer, if mediated by the iminosugar headgroup.

Initial docking studies on monomeric p7 model located *N*N-DNJ at what would be expected to be the protomer interface at residue 25. This is expected to be towards the end of TM1, yet probably still partially buried in the hydrophobic membrane core. However these studies were done *in silico* and in the absence of a membrane [137]. Further to this, chemical shift changes are reported primarily of the p7 termini upon *N*N-DNJ interaction, which strengthens this hypothesis [87]. Other membranes apart from the ER membrane, where p7 primarily resides, are equally important consideration for potential drug-membrane interactions, which might affect the overall cytotoxicity of the drug to the cellular environment.

This study illustrates the importance of the lipid environment for drug development. This is an area that is often overlooked by drug development programmes, yet a bilayer can interact with small molecules and possible morphological changes can affect function of embedded proteins. This is also an important consideration for to the toxicological profile.

6

PISEMA studies of p7 topology

Contents

6.1 Introduction 155
6.1.1 Detergent- and solvent-based p7 structures in literature 155
6.1.2 Oriented systems for solid-state NMR 158
6.1.3 PISEMA 159
6.2 Results 161
6.2.1 Expression and uniform ^{15}N labelling of p7 161
6.2.2 Reconstitution of p7 164
6.2.3 Membrane alignment for oriented solid-state NMR 165
6.2.4 Oriented solid-state NMR of p7 167
6.3 Discussion 174

6.1 Introduction

6.1.1 Detergent- and solvent-based p7 structures in literature

As outlined in section 5.1, p7 has been recognised as a potential drug target, however only limited structural information is available, especially in a membrane environment. Most structural studies of p7 to date are solution NMR or EM based in a detergent or solvent environment. Most of the structures share the same topology: a hairpin conformation with two predicted trans-membrane helices (TM1 and TM2) that are connected by a short loop

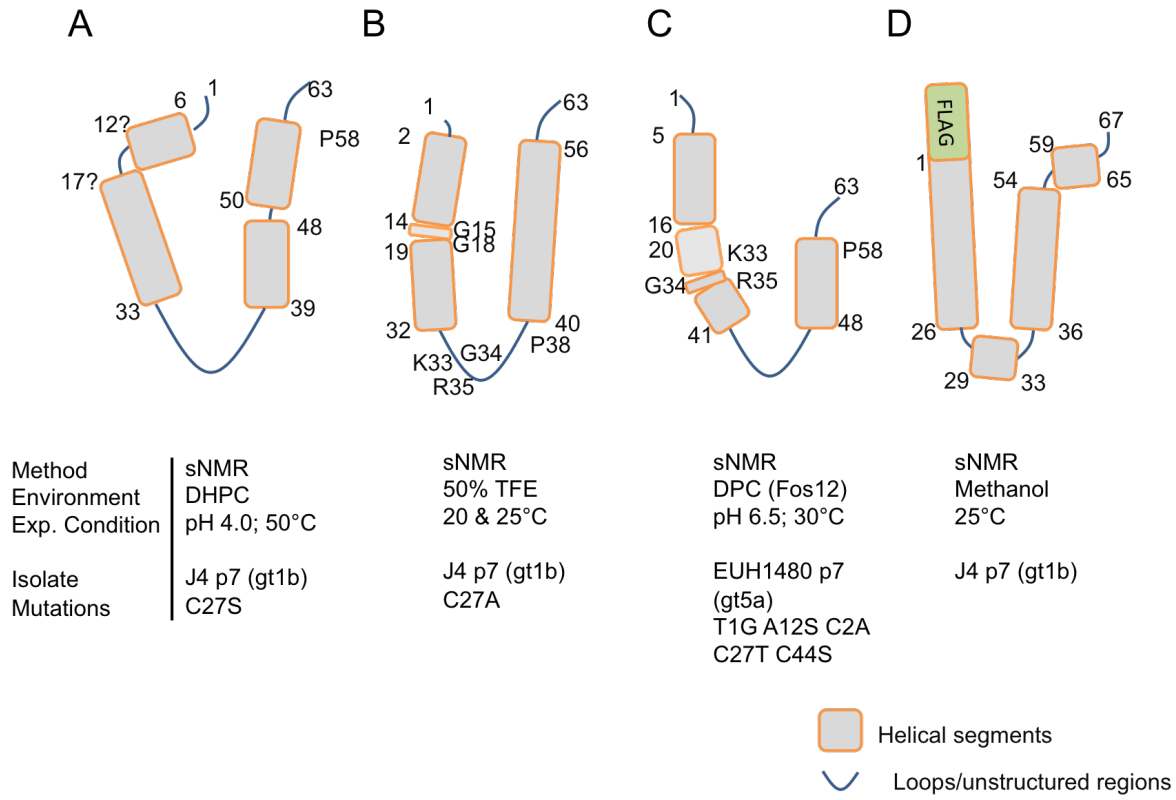

Figure 6.1: Structural schematics of different proposed p7 structures. The genotype and specific mutations are listed under each representation. The specific experimental environment and technique are also included, where sNMR is solution NMR and ssNMR is solid-state NMR. (A) Monomeric p7 in detergent [87]; (B) Monomeric p7 in 50% TFE [74]; (C) Hexameric p7 in detergent, where the topology of one individual monomer is illustrated [66]; Flag-tagged monomeric p7 in methanol [139]. Note that an additional solution NMR (hair-pin) structure has previously been reported by GA Cook *et al.* including solid-state NMR constraints in bicelles [356]

region, with some models predicting kinks in the transmembrane segments (Figure 6.1). Both termini are expected to face the ER lumen [73; 357].

Initial studies suggested that p7 exists as hexameric or heptameric oligomers. These studies were based on cross-linking FLAG-tagged p7 as well as TEM (Gt1b) [68; 70]. Similar observations were made from sedimentation studies in detergent, which predicted the oligomeric p7 state to be 6 +/- 1 for chemically synthesised p7 from HCV-J (GT1b, isolate J4) [74]. Luik *et al* 2009 published the first three dimensional structure at 16 Å resolution based around transmission electron microscopy (TEM) analysis of synthesised full-length p7 (Gt2a, isolate JFH) in 1, 2-diheptanoyl-sn-glycero-3-phosphocholine (DHPC) micelles [73]. Here, hexameric p7 adopts an "open flower"-like shape with the termini constituting what would be the "petals" of the flower, confirmed by immuno-gold labelling.

Several high resolution monomeric p7 structures, based on solution NMR studies in membrane mimetics, have been published. First, Monserret *et al.* 2010 confirmed secondary structural elements in 50% tetrafluoroethylene (TFE)/H_2O mixtures (Figure 6.1 B), which were modelled to a hairpin conformation based on previous data indicating that both termini face the ER lumen [357]. Foster *et al.* 2014 solved a three dimensional Flag-tagged p7 structure in methanol (Figure 6.1 D), with a similar hairpin structure observed containing an additional short helical element in the TM1 and TM2 connecting loop region; Long-range Nuclear Overhauser effects (NOEs) were observed confirming a hairpin topology in methanol [139]. More convincingly, Cook *et al.* 2013 solved a monomeric structure in DHPC micelles. Furthermore Cook *et al.* 2011 describe angular constraints based on solid-state NMR in oriented 14-0-PC/16-0-PC (14:0 Diether PC/16:0 Diether PC) bicelles, illustrating two transmembrane helical tilts of 10° and 25° relative to the bilayer normal [356; 358]. The solution NMR structure of Gt1b (J4) by Cook *et al.* 2013 shows an N-terminal helical domain that is predicted to interact with the membrane interface region and is oriented nearly parallel to the bilayer plane. However, this could be an effect of the α-helical clustering within the micelle to prevent exposure to the aqueous environment [87]. Additionally, an unpublished solid-state NMR structure in DMPC bilayers shows this N-terminal domain in an extended conformation [359]. All monomeric structures report a general hairpin-like conformation for monomeric p7. Interestingly, the only high-resolution oligomeric structure reported by Ouyang *et al* 2013, on Gt5a (EUH1480) in Fos-choline-12 (DPC) micelles, assumed to be hexameric based on complementary EM experiments, and describes a strikingly different monomer confirmation [66]. The individual protomers are shown to open up in an unusual way, interacting with the neighbouring i+1, i+2 and i+3 monomers in an entangled mode (Figure 6.1 C). This structure contains three main helical domains compared to the mainly two helical segments conserved in two transmembrane helices in the "hairpin-like" monomeric structures. The loop region separating the two transmembrane domains in a hairpin conformation is no longer present as such.

Care should be taken when analysing published p7 structures, as the environment can greatly impact membrane protein structure [360]. The often used solvent mixture of 50% TFE and H_2O is known to stabilise α-helical secondary structure [359]. Similarly, micelles can reorient transmembrane helices in order to maintain them in the hydrophobic environment.

This has been recently observed for p7, which shows its N-terminal domain bending inwards closing the hairpin in DHPC micelles whereas it is extended in DMPC membranes [87; 359]. Molecular dynamics simulations predicted this helix to interact with the headgroup region in a bilayer and thus this domain might be sensitive to bilayer thickness [74; 361]. The hexameric p7 Gt5a conformation (B OuYang *et al.* 2013) of p7 solved in DPC micelles has 18 arginine residues exposed to what would be predicted as the hydrophobic membrane core, whilst this might be favourable in a micelle, it would result in a large thermodynamic cost in membrane environment [66; 360]. In agreement with this, the structure was confirmed as only partially stable in a membrane environment by MD simulation [362; 363].

A atomistic three dimensional understanding of p7 structure in a native-like environment is essential for the description of protein function. p7 is a minimalistic yet highly complicated protein as illustrated by the many different structures reported to date. Protein solubilisation in detergent mainly results in monomeric p7 apart from one study that reported a hexameric channel [66], thus this emphasises the need to understand p7 structure in a bilayer, that allows for dynamic protein behaviour and oligomerisation. In this chapter relative transmembrane helix tilts are investigated in a model system resembling the ER membrane (DOPC:POPE (4:1), wt:wt) and in which p7 ion channel activity was previously confirmed [72].

6.1.2 Oriented systems for solid-state NMR

The helical tilt in oriented planar bilayers can be investigated by oriented solid-state NMR. Sample homogeneity is essential in order to resolve angular restraints in oriented NMR. Different methodologies have been proposed to achieve an aligned sample in a magnetic field. Bicelles and macrodiscs (ca. 30 nm diameter) have been shown to spontaneously align in large magnetic fields [364; 365]. Potential drawbacks are the presence of short acyl chain lipids in bicelles and the membrane scaffold protein in macrodiscs that potentially can interact and affect the protein of interest. Here, bilayers mechanically aligned between microscope glass slides are used. Controlled rehydration of dry lipid films deposited on glass slides results in the spontaneous formation of macroscopically oriented bilayers [366], where the bilayer normal and the normal of the glass slides are aligned. Mechanically aligned samples have the advantage that highly ordered membranes can be achieved with order parameters

close to one (representing a total relative membrane alignment with respect to each other). On the other hand, uniform sample hydration during the normally relatively long NMR measurement times (up to 10 days) can be a problem for mechanically oriented samples, especially under high power rf irradiation. Further to this, bicelles tend to have a higher sample stability (up to one year in a sealed sample tube) however the lipid species suitable for bicelle preparation are somewhat limited [364]. In the following results mechanically aligned bilayers between microscope cover slides, allowing for the use of multiple lipid species, were used to resolve structural constraints of p7 in DOPC:POPE (4:1, wt:wt) using PISEMA (*Polarization Inversion Spin Exchange at the Magic Angle*).

6.1.3 PISEMA

PISEMA, is a 2D solid-state NMR experiment that correlates the dipolar coupling to the chemical shift anisotropy in oriented samples. This gives rise to distinct orientation-dependent spectral patterns, which are called *Polar Index Slant Angle* (PISA) - wheels (Figure 6.2). Depending on spectral resolution and resonance overlap, distinct residues can be assigned or alternatively PISA wheels can be used to report more generally on α-helix orientation within a membrane and secondary structural elements. This orientational dependency makes PISEMA a powerful solid-state NMR technique that allows for structural characterisation of membrane proteins.

In the basic PISEMA pulse sequence an initial CP is followed by a 35.3^{o} pulse to flip the effective field to the magic angle (Figure 6.3 A). This is followed by the SEMA train consisting of a frequency-switched Lee-Goldburg sequence on the abundant high $\gamma - I$ spin under Hartmann-Hahn conditions. The frequency of the Lee-Goldburg decoupling is switched by 2π rotations (Figure 6.3 B), which improves the decoupling procedure [367]. The SEMA pulse train allows for magnetisation transfer between the I and S spin and decouples the homonuclear proton interaction resulting in narrow line widths [368]. PISEMA has a comparably large scaling factor of 0.82 of the heteronuclear dipolar couplings compared to other methods [367; 368].

One drawback of the common PISEMA pulse sequence is the dependency on the ^{1}H offset [370]. The exact field direction during the frequency switched Lee-Goldburg pulse sequence is dependent on the proton offset and hence this has an effect on the rate of spin exchange, the

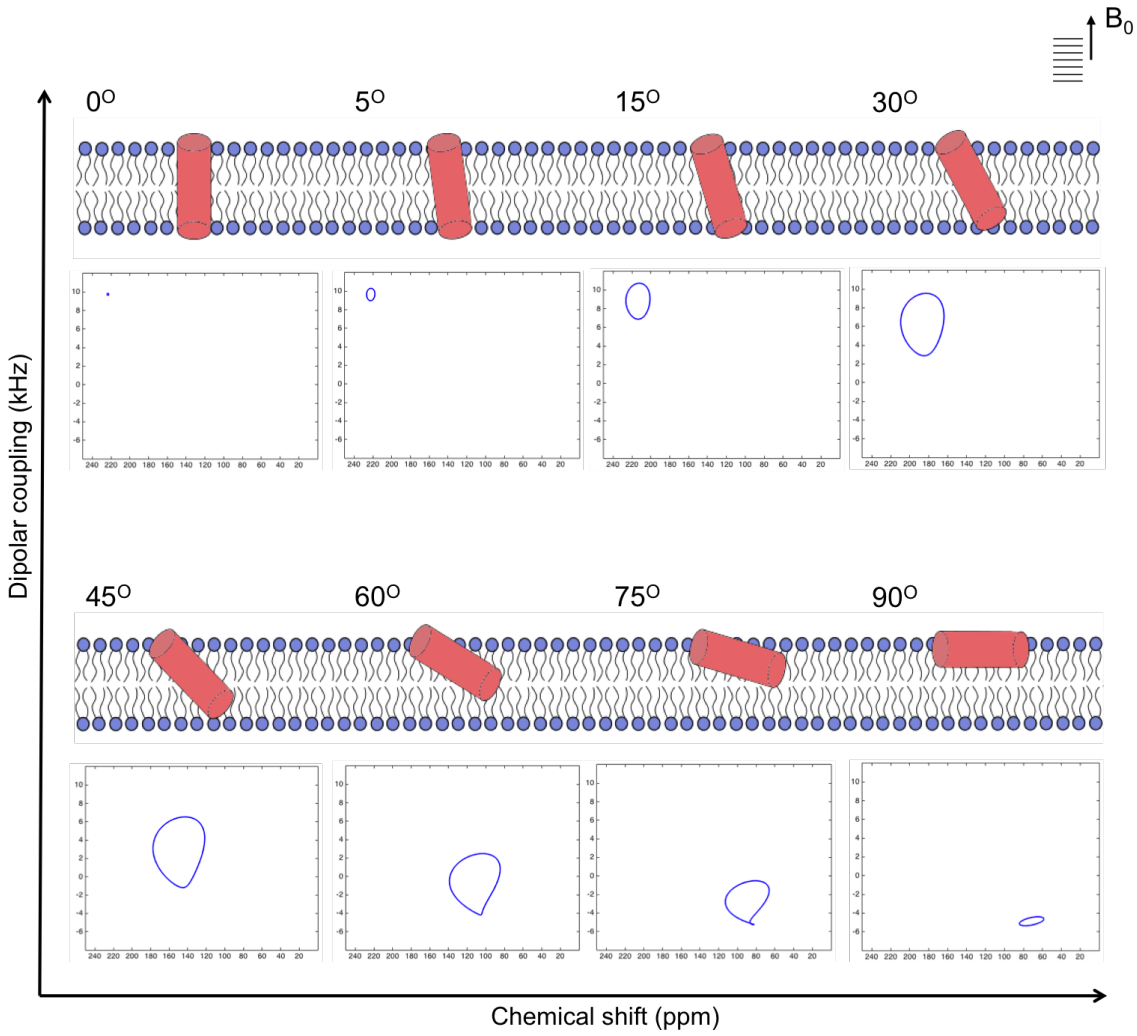

Figure 6.2: The characteristic PISA wheels describing the relative helix orientation in a bilayer are shown ranging from 0° to 90°. The PISA wheels were simulated using a Matlab script made available by Rick Page: https://sites.google.com/site/rickcpage/Home/biomolecular-nmr

scaling factor and the efficiency of ^{1}H-^{1}H decoupling [370]. Potential solutions to overcome the proton offset effects are to use high-power rf pulses, which are often demanding to the spectrometer. More recently alternative pulse programs have been proposed, that are similarly built around the SEMA pulse train, but are shown to be more robust with respect to proton offset effects. Examples are the SAMMY and 2_4-SEMA experiments [369; 371]. In this thesis a pulse sequence is used that is built around the previously reported 2_4-SEMA experiment [369], which cycles the magnetisation through all four quadrants (compared to only two for PISEMA), leading to cancelation of the proton offset and a more robust experiment.

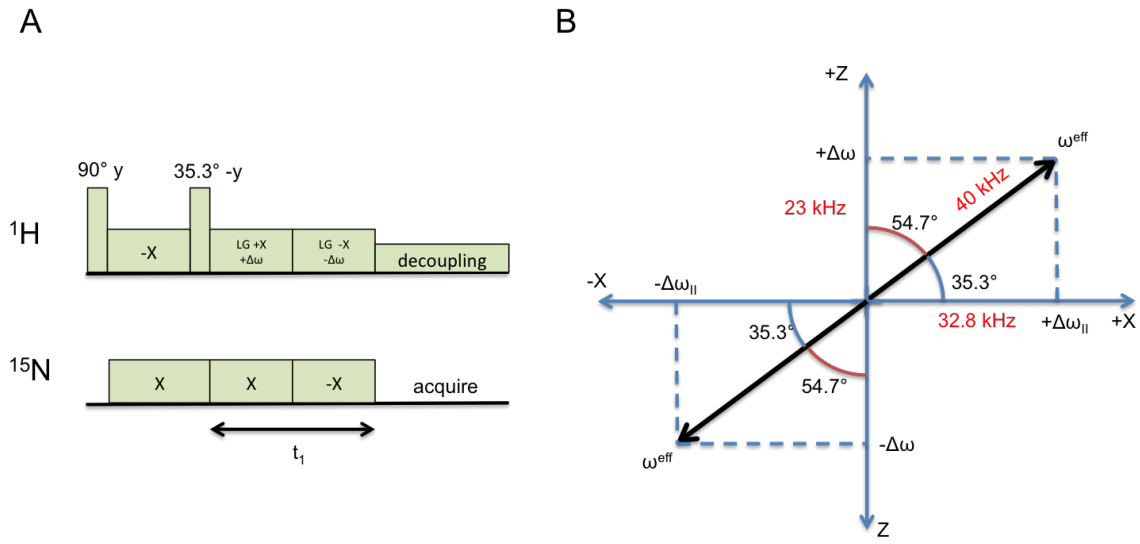

Figure 6.3: (A) The basic PISEMA pulse sequence is illustrated [368]. (B) The magnetisation orientation in the rotary frame is illustrated using the example of an frequency offset of 23 kHz and an effective field of 40 kHz. ω_{eff} is the effective field, $+\Delta_\omega$ and $-\Delta_\omega$ are the frequency offsets. Figure adapted from [369].

6.2 Results

6.2.1 Expression and uniform ^{15}N labelling of p7

HCV p7, from genotype 1b, isolate J4 with mutation C27S was expressed in *E. coli* (BL21 (DE3) pLysS) as a fusion construct fused to TrpΔLE and purified as previously described by G Cook *et al.* 2011 (summarised in Figure 6.4 [372]). The C27S mutation made by Cook *et al.* 2011 was retained to avoid disulphide bridge formation during the purification process. The process is summarised in Figure 6.4. In brief, the cloned plasmid (pMM-LR6; a gift from S Blacklow, Harvard Medical School, Boston, provided by J Schnell, Oxford) was transformed into chemically competent BL21 (DE3) pLysS cells. The transformed cells were grown from a single colony to OD_{600} of ~0.6 - 0.9 in Terrific Broth (TB) Media and induced with a final IPTG concentration of 1 mM. For uniformly ^{15}N labelling, cell cultures were grown to an OD_{600} of ca. 0.6, following which the cells were harvested by centrifugation, washed in M9 salt solution, condensed four fold and resuspended in M9 media. The cells were allowed to requilibrate in M9 media prior to induction of protein expression. Using this method final OD_{600} of up to 3.5 - 4 were achieved. Expression lasted for 12-18 h at 37 °C.

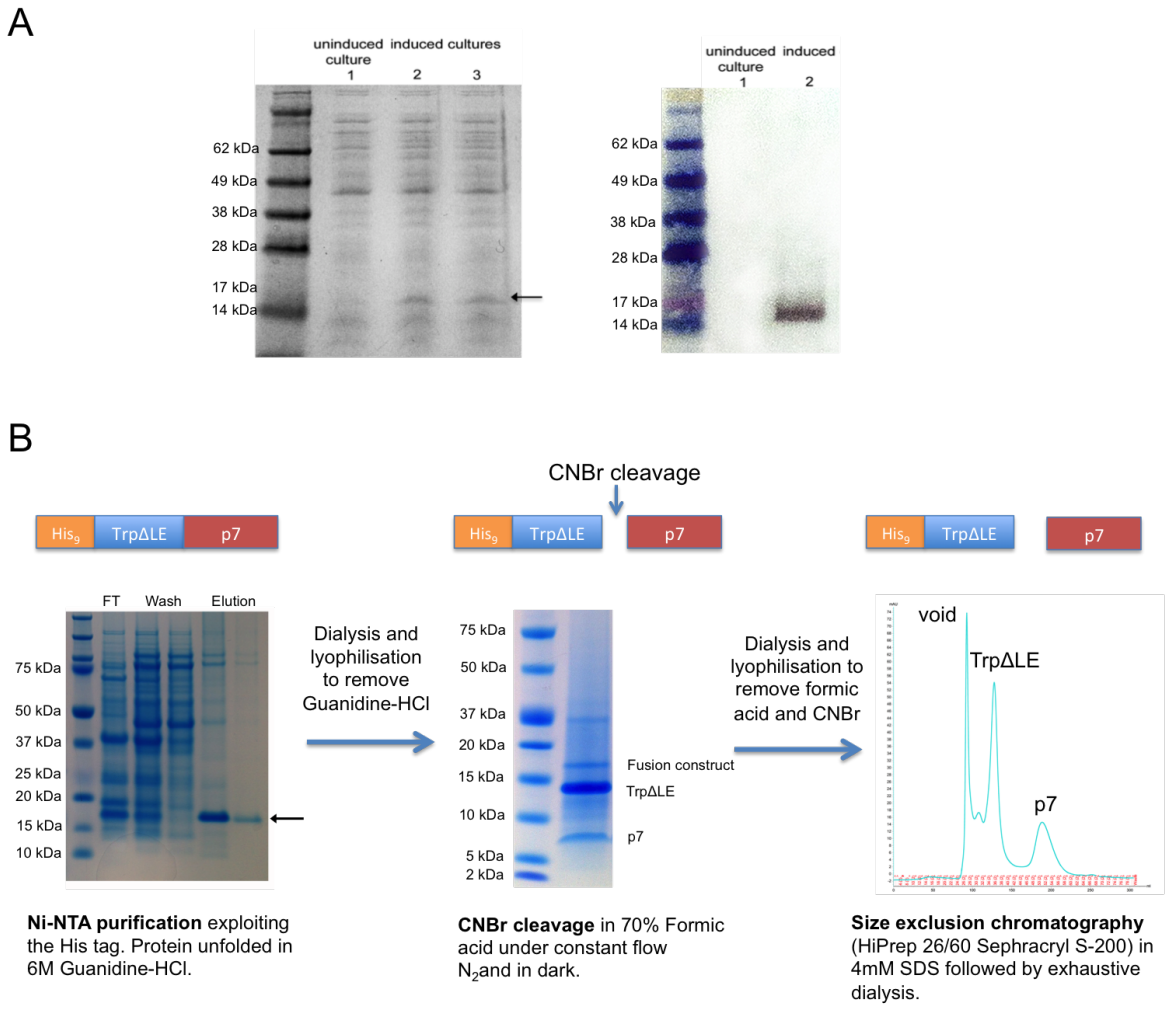

Figure 6.4: The expression and purification of p7 is summarised. (A) Left: SDS-PAGE showing successful expression of p7 in BL21 (DE3) pLysS (Coomassie blue stain). Lane 1: prior to IPTG-induction; Lane 2 and 3 are post induction (12 h) for two separate cultures. Both show an expression band running between 14 kDa and 17 kDa illustrated by a black arrow. Right: Western plot using a generic anti-His antibody to verify expression. (B) A summary of the purification. (I) SDS-PAGE illustrating the nickel affinity chromatography purification, showing samples of the flow-through, washing steps and two subsequent elution steps (500mM imidazole). The eluted fusion protein is indicated by a black arrow. (II) SDS-PAGE illustrating the cleavage off the fusion protein by CNBr. (III) Elution profile of the size exclusion chromatography after the CNBr cleavage.

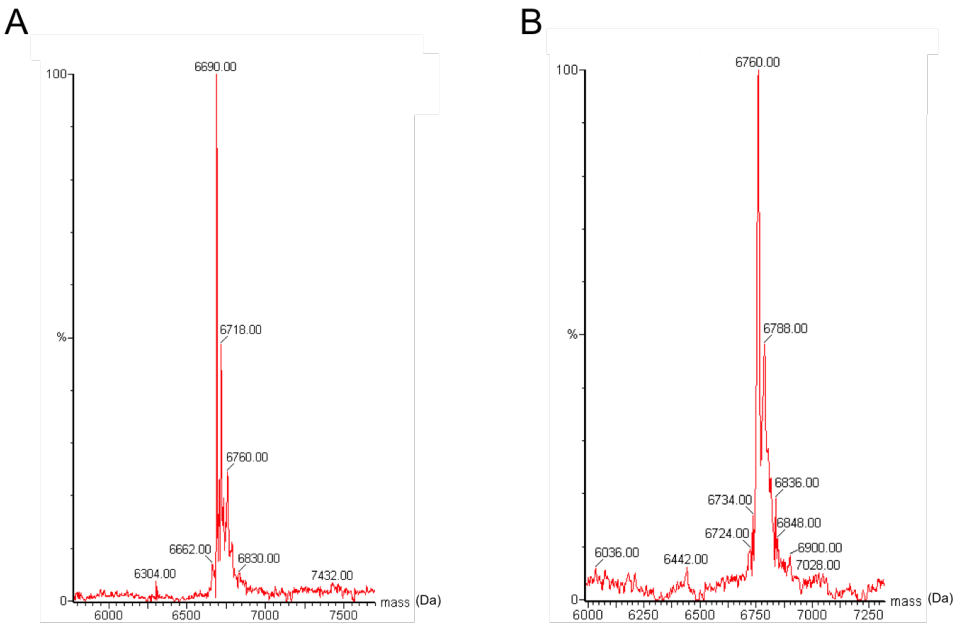

Figure 6.5: Purity and uniform ^{15}N labelling are evaluated by electron ionisation (EI) mass spectrometry. (A) Unlabelled p7 J4 C27S with an expected mass of 6690 Da (B) Uniformly ^{15}N labelled p7 J4 C27S with an expected mass of 6766 Da.

Cell pellets were resuspended in buffer, lysed by sonication and membrane fractions were removed by solubilisation in IGEPAL CA-630 and sonication. The inclusion bodies were isolated by centrifugation and solubilised and sonicated in 6 M Guanidine hydrochloride for unfolding and purification by Nickel affinity chromatography. The bound inclusion bodies were eluted at a final imidazole concentration of 500 mM (Figure 6.4 C). The purified inclusion bodies were dialysed extensively against H_2O to remove Guanidine hydrochloride followed by lyophilisation. The single methionine residue separating p7 and TrpΔLE was used for cleavage by cyanogen bromide in 70% formic acid, afterwards removed by extensive dialysis followed by lyophilisation. p7 was isolated from TrpΔLE using Fast Protein Liquid Chromatography (FPLC) on a Sephacryl column (HiPrep 26/60 Sephacryl S-200, GE Healthcare, www.gelifesciences.com) in the presence of 4 mM SDS (Figure 6.4 D, E). Protein purity was checked by EI mass spectrometry (Figure 6.5).

^{15}N labelling efficiency and purity was checked by EI-MS giving a mass of 6760 slightly below the expected 6766 for uniformly labelled p7, nonetheless with an avarage labelling efficiency of >90%, which is high enough for solid-state NMR evaluating the global helical orientations in a bilayer.

6.2.2 Reconstitution of p7

The protein was reconstituted into vesicles of DOPC:POPE (4:1, wt:wt) by a rapid dilution procedure prior to mechanical membrane alignment. Both lipid constituents and the protein were equally taken up in Cyclofos-6 (27 mM) and mixed. This is followed by a rapid dilution process into detergent-free buffer [373; 374]. The dilution (ca. 25 fold) below the critical micelle concentration (CMC) results in rapid release of lipids and proteins from micelles and leads to spontaneous formation of bilayers (Figure 6.6 A). The CMC of cyclofos-6 is 2.68 mM and thus this dilution process leads to a final detergent concentration 15 fold below its CMC, although detergent removal is incomplete. The residual detergent present after dilution is removed by dialysis and the proteoliposomes are retained by concentration across a 10 kDa membrane. A sucrose gradient was performed to confirm a homogenous membrane density represented by a single band in the gradient (Figure 6.6 B); the lipid was doped with 0.4% rhadamine-PE to easily visualize the proteoliposomes in the sucrose density gradient.

The relative affinities of detergent to lipids and proteins are an important consideration

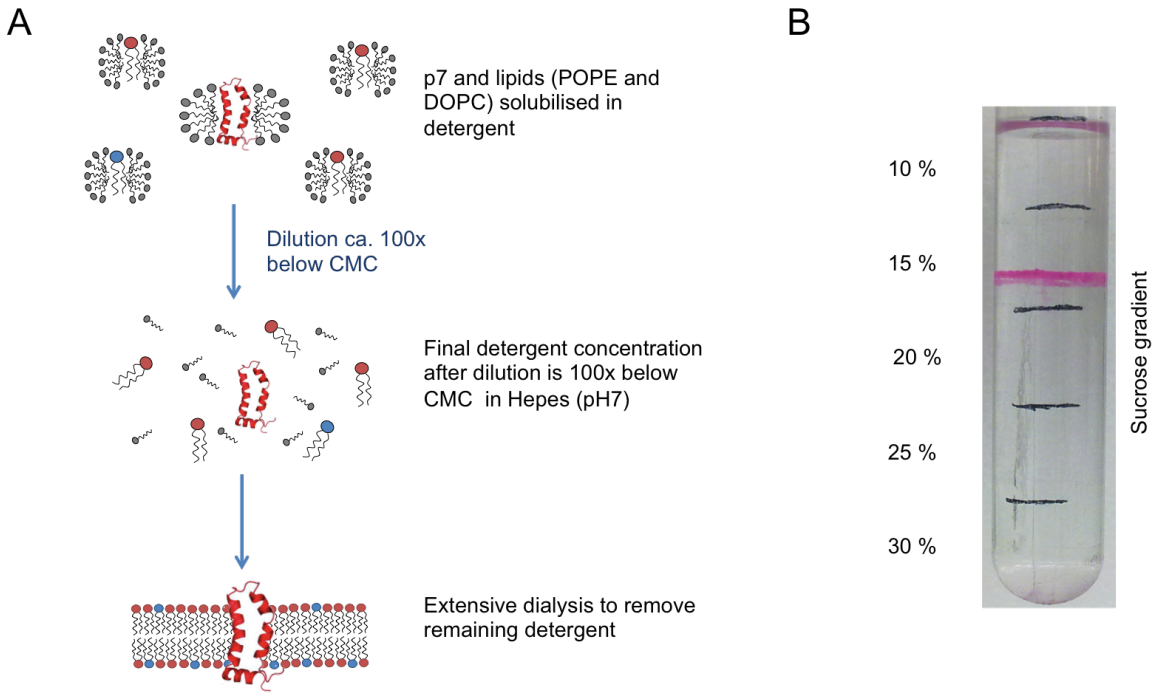

Figure 6.6: (A) A schematic illustrating membrane reconstitution by rapid dilution starting from detergent-solubilised lipid and protein. (B) Sucrose gradient illustrating a homogenous reconstitution post dilution, dialysis and proteoliposome recovery.

for homogenous reconstitution; if detergent binds more strongly to the protein compared to lipids, the temporally separated release of lipids and protein can result in the formation of empty liposomes. However, this would have been observed by a distinct band on the sucrose gradient at lower density [375]. Similarly this can lead to protein aggregation and thus the process is dependent on the nature of the detergent used. For p7, cyclofos-6 was previously used for solution NMR studies (B Oestringer *et al.*, unpublished), and was the first choice for successful membrane reconstitution.

6.2.3 Membrane alignment for oriented solid-state NMR

As a starting point, empty liposomes of DOPC:POPE (4:1, wt:wt) were mechanically oriented on glass slides to assess the formation of well aligned samples. In particular the favoured curvature induced by PE lipids and the different phase transitions of the two lipid species could be problematic (DOPC: -20°C and POPE: 25°C). For this reason reconstitution, rehydration and NMR experiments were all performed at 37 °C, well above the phase transition of both lipid species. The general methodology used for the preparation of aligned lipid samples is illustrated in figure 6.7 A, with a detailed schematic of the expected sample configuration shown in figure 6.7 B [366].

The vesicle dispersion is distributed across microscope glass slides at a lipid concentration of ca. 1.5 - 2 lmg/cm^2, which is followed by drying at room temperature and afterwards under vacuum for ca. 12 h to remove any remaining water. The sample is then rehydrated in a hydration chamber containing a supersaturated salt solution (here K_2SO_4 giving rise to 96% relative humidity at 37 °C) and the hydrated membranes are stacked on top of each other. This is followed by additional hydration and membrane alignment is confirmed using ^{31}P-NMR (Figure 6.7 C). The final samples show a clear transparent membrane, indicative of well hydrated samples; typically an overall hydration of 40 - 50% is achieved [366]. It was found that repeated dehydration and rehydration cycles leads to significantly improved sample alignment, as characterised by a reduced underlying powder and isotropic components. After several successive rehydration cycles good alignment was achieved (Figure 6.7 C, right panel), with two distinct resonances observed corresponding to the ^{31}P chemical shifts of PC and PE. Integration of the peaks resulted in a relative proportion of ca. 80:23 which agrees

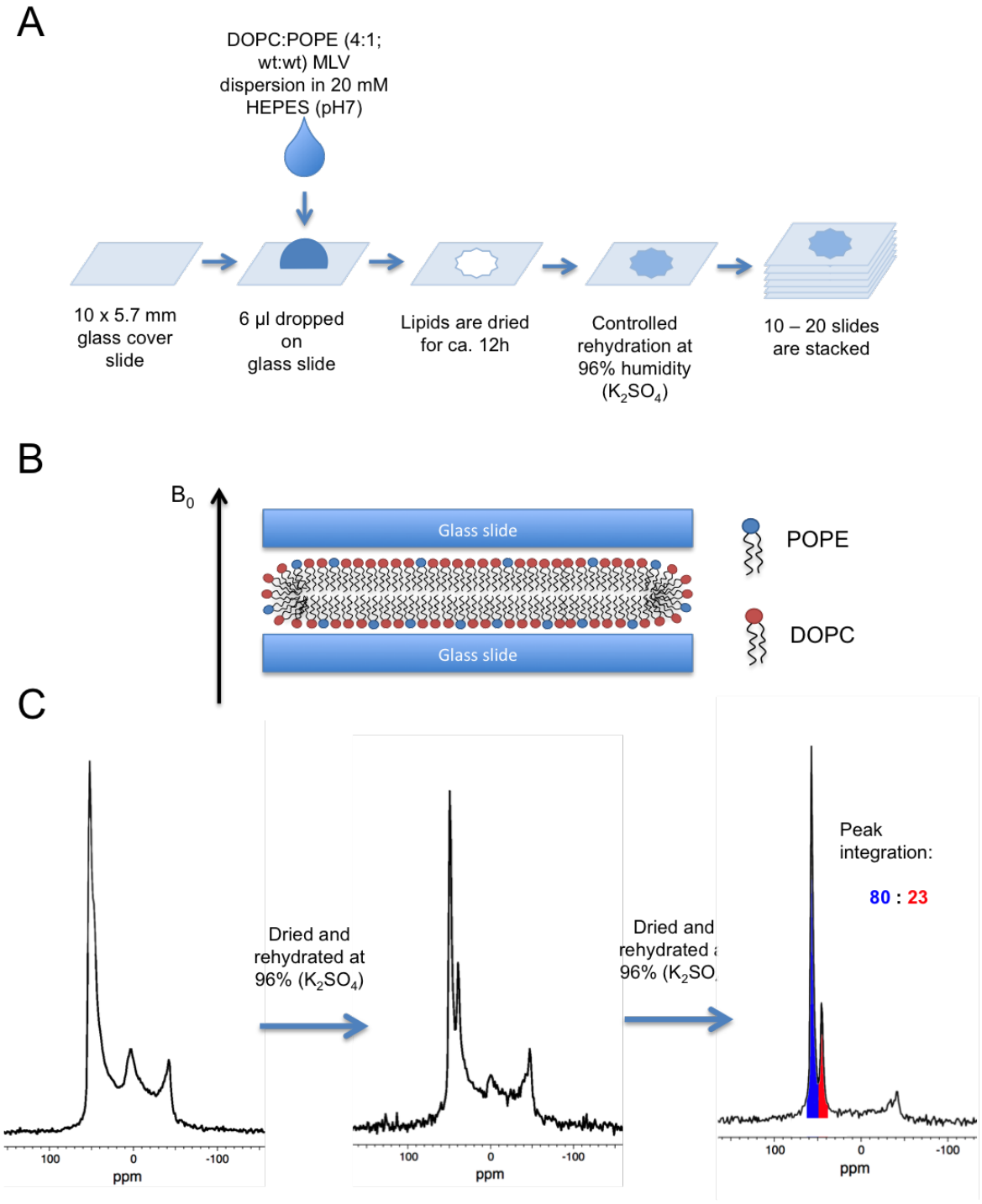

Figure 6.7: The sample preparation procedure and final allignment of pure DOPC:POPE (4:1, wt:wt) is illustrated. (A) Sample preparation procedure for alignemnt of reconstituted DOPC:POPE (4:1, wt:wt) on microscope cover slides is illustrated. (B) Microscopic sample configuration of an aligned sample is shown. Note that in practice many thousands of individual bilayers are stacked between glass slides. (C) ^{31}P NMR spectra of aligned DOPC:POPE (4:1, wt:wt) membranes recorded with the bilayer normal parallel to B_0 and at 800 MHz and 37 °C.

well with the expected 4:1 (wt:wt) ratio that translates to a 3.65:1 molar ratio. The small underlying powder component, visible at negative ppm resonances, is most likely due to lipid curvature at the bilayer edges that leads to bridging between the two leaflets.

Overall, good lipid alignment was achieved for a two-component lipid system, resembling the ER membrane, and the negative curvature constraint caused by the small PE-headgroup seems not to be problematic for membrane alignment at least in the presence of excess PC. Pure DOPE was previously reported as non-bilayer forming [366].

6.2.4 Oriented solid-state NMR of p7

Reconstituted p7 in DOPC:POPE (4:1, wt:wt) at a peptide to lipid molar ratio of 1:100 was mechanically aligned as previously described (Figure 6.7). It was found that this worked relatively well for small-scale preparations, however limitations of the sample coil dimension and the inherent low sensitivity of ^{15}N resulted in larger lipid deposition on the microscope cover slides (up to 3 mg/cm^2), which might have impacted the overall alignment. Further to this, lipid-protein interactions can perturb the bilayer leading to less uniformly aligned membranes. Nevertheless, a large sample containing 35 mg of lipids was prepared with an overall lipid-sample alignment of ca. 42% (Figure 6.8); note that the lipid alignment

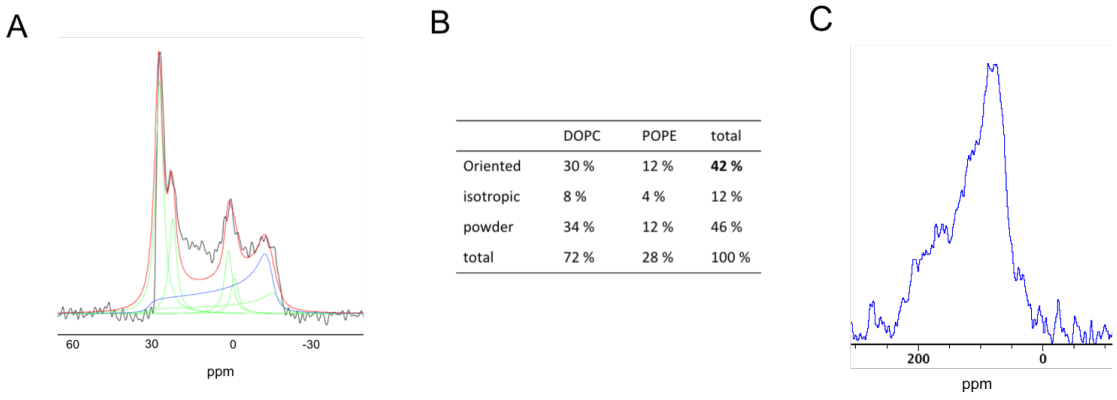

	DOPC	POPE	total
Oriented	30 %	12 %	**42 %**
isotropic	8 %	4 %	12 %
powder	34 %	12 %	46 %
total	72 %	28 %	100 %

Figure 6.8: One dimensional NMR spectra are shown in order to evaluate the global alignment in the sample. (A) The NMR spectrum together with its fitted components is shown. Two aligned lipid populations are seen, one corresponding to the DOPC component and the other to the POPE component. (B) The relative proportions of aligned, isotropic and powder components are summarised in a table. (C) The one dimensional ^{15}N CP acquisition of uniformly labelled p7. Note that all spectra shown are acquired of the same sample as used for the spectrum shown in Figure 6.9

does not necessarily correlate with overall protein alignment in the sample. Further to this some resonance could not be fully fitted to the simulated spectra and might be due to additional mosaic spread in the sample.

6.2.4.1 PISEMA

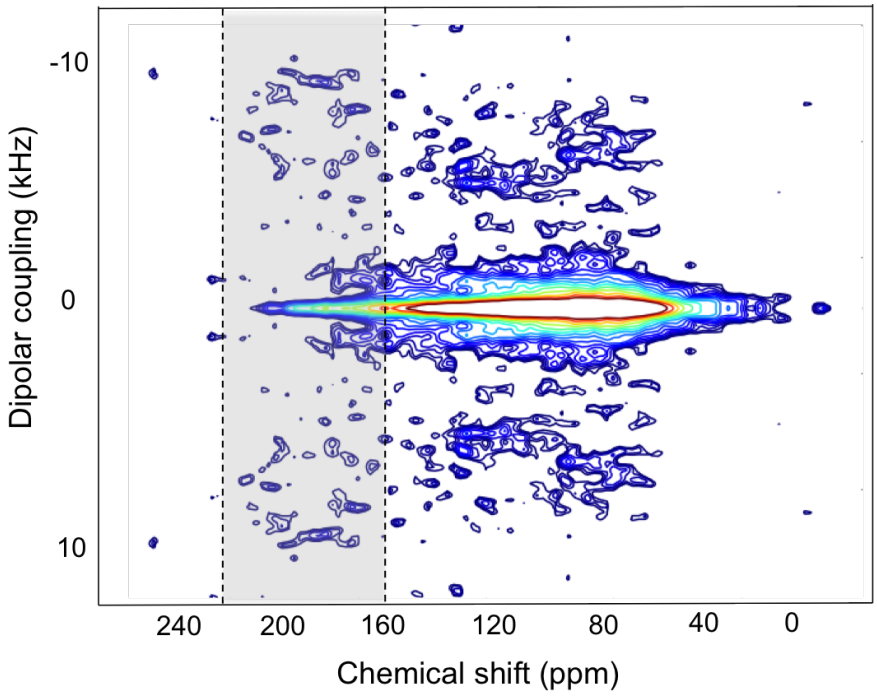

Figure 6.9: PISEMA spectrum of mechanically aligned p7 in DOPC:POPE (4:1, wt:wt). The area of expected PISA wheels for α-helical transmembrane domains is highlighted (shaded in grey). The spectrum was recorded at an effective ^{1}H field of 40 kHz (Figure 6.3 B), a temperature of 37 °C and a magnetic field strength of 750 MHz. The total acquisition time was 8 days. The spectrum is processed at a resolution of 512 x 512 points.

The standard PISEMA experiment was used for an initial characterisation of the uniformly ^{15}N-labelled p7 (Figure 6.9, [368]). Qualitatively, the spectrum is very noisy and has an underlying powder component in the shape of a characteristic butterfly, which may be caused by incomplete sample alignment or unordered loop regions. A large central resonance is seen close to 0 kHz, which is most probably caused by weak couplings to remote protons. Nevertheless, characteristic PISA wheel patterns are visible in the spectral "wing-region" between $\sim$ 160 and 220 ppm, that indicate α-helical transmembrane domains (Figure 6.9, highlighted in shaded grey). Overall the quality of the spectrum is comparably poor and the high underlying noise might be due to an inaccurately matched proton offset in addition to the

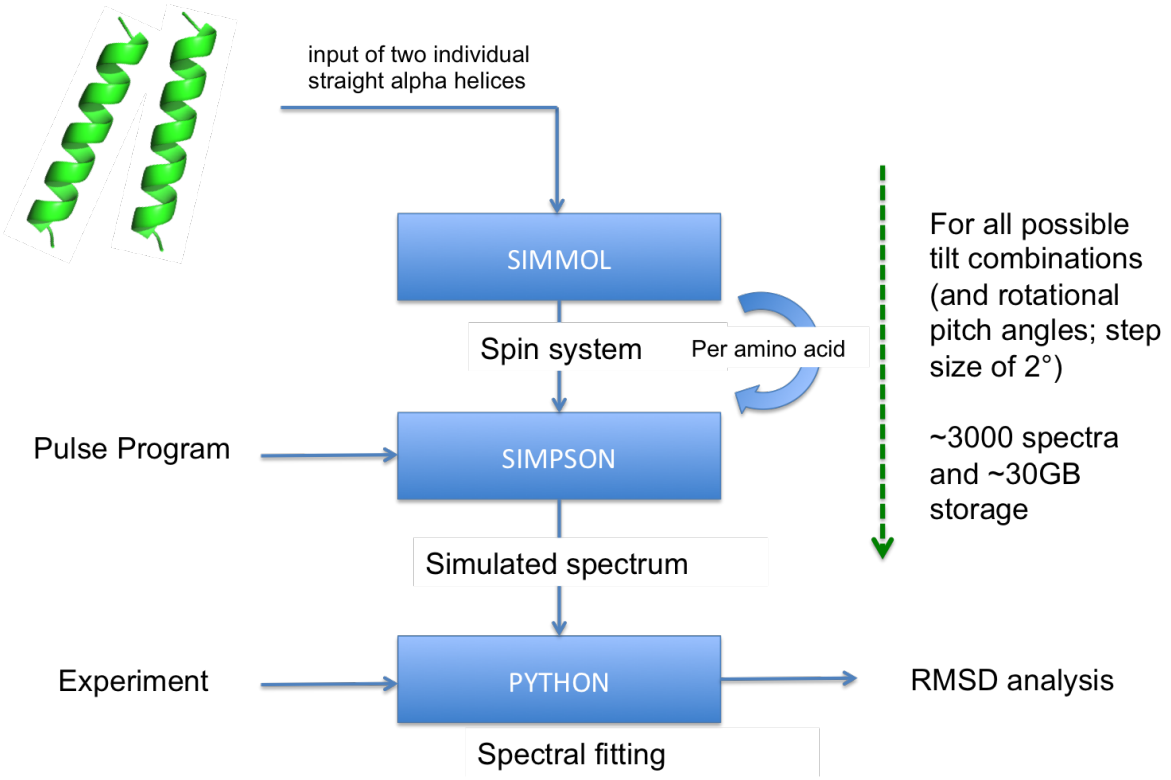

Figure 6.10: The overall applied analysis strategy for PISEMA is illustrated. The most simplistic hairpin model (two straight α-helices) was used as an initial starting point. SIMMOL was used to describe the spin system of both helices at each residue position individually. The PISEMA experiment was described by a pulse program for SIMPSON and the spectrum was simulated on a "per-amino-acid" basis. The individual spectra were added to yield an overall PISEMA spectrum, which was fitted to the experimental spectrum using a RMSD based python script. This was repeated for all possible combinations of relative helical tilt angles.

underlying powder component. The effective fields were measured using nutation experiments prior to PISEMA set-up in order to optimise for the proton offset (as described in [376]), however accurate determination of B_1 field strength remains difficult.

Despite a high noise level the spectral "wing-region" was isolated by post-experimental processing and simulated PISEMA spectra for two straight α-helices were fitted at a combination of different tilt angles relative to each other and relative to B_0 (see Figure 6.10 and 6.11; details on spectra simulation is given in section A.1.4). The alpha helices were generated considering only the backbone, each 30 amino acids long with phi (ϕ) and psi (ψ) taken to be -60° and -45° respectively. Based on previously determined monomeric p7 structures, the two transmembrane α-helices can be considered as the most simplistic model for a hairpin conformation. For spectral simulation SIMMOL and SIMPSON programs

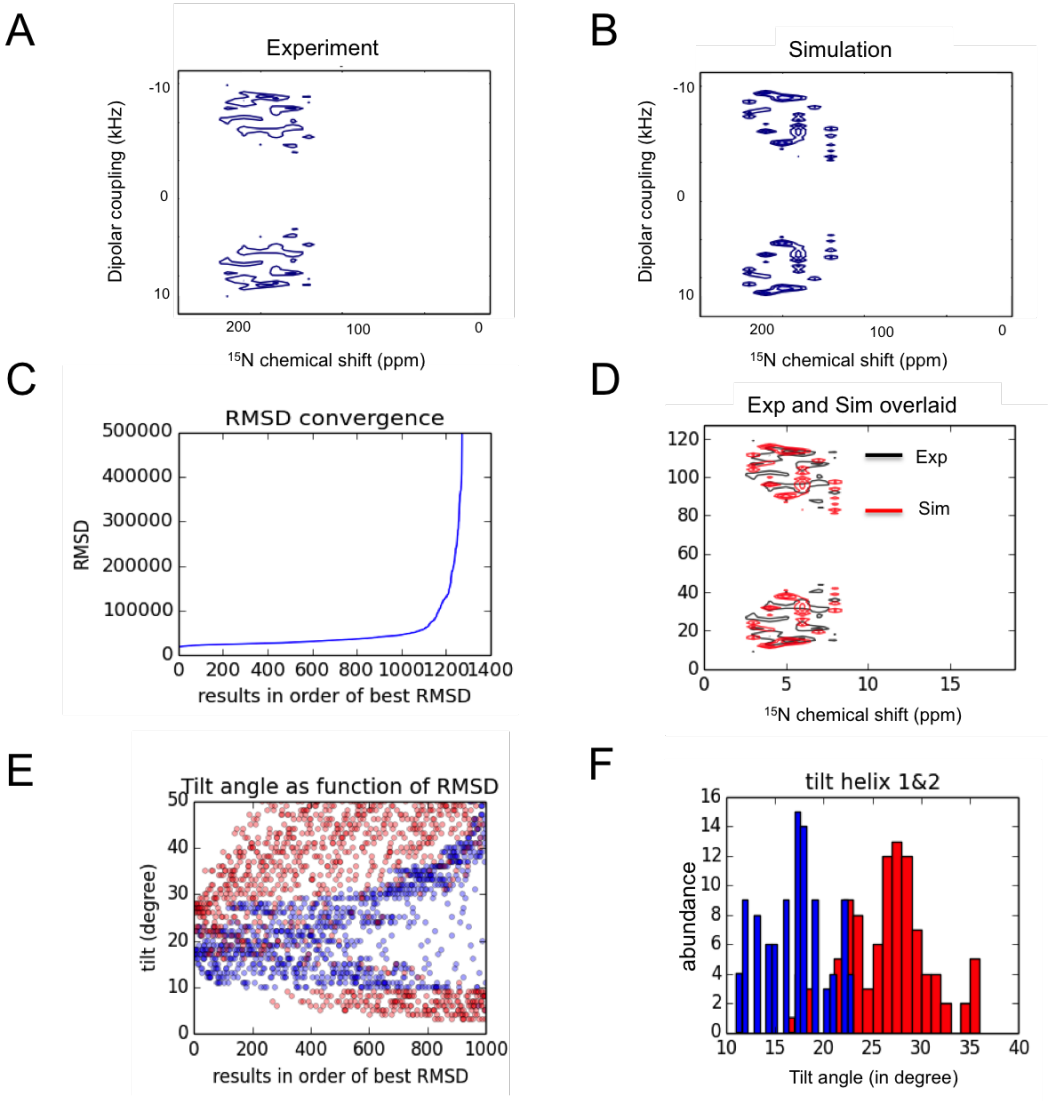

Figure 6.11: The simulated PISEMA spectrum for two transmembrane helices at a resolution of 128 x 128 points are shown. (A) The "wing-region" of the experimental spectrum is shown, giving information on the transmembrane domains. (B) The "best-fit" simulated spectrum of two straight transmembrane helices is shown. (C) The RMSD values of all fitted spectra are shown in order of the best achieved fits. (D)An overlay of the experimental and simulated spectrum is shown. (E) Relative helical tilts (best 1000 results) are shown as a function of best RMSD values (for helix "one" (blue) and helix "two" (red)). (F) The relative abundance of the specific tilts in the 100 lowest RMSD fits is shown (for helix "one" (blue) and helix "two" (red)). Details of spectral simulations are provided in section A.1.4. Simulations and analysis were performed in collaboration with L Vermeer (Strasbourg).

were used [204; 291]. SIMMOL allows the CSA and dipolar couplings to be described by a model alpha helix or based on PDB structures, whereas SIMPSON can be regarded as the spectrometer simulating the actual magnetic interactions and a full 2D PISEMA spectrum. The general simulation strategy is based around the previously reported analysis on oriented bacteriorhodopsin and summarised in Figure 6.10 [377]. In short, resonances for specific

amide groups were simulated individually and added to a full spectrum post simulation. The simulations are fitted to minimise the following equation: $[Sim - Exp]^2$; where Sim and Exp are the simulated and experimental spectra respectively.

Note that the powder component of the spectrum was isolated by post-experimental processing and the simulation and fitting was focused on the important wing regions that describe the transmembrane helical configurations. It should be noted that a powder also gives rise to resonances in the wing-region, which could not be excluded without removing resonances arising from transmembrane domains, yet powder-resonances in this region are of considerably lower intensity and focused around the "wing-edges" (Figure 6.13 B). This should not considerably affect resonances arising from transmembrane domains. Further to this, it is common procedure to overlay manually drawn PISA wheels onto the wing regions, this procedures excludes the powder component in a similar way. Yet, in an ideal scenario no powder component should be present, which should render such a procedure unnecessary, however PISEMA experiments are often limited by the complexity of sample preparations.

The tilt angles of the two straight model α-helices were varied in steps of 2° between 0 and 50° with respect to the bilayer normal. In order to limit the overall simulation time the spectral resolution was decreased to 128 x 128 points. Despite these limitations, a convergence of the relative orientation of the individual model helices was still observed (Figure 6.11 E and F). The helices seem to converge to two specific overall tilt angles at ca. 28° and 18°. The observed tilt distributions are comparatively wide and thus the error on this also comparatively large; the 100 best RMSD values vary +/- 10° (Figure 6.11 F).

6.2.4.2 2^4-SEMA Experiments

Similar to the PISEMA experiment, an alternative pulse sequence was used in order to obtain a higher resolution spectrum (Figure 6.12). 2^4-SEMA uses an additional frequency switch, cycling the effective magnetisation through all quadrants, which leads to cancelation of the proton offset. The initial one dimensional ^{15}N-spectrum of the sample showed a different line shape from an expected powder pattern, yet no exclusively aligned alpha helices could be observed (Figure 6.13 A). This possibly represents the overlap of different orientations as well as unstructured loops within the sample. In the 2D spectrum distinct resonances

are resolved that are at a higher intensity compared to the expected resonances of a scaled powder spectrum (Figure 6.13 D). Note that this spectrum is recorded on a different sample, as the previously prepared sample was not usable anymore due to the long experimental times (acquisition times range from 7-10 days at 37°C).

The two dimensional 2^4-SEMA - like experiment showed a large underlying powder component similar to the PISEMA experiment, which is unsurprising from the broad one dimensional ^{15}N - spectrum. Yet, the overall noise level is considerably less indicating that the high noise level in the PISEMA spectrum might be due to an inaccurately matched proton frequency. Nevertheless, despite a different sample preparation the larger underlying powder component could not be removed. Similar to a typical PISEMA - powder pattern, a resonance pattern that divides the wing region in two parts is observed (Figure 6.13 B, highlighted by arrows). These intensities are also present in the p7 containing sample and hence are ignored for analysis. Note that if scaled relatively to each other the resonances in the "wing region" of the p7 sample are above the noise level expected for a powder at this

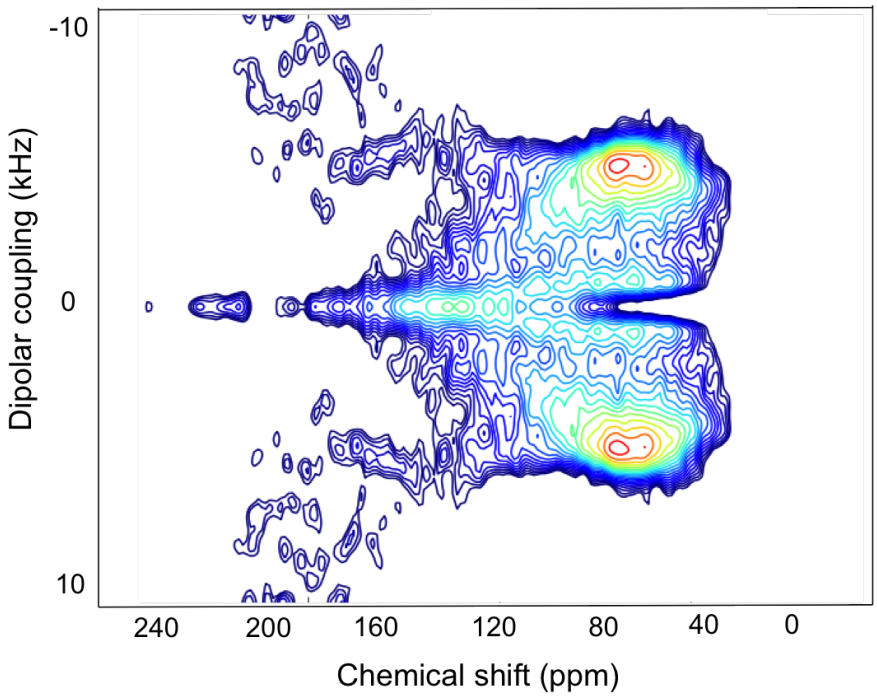

Figure 6.12: The experimental 2^4-SEMA experiment of uniformly ^{15}N labelled p7 in aligned DOPC:POPE (4:1; wt:wt) bilayers, acquired at a ^{1}H-frequency of 750 MHz, effective B_1 field of 57 kHz, 64 increments, temp of 37°C. The spectrum shown was processed at a resolution of 512x512 points.

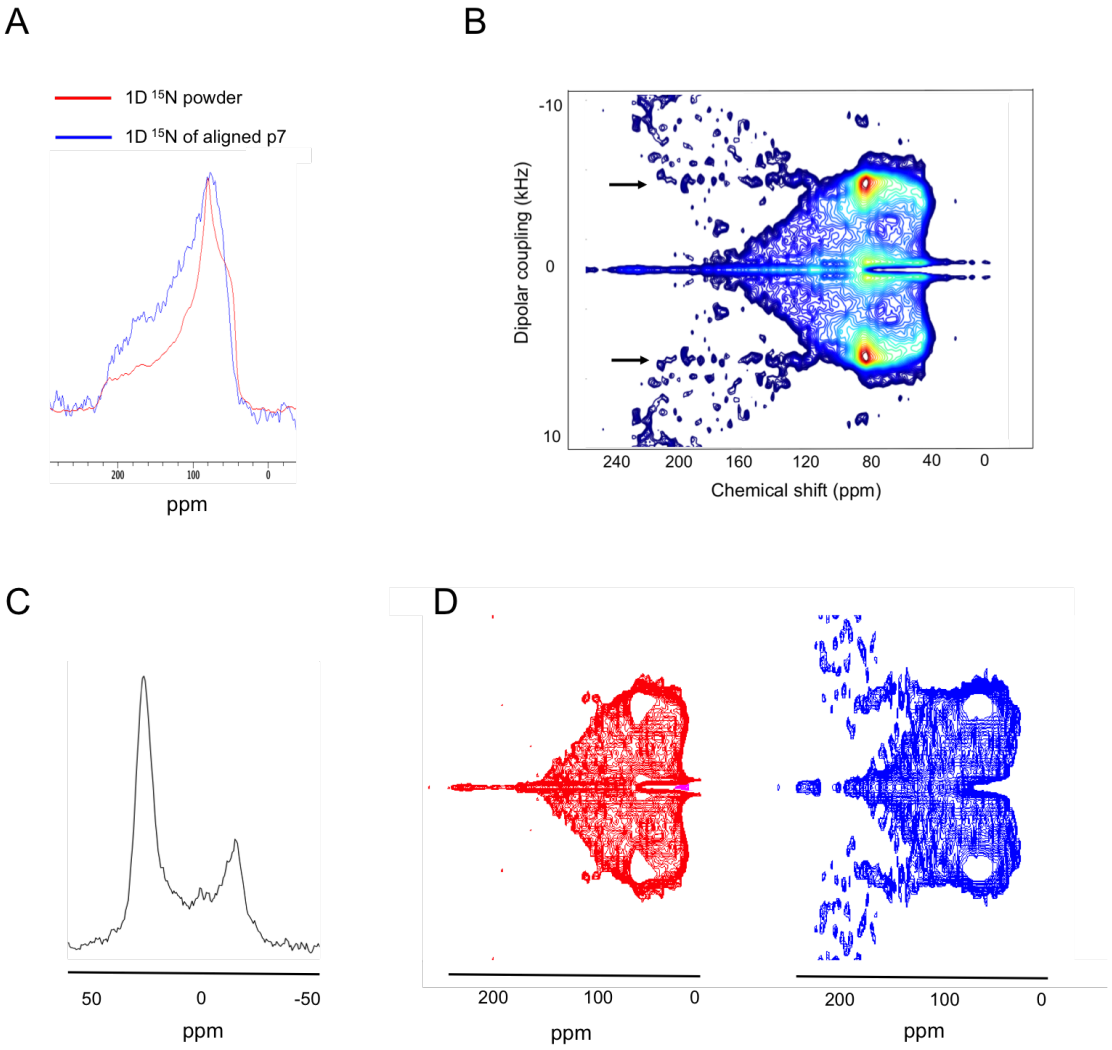

Figure 6.13: 2D and 1D NMR spectra comparing the sample from Figure 6.12 to expected powder shapes. (A) A Comparison between a typical 1D ^{15}N powder pattern (blue) recorded from N-acylated leucine powder and the 1D ^{15}N - spectrum of uniformly aligned ^{15}N - labelled p7 (red) are shown. (B) The typical butterfly shape of a powder PISEMA (acquired by a 2^4-SEMA based experiment) spectrum recorded on N-acylated Leucine is shown. (C) ^{31}P NMR of reconstituted p7 into mechanically aligned DOPC:POPE (4:1, wt:wt). (D) Comparison of a PISEMA powder (acquired by a 2^4-SEMA based experiment) to the experimental spectrum at matched intensity levels. Note that the resonances in the wing-region of the p7 spectrum (blue) are above the level of the wing region of the powder (red), where no signals are observed at these contour intensity levels. However, there is also a large underlying powder pattern present.

signal intensity and hence arise due to oriented transmembrane domains. These observed resonances give rise to seemingly entangled PISA wheels indicating multiple orientations are present for transmembrane domains. It should be noted that the underlying powder pattern can give rise to resonances in this region too, yet if scaled accordingly these would be expected of lower intensity compared to the resonances that are observed.

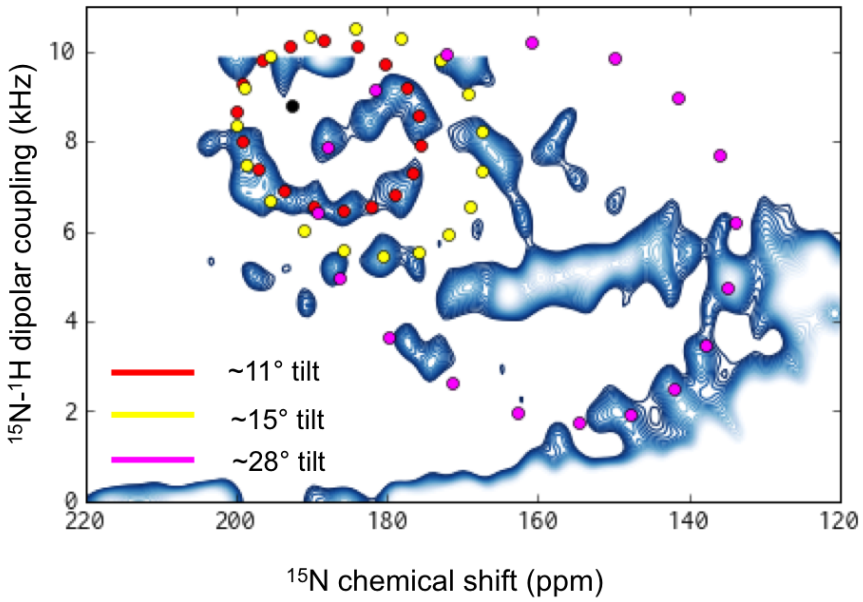

Figure 6.14: PISA wheels were superimposed to the experimental spectrum at relative tilt angles 11°; 15° and 28°. The superimposition was done manually compared to the computational fitting approach outlined in Figure 6.11 .Focus is on the wing region where transmembrane domains are expected to appear. Analysis by L Vermeer (Strasbourg).

The spectrum had a comparatively high signal-to-noise ratio which allowed for the superimposition of individual PISA wheels (Figure 6.14). A total of three different PISA wheel pattern could be fitted: (I) 11°, (II) 15° and (III) 28°. Tilt angles of 15° and 28° are surprisingly close to the spectral simulation analysis presented before (convergence to 18° and 28°), suggesting that the convergence observed before was real, despite high spectral noise. The additional tilt at 11° observed here was not seen by spectral simulation.

6.3 Discussion

The 2D spectra obtained of uniformly ^{15}N-labelled p7 (^{15}N) provides new insight into the topology of p7 in a membrane environment (Figure 6.11 and 6.14). These spectra are recorded in a two-component lipid system (DOPC:POPE (4:1; wt:wt)) and provide topological information of p7 in an environment with previously reported functional activity of p7, it should be noted that the signal to noise ratio for some of the spectra is low. The experiment was performed in the presence of PE, which forms part of ER membrane: PC and PE represent a total of 75% of the ER membrane components [337] and is thought to be important for

p7 function [72]. Further to this, PE-lipids were previously shown to be of important for protein folding and function in case of transmembrane domains (e.g. LacY), which might imply an importance to protein function [360; 378].

The spectral quality at first seemed poor for a traditional PISEMA experiment, however some resolution of helical PISA wheel patterns in the "wing" region could be identified. Similarly the experiment based around the 2^4-SEMA pulse sequence showed resonance above those expected for a powder in the same region. This lead to the observation of resolved entangled PISA-wheel characteristics that could be analysed. The overall spectral quality is limited (Figure 6.12) and a large powder component is evident, which had to be ignored for analysis. It should be noted that the one dimensional ^{15}N spectrum resembles a powder like line shape yet the precise sample orientation cannot be deduced from a one dimensional spectrum and can only be an indication. Tilt angles of $\sim$11°, $\sim$15° and $\sim$28° are suggested despite a poor signal to noise ratio (Figure 6.14). Due to relatively small transmembrane tilts the individual resonances are not very well dispersed and are relatively clustered. Previously, a similar spectrum on uniformly ^{15}N-labelled p7 has been published recorded in magnetically aligned bicelles reporting relative helical tilts of 10° and 25° (shown for comparison in Figure 6.15 [358]). Despite having a comparably better alignment (based 1D ^{15}N spectra, see [358]), the qualitative overall appearance of the reported 2D - SAMMY experiment appears to be noisy under similar experimental conditions (Figure 6.15). The following discussion relates the suggested results from this chapter to the literature, however the experimental limitations discussed above should be taken into account and hence these results are by no means unambiguous.

The helical tilts reported here are close to previously reported tilts in 14-0-PC/6-O-PC - bicelles (25° and 10°), where the tilt of the TM2 was shown to be 25° relative to the bilayer normal in 14-0-PC/6-O-PC - bicelles using a truncated p7 construct. This is interesting since the membrane composition and the hydrophobic membrane thickness differs between the two experiments. Thus, it seems that p7 is fairly robust to changes in hydrophobic membrane thickness and unlike VpU does not respond dramatically to changes of the bilayer thickness [47]. However, the seemingly robust helical tilt angles can also be due to differences in oligomeric state between the two environments probed, where oligomerisation to an active state and/or interaction with PE might stabilise a specific p7 conformation. The oligomeric state in this membrane composition and at this peptide to lipid ratio is unknown and it can be speculated

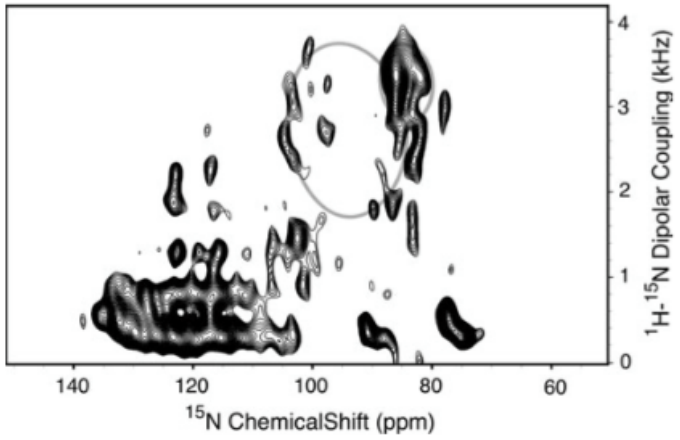

Figure 6.15: Experimental SAMMY spectrum of uniformly labelled p7 in magnetically aligned 14-0-PC/6-O-PC - bicelles oriented perpendicular to B_0 is shown. The experiment was recorded at 42°C at 700 MHz. PISA wheels for relative helical tilts of 10° and 25° are overlaid (grey). Figure taken from [358].

to be a mixture of different states. This might explain the observation of three different tilt angles. Alternatively a kinked transmembrane domain might be plausible. MD analysis of different oligomeric models in POPC revealed tilt angles in the range of 5-10° for TM1 and 10-15° for TM2. Oligomeric structures fitted to the EM density described by Luik *et al.*, modelled TM tilts of ∼15° and ∼25-30° for TM1 and TM2 respectively [361]. Simulation of monomeric p7 (Figure 6.1 B) in a POPC bilayer showed tilt angles of ∼15° and ∼5° for TM1 and TM2 respectively, an additional N-terminal domain is described by tilts ranging from 0-25° [74].

It was also suggested that in the previously reported monomeric p7 conformation in DHPC micelles, the largely bent N-terminal domain might fold up and bridge the hydrophobic bilayer thickness in a membrane (Figure 6.16), which would possibly explain the tilt of 28°, with two larger transmembrane domains, the N-terminal transmebrane domain TM1 and the C-temrinal TM2 at 11° and 15° or vice versa. Note that in this scenario the C-terminal TM domain would have straightened up to bridge the increased hydrophobic thickness, whereas the N-terminal domain would compensate for this by a slight outward folding of the otherwise bent domain. Indeed simulations of monomeric p7 in POPC showed a bending of this N-terminal domain despite a straight single N-terminal trans-membrane helix as a starting point [363]. The adaptability of this N-terminal helical domain may explain the lack of adaptation of the overall protein tilt to different hydrophobic membrane thicknesses, as small alteration of the tilt of this domain would be sufficient to allow adjustment to changes in the hydrophobic thickness.

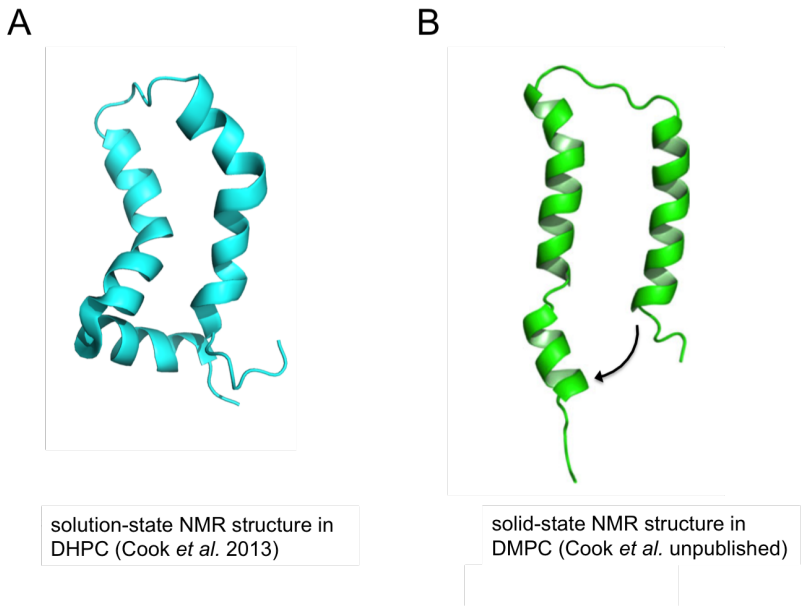

Figure 6.16: A comparison between a solution NMR structure of p7 (A, blue; PDB: 2MTS) and a solid-sate NMR structure in DMPC (B, green; unpublished, taken from [379]). The N-terminal helix seems to be lying on top of the "open" hairpin confirmation in a micellar environment. Upon insertion into a bilayer this helix adapts to by opening up as illustrated by the black arrow.

Previously a published monomeric p7 structure suggested a break of TM1 at residues 15-18 possibly by two relatively conserved glycine residues at position 15 and 18 [74]. Further to this, an unpublished monomeric Rosetta model of monomeric p7 in a detergent micellular environment (B Oestringer *et al.* unpublished) showed a similar feature of a near in plane helix "lying" on top of the hairpin configuration. Again it is plausible that this domain folds up in a bilayer environment. If such a model is correct (Figure 6.16 B) it would suggest that p7, like in most micellar environments, exists broadly in a hairpin conformation in a bilayer. If p7 is active in the membrane environment reported here, then it follows that p7 hairpin-shaped monomers oligomerise to form functional ion channels. The seemingly flexible short N-terminal helix might be important for this process, however, based on the data reported here, this remains speculative. Nevertheless, the N-terminal helical region of residues 1-18 was previously reported to be important for protein-protein interactions and viral infectivity [380].

In order to portray accurately the different helical domains, the precise start and end points of secondary structural elements within the sequence need to be known. Similar to the structural variance across the different published models these also vary significantly (Figure 6.17). In particular, the length and position of TM2 differs significantly. Most TM1

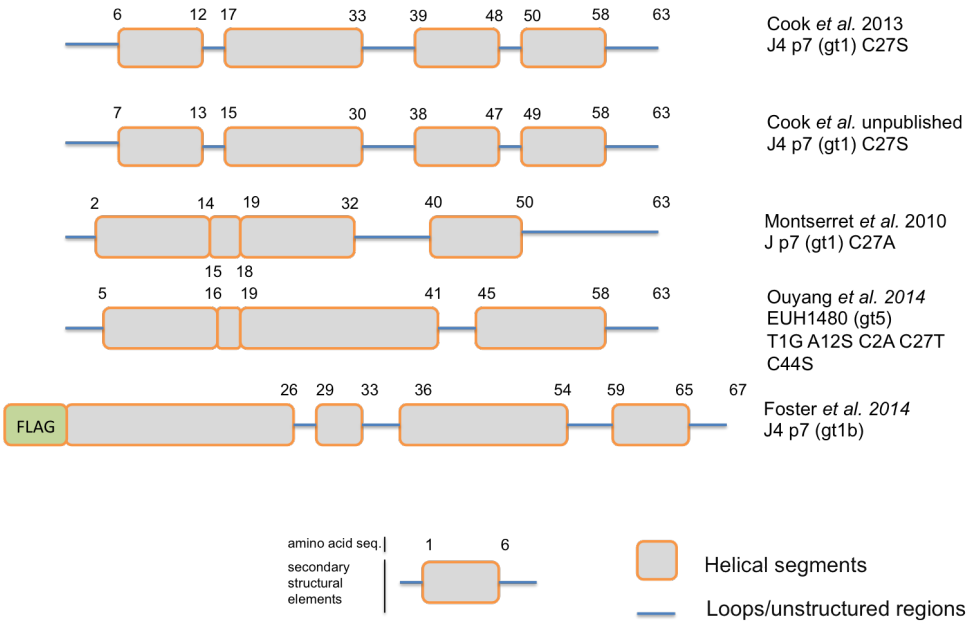

Figure 6.17: The locations of the secondary structural elements along the structurally studied p7 sequences. Note that all shown structures are from genotype 1 apart from the Ouyang *et al.* 2013 structure, which is genotype 5. The structural information for Cook *et al* (unpublished) is taken from [381] and is the only solid-state NMR structure in a membrane environment to date (Figure 6.16 B). All other structures are solution NMR based as outlined in Figure 6.1.

segments show a break in the region of amino acid residues 13-19, and there is ambiguity on the precise end of TM1. Cook *et al.* 2013 propose the Tyr at position 31 as the terminus of TM1 facilitated by a break due to the bulky side chain [87]. The authors propose that TM2 is separated into two domains by the Trp48 and Pro49 motif. Interestingly Trp48 residue is buried in the bilayer and not as expected at the interface region, confirmed by a Y48A mutation. This mutation was shown to also affect central regions of TM1, namely the phenylalanine cluster at residues 22,25 and 26 [381]. Interestingly a triple mutation of F22A, F25A and F26A lead to increased p7-mediated dye release from liposomes [136].

In summary this study underpins the remarkably complex nature of p7 assembly, despite its comparatively small size of 63 amino acids. Yet, it is this complexity that may account for the multiple functions of p7 in the viral lifecycle. The topological information reported here is a small step to further understanding the behaviour of p7 in different membrane types. In order to get a more holistic picture of p7 conformation in this membrane environment, secondary structural elements need to be assigned; improved sample preparation in combination with selective labelling and truncated constructs should help to achieve high-resolution spectra

that allow for residue assignment and secondary structure determination. Although the simulation approach presented here can be used to achieve amino acid assignments as simulated residues can be directly overlaid to the spectrum allowing for assignment and model based analysis. Relating monomeric structural information to the oligomeric state and channel function remains a major challenge for the field. A further challenge is characterisation of oligomerisation behaviour and associated relative oligomeric states within a particular sample, which is important for accurate interpretation. Taken together with the results presented in Chapter 5 it would be of interest to analyse the effect of *N*N-DNJ on p7 topology in a membrane environment.

7

Towards the oligomeric state of p7 in a membrane

Contents

7.1 Introduction 180
7.1.1 p7 mutants 183
7.1.2 Stoichiometric analysis based on ensemble FRET 186
7.1.3 Introduction to DEER techniques used 190
7.2 Results 192
7.2.1 Oligomeric stoichiometry by FRET 192
7.2.2 p7 mobility profile by cwEPR 194
7.2.3 Oligomeric state and protomer conformation by DEER 197
7.2.4 DEER of Gadolinium (Gd^{3+}) ions 214
7.3 Discussion 216

7.1 Introduction

The viroporin p7 is involved in different stages of the viral life cycle of Hepatitis C [83; 126; 127; 133; 382; 383]. Its likely primary function is as an ion channel similar to previously reported viroporins such as M2 (influenza A virus) or VpU (HIV-1), mediating proton gradients across cellular membranes [82]. However, other functions have also been reported, and p7 was shown to colocalise with the viral structural protein E2 and non-structural proteins NS5A, core, NS2 and NS3, suggesting a possible involvement in viral maturation

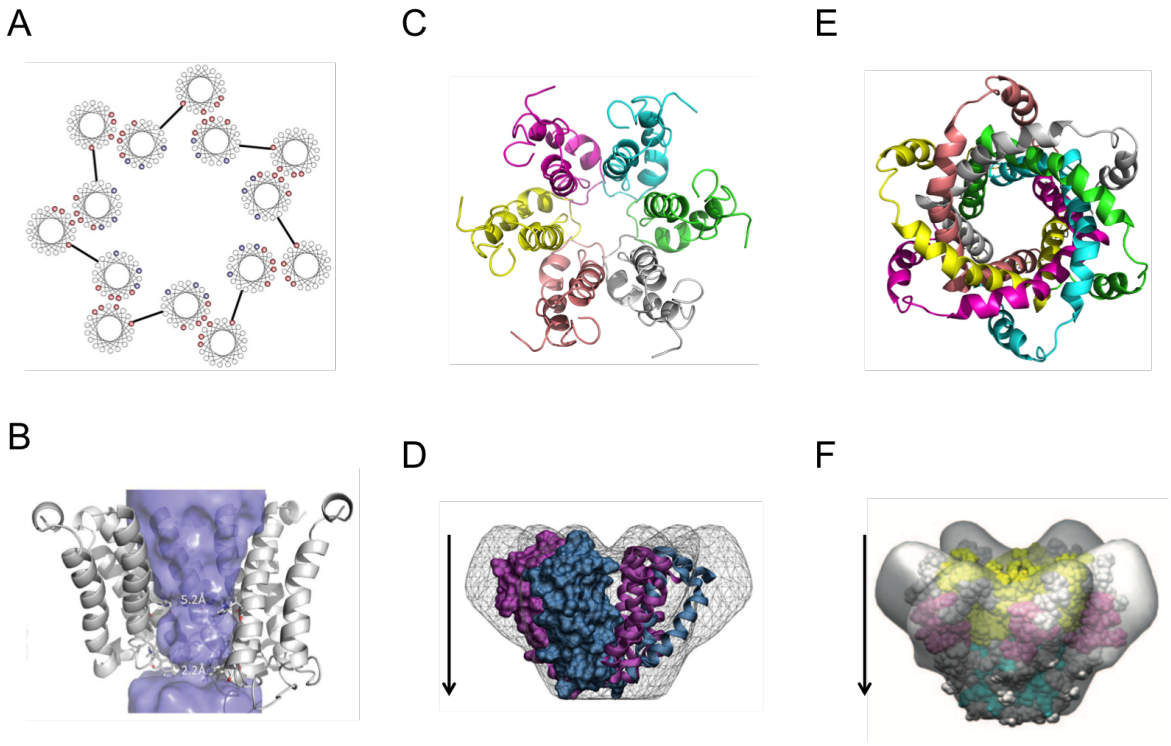

Figure 7.1: Different proposed models and high-resolution structures of oligomeric p7. (A) A heptameric FLAG-p7 model based on TEM studies in liposomes [68]. (B) A heptameric (Gt1b J4) model based on a monomeric p7 structure (FLAG-tagged; PDB: 3ZD0,[139]). (C) Hexameric p7 (Gt2a JFH1) based on simulated p7 monomers fitted into a high-resolution TEM density (top view, [73]). (D) Some models as shown in "C" form a side view. The perspective of (C) is illustrated by a black arrow. Note that the termini are pointing towards the paddles of the flower-like oligomeric complex. (E) High-resolution solution NMR structure of p7 (Gt5a EUH1480) viewed from the top. Note the entangled monomer conformation (PDB: 2M6X, [66]) and that the termini are pointing towards the closed face of the flower-like shape. (F) Same hexameric model as shown in (E) in a side view. The perspective shown in "E" is illustrated by a black arrow.

[83; 126]. Not all of these functions requires p7 to oligomerise, yet p7 is expected to homo-oligomerise to form a membrane channel for it to achieve its reported role as a viral ion-channel [68; 70; 71; 73; 74; 122]. Most investigations to characterise the oligomeric form of p7 agreed on a 6 +/- 1 protomer stoichiometry. Sedimentation analysis of p7 in detergent micelles yielded a oligomeric stoichiometry of 6 +/- 1 monomers, with a dependency on the detergent to protein ratio [74]. Initial transmission EM (TEM) studies on FLAG-tagged p7 yielded models of six and seven monomers for oligomers in vesicles (Figure 7.1 A [68; 70]). This was followed by the first low resolution (16 Å) structure of hexameric p7 in DHPC micelles by negative stain TEM, of p7 Gt2a JFH-1 (Figure 7.1 C and E ,[73]), revealing a flower-like shape with termini projecting towards the flower paddles. More recently a high-resolution NMR structure of hexametric p7 in DPC micelles has been reported, based on negative-staining TEM experiments performed

in parallel (Figure Figure 7.1 E and F [66]). Interestingly, the termini in this structure point towards the narrow side of the flower predicted to be the lumen-facing, in conflict with previous observations (Figure 7.1 D and F; [73; 357]). This proposed model of hexameric p7 (Gt5a) by B OuYang *et al.* 2013 shows an open "staple-like" protomer conforamtion that contrasts with the "hairpin-like" conformation of monomeric p7 (Figure 6.1; [74; 87; 139]).

It should be noted that the two reported oligomeric structures varied in genotype and detergent used [66; 73]. The structure and/or stoichiometry of oligomeric p7 in a membrane may differ from detergent; for example the lateral pressure profile across a membrane might possibly perturb the flower architecture into transmembrane domains that are oriented at a smaller angle to the bilayer normal [360; 361]. The feasibility of the oligomeric structure reported by OuYang *et al.* 2013 in a physiological setting remains controversial, as the structure would need to simultaneously co-fold in order to achieve the inter-monomer contacts of subunits *"i"*, *"i+1"*, *"i+2"* and *"i+3"*, a process that would not fall into the common understanding of protein folding [382]. Further, charged amino acid side chains found at the predicted position of the hydrophobic membrane core might lead to destabilisation in a membrane environment [360].

In early studies performing heterologous over-expression p7 was mainly found in the ER membrane, but also in the plasma membrane [357], and in membranes associated with mitochondria (MAMs) [384]. However, a later study using a competent replicon genome only found p7 in the ER, with higher concentrations at the perinuclear region[385], and a more recent study, in cells producing infectious HCV particles with HA-tagged p7, found a similar distribution of p7 in the ER with an enhanced localization around the nucleus [83]. Nevertheless, p7 ion channel function has been predominantly been associated with the ER membrane [70; 72].

The overall aim of this chapter is to obtain single constraints, using distinct mutants that allow for tagging with nitroxide-spin labels and fluorophores in order to describe the behaviour of p7 in a membrane, including information on the ensemble number of protomers in an oligomer as well initial constraints describing the monomer conformation within an oligomeric complex. Most structural information of p7 is based on solution studies in detergent and solvents with only limited structural information on p7 stoichiometry in a membrane. The membrane composition is important for p7 and other alpha helical membrane proteins mediating function

[72] and here a model bilayer is used that broadly resembling the main components of the ER and in which p7 was reported to be active [72; 360]. This analysis aims to probe the different proposed p7 structures, for plausibility in a membrane environment, which is modelled to resemble the composition of the ER membrane (DOPC:POPE (4:1,wt:wt); see Section 6.3).

7.1.1 p7 mutants

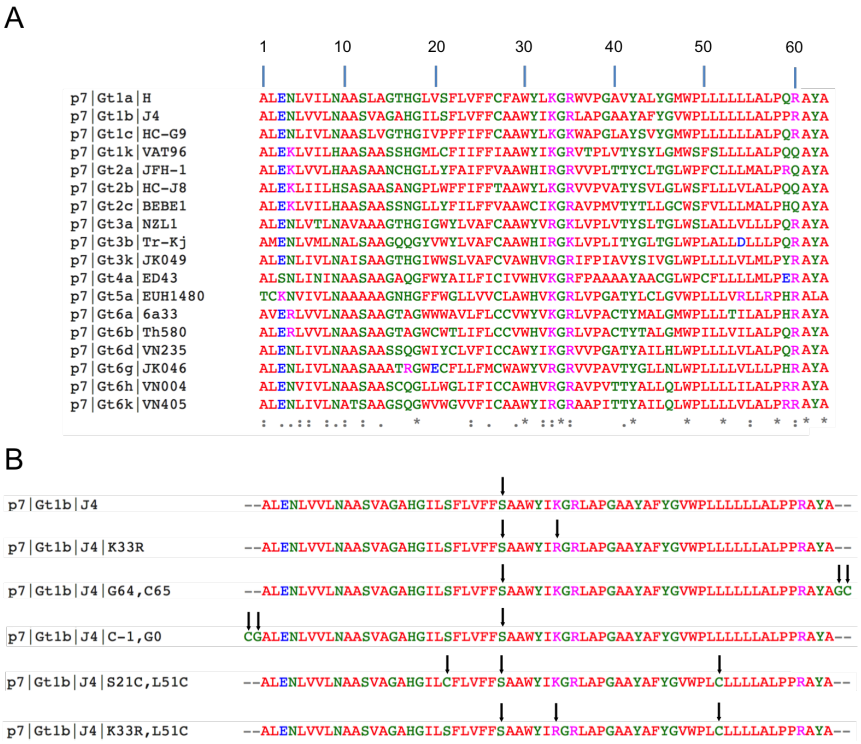

Figure 7.2: (A) p7 sequence alignment of representative members of the six most common genotypes illustrating the variance within the amino acid sequence. (B) Illustration of mutants used in this study in order to probe p7 Gt1b J4 oligomerisation and protomer structure upon oligomerisation. Note that all p7 mutants are based on Gt1b isolate J4 and the C27S mutation previously used for characterisation of this isolate [372] is kept across all mutants and is not mentioned in the name or further reference anymore. Mutations are highlighted by black arrows and sequence alignment was generated using ClustalW, where "red" illustrates samll and hydrophobic residues, "blue" represents acidic residues, "magenta" basic residues and "green" for hydroxy-, sulfhydryl- and amine containg residues including glycine; *"*"* indicates fully conserved residues, *":"* indicates conservation of similar properties and *"."* indicates conservation of weakly related properties. See Table 7.1 for explanation of each separate mutant.

Different mutants were designed in order to probe specific aspects of p7 oligomerisation in a membrane environment (DOPC:POPE (4:1, wt:wt) using cwEPR, pulsed EPR (DEER) and fluoresence (FRET) approaches (Figure 7.2). The sequence of p7 varies across all genotypes with only 9 of the 63 amino acids being fully conserved across all types (Figure 7.2 A).

Care was taken that the mutations made do not fall within in these conserved or other partially conserved residues and are naturally occurring (Figure 7.2 B). Further to this most of the mutations made within the p7 sequence (excluding termini extensions) are all naturally occurring in other HCV genotypes and thus are not expected to alter p7 behaviour significantly. The mutant genes were cloned into expression vector (pMM-LR6) and expressed as described previously (Section 6.2.1), for the cysteine containing mutants, reducing agent (tris(2-carboxyethyl)phosphine (TCEP)) was added during the FPLC purification to prevent disulphide bridge formation. The protein was precipitated out of solution by dialysis in presence of reducing agent to allow immediate labelling with S-(1-oxyl-2,2,5,5-tetramethyl-2,5-dihydro-1H-pyrrol-3-yl)methyl methanesulfonothioate (MTSL) nitroxide spin label upon subsequent resolubilisation. Reconstitution was performed analogous to the procedure outlined in section 6.2.2, using SDS and sodium cholate as solubilising detergents.

The mutants and their rationale are summarised in Table 7.1; mutants are named as illustrated in Figure 7.2 B.

Table 7.1: Different p7 mutants used for characterisation of p7 oligomerisation and protomer conformation

p7 mutant	Design rationale
p7 K33R Gt1b J4	The single lysine residue has been replaced by an arginine, which is naturally occurring at this position across other genotypes. arginine and lysine are the only two residues tolerated at this position. This replacement removes the single primary amine located within an amino acid side chain, leaving the N-terminus the single remaining primary amine, which was exploited for fluorescent labelling using cyanine dyes coupled to a reactive *N*-hydroxysuccinimide (NHS) ester to analyse the stoichiometry of p7 oligomers.
p7 G64,C65 Gt1b J4	The C-terminus was extended by a single glycine residue followed by a cystine residue for tagging p7 with MTSL to introduce a nitroxide spin for pulsed EPR studies and investigation of the interproteomer C-terminal distances in an oligomeric complex. The glycine extension was introduced as a spacer between the spin-probe and the strictly conserved C-terminal alanine residue
p7 C-1, G0 Gt1b J4	The corresponding mutant to p7 G64,C65 in order to compare N- and C-terminal constraints in an oligomer. Again a glycine residue was introduced a spacer to the fairly conserved N-terminal alanine and Leucine residues (all genotypes but Gt5a (EUH1580). A previously reported A0C (an added cysteine to the N-terminus) mutant of genotype 1b (J4) reported chemical shift changes and hence the extending glycine was introduced [139] .
p7 S21C,L51C Gt1b J4	A double cysteine mutant for labelling with MTSL in order to probe intraprotomer distances of p7. The expected distance between these residues differs significantly for monomer conformations of a hairpin structure and the protomer confirmation proposed by OuYang *et al.* 2013 within the oligomeric form. Note that cysteine residues are naturally occurring at these sites in other genotypes.
p7 K33R, L51C Gt1b J4	A double labelled mutant to probe N-terminus location in respect to the C-Terminal domain. Note that the N-terminus is directly labelled using NHS ester in contrast to the cysteine labelled with MTSL. This avoids possible difficulties of disulphide bridge formation between two mutated cysteine sites.

The studies presented in this chapter were performed in collaboration with the Nicole Zitzmann's laboratory (Oxford), where the mutants G64 C65, C-1 G0 and S21C L51C were cloned, purified, reconstituted into lipid bilayers and measured by cwEPR by Juan H Bolivar and Mario Hensen.

7.1.2 Stoichiometric analysis based on ensemble FRET

The underlying principles of FRET are summarised in Section 2.3.2. The FRET pair of cyanine 3 (Cy3) and cyanine 5 (Cy5) was used (Figure 2.11), having a Förster radius of ∼ 50 Å [386] in order to investigate p7 stoichiometry in a membrane environment by principles described in literature, which are summarised below [387; 388; 389]. Note that similar FRET analysis was also used to investigate the assembly mechanism of the viroporin M2 [390].

The stoichiometric analysis presented here is based on sensitised acceptor emission ($E_{app,se}$) as a function of different donor to acceptor molar ratios (x_D), which correlates with n, the number of protomers in the nano-object. $E_{app,se}$ is described by:

$$E_{app,se} = \frac{\epsilon_A(\lambda_D^{ex})}{\epsilon_D(\lambda_D^{ex})} \cdot (\frac{F_{AD}}{F_A} - 1) \tag{7.1}$$

where, $\epsilon_A(\lambda_D^{ex})$ and $\epsilon_D(\lambda_D^{ex})$ denotes the molar extinction coefficient of donor and acceptor at the donor excitation wavelength respectively. F_{AD} and F_A describe the emission of the acceptor in the presence and absence of a donor respectively. Note that for F_A the sample was excited at the acceptor excitation wavelength [387].

As an alternative apparent FRET emission can be measured by donor quenching ($E_{app,dq}$):

$$E_{app,dq} = 1 - (\frac{F_{AD}}{F_D}) \tag{7.2}$$

Under the rules of energy conservation and based on the relative quantum yields of the FRET pair $E_{app,dq}$ and $E_{app,dq}$ can be related to each other (for full explanation see [388]):

$$E_{app,se} = E_{app,dq} \cdot \frac{x_D}{x_A} \tag{7.3}$$

where x_D and x_A correspond to the molar fraction of donor and acceptor respectively.

Apparent FRET emission ($E_{app,dq}$), measured by donor quenching, and can be related to the molar donor fraction as previously reported [389]:

$$E_{app,dq} = E(1 - x_D^{n-1}) \tag{7.4}$$

where E is the true FRET efficiency and n represents the number of monomers in an oligomeric complex.

Using equation 7.3 this relationship can be rewritten as:

$$E_{app,se} = E \cdot \frac{x_D}{1 - x_D} \cdot (1 - x_D^{n-1}) \tag{7.5}$$

In order to compensate for incomplete fluorophore labelling the model was extended taking into account labelling efficiencies [389]:

$$E_{app,se} = E \cdot \frac{x_D}{1 - x_D} \cdot [1 - x_D(1 - x'_U) + {x'_U}^{n-1}] \tag{7.6}$$

where x'_U corresponds to the unlabelled molar fraction of the sample. Note that the sum of labelled donor and unlabelled donor x_{DU} is given by:

$$x_{DU} = x_D \cdot (1 - x'_U) + x'_U \tag{7.7}$$

The dependency of $E_{app,se}$ and $E_{app,dq}$ on x_D and n is illustrated in Figure 7.3.

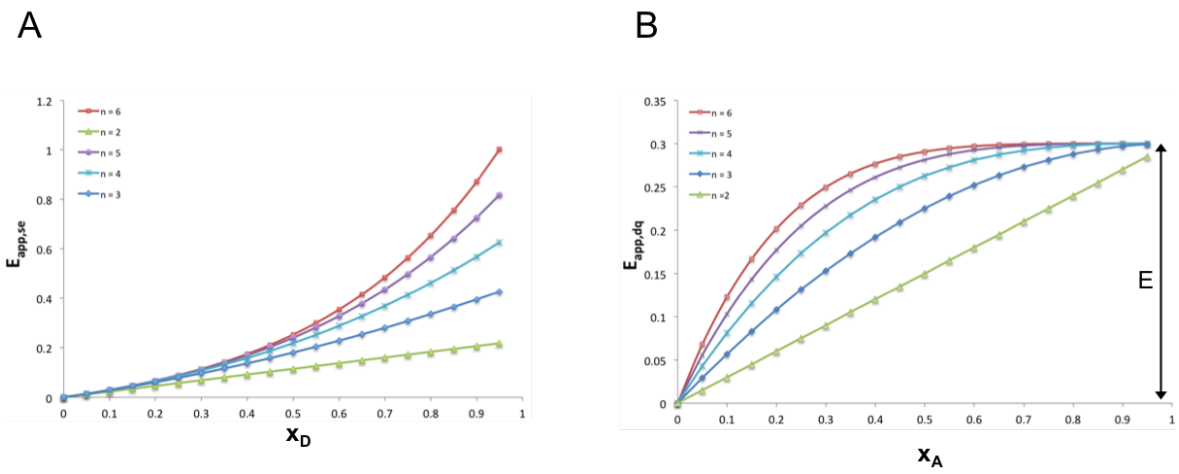

Figure 7.3: (A) The relationship described by function 7.6 is illustrated. Theoretical $E_{app,se}$ dependencies for oligomeric complexes with $n = 2$, $n = 3$, $n = 4$, $n = 5$ and $n = 6$ are plotted as a function of the molar donor fraction x_D. (B) The same relationship is described as a function of $E_{app,dq}$ and x_A the molar acceptor ratio for different values of "n", based on function 7.4 and the fact that $x_A = 1 - x_D$. This relationship was used in order to estimate E, the true FRET efficiency of the system, as the maximum FRET transfer possible in the investigated system $x_A = 1$. Note that experimentally $x_A = 1$ is not possible and thus the function was extrapolated to $x_A = 1$.

7.1.2.0.1 Practical implications of FRET

In order to analyse the stoichiometry of p7 in a DOPC:POPE (4:1, wt:wt) membrane, p7 J4 Gt1b K33R (Table 7.1) was tagged with water-soluble sulfo-cyanine 5 NHS ester and sulfo-cyanine 3 NHS ester at the N-terminus. The Cy3-Cy5 FRET pair is illustrated in Figure 2.11. The labelling efficiency was determined comparing relative dye absorbance to A_{280} absorbance and was represented as x'_U in the data fitting. Labelling efficiencies in the range of 85% were achieved for both dyes. Further to this, the experimentally determined FRET signal was corrected as described in Figure 7.4, in short the "bleed-through" fluorescence attributed to emission by the donor was estimated from relative scaling of a donor-only sample and subtracted (Figure 7.4 A). The "cross-talk" fluorescence attributed to partial excitation of the acceptor fluorophore at the donor excitation wavelength was approximated based on an acceptor-only sample excited at the donor and acceptor wavelengths in order to scale the "cross-talk" signal accordingly (Figure 7.4 B) and was subtracted from the experimentally determined FRET signal to obtain a corrected FRET signal (Figure 7.4 C).

The relative absorbance values of the donor and acceptor at the donor excitation wavelength (ϵ_A^{538nm} and ϵ_D^{538nm} respectively) were determined and corrected for calculation of $E_{app,se}$ as described by equation 7.1:

$$\epsilon_A^{538nm} = 0.076 \cdot \epsilon_{A,max} \tag{7.8}$$

$$\epsilon_D^{538nm} = 0.629 \cdot \epsilon_{D,max} \tag{7.9}$$

where ϵ_A^{538nm} and ϵ_A^{538nm} are the relative extinction coefficients for acceptor and donor respectively when excited at 538 nm. $\epsilon_{D,max}$ and $\epsilon_{A,max}$ are the maximum extinction coefficients for donor and acceptor respectively (Donor (Cy3): $\epsilon_D^{548nm} = 162\ 000$; Acceptor (Cy5): $\epsilon_A^{646nm} = 271\ 000$).

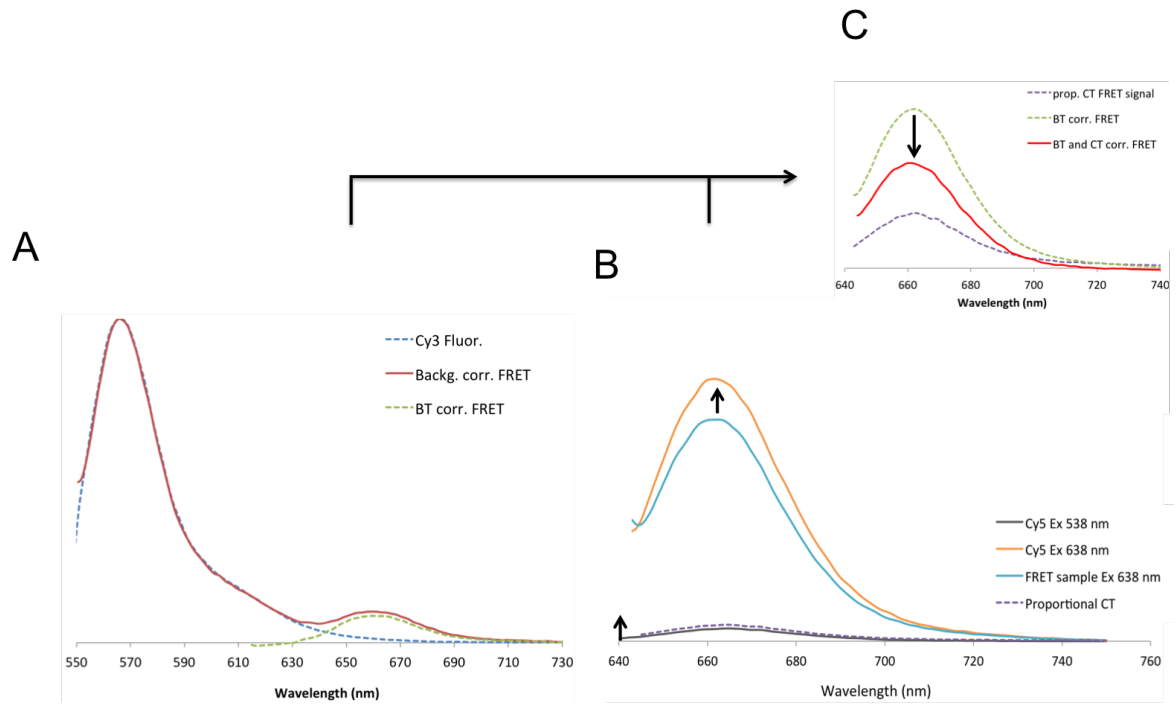

Figure 7.4: The corrections applied to the measured raw FRET signal are illustrated. (A) The "bleed-through" correction of donor emission to the measured acceptor emission is illustrated. The emission of Cy-3 (Donor) is shown in blue line, measured FRET signal in red (corrected for vesicle scattering; background) and the corrected (by subtraction) FRET signal in green. The "bleed-through" is estimated from a scaled donor-only sample. (B) The correction of cross-talk, the relative proportion of acceptor exited by the excitation at the donor excitation wavelength, is illustrated. This is a constant approximation from an acceptor-only sample excited both at the donor excitation wavelength (black) and the acceptor excitation wavelength (orange). This is then placed into proportion to the observed FRET signal (blue, containing Cy3 and Cy5 dyes). (C) The FRET intensity attributed to "cross-talk" (dashed purple) is subtracted from the "bleed-through" (dashed green) corrected FRET signal leaving a corrected FRET intensity (red).

7.1.3 Introduction to DEER techniques used

Complementary to FRET analysis, DEER experiments were preformed to gain more detailed understanding of the oligomeric complex and for verification of FRET data. DEER experiments were performed to analyse distance distributions of coupled spins within the oligomeric complex at both the N- and C-termini. Further to this intramolecular constraints were used to evaluate the presence of an overall hairpin conformation in a membrane as suggested from high-resolution studies in detergent [74; 87; 139]. This is complemented with spin-counting experiments in order to verify the overall stoichiometry of the oligomeric complex.

Distance constraints in a nano-object

The basic underlying principles of DEER are outlined in section 2.2.2. DEER is a powerful technique to resolve the dipolar coupling between two isolated electron spins, however, in the case of multiple spins in the same nano-object, a group of coupled spins, this becomes problematic and leads to multi-spin artefacts [391; 392]. Increased numbers of dipolar coupling contributions can cause the appearance of ghost distances that are not present within the nano-object [392]. The resulting dipolar spectrum of a multi-spin system is a multiplication of dipolar contributions, which leads to sum and difference frequencies, which in turn can alter the Pake doublet and deviate from the simple superposition of multiple individual Pake doublets and becomes dominated by the stronger coupling [392]. High-order symmetric oligomers are not a linear combination of individual spin-pairs and are difficult to analyse reliably using common DEER approaches (Figure 7.5; [391]).

DEER experiments measure frequency modulations in the dipolar evolution function of a spin-pair, with Tikhonov regularisation methods being applied in order to obtain distance distributions [393; 394]. This method is reliable for individual spin-pairs. For multi-spin oligomers two different approaches have been proposed to circumvent the aforementioned data analysis problems, most of which rely on trying to reestablish a linear combination of individual spin-pair frequency contributions from within the oligomeric nano-object. A common approach is spin-dilution in order to limit multi-spin interaction within the sample to the point that mostly interactions of spin-pairs are observed [395; 396]. An alternative is to lower the pump-pulse amplitude in order to reduce the flip-angle and only pump a

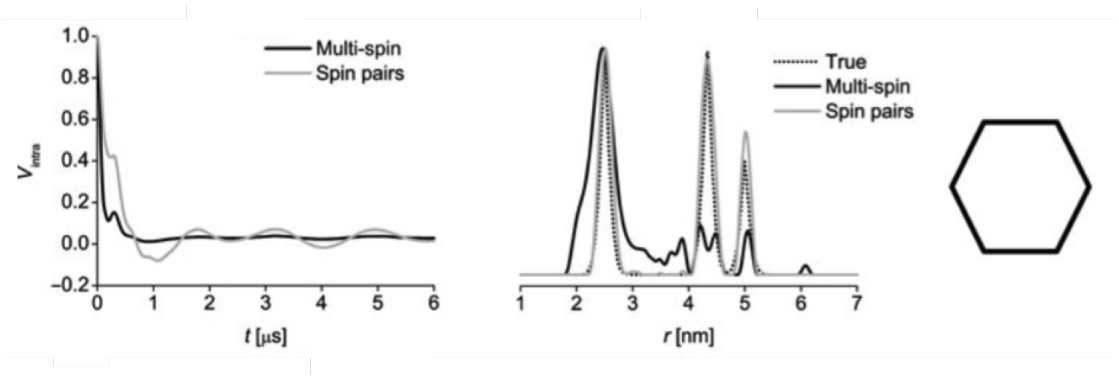

Figure 7.5: Simulated DEER dipolar evolution function and corresponding distance traces of a symmetrical hexamer are illustrated. The dipolar evolution function is shown on the left: dipolar evolution function treating all spins by multiplication (black), dipolar evolution function based on individual spin-pairs within the hexamer (grey). The distance distribution is shown on the right and overlaid with the "true" distance trace resulting from the theoretical hexamer. Black and grey distance distributions are based on Tikhonov regularisation of the corresponding dipolar evolution function respectively. Figure taken from [391].

certain sub-population of the coupled spins while maintaining a fully labelled sample. More recently power scaling of the experimental data was proposed as a successful method to suppress multi-spin artefacts for oligomeric states of up to five [397]. Despite these problems of homo-oligomers, DEER approaches have been successfully applied to oligomers of up to heptameric and octameric complexes [395; 396].

Two different experimental approaches are used here: (I) Single-labelled monomers with a single nitroxide are used in order to investigate intermolecular distance constraints within the nano-object (mutants: p7 Gt1b J4 G64,C65 and C-1, G0; table 7.1). (II) Double-labelled monomers in order to investigate intramolecular distance constraints (mutants: p7 Gt1b J4 S21C, L51C and p7 Gt1b J4 K33R L51C table 7.1). In case of approach (I), the samples were spin diluted with non-labelled monomers to final spin-label concentration of 33%, based on the assumption of hexameric complexes, which would yield two coupled spins per nano-object on average. For approach (II), samples were spin diluted to a final spin-labelled p7 concentration of 16% in order to have one double labelled monomer per hypothetical hexameric nano-object. DEER experiments were performed at a frequency of 34 GHz (Q-band), with the pump-pulse frequency coinciding with the maximum absorption of the nitroxide spin, a 12 ns pump-pulse at a 90 MHz separation to the observer frequency and at 30 K, using a 4p DEER pulse sequence (Figure 2.7 and 2.8 B). Observer pulse length varied between samples.

Modulation depth and spin-counting

The observed dipolar evolution function depends on the number of coupled spins within a given nano-object. The presence of more than a single spin-pair leads to an increased modulation depth ($\Delta(\rho)$; Figure 2.9), which is defined as [79; 210; 392; 398]:

$$\Delta(\rho) = 1 - \frac{DEER_{t=\infty}}{DEER_{t=0}} \tag{7.10}$$

where ρ is the proportion of spins flipped by the pump-pulse, $DEER_{t=\infty}$ the form factor of the time-dependent domain (dipolar evolution function) at time (t) $t = \infty$ and $DEER_{t=0}$ the form factor of the time-dependent domain at $t = 0$.

The increase in modulation upon the addition of additional spins to a given nano-object is described by:

$$\Delta(\rho, N) = [1 - (1 - \rho)^{N-1}] \tag{7.11}$$

where N corresponds to the number of spin coupled in a nano-object. Note that for a spin-pair $\Delta(\rho, 2) = \rho$.

7.2 Results

7.2.1 Oligomeric stoichiometry by FRET

Initial FRET experiments were performed to investigate the ensemble oligomerisation behaviour of p7 in a DOPC:POPE (4:1, wt:wt) membrane. The $E_{app,se}$ was measured as described in section 7.1.2, using a relative donor molar fraction ranging from $x_D = 0.1$ to $x_D = 0.9$. The total fluorophore concentration was kept at 150 μM and the total lipid concentration per sample was constant. Experiments were performed at 27°C above the phase transition of both lipid components (DOPC = -20°C and POPE = 25°C). As an initial characterisation step three different hexamer to lipid molar ratios[1] were chosen in

[1]The peptide to lipid ratios are based on the assumption of hexameric p7 in a membrane and are reported accordingly

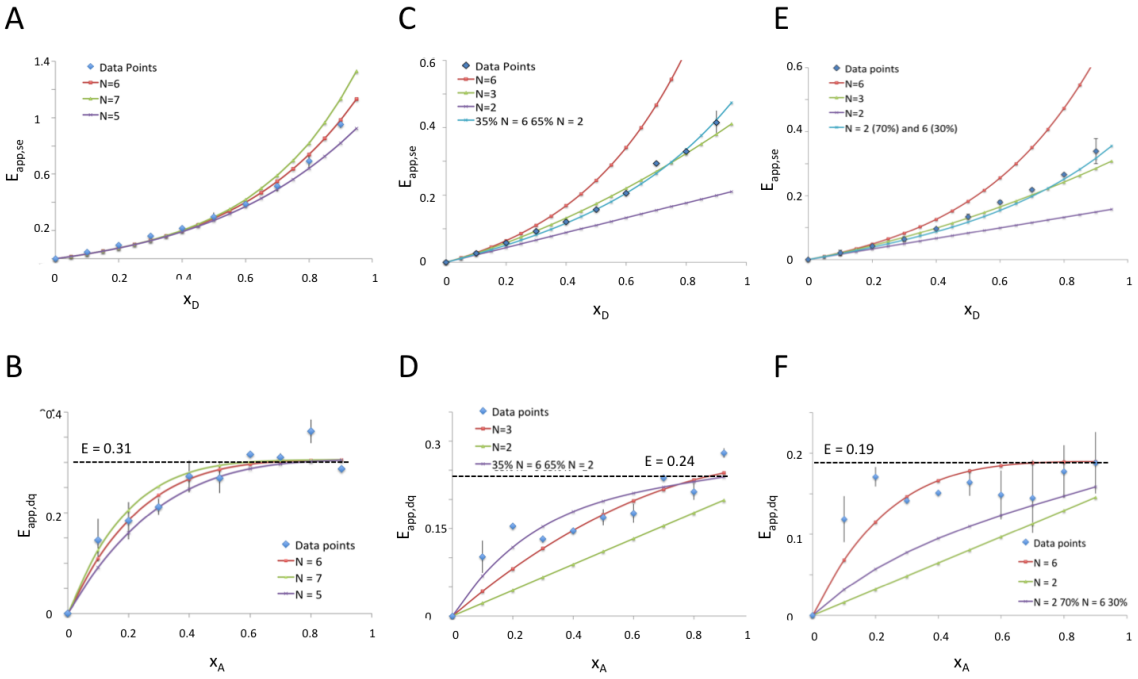

Figure 7.6: The stoichiometric analysis is shown for apparent FRET efficiency based on emission (top panel) and donor quenching (bottom panel). The individual data points are shown in blue, theoretical expected trends as described in section 7.1.2 are overlaid for different oligomeric complexes with a varying number n. The true FRET efficiency was estimated based on the relative donor quenching observed and used to analyse the apparent FRET intensity based on emission. The protein to lipid molar ratios are as follows: (A and B) 1:150; (C and D): 1:1,000 and (E and F) 1:2,000.

order to investigate a possible effect on the oligomeric behaviour of p7: (I) 1:150, (II), 1:1000 and (III) 1:2,000. These lipid compositions were based on initial CD characterisation in these environments and showed minor changes in secondary structure (data not shown). The labelling efficiency was estimated based on comparison of absorbance A_{280} to $A_{max(dye)}$, giving a relative labelling efficiency of 0.85%.

The high density membrane with a molar hexamer to lipid ratio of 1:150 gave rise to an estimated true FRET efficiency of $E \sim 0.31$ (Figure 7.6 B), however a clear stoichiometric trend could not be established based on $E_{app,dq}$, measured by relative donor quenching, and the theoretical trends for $n = 5, n = 6$ and $n = 7$ appear to be in reasonable agreement (Figure 7.6 B). In general the $E_{app,dq}$ is prone to a higher relative error compared to $E_{app,se}$ as it is not possible to quench the acceptor in a given sample in order to determine donor fluorescence in the absence of an acceptor and is estimated from a sample containing only the FRET donor. The $E_{app,se}$, measured by FRET emission, gave rise to a trend that fitted

to a stoichiometric trend with $n = 6$ and thus in a DOPC:POPE(4:1, wt:wt) membrane p7 might indeed exist as a hexamer (Figure 7.6 A), as previously suggested [70; 73; 74].

In lipid samples containing lower protein to lipid molar ratios the analysis was less clear. The true FRET efficiency decreased at these ratios (Figure 7.6 D and F) and is comparably low at a hexamer to lipid molar ratio of 1:2,000 with $E \sim 0.19$. There is a large error associated with lower protein to lipid molar ratios. The $E_{app,se}$ values are of lower intensity and do not follow a clear stoichiometric trend (Figure 7.6 C and E). The $E_{app,se}$ fits reasonably to a trimeric complex (Figure 7.6 C and E, green line), however other scenarios including a mixture of dimers and hexamers are plausible (Figure 7.6 C and E, turquoise line), which would suggest the existence of dimeric p7 possibly as a sub-assembly unit similar to the suggested dimer-of-dimers assembly for M2 [79; 390; 399; 400], note that in the case of M2 the dimers are stabilised by a disulphide bond. However, based on the data presented here this remains speculation and cannot be concluded. In summary p7 might possibly exist in a subform in a membrane in addition to hexameric p7 at high protein to lipid molar ratios. Furthermore, protein concentration in a membrane might be of importance for p7 assembly into oligomers.

Based on these results the following experiments were performed in comparably dense membranes at a high hexamer to lipid molar ratio of 1:150, which fitted to a hexameric stoichiometry, in order to further characterise and possibly verify the existence of p7 as a hexamer in a DOPC:POPE (4:1, wt:wt) membrane environment.

7.2.2 p7 mobility profile by cwEPR

The dynamic behaviour of spin-labelled p7 was investigated in high-density membranes using spin labelled p7 Gt1b J4 G0,C-1 (Table 7.1). Based on the stoichiometry analysis by FRET a large proportion of p7 is expected to form oligomeric complexes of six protomers at this protein to lipid ratio. A large change in the oligomeric state could result in a detectable change of the overall protein dynamics and in turn also in the nitroxide correlation on the *ns* timescale. A change in the oligomeric state of the protein could affect the local environment of the spin label, affecting its motional regime, which would be reflected in the cwEPR spectrum if the exchange between the two environments is slow on the EPR timescale ($\sim$ ns; [401]). The cwEPR spectrum of spin-labelled p7 resulted in multi-component spectra

in all lipid to protein ratios tested (Figure 7.7). The composite spectrum was fitted to two individual components using spectral simulation (*EasySpin*). In short, an initial fit for two dynamically distinct environments was generated using a global search, based on a genetic algorithm. The result of this was used as the starting point for a local search utilising a Levenberg-Marquardt algorithm to find a good fit. Fitting to two-component systems yielded overall good approximations of the dynamic system with RMSD values in the range of 0.01 - 0.015. The relative proportions of the motionally distinct environments were analysed (Figure 7.7) and at a hexamer to lipid molar ratio of 1:150, ∼60% of the spin-labelled is in the slow-motion component (Figure 7.7 A), which is believed to be a motionally restricted homo-hexamer based on the FRET stoichiometry (Section 7.2.1). The relative proportion of spin-label contained within the slow mobility component seems to correlate with protein to lipid molar ratio. At the more dense environment of protein to lipid molar ratio for 1:100 ∼65% are contained within this proportion (Figure 7.7 B) and for a molar ratio of 1:70, ∼72% of p7 is motionally restricted (Figure 7.7 C). The relative correlation times of the two distinct environments were estimated to be $1.6 - 2 \cdot 10^{-9}$ s and $5.4 - 7.8 \cdot 10^{-9}$ s for the slow and fast mobility components respectively. The estimated correlation times are expected to be faster than the overall protein correlation based on the fact that the terminus is extended and already expected to be dynamic. Thus, the protein dynamics as a whole within an oligomer might deviate significantly from the local nitroxide correlation time.

Overall these results suggest, that the local protein concentration within a bilayer might be of importance for protein oligomerisation. It seems that a high protein concentration is needed in order for a large proportion of p7 to form oligomeric complexes as suggested by FRET analysis (Figure 7.6), the resulting slow mobility component of the composite cwEPR spectrum could indicate the oligomeric p7 population. Note that the peptide to lipid ratio causes very dense membranes that may effect overall diffusion rates observed. Nevertheless, for both experimental techniques a correlation of oligomerisation to the protein to lipid ratio was observed, similar to M2 assembly [79; 402].

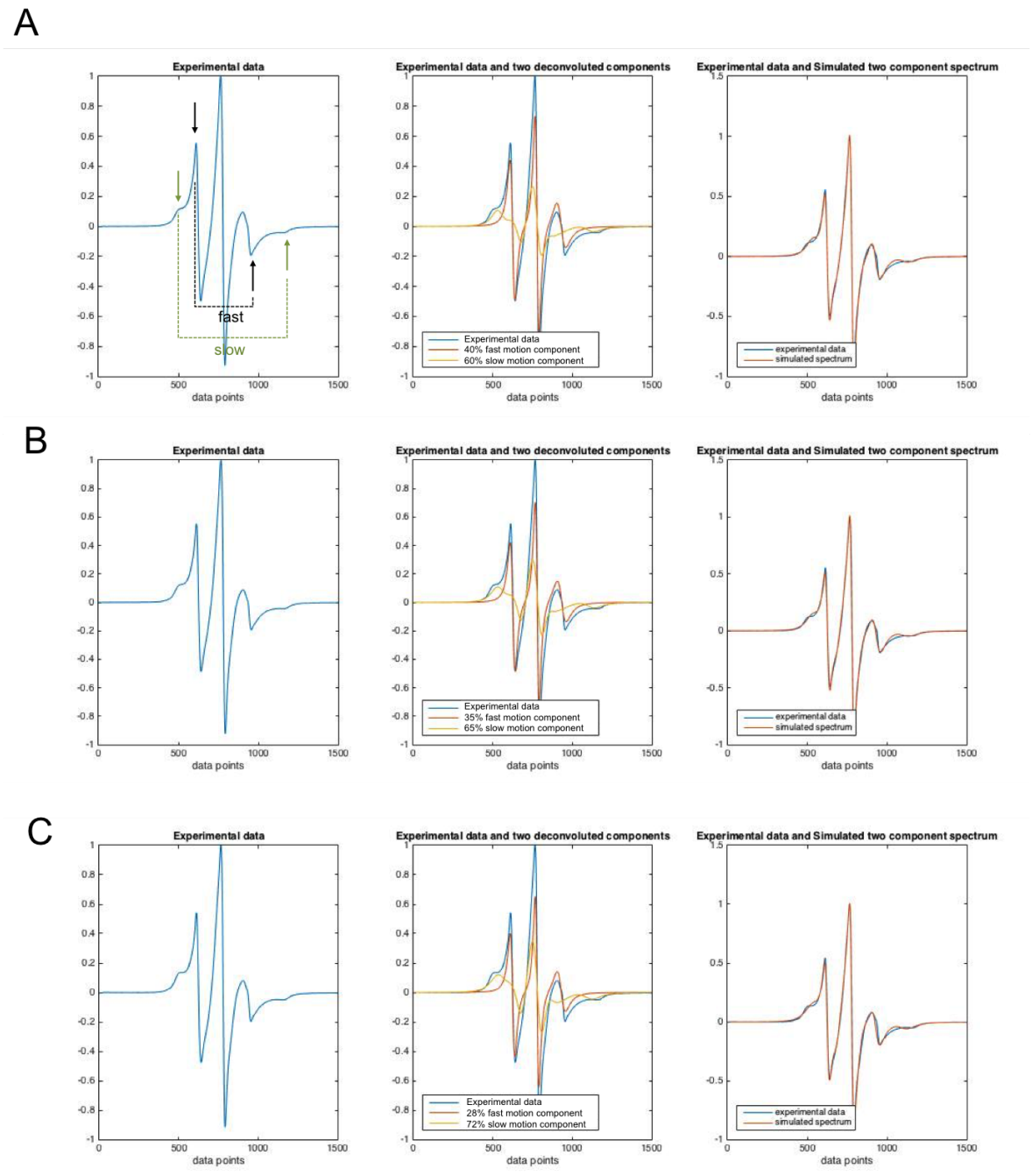

Figure 7.7: cwEPR spectra of p7 spin labelled at the N-terminus are shown at different peptide to lipid ratios showing a composite spectrum of a slow and a fast mobility component (illustrated by arrows: fast (black) and slow (green). The experimental spectrum is shown in the left panel. The spectra were deconvoluted for two sub-populations, one fast mobility and a slow-mobility component. Individual components are overlaid in the middle panel. The sum of the individual components and the experimental spectrum is shown in the right panel. Lipid to a suggested p7 hexamer molar ratios are 1:150 (A), 1:100 (B) and 1:70 (C).

7.2.3 Oligomeric state and protomer conformation by DEER

7.2.3.1 Modulation depth behaviour based on spins within the nano-object

A comparably large proportion of p7 seems to reside as part of a slow-mobility population, possibly describing the oligomeric complex, in a membrane containing p7 (p7 Gt1b J4 C-1,G0; Table 7.1) at a 1:150 protein to lipid molar ratio (60% - 70% based on cwEPR analysis; Figure 7.7). In an attempt to verify the suggestion that p7 forms hexamers under these experimental conditions, the behaviour of modulation depth of the time dependent DEER trace was investigated at different overall p7 labelling efficiencies. In a theoretical hexamer, spin dilution with unlabelled p7 to a final spin-label proportion of 33% should yield on average two spins per hexameric complex (Assumption 1). Under assumption 1, $\Delta(\rho, 33\%) = \rho$ should hold (equation 7.11). The obtained value for ρ under these conditions was then used in order to investigate n as part of equation 7.11. A sample containing 100% labelled p7 protein was used to analyse the change in modulation depth in order to obtain "n" under assumption 1; if p7 resides in hexamers n should equal six.

The observed modulation depth for the fully spin-labelled sample (100%) at a constant protein to lipid molar ratio of 1:150, comparable to the experimental setting in section 7.2.1, increased as expected when compared to the spin-diluted sample at 33% relative labelling (Figure 7.8). The modulation depth correlates with the number of coupled spins in a given nano-object and thus this increase is attributed to replacing unlabelled protein within a nano-object by labelled p7 [392]. The observed modulation depth of the spin-diluted sample is comparably low at 0.057, whereas the modulation depth for a fully labelled sample was determined to be 0.244.

under assumption 1:

$$\Delta(\rho, 33\%) = \rho \tag{7.12}$$

$$\Delta(\rho, 33\%) = 0.057 \tag{7.13}$$

$$\Delta(\rho, N) = [1 - (1 - 0.057)^{N-1}] \tag{7.14}$$

$$0.244 = [1 - (1 - 0.057)^{N-1}] \tag{7.15}$$

$$N = 5.77 \tag{7.16}$$

Thus, the relative increase in modulation depth observed by adding in spins is in relative good agreement with the behaviour expected for a hexamer as observed by FRET. However, it should be noted that, for real spin counting, ρ should be related to a real spin-pair as found in a synthetic biradical. Nevertheless assuming same sample preparation and importantly same labelling efficiencies, this can be an indication of the overall behaviour of an expected hexamer. The overall low modulation depth observed, even for a fully labelled sample, is an indication of possible incomplete labelling (represented by the labelling efficiency f), or a large proportion of labelled p7 is not contributing to spin-coupling in a nano-object (an estimated ~40% of the total p7 population in the sample is expected not to contribute to the spin-coupling in the nano-object based on cwEPR and the hypothesis that the different mobility components arise due to oligomerisation; Figure 7.7 A). This will lead to a reduced modulation depth as monomers will be perceived as uncoupled spins. Imperfect removal of

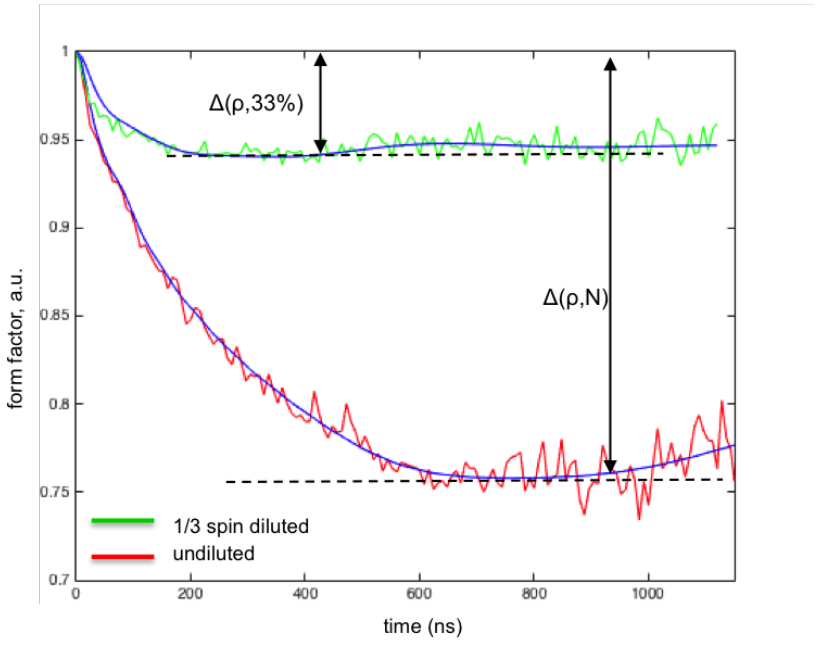

Figure 7.8: The dipolar evolution is shown for p7 Gt1b J4 C-1,C0 is shown for a sample spin-diluted to an overall labelled proportion of 33% (green) and fully spin labelled (100%, red). The corresponding modulation depths are highlighted by black arrows as $\Delta(\rho, 33\%)$ and $\Delta(\rho, N)$.

spin label can also affect the observed modulation depths. Free spin-label was removed by extensive dialysis after the labelling reaction, validated by cwEPR.

7.2.3.2 Channel stoichiometry based on inter- and intra-monomer distance constraints

7.2.3.2.1 Inter-monomer constraints

The proposed hexameric assembly of p7 in membranes was further investigated using single-labelled p7 C-1,G0 (Table 7.1) in high protein density membranes. The aim is to obtain absolute distance constraints between the individual N- and C-termini within the nano-object in order to determine the dimensions of the nano-object as well as the overall symmetry of the assembly. Having all monomers labelled with nitroxide spins allows modulation depth-dependent parameters to be measured but perturbs the dipolar evolution as discussed in section 7.1.3. Two approaches were used in order to obtain resolved distance constraints: (I) a fully labelled sample was prepared and the pump-pulse amplitude was reduced in steps of 20%, lowering the relative proportion of flipped spins in the spin population at the pump frequency v_{pump}. (II) Samples were spin-diluted as previously described to a total of 33% spin-labelled p7, based on the assumption that six monomers are present in the nano-object. Either approach should give rise to dipolar evolution functions based on the sum of individual spin-pairs rather than coupled multi-spin complexes.

As expected, a reduction in the pump-pulse amplitude led to reduced modulation depths (Figure 7.9 A), at a comparable absolute noise level. This in turn increased the relative noise level for low pump-pulse amplitudes with low modulation depths. The corresponding distance traces obtained by Tikhonov regularisation are plotted in Figure 7.9 B. The distance distributions for pump-pulse amplitudes of 100%, 80% and 60% are dominated by a large distance around ∼4 nm. This large contribution might be due to nonspecific long-range distance coupling due to the comparably high spin density in the membrane, which is indicated by the upwards trend (an unresolved oscillation) at the end of the time-dependent domain of these samples (Figure 7.9 A). Note that 4 nm is comparably close to the expected bilayer thickness of ∼4.5 nm of DOPC [403]and this distance could also arise from antiparallel aligned p7 monomers with opposing termini. The shorter distances are not well resolved for high

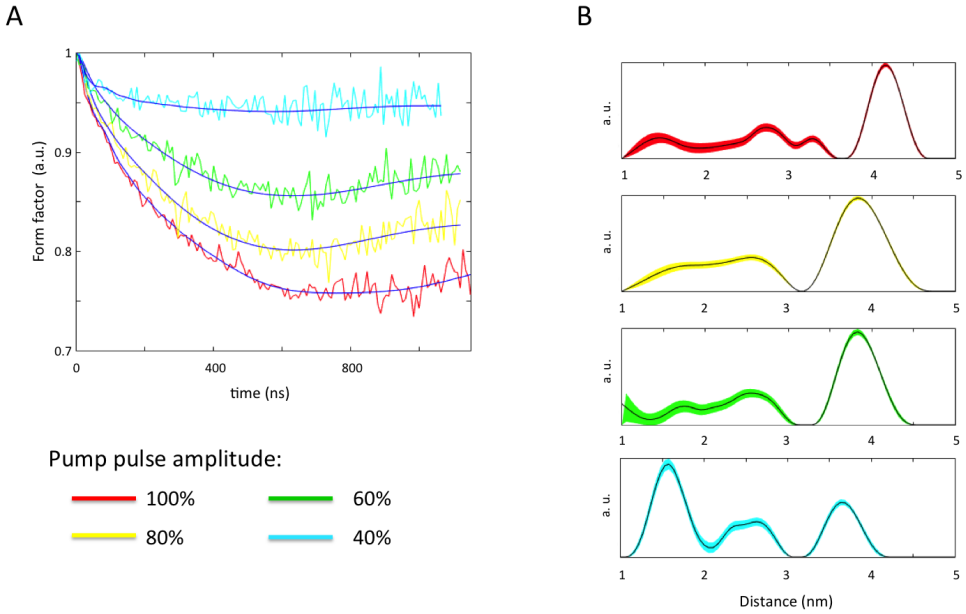

Figure 7.9: The dipolar evolution functions and corresponding distance distributions obtained for p7 labelled at the N-terminus. (A) The time-dependent dipolar evolution is shown for different pump-pulse amplitude, keeping the pump-pulse length constant at 12ns. (B) Corresponding distance distributions as obtained by Tikhonov regularisation. 4p DEER experiments run at 30K, Q-band, 90 MHz frequency separation and a hexamer to lipid molar ratio of 1:150.

pulse amplitudes and only become visible at low pump-pulse amplitude. However, due to comparably high noise in the time-dependent domain at low pump-pulse amplitudes and due to the possibility of spin crowding in the membrane, the sample was spin-diluted to 33%, which should have a similar effect on the dipolar evolution with the benefit of reducing the overall spin density by a factor of three (Figure 7.10). The same high-density membranes were analysed by DEER using spin dilution to 33% (Figure 7.10).

The dipolar evolution functions obtained show a moderate modulation depth of ~ 0.07, however, an oscillation is observed in the time-dependent trace across all three tested protein to lipid molar ratios (Figure 7.10 A,C and E). Overall the distance distribution obtained by Tikhonov regularisation seems to be better resolved as previously observed for low pump-pulse amplitudes (Figure 7.10 B,D and F). In the case of a hexamer to lipid molar ratio of 1:150 (Figure 7.10 B), three main distance populations can be observed at $\sim$1.7 nm, $\sim$2.4 nm and $\sim$3.1 nm. Under the assumption of a symmetric homo-oligomer this could correspond to a hexamer or heptamer. The geometric relationships of a hexagon and heptagon are illustrated in Figure 7.10 G and H respectively. For a shortest distance of 1.7 nm the longest distance

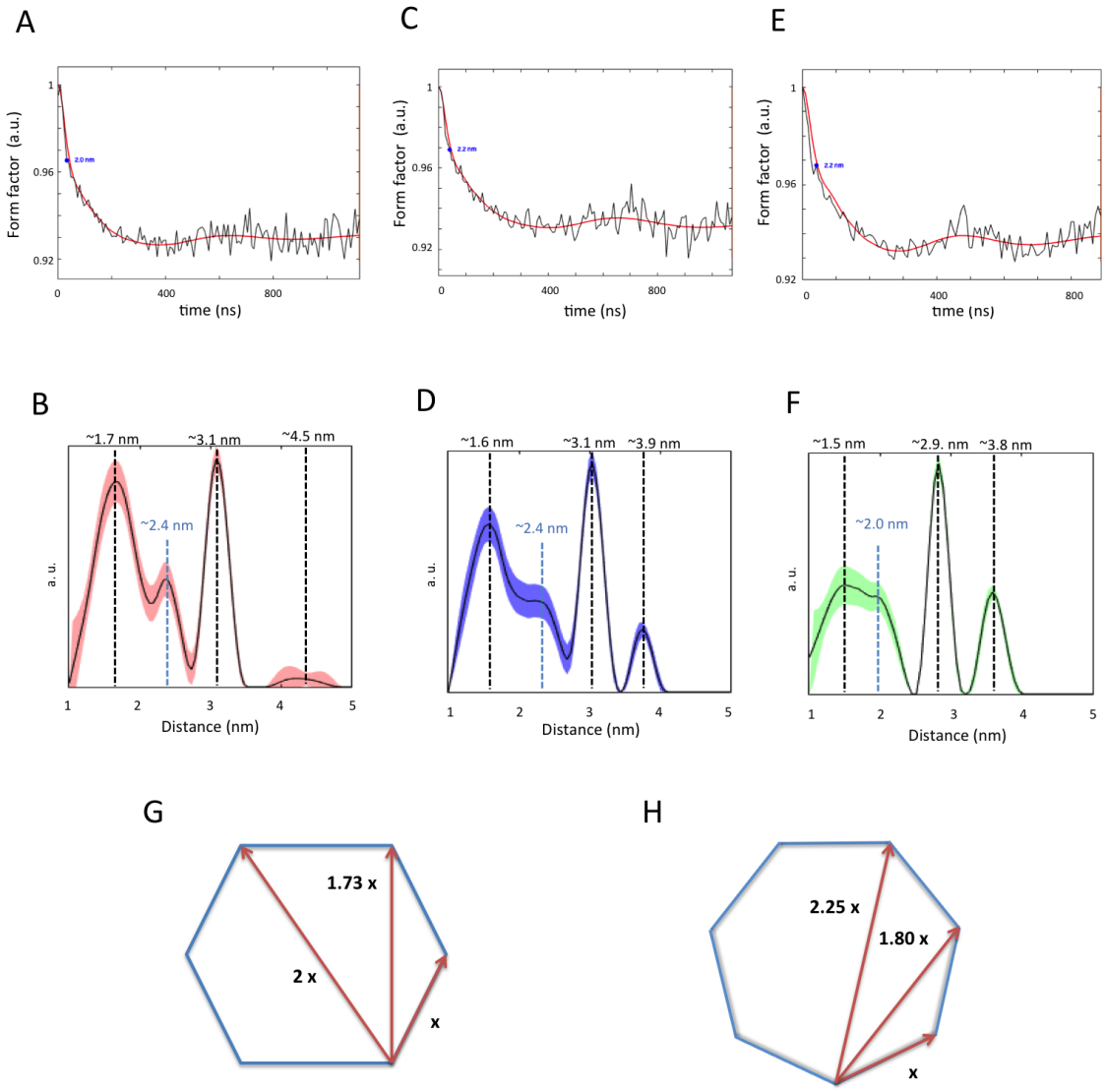

Figure 7.10: DEER traces of spin-diluted p7 in a membrane at different protein to lipid molar ratios are shown. The top panel shows the time-dependent dipolar evolution function, the bottom panel illustrates the distance constraints obtained based on Tikhonov regularisation. Probed hexamer to lipid molar ratios are: 1:150 (A and B); 1:100 (C and D) and 1:70 (E and F). The distance relationships in a symmetric hexagon and heptagon are illustrated in (G) and (H) respectively. The 4p DEER experiments were performed at 30 K, Q-band and with a 90 MHz frequency separation.

of 3.4 nm would be expected in a symmetrical hexamer, the observed 3.1 nm is slightly too short but in the expected range, considering the comparably broad distance distributions.

For a higher hexamer to lipid ratio the relationship between the shortest and longest distance (excluding the furthest distance in all cases ∼4.0 - 4.5 nm) is also close to the expected geometric arrangement of a hexamer (Figure 7.10 D; 1.6 nm and 3.1nm; Figure 7.10 D; 1.5 nm and 2.9 nm). For a symmetrical heptamer the largest expected distance would be around 3.8 nm related to the shortest observed distance. An additional distance contribution is observed across all samples, only poorly resolved for hexamer to lipid molar ratio of 1:150, around ∼4.5 nm. At increasing protein to lipid molar ratios this long distance distribution becomes more dominant and shortens to ∼4 nm (Figure 7.10 D and F), which is close to the dominant distance previously observed for a fully labelled p7 sample at 1:150 molar ratio (Figure 7.9 B). The long distance contribution translates into an unresolved upwards trend at the end of the time-dependent trace (Figure 7.10 C and E), which is more pronounced for a long DEER trace recorded as a combination of a 3p and 4p experiment that revealed clear long-range contributions that made background correction not possible (see appendix, Figure A.9). The absolute distance of this contribution correlates with protein to lipid molar ratio; e.g. in a more dense membrane environment it becomes slightly shorter. It should be noted that this distance distribution is also in close proximity to what could be expected of a heptameric configuration (3.8 nm; Figure 7.10 H), however based on the large observed unresolved oscillation seems unlikely (Figure Figure A.9). Based on these results it was decided to take the 1:150 hexamer to lipid molar ratio forward, which under spin dilution, seems to result in distinct distance populations and in which the effect of spin overcrowding in the membrane does not dominate.

Based on this, the C-terminus was investigated under similar experimental conditions using mutant p7 Gt1b J4 G64,C65 (Table 7.1, Figure 7.11 B).

The dipolar evolution function of p7 spin-labelled at the N- and C-termini are overlaid (Figure 7.11 C). It is notable that the modulation depth of the C-terminally labelled trace is larger compared to the trace obtained of the N-terminus, which might be due to sample preparation differences, e.g. a larger labelling efficiency f for a different mutant. Additionally, a comparably higher signal-to-noise is achieved for the C-terminal sample, probably attributed

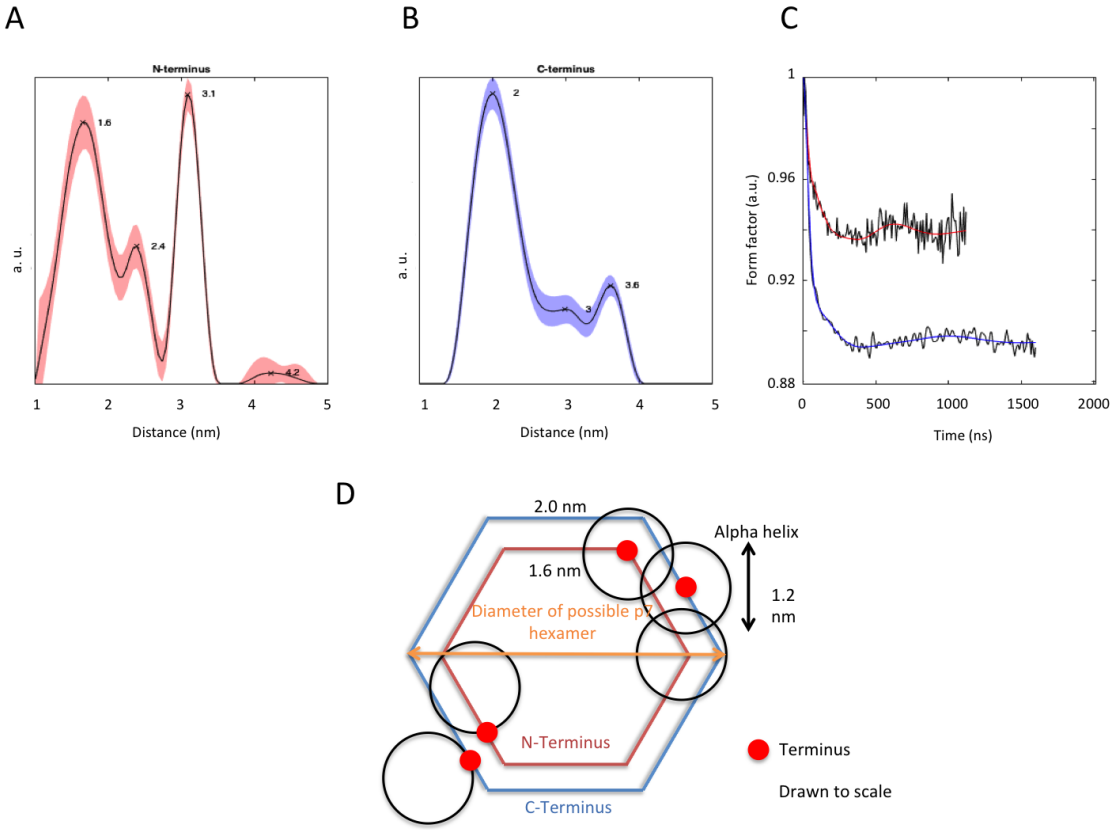

Figure 7.11: The distance distribution obtained for p7 spin-labelled at the N-terminus and C-terminus are shown in (A) and (B) respectively. The time-dependent dipolar evolution functions are overlaid in (C). A schematic illustrating a symmetric hexagon taking the shortest resolved distance of both N- and C-terminus as a guide is illustrated (D).

to longer T_2 times (∼1,000 ns compared to ∼600 ns) due to the addition of D_2O (40%, see appendix, table A.1).

The distance distribution of the C-terminus shows a well resolved short distance and a distribution of two overlaid longer populations (Figure 7.11 B). The short distance at ∼2 nm is dominant, which might be indicative of multi-spin effects if approximated as spin-pairs [391; 396]. The distance distribution obtained for the C-terminus are shifted about ∼0.5 nm with respect to the data obtained for N-terminally labelled p7, with the longest distance observed being ∼3.6 nm compared to ∼3.1 nm for the N-terminus. Similarly the differences observed between shortest and longest distance are broadly consistent with a hexagonal geometry, yet the longest distance at ∼3.6 nm falls slightly short of the expected ∼4 nm based on the shortest distance of ∼2 nm.

Overall, the data suggests that if p7 Gt1b J4 forms oligomeric complexes that the C-terminus is the outwards facing helix, where the N-terminus would face the pore itself. A basic schematic is drawn based on the shortest distances measured for N- and C-termini respectively (Figure 7.11 D) and circles representing the diameter of an alpha helix (taken to 1.2 nm [404]). Note that the only small difference between the individual termini is too small in order accommodate two transmembrane helices within the oligomer under the assumption that the respective termini are centred to the helical diameter (Figure 7.11 D, filled red circles). If however these are not centred and the termini have a rotational pitch, this schematic illustration becomes possible. Both termini were shown to be mainly unstructured in previous studies (Figure 6.17), and additionally the termini were extended by a glycine and a cysteine residue adding to the flexibility. This might give sufficient flexibility for the nitroxide radicals to locate to a common preferred environment such as the interface region, which might lead to a reduced observed difference.

7.2.3.2.2 Model-based DEER analysis

The model-based analysis of the experimentally obtained DEER traces is based on two hexameric models: (I) The high-resolution structure proposed by B OuYang *et al.* 2013 and (II) a partially stabilised hexameric model (5 ns simulation) based around a hairpin conformation in a bilayer (obtained from N Zitzmann (Oxford)) [2]). The Multiscale Modeling of Macromolecular systems (MMM) software [210; 405] was used to calculate spin-label rotamer populations for residues spin-labelled in the experimental setting (Figure 7.12 B and D and Figure 7.13 B and C). These spin-label densities were used in order to simulate a theoretical distance distribution, which was compared to the experimental DEER distance distribution (Figure 7.12 C and E and Figure 7.13 D and E).

The rotamer spin labelled N-terminus of the hairpin-based oligomer gave rise to a distance profile ranging from ∼1 nm - ∼ 3.5 nm (Figure 7.12 C, red), which is in good agreement with the experimental trace obtained for N-terminally labelled p7 in a membrane (Figure 7.12 C, black). Shorter distances than 1.5 nm are not reported for the experimental trace, which is the lower limit for accurate distance determination using DEER. Note the experimental p7 construct

[2]The model is based on sequence data analysis and no experimental constraints are included. The N-terminal helix was placed pore-facing based on [69]. The bilayer for simulation is DOPC:POPE (4:1, molar ratio)

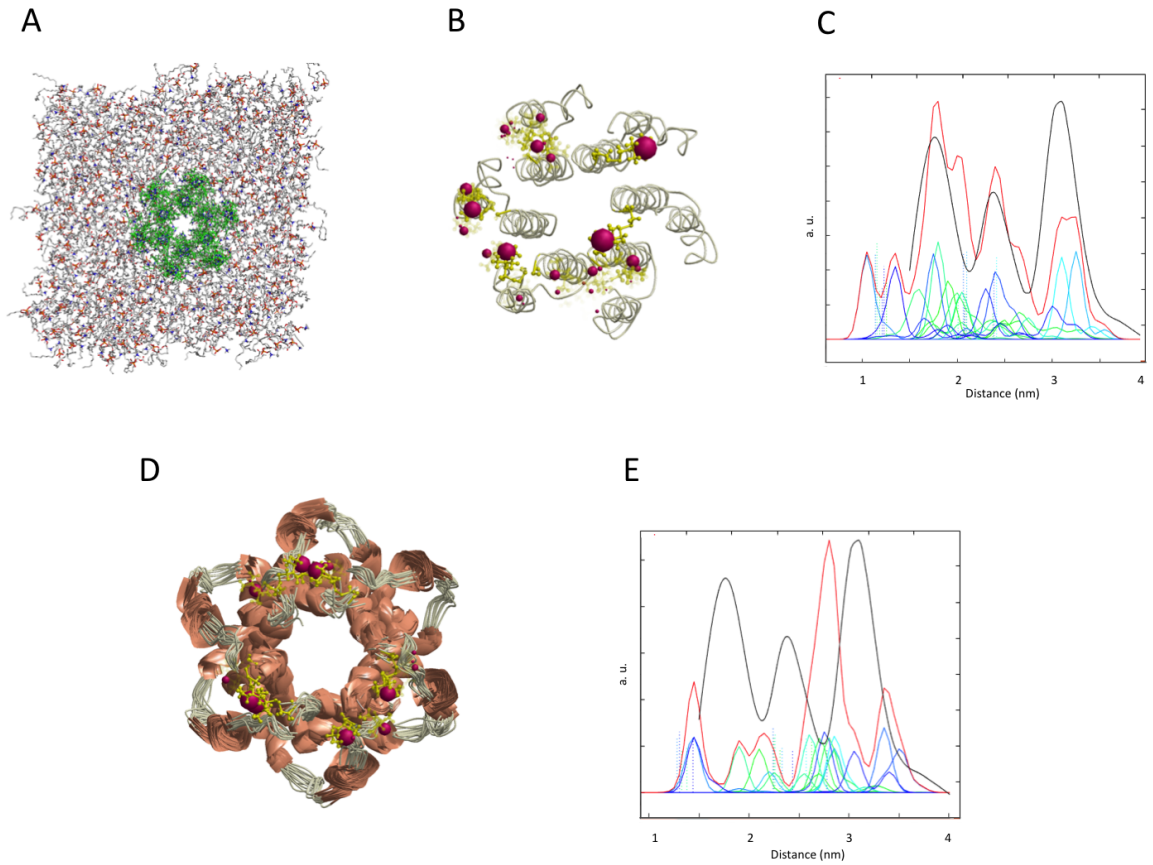

Figure 7.12: Theoretical DEER distance distributions calculated for two different p7 models using the MMM software package [210; 405]. The MTSL rotamer analysis was performed at residue 1 of all monomers of each structure. (A) Model one is a membrane stabilised (5ns simulation) of a p7 hexamer composed of monomers in a hairpin conformation (obtained from N Zitzmann. (B) The predicted MTSL rotamers of model (A) were calculated in absence of the lipid environment, and the expected spin density is shown as spheres in magenta and the MTSL side chain is in yellow in ball and stick representation. (C) The MMM simulated distance distribution expected from the spin density shown in (B): simulated trace (red); experimental trace (black); individual spin-pair components (ranging from green to blue). (D) The ensemble hexameric NMR structure proposed by B OuYang *et al.* spin labelled at residue one is shown. (E) The simulated distance distribution expected from the spin density shown in (D): simulated trace (red); experimental trace (black); individual spin-pair components (green and blue).

used was extended (G0, C-1), while for the simulation the spin-label was placed at residue one. In comparison the simulated distance distribution for calculated MTSL rotamers based on the high-resolution structure proposed by B OuYang *et al.* 2013 gave rise to a different distance profile and individual distances are shifted with respect to the experimental trace (Figure 7.12 E). This could be attributed to a slightly different helix arrangement in a membrane compared to detergent or variation across genotypes or the extension of the N-terminus for spin labelling.

A similar model based comparison was performed for rotamers attached to the C-terminus (residue 63) for the same two models (Figure 7.13). The membrane stabilised hairpin-model gave rise to a different distance distribution compared to the experimental distance profile (Figure 7.13 D). However, a small alteration of the C-terminal away from a helix to a more unstructured motif (explained in Figure 7.13 A and C), leads to a distance profile that is broadly consistent with the experimentally determined profile (Figure 7.13 E). An unstructured C-terminus seems likely since the two consecutive proline residues at positions 58 and 59 (for genotype 1b J4; Figure 7.2 A) most probably lead to a discontinuation of the C-terminal helix. For comparison theoretical DEER distances in the entangled oligomeric structure by B OuYang *et al.* 2013 were simulated for rotamers attached at the C-terminus (Figure Figure 7.13 F and G), showing some overlap with the experimental spectrum.

The poor overall fits (apart from Figure 7.12 C) for N and C-terminus cannot exclude distinct oligomeric models. The termini are expected to be flexible [74; 406] and the added glycine residue will add to this flexibility resulting in broad experimental DEER distributions. Furthermore the rotamer populations are calculated in the absence of a membrane environment and these might differ due to restrictions induced by the lipid environment. Thus, these experiments yield initial insight into the oligomer stoichiometry and oligomerisation behaviour but cannot reliably propose a model of p7 oligomerisation, without the inclusion of further constraints. However, in general terms a hexameric homo-oligomeric pore structure still remains plausible.

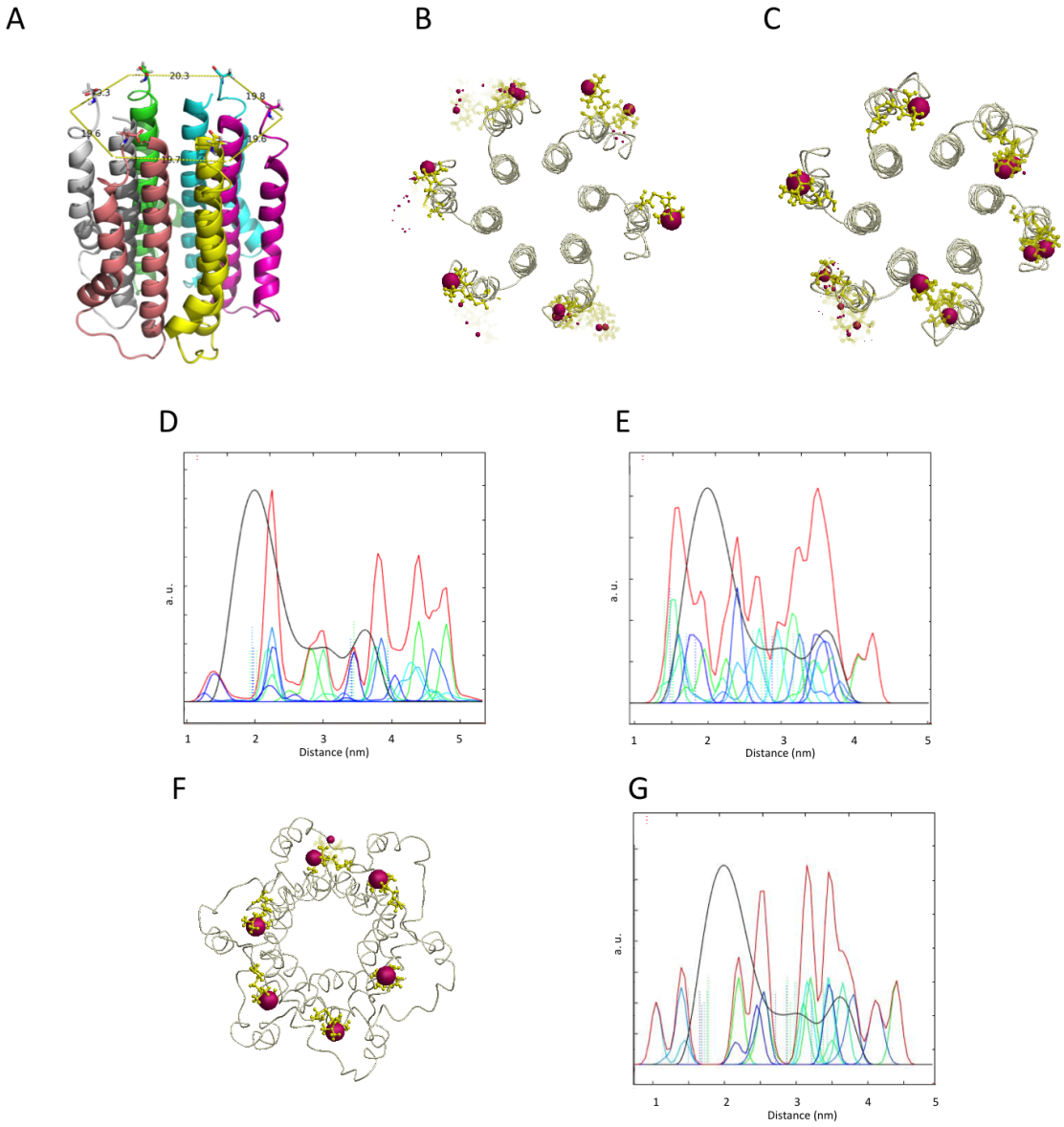

Figure 7.13: Structure-based DEER simulation of the spin-labelled C-terminal residue (residue 63) are shown, which are based on the hexameric structure shown in Figure 7.12 A and the high resolution structure by B OuYang *et al.* 2013. (A) The membrane stabilised model (N Zitzmann (Oxford)) is shown. The C-terminus is highlighted in "stick" representation of the alanine 63. The dashed yellow line illustrates the termini positions in the initial model as shown in Figure 7.13 A, the C-terminal alanine residues are altered to mimic a more unstructured terminus. (B) Nitroxide spin-label rotamers attached to the C-terminus (residue 63) at position illustrated by the yellow frame (line). (C) Nitroxide spin-label rotamers calculated for a slightly amended C-terminus shown by alanine in stick representation in (A). (D) Corresponding simulated DEER distance distribution as described by the spin-density shown in (B). (E) Corresponding simulated DEER distance distribution as described by the spin-density shown in (C). (F) Spin-label density as described by rotamer population for the structure proposed by B OuYang *et al.* 2013. (D) Corresponding simulated distance distribution for system described in (C); colour code as before described in Figure 7.12.

7.2.3.2.3 Intra-monomer constraints

Following on from the characterisation of the inter-molecular configuration of the oligomeric p7 complex, double mutants (p7 Gt1b J4 S21C, L51C and p7 Gt1b J4 K33R, L51C; Table 7.1) were used to probe the overall hairpin configuration of p7 within a membrane. The aim is to probe for conformational changes upon oligomerisation as described by B. OuYang *et al.* 2013, the residues have been chosen in order to report on a possible opening of the otherwise proposed hairpin conformation (Figure 7.14). Based on the C_α - C_α distance a separation of 8.8 Å between residues 21 and 51 (p7 Gt1b J4 S21C, L51C) was observed for a monomeric hairpin conformation (Figure 7.14 A; [87]), whereas for the open conformation a separation of 37.8 Å would be expected (Figure 7.14 B; [66]). It should be noted that the open monomeric conformation was observed in Gt5a where residue 21 is a tryptophan instead of the serine in genotype 1b, which is used throughout this thesis.

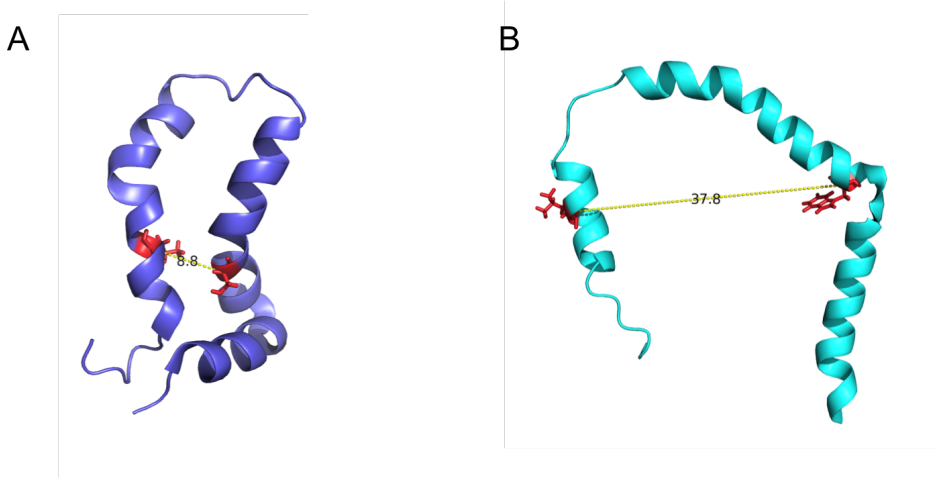

Figure 7.14: The C_α - C_α distance between residues 21 and 51 are shown in angstrom for two proposed p7 monomer conformations. Residues 21 and 51 are highlighted in red. Note that the spin label rotamer population will ad to the shown distance. (A) A monomeric solution NMR structure in DHPC (PDB:2MTS; [87]). (B) A monomer within the oligomeric proposed structure based on solution NMR in DPC (PDB: 2MGX; [66])

As a first proof-of-concept p7 S21C L51C was labelled and an initial DEER trace was recorded in 27 mM cyclofos-6 in order to compare the obtained distance distribution to a monomeric p7 Rosetta model of the same genotype and same detergent environment (B Oestringer *et al.* (unpublished); Figure 7.15).

The dipolar evolution function shows a single decay with a modulation depth of ∼0.14 with limited oscillations, an indication of a single short distance, which was analysed by

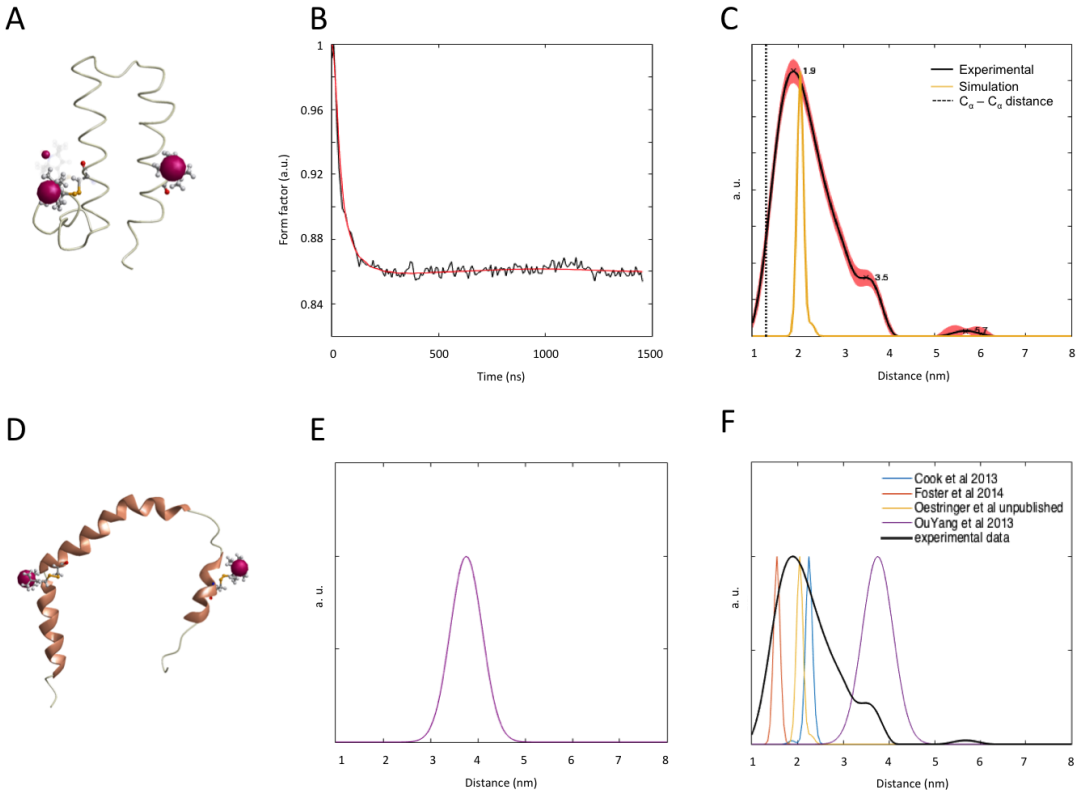

Figure 7.15: Simulated and experimental DEER spectra for p7 Gt1b J4 S21C L51C in detergent (27mM cyclofos-6). (A) Nitroxide spin-label rotamers were calculated for the corresponding labelled positions attached to Rosetta model of same p7 Gt1b J4 in the same detergent environment (B Oestringer *et al.* (unpublished)), rotamer calculation performed using matlab based Multiscale Modeling of Macromolecular systems (MMM) software [210; 405]. The location of the predicted spin-density are shown as a magenta sphere. (B) Dipolar evolution function of experimentally recorded p7 Gt1b J4 S21C L51C in detergent. (C) Experimental distance distribution (by Tikhonov regularisation) and simulated expected distance are overlaid. (D) For comparison rotamers were attached to the same residues in a monomer corresponding to the open monomer conformation suggested by B. OuYang *et al.* 2013, the expected DEER distance is plotted in (E); the individual monomer in the assembly differ and an average is displayed (see appendix Figure A.12). (F) Expected distance distribution for published hairpin structures and oligomer structure are overlaid, structures are described in Figure 6.1.

Tikhonov regularisation (Figure 7.15 B and C). The expected distance distribution, based on calculated rotamer populations attached to a monomeric p7 model obtained in similar experimental conditions by solution NMR (B Oestringer *et al.* 2013), is overlaid and in relative agreement indicating helix packing in a hairpin orientation under these experimental conditions. The experimental distribution is broad, which might indicate some rotamer and/or protein flexibility in the experimental environment. The rotamer calculations are based on the low energy model rather than an ensemble of the Rosetta structure. In the experimental trace an additional population seems to be present at a distance of ∼3.5 nm (Figure 7.15

C). For comparison the simulated expected distance for the corresponding open monomer suggested by B OuYang *et al.* 2013 (Figure 7.15 D and E) and other proposed monomer structures are shown (Figure 7.15F, see appendix Figure A.11 for PDB structures indicating spin-label positions), the expected distance for the open monomer structure (B OuYang *et al.* 2013) is comparably long at ∼3.8 nm. The proposed monomeric hairpin structures are in relative agreement with the experimental distance distribution (Figure7.15 F).

Following on from this the same mutant was reconstituted (see section 6.2.2 for detail) in different model membranes consisting of DOPC, DOPC:POPE (4:1, wt:wt) and DOPC:POPE (1:4, wt:wt) at two different hexamer to lipid molar ratios (1:150 and 1:2,000). These membrane environments are analogous to membrane environments previously used to test p7 activity [72]. The aim is to obtain distance information in order to investigate conformational changes in an environment deviating from a detergent as well as between different lipid compositions. Furthermore, the opening of the hairpin into an open conformation as part of oligomers will be investigated (Figure 7.14). Note that due to small PE head-group and associated curvature constraint the formation of vesicles in DOPC:POPE (1:4, wt:wt) was monitored by static ^{31}P solid-sate NMR and powder-like spectrum was observed (see appendix, Figure A.10). The samples used were spin-diluted to a final concentration of 16% in an attempt to avoid multi-spin coupling, based on the hypothesis of hexameric p7 [3].

The results are summarised in Figure 7.16. The hexamer to lipid molar ratio of 1:150 in a DOPC:POPE (1:4, wt:wt) and in a DOPC membrane give rise to a distance distribution profile similar to the profile observed in cyclofos-6 (Figure 7.15 C), with a main distribution at ∼2.1 nm and a minor populations at ∼3.5 nm, suggesting that an overall hairpin topology is plausible in a lipid environment. For the same protein to lipid molar ratio in a DOPC:POPE (4:1, wt:wt) membrane the distribution at ∼3.5 is more pronounced. Interestingly the data obtained at a lower peptide to lipid ratio 1:2,000 show similar results, despite conflicting results for stoichiometric FRET-based analysis at this protein to lipid molar ratio (Section 7.2.1), which might attributed to different sample preparation procedures leaving some remaining detergent in the FRET sample (∼ 0.4 μ M cyclofos-6). The experimental distance constraints (DOPC:POPE (4:1; wt;wt) at hexamer to lipid molar ratio of 1:150) are overlaid with model-based DEER distances calculated using MMM in Figure 7.16 B; the major distance distribution

[3]Note that the p7 to hexamer 1:2,000 molar ratio was not spin diluted as at the time of the measurement we did not expect to observe oligomeric complexes at this protein to lipid molar ratio.

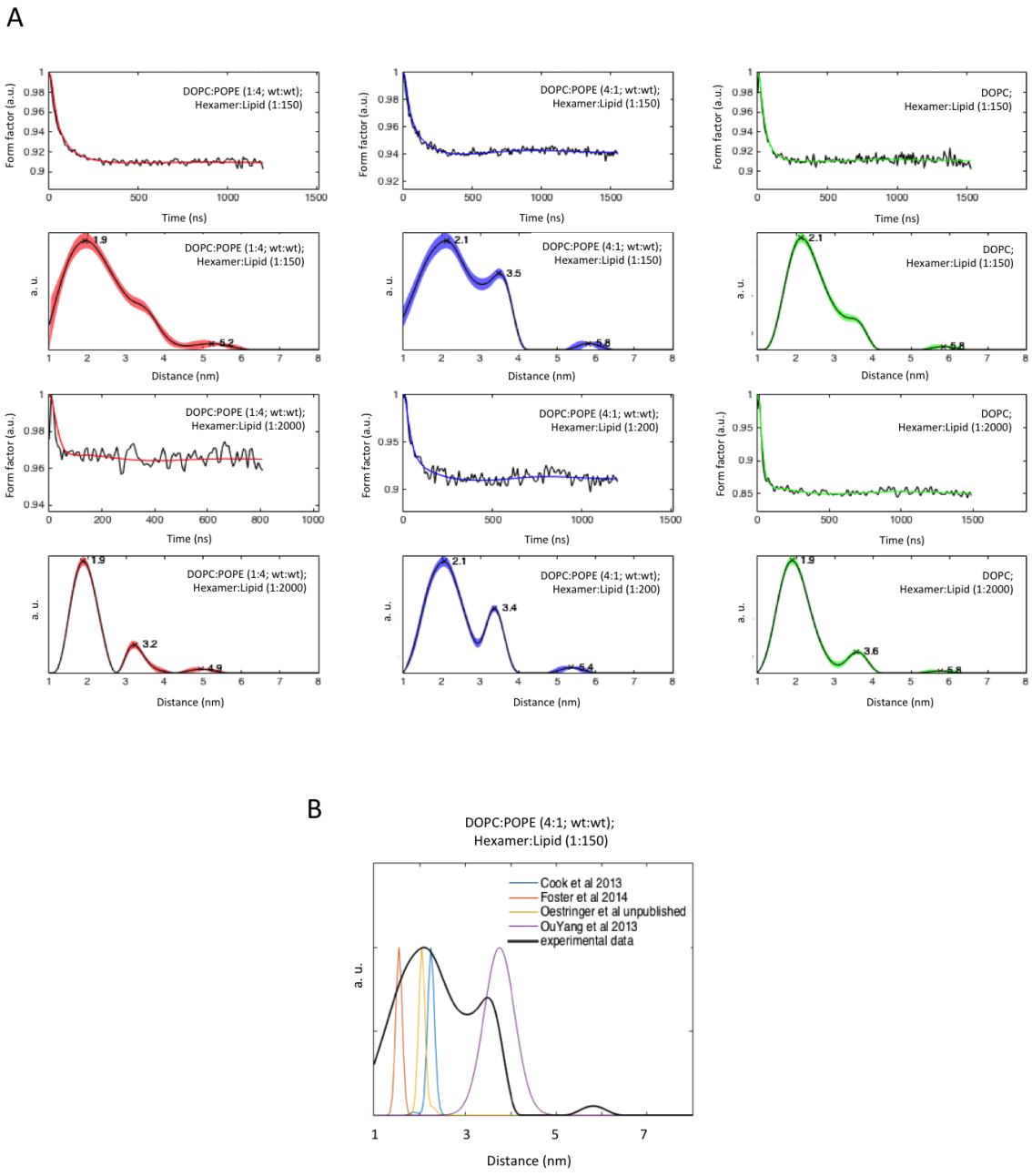

Figure 7.16: (A) The dipolar evolution function and resulting distance distributions by Tikhonov regularisation in different lipid environments are plotted: DOPC:POPE (1:4, wt:wt) in red; DOPC:POPE (4:1, wt:wt) in blue and DOPC in green. The top two panels show a hexamer to lipid molar ratio of 1:150 and the bottom two panels show a hexamer to lipid molar ratio of 1:2,000. (B) The experimental trace recorded in DOPC:POPE (4:1: wt:wt) at hexamer to lipid molar ratio of 1:150 is overlaid with expected distance distributions expected for different published p7 structures (Figure 6.1) based on residue 21 and 51; simulated using MMM, corresponding PDB structures are found in Appendix A.2.3.3.

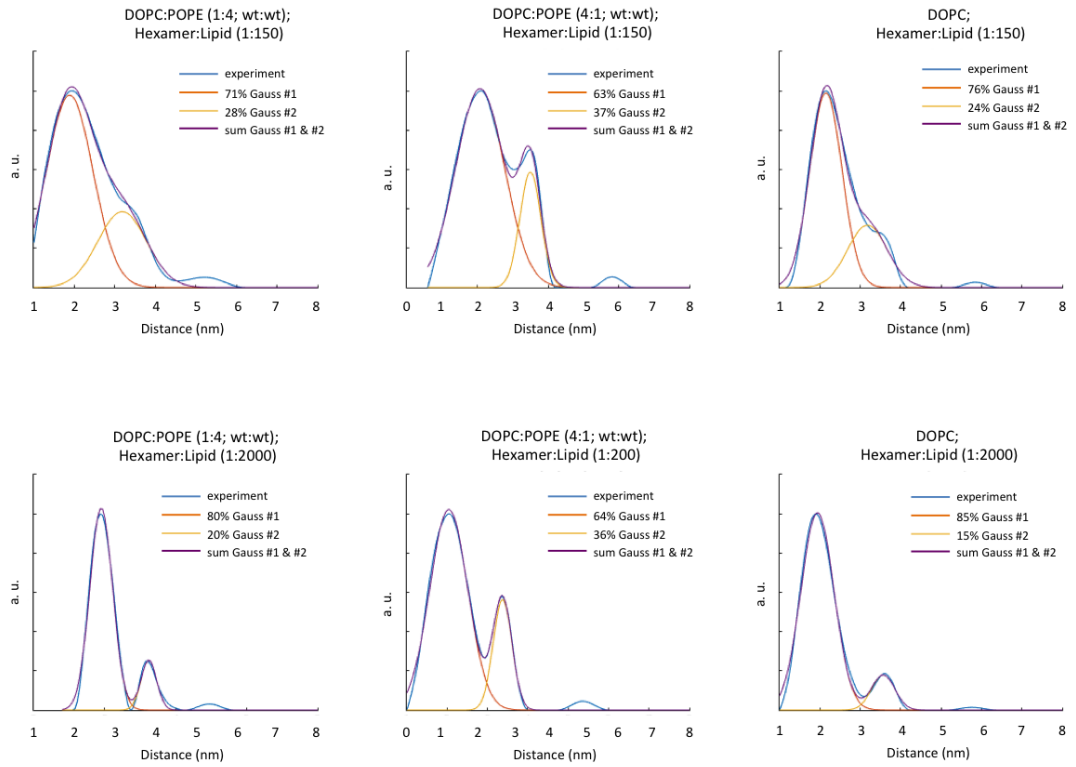

Figure 7.17: The experimental distance distributions for p7 S21C,L51C in various lipid environments fitted to two Gaussians are shown. The individual Gaussians and the sum of both are plotted. The relative proportions of each population are mentioned in the corresponding figure legend. Note that the small population at ∼5 - 6 nm was excluded from fitting. The top panel shows hexamer to lipid molar ratios 1:150, whereas the bottom panel shows hexamer to lipid ratios of 1:2,000.

of ∼2.1 nm overlays with hairpin configurations, whereas the long distance at ∼3.5 nm overlays in part with the expected distance for an entangled oligomer. The relative proportions were fitted to two Gaussian population in order to quantify the relative proportions (Figure 7.17).

The relative population of the two distance distributions at a hexamer to lipid molar ratio 1:150 in a DOPC:POPE (4:1, wt:wt) membrane gave a relative fit of ∼37% to ∼63%. This is in good agreement with the distribution of slow to fast mobility components observed by cwEPR in this environment (∼40% to ∼60%; Figure 7.7 A), which may possibly indicate a correlation between distance and mobility profiles. However, the relative proportions of the two distances seem not to correlate with protein to lipid molar ratio (∼36% to ∼64% at a 1:2,000 protein to lipid molar ratio; Figure 7.17). An opening of the hairpin topology to the extent predicted from the oligomeric model presented by B OuYang *et al.* 2013 with an

expected distance separation of ∼3.8 nm (Figure 7.15 F) between these two residues could not convincingly be confirmed in a bilayer (partial overlap) or detergent environment, note however that the p7 genotype differs from that used here.

In an attempt to further characterise p7 topology in a membrane environment an additional double mutant (p7 K33R L51C, Table 7.1) was included. This mutant, labelled directly at the N-terminus has a large theoretical distance separation between a hairpin (based on B Oestringer *et al.* unpublished) and open p7 conformation [66] (B Oestringer et al. unpublished: separation of 2.2 nm; and B OuYang *et al.* 2013: separation of 5.1 nm between residues 1 and 51 based on MMM rotamer analysis, Figure 7.18 E).

Despite being labelled at the N-terminus directly, the obtained distance distributions (Figure 7.18 B and D) look similar to distance profiles recorded for p7 labelled at residues 21 and 51. Comparing the data to the proposed models it becomes evident that most hairpin structures

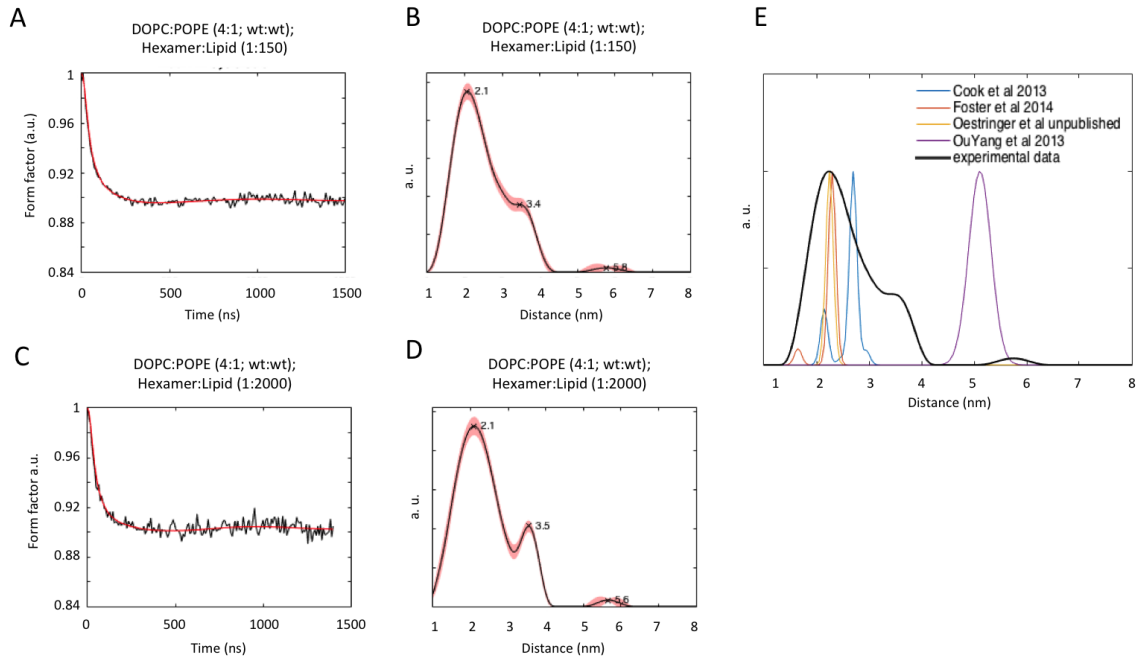

Figure 7.18: The DEER data recorded for p7 K33R L51C in DOPC:POPE (4:1; wt;wt) is illustrated. (A and B) Samples are recorded at a hexamer to lipid molar ratio of 1:150, where (A) shows the time-dependent domain and (B) the obtained distance distribution. (C and D) Samples are recorded at a hexamer to lipid molar ratio of 1:2,000, where (C) shows the time-dependent domain and (D) the obtained distance distribution. (E) Theoretical DEER distances calculated by MMM between MTSL at residues 1 and 51 in the indicated model structures compared to the experimental data of (A); see appendix Figure A.13 and Figure A.14 for detail and PDB structures.

overlap with the experimental trace (Figure 7.18 E), the open conformation of p7 as proposed by B OuYang *et al.* 2013 does not overlap suggesting that the p7 topology in a membrane is an overall hairpin configuration for genotype 1b J4. Similar to previous observations an additional distance contribution at ∼3.5 nm is observed, that does not correspond to any of the reported p7 models. A common feature between the data presented in Figure 7.18 and Figure 7.17 is that both mutants are spin-labelled at position 51, which falls in the hydrophobic leucine cluster at the end of proposed TM2 (Figure 7.2), which is "gated" by two proline residues at positions 49 and 58 (proline 58 is fully conserved). This might give rise to cis isomerisation leading to structural rearrangements for this transmembrane helix or alternatively lead to different preferred rotamer populations, that becomes detectable upon isomerisation.

The monomeric structures reported by Foster *et al.* 2014 contains a FLAG-tag at the N-terminus and consequently has a straight N-terminal helix. In contrast the Rosetta model by B Oestringer *et al.* (unpublished) shows a largely bent N-terminal domain similar to the structure presented by Cook *et al.* 2013 (Figure 6.1). The structure of Cook *et al.* 2013 is slightly shifted compared to the reported data (Figure 7.18 E), the other two hairpin configuration align well with the maximum of the experimental distance trace, despite significantly different N-terminal configurations.

7.2.4 DEER of Gadolinium (Gd^{3+}) ions

Due to experimental difficulties using nitroxide spins in multi-spin containing nano-objects, Gadolinium (Gd^{3+}) has been proposed as an alternative spin probe avoiding some of these limitations [407; 408; 409; 410]. The approach of nitroxide spin-dilution presented here lead to reduced signal, while reducing multi-spin artefacts, yet these could not be fully eliminated. The feasibility of Gd^{3+} DEER experiments were tested using a Gd^{3+}-Gd^{3+} ruler (Figure 7.19 A) kindly provided by A Godt (Bielefeld, Germany) on our system, using a conventional DEER set-up, and two consecutive pump-pulses of different shapes: (I) Square, (II) Gaussian and (III) Chirp (construction of Chirp pulses is outline in Appendix A.2.3.5). The data for squared pulses is not shown as these lead to a strong ESEEM effect of the Nitrogens in close proximity to Gd^{3+}. The experimental data for Gaussian- and Chirp-shaped pump-pulses are shown in Figure 7.19 B, C and D. Both approaches lead to well resolved distance distributions

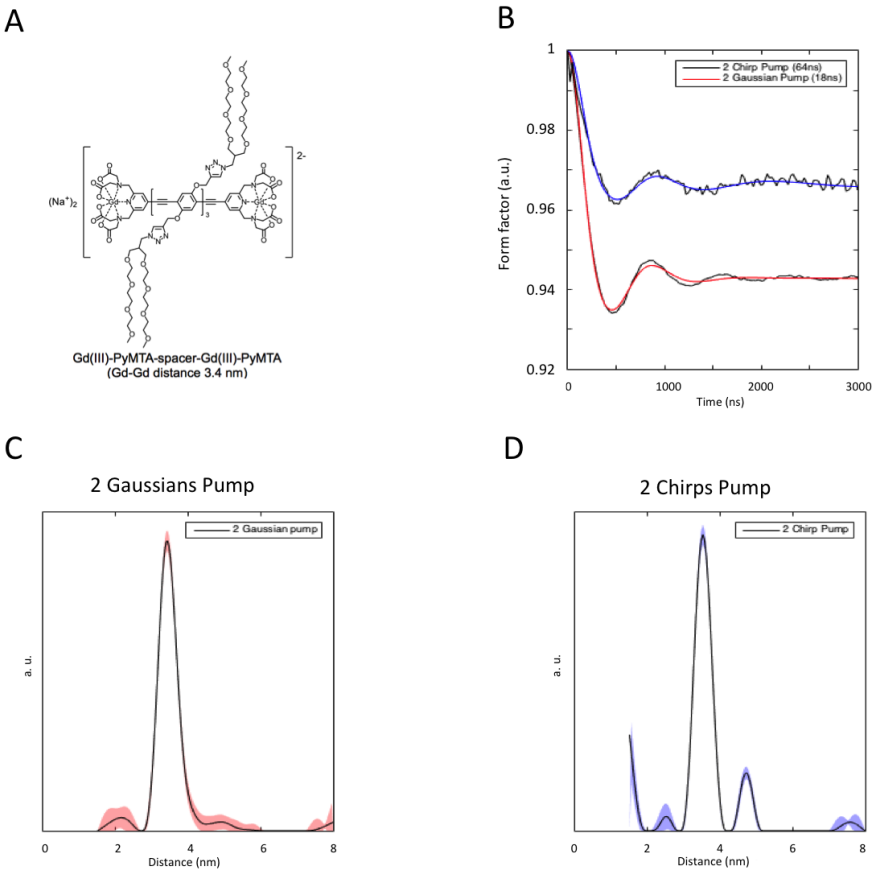

Figure 7.19: Gadoliunium (III) (Gd^{3+}) DEER on a Gd^{3+}-ruler with Gd^{3+}-Gd^{3+} separation of 3.4 nm (a gift obtained from A Godt). (A) The Gd^{3+}-ruler is shown; the individual Gd^{3+} ions are separated by a rod-like spacer [407]. (B) The DEER form factor is plotted for a DEER set-up with two consecutive pump-pulses as Chirp pulses (blue) and Gaussian pulses (red). (C) Distance distribution obtained for two consecutive Gaussian pump-pulses of 16 ns each and (D) two consecutive Chirp pulses of 64 ns each. Experiments performed in collaboration with William Myers (Department of Chemistry, Oxford).

with the Gaussian pulse shape giving slightly better modulation depths, resulting in a slightly better resolved distance. The quality of the spectrum recorded using Chirp pulses is lower compared to spectra reported in literature [407], probably due to limitations of the resonator band width of the instrumentation available. The reported distance is as expected from the moleuclar ruler 3.4 nm. Using this approach up to 80% labelling and well resolved distance distributions are reported for hexameric proteorhodopsin [411]. This approach will hopefully lead to better resolved distance profiles without distortions due to multi-spin interactions and help to answer some of the questions addressed here in more detail.

7.3 Discussion

The pulsed and cwEPR analysis together with FRET shine some new light on p7 stoichiometry in an membrane environment. The FRET analysis showed oligomeric p7 at various peptide to lipid molar concentrations where the $E_{app,se}$ in a high density membrane of 1:150 protein to lipid molar ratio was fitted to a stoichiometry of a hexamer (Figure 7.6). The cwEPR spectrum of N-terminally spin-labelled p7 at this peptide to lipid molar ratio showed two motionally distinct environments that are not exchanging fast on the EPR timescale (∼ns). By simulation these could be quantified in a 60:40 ratio, suggesting that 60% of the spin-label population resides in the slow motion component (Figures 7.7). There is a detectable change in the proportion of slow motion component with increasing protein concentration, which suggest a correlative change in oligomeric state (as seen for M2, [79; 402]). Further to this, the relative behaviour of the modulation depth at different proportions of spin-dilution met the expected relative behaviour of a hexameric complex (Figure 7.8). The relative separation between the shortest and longest measured distances within an oligomeric complex were also broadly consistent with a symmetrical hexamer (Figure 7.10).

Analysing the C- and N-terminus individually as part of an oligomeric complex showed three distance populations respectively that could indicate either hexameric or heptameric nano-objects. The relative distributions of the population intensities showed some deviation possibly due to multi-spin effects despite spin dilution. The shortest distance measured for the C-terminus shifted by 0.3-0.4 nm to longer distances (Figure 7.11), assuming that this is the distance corresponding to the separation of neighbouring monomers within the oligomeric complex, this would place the C-terminal transmembrane helix outward facing and the N-terminal helix the pore facing domain. A model based analysis showed good agreement between experimental data and a hexameric hairpin based p7 model structures for spin-labels located at the N-terminus, however this could not be confirmed for the C-terminus (Figure 7.12 and 7.13). This is consistent with reports in literature, where the N-terminal transmembrane helix has been reported in models as the pore-lining transmembrane domain [69; 74; 139; 361; 363; 412]. Residues H17 [69], F25 and S21 have previously been associated with direct pore lining, being located within the N-terminal half of the protein [137; 413]. Residue 25 is conserved across all genotypes and based on computational models is thought to face the pore, suggested to

form a hydrophobic ring lining around the interior of the pore and thus be involved in channel gating[74; 361]. This is consistent with the data reported here in lipid bilayers.

Monomeric p7 in detergent showed helix-helix packing consistent with the expected hairpin conformation (Figure 7.15). A similar residue-to-residue separation was observed in a membrane, suggesting that a similar hairpin configuration could be possible in a membrane environment. However, an additional slightly larger distance contribution was observed in a membrane environment that might indicate a slight opening up of the hairpin, however this could equally result from a different rotamer population that might become more favourable upon oligomerisation. The fact that this distance contribution was observed in two mutants might point towards cis isomerisation of either proline at residues 49 and 58, which are close to the common spin-labelled residue of position 51 in both probed mutants. Nevertheless, consistency between the two observed distance populations and the proportion of slow-mobility component in cwEPR at a protein to lipid molar ratio of 1:150 was observed, each at a relative 40:60 split (Figures 7.7 and 7.17), which might indicate that different protein conformations correlate with the dynamical profile and thus perhaps oligomerisation. Based on the limited data reported here this remains speculation and needs to be confirmed in future experiments. A large opening of the hairpin structure as described in the oligomeric complex by B OuYang *et al.* 2013 could not be confirmed for genotype 1b in the here reported membrane composition (Figure 7.18). Note that this can be due to a different genotype or due to the membrane environment being significantly different to a detergent micelle leading to structural rearrangements. The solution NMR structure by B OuYang *et al.* 2013 was only partially stable in MD simulations in a POPC bilayer [363], which might indicate that the p7 oligomeric structure might differ in a membrane. The same study also reported oligomeric models for p7 monomers in a hairpin conformation as plausible in a simulated membrane environment.

Distance traces reported using mutant p7 Gt1b J4 K33R L51C in a membrane showed good agreement with monomeric p7 hairpin conformations. It is noteworthy to point out that the monomeric structure of Foster *et al.* 2014 and the structural model by B Oestringer *et al.* (unpublished) showed good agreement, despite drastically different N-terminal domains (one spin-label directly located at the N-terminus), with the structure presented by Foster *et al.* 2014 showing a straight N-terminal helix, whereas it is largely bend for the model proposed by B Oestringer *et al.* (unpublished). Thus, as speculated in the discussion of

chapter 6 a straightening of this domain in a membrane might be plausible. However, this needs to be confirmed using a suited mutant that can report on such a structural change with more confidence (e.g. both termini labelled with a nitroxide).

In the C27S mutation made for this construct and in constructs of the same genotype in previous studies (C27S gt1 [87], C27A gt1 [74] and C27T gt5 [66]) a cysteine residue is replaced, in what is expected to be close to the end of the N-terminal transmembrane helix, which might be of importance for inter-monomer disulphide bridge formation and added stability of a potential oligomeric complex, similar to previously reported disulphide bridge stabilised M2 dimers [414]. Cysteine 27 is fairly conserved across most genotypes, but not fully. However, the mutation in p7 Gt1b J4 of C27A was shown to only have a slight reduction in channel activity based on cell proton dependent haemadsorption assay [415]. A more recent study showed that for p7 from genotype 2a isolate J6, the mutation of V27W did not affect infectious virus production in cell culture [380]. Nevertheless this has not been analysed in a structural context yet, and if valid might be an explanation for the comparably low proportion of p7 found in oligomeric forms despite relatively high local protein concentrations.

In summary, this suggest a certain degree of structural plasticity of p7, behaving differently in different environments. Local protein concentration might be of importance as shown by cwEPR analysis (Figures 7.7), indicating a correlation between protein to lipid molar ratio and the relative spin-label mobility. It is speculated that this could indicate different local spin-label environments upon oligomerisation. Structural constraints of coupled spins in a nano-object were resolved using DEER approaches, yielding insight into oligomer stoichiometry. p7 might exists as oligomeric complexes lower than hexamers, and/or in coexistence with a large monomeric proportion in a membrane (Figure 7.6). This is not surprising in the light of the different functions that have been reported for p7 to date and for different oligomeric states could have different biological functions [83; 126; 127; 133; 382; 383]. Despite its significance as a drug target, this makes p7 also a highly interesting protein to investigate in light of general Biology, as viroporins are conserved across many viruses and encode a high functional diversity in a minimalistic protein architecture.

The model-based analysis presented here illustrates how DEER constraints can be used in order to differentiate between different proposed p7 structures. However, a more elaborated

fitting procedure together with more experimental constraints are need in order to find a unique model for oligomeric p7 in a membrane. Steered MD simulations incorporating the experimental DEER constraints, possibly in combination with angular constraints from ssNMR (Chapter 6) might help to generate an oligomeric membrane model based on individual structural constraints.

8

Conclusion and Discussion

It becomes increasingly evident that proteins respond structurally and functionally to the local environment [360]. This is an important consideration for membrane protein structure determination, as it is preferable to use proteins naturally embedded in an anisotropic bilayer. Sensitivity to the local environment is most likely enhanced relative to soluble proteins, due to relative high hydrophobicity and the limited inter-TM interactions in a membrane [416], however soluble proteins were also shown to adopt to an overall fold that depends on the solvent in which they are studied [360]. In this thesis the relative structural dependancy of the viroporin p7 to its local environment is discussed, which has been structurally characterised before in detergent micelles and solvents, with only limited structural data in a bilayer. This is to aid the understanding of p7 behaviour in an environment with previously reported p7 channel function. However, this remains a model environment, and to date it has not been possible to obtain a high-resolution 3D structures of a transmembrane protein in its native environment (exception of bacteriorhodopsin [417]); which remains a major challenge for the field. The need for more native-like environments is also a major challenge for the study of AMPs, similar to the presented work on p7, the characterisation of AMP function is biased towards the model membrane used here. The bacterial cell envelope however is complex; this complexity is of important consideration for the future design of antibiotics targeting the cellular membrane. Recently, progress towards a more bacteria-like environment has

been made by introducing a LPS layer to supported bilayers [36], however, the preparation of these mimics is still laborious and cannot be produced on the scale needed for oriented solid-state NMR or in a vesicle dispersion.

Further to this advancement in in-cell NMR has been achieved, which is a further step closer to the native environment of proteins, yet this approach is still restricted to mainly bacterial systems, which could become advantageous for studying the antimicrobial activity of AMPs directly on an intact bacterial cell envelope. Artificially labelled proteins are still required to be introduced to these system. Alternatively, relative progress has been made in the isolation and orientation of bacterial extracts of *E. coli* and *M. luteus* for oriented solid-state NMR [418; 419], which is a step closer to the native bacterial cell envelope, yet the intrinsic membrane asymmetry is lost during the purification.

Structure determination principles by solid-state NMR are based around magic-angle spinning (MAS) and oriented sample (OS), and these methods have been used to obtain structural constraints in model bilayers, mainly of small transmembrane proteins. A combination of restraints obtained by a combination of techniques (OS, MAS and solution) shows great promise in order to narrow the structural constraints needed for structure determination [360; 420; 421]. More recently, rotationally aligned NMR experiments relying on the fast protein rotational diffusion around the bilayer normal, have been reported, which lead to the first backbone structure of a GPCR in a model membrane [422]. The advantage of this method is that multiple structural constraints, high resolution assignments based on MAS and angular restrains based on rationally aligned proteins in the membrane [423], can be obtained from the same sample, using triple resonance experiments and non-oriented liposomes. This technique can help to determine protein structure in bilayers for membrane proteins that often suffer from poor expression yields.

Oriented solid-state NMR and DEER techniques were used here to probe protein conformation in a model bilayer for comparison to structural data acquired in different local environments. The further aim of this study would be to characterise the monomeric and oligomeric structure in a model membrane by solid-state NMR means. This will be a difficult task due to the uncertainty of the oligomeric state in the bilayer and the presence of subpopulations of different oligomeric forms, nevertheless a high resolution structure of

the functional form in a membrane is essential to further advance p7 as a drug target. The advantage of the pulsed EPR approach outlined in this thesis is that it only reports on coupled spins in a membrane, ignoring uncoupled monomeric species, yet the obtained resolution is too low to report a detailed structure. Thus, some initial insights into the pore architecture are obtained but in future works this needs to be combined with structural constraints based on other techniques in order to report on a structure. Combining the inhibition by iminosugars to structural data is also of great interest to the field, as a verified drug binding site would most likely allow for the development of new (cheaper) therapeutics. This could potentially be achieved using REDOR experiments on uniformly ^{13}C-labeled p7 in combination with a perdeuterated iminosugar in order to map a binding site. The deuterated drug can also be used to find a precise orientation within a membrane or bound to the ion channel [99].

Antimicrobial peptides, on the other hand, show great promise for future development into antibiotics for the clinic. The broad activity against bacterial membrane integrity as a whole makes the development of resistance difficult and only reported in rare cases, which is in contrast to conventional antibiotics that target specific pathways and proteins [424]. The results demonstrated here illustrate an example of the biochemical engineering steps that could create a platform for development of new antibiotics. However, the structure-function relationship of AMPs still requires extensive characterisation; the example demonstrated here indicates how such information could be generated on a case-by-case basis progressing towards a holistic understanding of AMP function. A precise understanding of sequence identity could advance the field towards modular peptide design principles allowing for a large arsenal of potent peptide antibiotics, possibly leading to peptide-based therapeutics for personalised medicine. Furthermore, this could open up other strategies for peptide therapeutics such as drug delivery using peptide conjugates, whereas some AMPs also show significant anti-cancerous potency. The understanding of peptide-membrane interaction is also of importance for peptide therapeutics with other implications that need to cross the membrane barrier to reach its target. Some of the main obstacles that still remain, are the comparable high manufacturing cost (estimated to be 300 - 500 USD per gram [425]) and the biodegradability of peptide sequences administered to patients. Cyclic peptides have been shown to be less prone to degradation. Some peptide therapeutics are also biologically produced (e.g. Kalbitor (Ecallantide) is expressed in yeast; [426]). Despite these obstacles

the first AMPs are reaching late stages of clinical trials showing promise for therapy (e.g. Brilacidin is currently undergoing phase III clinical trials (Cellceutix Corporation)).

Appendices

A

Appendix

A.1 Material and Methods

A.1.1 Chapter 3

Solid-phase synthesis

Solid-phase peptide synthesis was performed on a Liberty-1 microwave synthesiser (CEM Corp.) using standard peptide synthesis protocols with Fmoc/tBu chemically protected amino acids. The coupling agent was HBTU/DIPEA and Rink amide 4-methylbenzhydrylamine (MBHA) resin (Novabiochem, UK), at a substitution of 0.6 mmols/g was used. For peptides containing deuterated Alanine side chains (Ala-d_3) Fmoc-Ala-OH-3,3,3-d3 (Sigma Aldrich) was used for peptide synthesis. Amino acids were solubilised in Dimethylformamide (DMF) and the C-terminus was protected with an amide group.

Post amino acid coupling the peptides were cleaved from the Rink amide (MBHA) resin using 95% Trifluoroacetic acid (TFA), 2.5% Triisopropylsilane (Tis) and 2.5% H_2O. Note that for peptide containing Cysteine residues H_2O was replaced by 1,2-Ethanedithiol (EDT). The reaction mixture was incubated overnight at room temperature. The cleaved peptide was recovered and diluted in Diethyl ether to a final Diethyl ether concentration of 90%. The

precipitated peptide was centrifuged at 3500 rpm (swing-out rotor T516) for 45 min at 4 °C. The supernatant was discarded and the pellet was resuspended in H_2O followed by lyophilisation.

Crude peptide powder was solubilised for reverse-phase high performance liquid chromatography (RP-HPLC) at $\sim$ 20 mg/ml (tilamin in Buffer A; QAELA in Buffer B plus 40% Methanol and ChoM in Buffer A). RP-HPLC purification was performed on JASCO systems and semipreperative and analytical columns supplied by Vydac (C18 for tilamin and ChoM, C8 for QAELA). A 10%-60% gradient of Buffer B (40-90% for QAELA) was used with a system flow rate of 4.7 ml/min. A loop-size of 5 ml was used for semipreparative peptide purification. Peptide elution was monitored at wavelength 220, 230 and 280nm.

Collected fractions were analysed using Matrix Assisted Laser Desorption/Ionization (MALDI) time-of-flight (TOF) mass spectrometry using 2,5-dihydroxybenzoic acid (DHB) as matrix. Pure fraction were pooled and analysed using analytical RP-HPLC. The analytical RP-HPLC was performed on Jasco system using Vydac C18 and C8 columns (Grace, Dearfield, IL, USA) using a linear gradient as described above. Injection volume was 100 μl. The pure peptide was repeatedly lyophilised before storage at -80 °C.

Buffer A: 95% H_2O; 5% Acetonitrile; 0.1% TFA
Buffer B: 5% H_2O; 95% Acetonitrile; 0.1% TFA

Minimum Inhibitory Concentration (MICs)

The general method of broth microdilution as suggested by Clinical and Laboratory Standards Institute was employed for MIC determination. Bacterial cultures were grown overnight (LB media) and diluted into Mueller Hinton media broth (Oxoid) at a final concentration of $\sim 4 \cdot 10^6$ CFU/ml as determined by $OD_{600} \sim 0.004$. The bacteria were distributed across a 96-well plate at 100μl aliquots in presence of a two-fold dilution series of peptide ranging from 0-100 μM. A positive control (absence of antibiotic) and a negative control (broth only) were included; all peptide concentrations were tested in triplicates. The 96 well plate was incubated shaking at 37 °C for 24 h. The MIC value was taken as the lowest concentration at which no visible growth (measured by OD_{600} on a Victor 2 plate reader (Perkin-Elmer)) could be observed. Following on from this initial test the step size was narrowed to one μM steps to determine the MIC concentration more accurately around the previously determined estimate.

The peptide stocks were prepared prior to testing according to peptide bond absorbance at 214 nm. Note that this concentration is an approximation and does not correspond to the true MIC, which might lie at a lower concentration between the reported value and the first point tested with visible bacterial growth. The MIC value reported corresponds to the lowest peptide concentration at which no bacterial growth could be observed after a 24h incubation period at 37°C and does this experiment does not allow for comments on peptide kinetics. Further to this the MIC value does not necessarily mean that under these condition the peptide is bactericidal and instead might simply inhibit microbial growth.

Preparation of spheroplasts

The general procedure described by D Birdsell and E Cota-Robles 1967 was followed [427].An overnight culture of *E. coli* was grown overnight. The cells palleted by centrifugation and resuspended in PBS (pH 7.2) for washing. After centrifugation the cells pallet was resuspended in 0.5 M sucrose (0.5ml per 1 ml of cell culture), A final concentration of 50 μg/ml of Lysozyme was added to cell suspension, and the mixture was incubated at 37 °C for 1-2 h. Following incubation the suspension was diluted 2-fold and EDTA was added to a final concentration of 10 mM. This was followed by an additional 10 min incubation period at 37 °C. The transformation into spheroplasts was qualitatively confirmed by confocal microscopy and a change in bacterial shape from a rod-like appearance into a spherical appearance. Following the transformation the cells spheroplasts were pelleted (15 min at 500 g) and washed and resuspended in PBS (pH 7.2) containing 0.25 M sucrose.

Atomic force microscopy (AFM)

A solution of 0.5% gelatine in Phosphate buffer was prepared. After cooling the mica chip used for imaging was coated with gelatine. The chip was allowed to dry in air in a vertical position. A dilute suspension of stationary *E. coli* are spheroplasts in phosphate buffer was applied to the chip and excess buffer was carefully removed after a short incubation time (10 min). For tilamin containing samples a final concentration of 10 μM was added to the buffer. Mica chips were imaged on a MFP-3D Asylum AFM instrument in tapping mode using super-sharp silicon probes (Nanosensors; resonant frequency ∼330 kHz, tip radius of curvature <5 nm). Images were processed using proprietary SPIP software.

Fluorescence microscopy and GUV preparation

A lipid film of POPC:POPG (3:1, molar ratio) was prepared. Lipids were taken-up in chloroform:methanol (2:1, vol:vol), dried under a stream of Nitrogen followed by additional drying under vacuum overnight. The film was solubilised in 1M sorbitol containing 2 μM of sulforhodamine B (Sigma Aldrich) to a final lipid concentration of 1 mM and sonicated for 30 s to solubilise the lipid film. The formed giant unilamellar vesicles (GUVs) were diluted 200 fold into phosphate buffered saline (PBS). 100 μl aliquots were deposited into an eight-well chamber (LabTek). CellMask^{TM} (molecular probes by life technologies) was added at a dilution of 1:2,000. The GUVs were allowed to equilibrate for 5 min prior to peptide addition (final concentration of 10μM. An Olympus IX81 inverted confocal microscopy and appropriate filters were used to monitor fluorescence.

For microscopy on live bacteria an overnight growth was diluted into PBS and following a 5-10 min equilibration period peptide was added at a final concentration of 10μM.

Circular Dichroism (CD)

CD experiments were recorded on a JASCO J-810 spectropolarimeter. The peptide concentration of 30 μM in 10 mM phosphate buffer at pH 7.4 with a total smaple volume of 300 μ. Vesicles of POPC and POPC:POPG (3:1; molar ratio) were prepared by solubilisation of lipids in chloroform:methanol(2:1; vol:vol) and drying of a lipid film under a stream of Nitrogen followed by additional drying under vacuum. The lipid film was solubilised in phosphate buffer (pH 7.2) followed by extrusion (21 times using polycarbonate filter (0.05 μm)). Vesicles were added to the peptide samples at peptide to lipid molar ratio of 1:100.

A.1.2 Chapter 4

cwEPR

Vesicles were prepared from a lipid film of POPC:POPG (3:1; molar ratio), by hydration in 10 mM phosphate buffer (pH 7.2) followed by five consecutive freeze-thaw cycles in order to for SUVs. Note that spin labelled lipids and SASL were included in the dried lipid film at 0.5% final concentration. The peptides were taken up in buffer or methanol

for tilamin and QAELA respectively and added to the vesicle suspension at the required peptide to lipid molar ratio. The vesicle suspension was loaded in 100 μl capillaries and flame sealed (Sigma Aldrich capillaries).

cwEPR experiments were performed on a Bruker EMX X-band cwEPR spectrometer (at ∼9.2-9.8 GHz). A nitrogen cryostat coupled to variable temperature control unit (Oxford Instruments) was used for temperature control. Experimental parameters include a sweep width of 150 gauss, modulation amplitude of 1G, a centre field at 3297 gauss and a receiver gain of 40-60 dB depending on the sample. Spectra are an average of three scans at each temperature point and the samples were equilibrated at the specific temperature prior to measurement.

The experimental trace was background corrected using a linear approximation and normalised to the first integral of the absorption spectrum.

Solid-state NMR

^{2}H - NMR. Tilamin and lipid mixture (POPC:POPG (3:1; molar ratio) or DLPC:DLPG (3:1; molar ratio)) were co-disolved in chloroform:methanol:water (45:45:10; vol:vol) and dried under a stream of nitrogen followed by drying under vacuum. The film was solubilised in the same solvent-water mixture at the required concentration and distributed across microscope cover slides (5.7 x 11mm (Paul Marienfeld GmbH & Co KG, Germany)) at an overall lipid concentration of ∼3 mg/cm^2 and 15 μl per slide. The slides were air-dried for 1 h, which was followed by additional drying under vacuum for 18h.

The sample was hydrated in a hydration chamber of super-saturated salt solution of K_2SO_4 at 37°C (relative humidity of 96%) for 12h [366]. Following the initial hydration step the microscope cover slides were stacked and covered by a non-sample containing glass slide. The stack was further hydrated under the same conditions for 24 h. After hydration the lipid stack was clear, an indication of relative hydration.

The hydrated lipid stack was inserted in a glass vial and sealed with bee wax to prevent dehydration [366]. The NMR experiments were performed on a 800 MHz Infinity plus wide pore spectrometer (Magnex, Varian). A low-e HX probe equipped with a flat-coil for static experiments was used [428]. NMR measurements were performed at 20°C using a quadrupole

echo pulse sequence was used. A typical ^{2}H-NMR experiment would be performed at deuterium frequency of 122.78 MHz and an spectral width of 100 kHz using a 90° pulse length of 4 μs an interpulse delay of 35 μs, followed by 60 μs pulse delay and a 0.5 s recycling delay. Between 400k and 600k scans were acquired per sample. The FID was left-shifted to the echo maximum and line broadening was applied.

^{2}H - NMR samples oriented with the bilayer normal orthogonal to the external magnetic field were recorded on a 400 MHz Bruker wide bore spectrometer using a converted MAS probe equipped with a home-build static flat coil. Typical experimental parameters used were a 6.5 μs pulse length for the quadripolar echo, an 50 μs interpulse delay and 35 μs delay prior echo detection. Recycle delay was 1 s.

^{31}P - NMR.

^{31}P - NMR samples oriented with the bilayer normal parallel to the external magnetic field were recorded on a 400 MHz Bruker wide pore spectrometer using a converted MAS probe equipped with a home-build static flat coil. Typical experimental parameters are a 6 μs 90° pulse and a recycling delay of 5 s. Continuous wave proton decoupling was applied during echo acquisition.

^{15}N - NMR.

^{15}N - NMR samples oriented with the bilayer normal parallel to the external magnetic field were recorded on a 400 MHz Bruker wide pore spectrometer using a home-build static probe equipped with a static flat coil. Typical experimental parameters were a 8 μs 90° proton pulse length, 1 ms contact time for a ramped CP and a recycling delay of 2.5 s. Continuous wave proton decoupling was applied during echo acquisition.

All spectra were analysed using NMRPipe [429].

Spectral simulation and deconvolution

Spectral deconvolution for SASL spin labels as shown in Figure 4.6

Spectral libraries of individual SASL spin labels (labelled at segment 5 and 14) in the absence of peptide at different temperatures were generated in order to match the line

shape of the multiple components observed in the tilamin EPR spectrum. The individual components were manually subtracted at different proportions (in steps of 5%) in order to recreate a single component spectrum of the resulting subtracted spectrum. Note that this approach is based on line shape appearances which are qualitatively judged by the scientist as the possible appearance of multiple minor populations all of very similar anisotropic splittings makes a simulation based de-convolution difficult. Hence this is a very basic approximation giving a comparably large error.

Spectral deconvolution of individual components summarised in Table 4.2 and Figure 4.21

The individual identified spectral components correspond to a powder slitting of ca. 38 kHz, a splitting arising from the selectively deuterated alanine side chain and the narrow splitting ($< 2kHz$) and were fitted to individual Lorenzian line shapes using the software *Spinsight* by minimising the obtained residuals as illustrated in Figure 4.21. The linewidths were determined as the half height of the fitted Lorenzians and the relative proportions are stated as integrated fractions based on the fitted curves. Note that for the powder component more accurately a Pake doublet should have been fitted, yet since the powder contributions are only very narrow the results would not have changed drastically.

EasySpin simulation of cwEPR sepctra

cwEPR spectra were simulated using *EasySpin* [214] at X-band with a frequency of 9.5 GHz and a center field at 338 mT. A spectral sweep of 30 mT was used. A single nitroxide radical was used for all simulations, which was described by principal hyperfine g-value tensors of $g_{xx} = 2.0085$,$g_{yy} = 2.0063$ and $g_{zz} = 2.0025$. The principle nitroxide anisotropy was set to $a_{xx} = 5.8$, $a_{yy} = 5.8$ and $a_{zz} = 30.8$. The dynamics were described by a spin correlation time of 10^{-7}s, which renders the spectrum immobile on the NMR time scale. The EPR line was broadened by 0.1 mT. The spectrum was simulated using the implemented *"chilli"* formalism, which solves the Stochastic Liouville equation.

Spinach simulation of ^{2}H NMR spectra

The Spinach software library [209] was used in order to simulate deuterium spectra for a single nucleus, which is an approximation to the C^2H_3 Alanine side chain, which due to

fast rotational motions averages to a single resonance. A magnetic field strength of 18.8 tesla was used at room temperature identical to the experimental setting. A sweep width of 100 kHz and 2048 points were simulated, the FID was zero filled by an additional 2048 points prior to Fourier transformation, lines were broadened by 100 Hz.

For simulation spherical tensors in the Liouville space were used. The basis set was approximated including all product states up to order n = 4 between directly coupled spins. The approximated basis set was calculated using full tensors for interactions and distance information. The quadrupolar coupling matrix was build using a quadrupolar coupling constant of 73 kHz as determined from contour plots using numerical approximations before (dee text Figure 4.25), an asymmetry parameter of 0 and a spin quantum number of 1. The orientation of the individual nucleus was described by Euler angles. This set the initial spin Hamiltonian, to which an additional angular constraint was added for all the individual peptide orientation simulated.

The spectra were plotted and the inter-maxima distance was measured and the absolute value was used for RMSD analysis of all four labelled peptide positions.

Molecular dynamics

Insertion angle of tilamin

The initial alpha helical peptide configuration was achieved using the XPlor-NIH structure determination algorithm. This peptide configuration was embedded into an 12 x 12 nm DLPC:DLPG (3:1, molar ratio) membrane, already equilibrated for 20 -40 ns. Chloride counter ions were used for charge neutralisation and the simulations were run using the CHARMM36 force field for a total of 100 - 500 ns.

The peptide tilt angle was measured between a defined axis along the helical axis and the membrane plane. The individual tilts along the trajectories were grouped into one degree intervals and histograms were plotted along the simulation time.

Radial density function (RDFs) were generated with the help of the GROMACS g_rdf tool. For Lysine residues these were measured between the lysine side chain nitrogen atom and the Phosphorous of the lipid headgroup. Similarly, for arginine the side chain terminal

carbon atom was related to the phosphorous atom in the lipid headgroup, whereas for tyrosine the hydroxyl oxygen atom was used.

Tilamin pore assembly

Tilamin pore structures of various oligomeric states were designed using x-plor scripting including a C-terminal amide cap. The pore structures at various relative tilt angles (see Figure A.7) with respect to the bilayer normal were inserted into a model membrane (POPC:POPG (3:1; molar ratio) manually and converted to coarse-grain. The molar peptide to lipid ratio was 1:70. The lipid membrane was solvated to a final concentration of 150 mM NaCl, which was achieved using the CHARMM-GUI Martini server [430]. The system was equilibrated prior to simulation using force field Martini 2.2 [431]. Trajectories of interest from the coarse-grain simulation were converted to atomistic models using the CHARMM-GUI Martini server and simulated for a total time frame of 70 ns. For a summery of the simulation process see Figure A.8. The trajectories were analysed using GROMACS 5.1 and VMD softwares.

A.1.3 Chapter 5

Solid-state NMR

A total 6.5 μmol of DOPC-d_4:POPC (4:1; molar ratio) was resuspended in chloroform and dried under a flow of Nitrogen and then under vacuum overnight. The lipid film was solubilised in 27mM cyclofos-6 to a final lipid concentration of 14 mM. The lipid sample was sonicated in a water bath for 15 min for complete lipid solubilisation. The sample was then diluted into 100 ml of corresponding buffer to dilute the detergent ca. 20 fold below its critical micelle concentration (CMC). This was followed by extensive dialysis against buffer. The samples were then concentrated to a final volume of $\sim$20 μl followed by a single freeze-thaw cycle, which resulted in a more homogeneous ^{31}P-NMR spectrum, and packed on a 2.3 mm rotor for static NMR analysis.

The drug (*N*N-DNJ) was added during the concentration process of the sample at the required concentration from a stock in methanol.

The solid-state NMR experiments were run on a 500 MHz Infinity Plus wide bore spectrometer (Magnex, Varian) using a quadrupolar echo pulse sequence with a weep with

of 100 kHz using a 90° pulse length of 4 μs an interpulse delay of 35 μs, followed by 60 μs pulse delay and a 0.5 s recycling delay.

DePaking

The NMR samples recorded (for this chapter) were vesicle dispersions and were dePaked in order to simulate the spectrum in an oriented system with the bilayer normal aligned with the external magnetic field. A vesicle morphology gives rise to the typical Pake pattern, which is dominated by the 90° orientation. A weighted Fourier Transform was used in order to simulate the 0° oriented spectrum [348] implemented into NMRPipe [429].

A.1.4 Chapter 6

Expression and purification of p7

Preparation of competent cells

Chemically competent cells were prepared by treatment with calcium chloride ($CaCl_2$). An overnight culture was grown of *E. coli* BL21 (DE3) pLysS and *E. coli* DHα including corresponding antibiotics respectively. Cells were diluted and grown to a final OD_{600} of 0.4 in presence of antibiotics (100 ml culture). Once the culture reached this density the cells were incubated on ice for 20 min and centrifuged at 2500 g for 10 min at 4°C. The supernatant was discarded and the pellet resuspended in 30 ml cold $CaCl_2$ at 0.1 M. The cells were incubated for 30 - 60 min on ice and centrifuged at 2500 g for 10 min at 4°C.

The pellet was resuspended in 0.1M $CaCl_2$ (cold) and a final concentration of 20% glycerol was added. Cells were aliquoted, frozen under liquid nitrogen and stored at -80°C.

Transformation

5 μl of plasmid DNA was added to 100 μl cold cell suspension of competent *E. coli* BL21 (DE3) pLysS cells and incubated on ice for 1h. This was followed by a heat-shock in a 42 °C water bath for 45 s. Following this cells were incubated on ice for 10 min to allow for recovery. 1 ml of warm (37 °C) LB media including 1% Glucose was added and cell suspension was incubated for 1h at 37 °C shacking (220 rpm). The suspension was plated on LB agar plates containing corresponding antibiotics for selection of successful transformation.

Expression in minimal media (M9)

BL21 (DE3) pLysS containing pMM6-LR6 (p7 gt1b J4 C27S) were grown in a 5ml culture of terrific broth (TB) containing kanamycin and chloramphenicol at 25 μg/ml 50 μg/ml respectively. The culture was expanded to 100 ml and grown overnight (37°C and 220 rpm shaking), which served as a starter culture for a large-scale growth. TB in 0.5 l aliquots (round bottom flasks) containing antibiotics were inoculated using the started culture and grown to a final OD_{600} of 0.6. Cells were pelleted for 20 min at 6000 rpm (Beckmann rotor J-LA 9.1000), following which the cells were resuspended and washed in M9 salts at two-fold concentration compared to the used TB media. This was followed by pelleting of the cells for 20 min at 6000 rpm (Beckmann rotor J-LA 9.1000) and the cells were resuspended in M9 media in baffled flasks (pre warmed to 37°C) at a four-fold concentration compared to the initial growth in TB media.

Cells were incubated at 37°C shaking at 180 rpm and the OD_{600} was monitored. After a short equilibration period the optical density started to increase at which point the cells were induced using a final Isopropyl β-D-1-thiogalactopyranoside (IPTG) concentration of 1 mM. Proteins were expressed for 18 h.

Purification of p7 Gt1b J4 C27S

The general purification protocol outlined by G Cook *et al.* 2011 was followed [372]. Broadly this involves a five step purification protocol: (I) Solubilisation of the cell pallet and removal of the membrane fraction; (II) Nickel-affinity purification followed by dialysis; (IV) cyanogen bromide cleavage in 70% formic acid followed by dialysis and (V) FPLC purification in an sodium dodecyl sulfate (SDS) buffer.

Cell pellets were solubilised in Resuspension buffer I (30ml per 1 l growth pallet), followed by 15 min sonication (15 s on/off cycle) and the cellular debris was pelleted (20 min, 17 500 rpm (Beckmann rotor JA 25-50)). The pellet was taken up in detergent containing (IGEPAL) resuspension buffer II (30 ml per 1 l growth pallet) and the sonication and pelleting steps were repeated. The resulting pelleted inclusion bodies were solubilised in Ni^{2+}-Binding Buffer containing 6 M guanidine hydrochloride at 4 °C overnight on a rotary wheel. The solubilised mixture was sonicated for 10 min (15 s on/off cycle) followed by centrifugation (20 min, 12 000 rpm (Beckmann rotor JA 25-50)) to remove non-solubilised material. The

solubilised inclusion bodies were added to 30ml bead volume Ni^{2+}-NTA Agarose (Thermo Fisher scientific) and incubated overnight at 4 °C on a rotary wheel. The column was washed with two times the bead volume using Ni^{2+}-Wash Buffer and eluted at a final imidazole concentration of 500 mM using four times the bead volume.

The Ni^{2+}-NTA elution was analysed by running the individual fractions on a SDS-PAGE Gel (4-12%; Novex NuPAGE Thermo Fisher Scientifc, MES running buffer, 200V, 35 min) post methanol/chloroform precipitation (see below). SeeBlue 2 Plus protein standard was used as a marker (Thermo Fisher Scientific). The pure elution fractions were dialysed against 5 l water using a 10 kDa molecular weight cut-off (MWCO) membrane (SnakeSkin Dialysis Tubing, Thermo Fisher Scientific). The water was changed regularly until the inclusion bodies precipitated. The precipitate was pelleted (10 min; 2 000 rpm, Beckmann JA-12 rotor) and lyophilised.

The powdered inclusion bodies were solubilised in 70% Formic acid and 100 mg/ml cyanogen bromide was added. The cleavage mixture was incubated for 3h under constant flow of nitrogen and in the dark. The reaction was quenched using an equal quantity of 1M sodium hydroxide (NaOH) and diluted 10-fold in water, followed by dialysis against 5 l water using a 1 kDa MWCO membrane (Spectra/Pro 6 Pre-wetted Dialysis Tubing, Spectrum Labs). The water was changed in 15 min intervals for the first 1 h and then after 1.5 h and thereafter regularly (∼40 l in total). Following exhaustive dialysis the cleaved reaction product was lyophilised.

The cleaved protein was taken up in 10% SDS for FPLC purification (Sephacryl column HiPrep 26/60 SephacrylS-200, GE Healthcare) to a final concentration of 25 mg/ml, which was then diluted into FPLC buffer by an equal volume to a concentration of 12.5 mg/ml and a final volume of 2 ml. The pH was adjusted to 8.2. FPLC fraction were analysed for purity using SDS-PAGE (4-12%; Novex NuPAGE Thermo Fisher Scientifc), pure fraction were pooled and dialysed extensively against water until p7 precipitated (1 kDa MWCO dialysis tubing; SpectrumLabs); the sample was lyophilised, analysed by EI Mass spectrometry and stored under Nitrogen at -20 °C.

Methanol/chloroform protein precipitation

One volume of protein solution in 6 M guanidine hydrochloride was diluted into four volumes of methanol and vortexed. One volume of chloroform was added and vortexed. Followed by the addition of three volumes of water and vortexted. The mixture was centrifuged for 2 min at 16 000 g (Eppendor Minispin) in order to form an interface layer between the aquous layer on top and the organic phase on the bottom. The top layer was removed and four volumes of methanol were added to the remaining solution followed by vortexing and centrifugation for 10 min at 16 000 g (Eppendor Minispin). The supernatant was removed and the pellet air dried prior to solubilisation in supplemented LDS-loading buffer for SDS-PAGE analysis.

Reconstitution of p7 Gt1b J4 C27S into a model membrane

Pure p7 was taken up in 27 mM cyclofos-6 by repeated hot-cold cycles (37°C and 4°C, each 6h and shaking) to a final concentration of 600 - 900 μM. A lipid film of DOPC:POPE (4:1, wt:wt) was prepared as described before (materials and methods chapter 5) and solubilised in 27 mM cyclofos-6 followed by bath sonication for 15min or until the solution became clear. Protein and lipid were mixed at the required protein to lipid molar ratio and diluted into 5 mM HEPES (pH 7) buffer by a 25-fold dilution factor (buffer and p7/lipid mixture were pre-warmed to 37°C to be above the phase transition of both lipid species). The resulting dilute vesicle dispersion was dialysed (10 kDa MWCO, SnakeSkin Dialysis Tubing) against 5 mM HEPES for detergent removal (4 x 5 l). The sample was recovered by concentration across a 10 kDa MWCO membrane to an estimated final concentration of 100 mg/ml for plating on microscope cover slides (10 μl per 5.7 x 11 mm slide).

For sucrose gradients 0.4% rhodamine-PE was included in the dried lipid film.

Note that lipid samples in the absence of protein were reconstituted using the same protocol to mimic these condition for NMR sample preparation.

Preparation of aligned NMR samples

20 μl of the concentrated samples were plated on microscope cover slides with dimension 5.7 x 11 mm (Paul Marienfeld GmbH & Co KG, Germany) and air dried. This was followed additional drying under vacuum for 12 h before the samples were rehydrated in a hydration

chamber of super-concentrated K_2SO_4 at 37°C (relative humidity of 96%) for 12 h. The individual glass slides were stacked and covered by a non-sample containing slide, which was followed by additional hydration for 48 h. The stack of glass slides was wrapped in teflon tape and sealed in a plastic bag using a heat sealer.

NMR parameters

^{15}N - one dimensional spectrum: A CP experiment with a Hahn echo was used to acquire a 1D ^{15}N spectrum at a ^{1}H frequency of 750.183 MHz and a corresponding ^{15}N frequency of 76.025 MHz. The CP contact time was 3000 μs at 60 kHz, and the recycling delay was 3 s. Continuous wave (cw) proton decoupling was applied at 90 kHz.

^{31}P - one dimensional spectrum: The 1D ^{31}P spectra was acquired using a standard Hahn-echo pulse sequence at ^{1}H frequency of 300.317 MHz and a corresponding ^{31}P frequency of 121.570 MHz. A spectral widths of 300 ppm and a recycle delay of 5 s. The echo delay was optimised to 34 μs to coincide with the top of the echo. CW decoupling was applied.

PISEMA: A standard PISEMA with Hahn echo was used at a ^{1}H frequency of 750.183 MHz and a corresponding ^{15}N frequency of 76.025 MHz. The on-resonace CP contact time was 1000 μs at 60 kHz. The off-resonance Lee-Goldburg (LG) effective field was set to 40 kHz at an offset of +/- 23 094 Hz. The LG pulse length of 25 μs, a dwell time of 5 μs and a recycling delay of 3 s was used. A total of 64 increments were recorded with 2048 scans per increment.

2^4-SEMA-like experiment: At the time of writing the precise pulse sequence was confidential and details are omitted.

Simulation of PISEMA spectra

The PISIMA spectra were simulated using SIMMOL and SIMPSON software packages [204; 291]. Ideal alpha helices were generated using the implemented *"make"* function defining $\phi = -60^o$ and $\psi = -45^o$. For each residue the helix tilt and pitch angles were varied in step sizes of 2° and the spin system was described using the default tensors. An example of a SIMMOL generated Nitrogen CSA is shown in Figure 4.15. For visualisation of the defined spin system the software "geomview" was used. Using this approach a spin system file for each individual amide at all tilt angles of interest was generated. The PISEMA spectrum for

each individual amide was generated and exported; the complete PISEMA spectrum for the full length peptide was constructed by spectral addition using Python scripting.

Simulation parameters used for SIMPSON included 128 sampling points in both the direct and indirect dimensions. A magnetic field strength of 750 MHz (proton frequency) was used, identical to the experimental set-up used. The effective ^{1}H field was set to 40 kHz effective field off-resonance for the SEMA train, which corresponds to 32.8 kHz projected on-resonance. The effective field was set at an angle of 35.26°. The crystalline sample orientation was described using the crystal file alpha0beta0, describing a single crystalline sample orientation. Protons were decoupled at 100 kHz, the spectral width was set to 25 kHz and 300 Hz line broadening was applied.

Post simulation the experimental and simulated spectra were overlaid with the help of a simulated powder, which allowed for precise matching of the whole "butterfly" shape and a good fit. Simulated and experimental data were normalised according to the mean spectral intensity prior to fitting. The individual simulated PISEMA spectra, each for a single alpha helix, were combined at all possible tilt combination to provide a library of composite spectra. The RMSDs were then calculated for the entire library and analysed as described in the text. Simulated and experimental spectra were plotted using the Python *"matplotlib.pyplot"* library.

A.1.5 Chapter 7

Cloning of p7 gt1b J4 mutants

The plasmid pMM6-LR6 (obtained from J Schnell (Oxford)), which includes a TrpΔLE fusion protein tagged to a His_9 tag was used for p7 expression into inclusion bodies. The open reading frame is controlled by a standard T7 expression system. A kanamycin resistance is included on the plasmid. The p7 gt1b J4 C27S sequence was cloned into the vector exploiting the HindIII and BamHI restriction sites of the plasmid. Respective p7 genes were ordered as DNA strings or plasmids (GeneArt Strings, Thermo Fisher Scientific; Integrated DNA Technologies). Genes were designed to have HinDIII and BamHI restriction sites incorporated, each with an overhang of six base pairs for improved restriction enzyme activity.

Genes were cloned into plasmid pMM6-LR1 by restriction enzyme digestion, fragments were purified on an agarose gel (1%). The purified cut vector was dephosphorylated for improved ligation efficiency and the gene was ligated at a 3:1 molar excess using standard procedures (T4 DNA-Ligase; invitrogen). The ligation product was directly transformed into *E. coli* DH5α chemically competent cells and positive clones were selected on an LB agar plate based on antibiotic resistance. Positive clones were grown overnight, DNA was isolated using a plasmid Miniprep kit (QIAGEN) and sequenced using a T7 forward primer.

Notes on purification

A similar purification procedure to the method outlined before (materials and methods Chapter 6) was followed. For Cysteine containing mutants reducing agent was included post cyanogen bromide cleavage in dialysis buffer and mutants were solubilised in 10% SDS plus 100 mM Dithiothreitol (DTT) prior to FPLC purification. The FPLC running buffer was supplemented with 1 mM TCEP. The LDS loading buffer was supplemented with 20 mM DTT final concentration. Some dimerisation for double Cysteine mutants was observed nonetheless, this fraction was excluded.

Spin-labelling

The purified p7 Cys mutants in SDS were precipitated in the presence of reducing agent by dialysis, lyophilised and solubilised in buffer containing 1.25 M Urea, 11 mM SDS and 20 mM sodium phosphate (pH 8) at a final p7 concentration of 5 mg/ml. A final concentration of 6 mM MTSL was added. The reaction mixture was incubated for 2 h under an argon atmosphere and at room temperaturein the dark.

Post labelling the sample was centrifuged (10 min; 16 000g, Eppendorf Minispin) to eliminate possible precipitate and the accurate protein concentration of the reaction mixture was determined by A_{280} measurement. Unlabelled p7 (gt1b J4 C27S) was added to the required spin-dilution level. The samples were dialysed against 15 mM SDS and 20 mM sodium phosphate (pH 7.2) using 12 kDa MWCO (Mini Pur-A-Lyzer Dialysis Kit, Sigma-Aldrich) in order to remove urea and refold the protein into SDS micelles. Following dialysis into 15 mM SDS, the SDS content was reduced to 4 mM SDS by dialysis (2 x 5 l). Post dialysis aliquots for CD and cwEPR were taken in order to verify folded protein and removal of unreacted spin-label.

Lipid films were dried under a stream of Nitrogen followed by additional drying under vacum (12 -18 h). The lipid film was solubilised in sodium cholate at 37°C (by sonication in a water bath for 15 min) at a concentration that, which will make the final concentration after mixing lipid and protein suspensions (at the required protein to lipid molar ratio) 20 mM sodium cholate. The protein and lipid mixture in detergent was incubated for 5 min to allow for full mixing of protein and lipids at 37 °C. The sample was diluted rapidly into buffer (at 37 °C) by a dilution factor of 25 reducing the sodium cholate concentration to 0.8 mM. The sample was dialysed against 20 mM sodium phosphate (pH 7.2) to remove remaining detergent (against 3 x 5 l).

The sample was recovered by ultracentrifugation (28 000 rpm, SW28 Ti rotor rotor for 4-6h) for high density samples or concentration for low density samples (Vivaspin 10 kDa MWCO). D_2O and deuterated glycerol were added to the sample at ∼30-50% and ∼10% respectively. The samples (∼ 30μl) were loaded into Q-band suprasil EPR tubes with dimensions 1.6 x 1.1 x 100 mm and when required cwEPR measurements were performed immediately, and then flash-frozen in liquid nitrogens. The samples were kept at -80°C until measurement.

For mutant p7 Gt1b J4 C27S K33R L51C, MTSL and 1-Oxyl-2,2,5,5-tetramethyl-pyrroline-3-carboxylate NHS ester (OXYL-1-NHS) were added at a final concentration of 6 mM to the reaction mixture.

Fluorophore labelling and FRET

The general principles were identical to the spin-labelling methods outlined above and Cy-5 and Cy-3 (in the form of water-soluble sulfonated NHS esters (Lumiprobe)) were added at 8-fold molar excess and the reaction mixture was incubated for 2 h at room temperature, dark and on a rotary shaker. The unreacted dye was removed by extensive dialysis against water followed by freeze drying. A small aliquot was dissolved in TFE and labelling efficiency was determined according to:

$$f = \frac{\epsilon_{dye}}{\epsilon_{protein}} : \frac{A_{dye} \cdot \epsilon_{dye}}{A_{280} \cdot 16960 - CF \cdot \epsilon_{dye}} \tag{A.1}$$

where f is the labelling efficiency, ϵ_{dye} and $\epsilon_{protein}$ are the respective extinction coefficients. A_{dye} and A_{280} are the relative absorbance at the wavelength of the respective dye and 280

nm. 16960 is the molar extinction coefficient of p7 gt1b J4 K33R. CF is a correction factor corresponding to the absorbance of the respective dye at A_{280}. The CF was determined by a titration of relative dye concentrations. A labelling efficiency of $\sim$ 85% was achieved for both Cy3 and Cy5 labelling.

The labelled protein was taken up in 27 mM cyclofos-6. The dried lipid films at DOPC:POPE (4:1, wt:wt) were also taken up in 27 mM cyclofos-6 by sonication in a water bath for 15 min. FRET samples were prepared ranging from donor molar fraction of 0.1 to 0.9, for a total fluorophore concentration of 150μM and a constant lipid quantity at the required protein to lipid molar ratio for a final sample volume of 1 ml.

The mixture was reconstituted by dilution as described before (materials and methods chapter 6), where sample and buffer were pre-warmed to 37 °C. FRET experiments were done on Perkin Elmer Luminescence Spectrometer LS55 at 27 °C using a 1 ml quartz cuvette. Lipid-, donor- and acceptor-only samples were included for purposes FRET signal correction. The donor (Cy3) was excited at 538 nm and the acceptor at (Cy5) at 638 nm. The slit width was 5 nm and spectra were recorded from 549 - 750 nm for excitation of the donor and from 643 - 750 nm for excitation of the acceptor. The FRET traces were corrected as described in the chapter 6.

Continuous-wave EPR

cwEPR spectra were acquired as described before (materials and methods chapter 4). The individual components were simulated using *EasySpin* [214].

Simulation parameters for EasySpin

The two-component systems were simulated using *EasySpin* [214]. The spectra were simulated at X-band with a frequency of 9.5 GHz, a centre field of 338 mT and a sweep width of 30 mT. Simulations were performed at 298 K. The experimental cwEPR spectra were baseline corrected by a linear approximation prior to fitting to two individual nitroxide spins, each initially described by principal hyperfine g-value tensors of g_{xx} = 2.0085,g_{yy} = 2.0063 and g_{zz} = 2.0025. The principle nitroxide anisotropy was set to a_{xx} = 5.8, a_{yy} = 5.8 and a_{zz} = 30.8. An initial weighting factor and spin labelled correlation times was guessed

for the individual contributions of each component (typical values for spin-label correlation times were in the range of 1 - 10 ns). The implemented least-square fitting algorithm *"esfit"* and *"Chill"* formalism were used to fit and simulate the experimental spectrum.

For spectral fitting limits for adjustments of each individual parameter describing the spin radical nature were defined and typically allowed for adjustment of anisotropy values by [1.5 1.5 3.0] gauss; the correlation time by one magnitude; line broadening of 0.2 mT; principle g-tensors by [0.003 0.003 0.003]. An initial genetic algorithm with a population size of 30 and 25 generations were run for an initial search of global minima. The parameters of the best fit were then used to describe a new pair of nitroxide spins and the limits for adjustment were narrowed. This description was then used in order to improve the EPR fit using a local search using a Levenberg/Marquardt algorithm.

Using this approach a good initial "guess" is required, yet the dependency on this could be reduced by introduction of the initial genetic fitting step. Generally RMSD values in the range of 0.01 - 0.015 were achieved.

DEER

All described DEER experiments were performed on an ELEXYS E580 (Bruker) spectrometer, operating at Q-band (∼33.4 GHz), which was equipped with a SuperQ-FT bridge (Bruker) and a 2 mm split-ring resonator (EN-5107D2, Bruker). Pulses were generated using an arbitrary waveform generator (AWG) at a sample temperature of 30 K (for nitroxide spins) and 10 K (for gadolinium). A helium cryostat combined with a variable temperature control unit (Oxford Instruments) was used to set the temperature. Field-sweep aborbtion spectra, T_2 and T_1 measurements were performed as part of the set-up procedure of a typical DEER experiment. The standard 4P DEER experiment was used [222]. A combination of a 3-pulse and 4-pulse DEER experiment has been used on occasion of short lived echos (Figure 2.8,[223]). For this approach each individual time-dependent trace was phased using DeerAnalysis and stitched together using Matlab based least square fitting, avoiding the inherent dead time to the 3-pulse experiment. Dipolar evolution functions were analysed using DeerAnalysis and implemented Tikhonov regularisation [432].

The absorption spectrum was recorded using a Hahn-echo ($\pi/2 \rightarrow \tau \rightarrow \pi \rightarrow \tau \rightarrow Echo$) where the echo intensity was measured as a function of the magnetic field. Typical parameters were $\pi/2$ = 6 ns, τ = 300 ns and π = 12 ns. The sweep width was 150 gauss for nitroxides. The T_2 was measured using a two pulse echo with an incremented inter-pulse delay ($\pi/2 \rightarrow T_0 + \tau \rightarrow \pi \rightarrow T_0 + \tau \rightarrow Echo$, where τ is the increment time). A typical set-up $\pi/2$ = 6 ns, τ = 300 ns, π = 12 ns incremented in 8 ns time steps. Typically T_2 times ranging from 700 - 1200 ns were achieved. The T_1 was measured using a inversion recovery experiment ($\pi \rightarrow T_{+t} \rightarrow \pi/2 \rightarrow \tau \rightarrow \pi \rightarrow \tau \rightarrow Echo$) with similar parameters to the experiments previously described. The T_1 time was used to set the recycle delay of the DEER experiment to $2.5 \cdot T_1$.

The 4-pulse DEER experiment was set-up with the π-pump pulse coinciding with the absorption maximum, determined by the field sweep. The pump pulse was set to 12 ns, whereas the observer pulses varied in length, depending on the sample. In general pulse length ranging between 12-24 ns were achieved. The τ_1 delay was set to 200 ns and the τ_2 delay was adjusted in accordance with the echo intensity, which varied across samples (Figure 2.8). A 16-step phase cycle was applied and τ_1 was incremented in steps of 16 ns (8 times) in order to suppress deuterium modulations [225].

A.1.6 Media and Buffers

Buffer A: 95% H_2O; 5% Acetonitrile; 0.1% TFA

Buffer B: 5% H_2O; 95% Acetonitrile; 0.1% TFA

TB Media (1 l): 24 g yeast extract. 12 g Tryptone; 8 ml Glycerol and 100 ml of 89 mM potassium phosphate at pH 7.2.

M9 salts (1 l): 6 g sodium phosphate (dibasic; Na_2HPO_4); 3 g potassium phosphate (monombasic; KH_2PO_4), 0.5 g sodium chloride (NaCl). Solution was prepared as a 10x concentrated stock and autoclaved.

M9 Media (1 l): 100 ml of 10x M9 salts, 1 g $^{15}NH_4Cl$, 4 g of glucose, 2 ml of 1 M magnesium sulphate ($MgSO_4$); 100 μl of 1 M calcium chloride ($CaCl_2$), 10 ml of MEM Vitamin solution

(Sigma-Aldrich), kanamycin (50 μg/ml final concentration) and chloramphenicol kanamycin (25 μg/ml final concentration)

Resuspension Buffer I: 1 mM ethylenediaminetetraacetic acid (EDTA), 50 mM trisaminomethane (Tris) pH 8, 1 mM sodium azide (NaN_3) and 15%gGlycerol.

Resuspension Buffer II: 1 mM EDTA, 50 mM Tris pH 8; 1 mM NaN_3, 1% deoxycholic acid (w/v) and 1% IGEPAL CA-630.

Ni^{2+}-Binding Buffer: 6 M guanidine hydrochloride, 0.5 M NaCl, 20 mM Tris pH 8.0 and 5 mM imidazole.

Ni^{2+}-Wash Buffer: 6 M guanidine hydrochloride, 0.5 M NaCl, 20 mM Tris pH 8.0 and 50 mM imidazole.

Ni^{2+}-Elution Buffer: 6 M guanidine hydrochloride, 0.5 M NaCl, 20 mM Tris pH 8.0 and 500 mM imidazole.

FPLC running buffer: 20 mM Sodium phosphate (pH 8.2), 4 mM SDS, 2 mM EDTA, 1mM NaN_3.

supplemented LDS-loading buffer: 1x NuPAGE LDS Sample Buffer (Thermo Fisher Scientific); 4.7 M Urea, 1% SDS and 42 mM DTT.

Resuspension Buffers and Ni^{2+}-purification buffers were prepared from following stock solutions: 8 M Guanidine hydrochloride; 2 M imidazole; 200 mM NaN_3; 0.5 M EDTA; 1 M Tris (pH 8); 4 M NaCl.

All lipids used in this thesis were acquired from Avanti polar lipids.

A.2 Additional information

A.2.1 Chapter 3

A.2.1.1 Solid-phase peptide synthesis

Solid phase peptide synthesis is a technique that is used for synthesis of organic compounds like oligonucleotides and short peptide sequences. The technique was first introduced in the 1960s by pioneering work of R. B. Merrifield, and since then has become a readily available, easy-to-use method for the production of organic compounds [433]. Solid phase synthesis relies on a solid support, coupled to a linker molecule, that serves as the starting point for the chemical synthesis. For peptide synthesis the linker provides a reactive centre for the attachment of N-α protected amino acid. The solid support is usually polymer based (eg. polystyrene) [434].

The N-α protection of the amino acids used for peptide assembly ensure a controlled step-wise reaction of a single amino acid at a time. The protecting group is only temporary and can be removed selectively post amino acid coupling to the growing peptide sequence.

The general method of solid phase synthesis is schematically outlined in Figure A.1. The process starts with the first amino acid reacting from the carboxyl group to the active reaction centre on the linker domain. A chemical coupling reagent is normally added to activate the carboxyl group to enhance the reaction rate (in this case N-[(1H-Benzotriazol-1-yl)(dimethylamino)-methylene]-N-methyl- methanaminium hexafluorophosphate N-oxide (HBTU)). This initial step is followed by washing of the reaction chamber to remove unreacted material. The normally chemically protected α-amino group of the reacted amino acid is then deprotected and the next amino acid can be loaded and coupled via the carboxyl group. In modern systems this reaction is facilitated by the application of microwaves to lower the energetic barrier and results in the formation of a peptide bond. This cycle is repeated until the full peptide sequence has been chemically synthesised. Note that reactive amino acid side chains are protected for the entirety of the amino acid addition cycles and become deprotected in acidic conditions post synthesis.

The addition of the first amino acid to the solid support is critical as it determines the density of peptides synthesised on the resin. The maximum loading depends on the

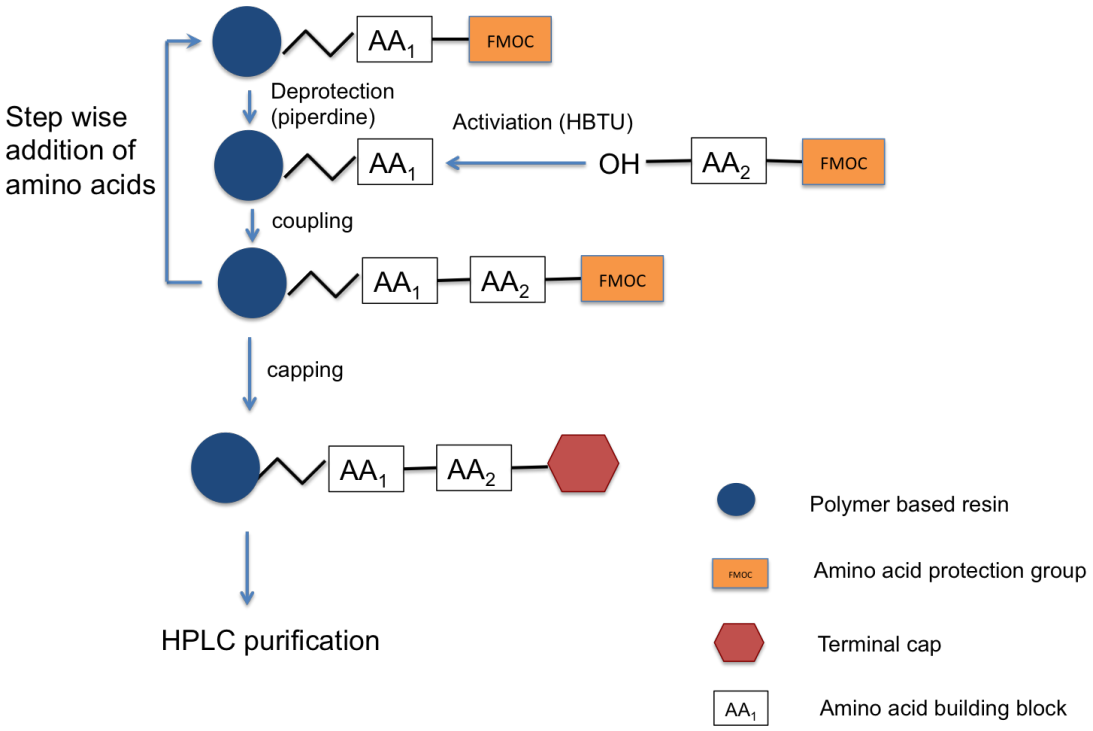

Figure A.1: A schematic illustrating of the chemical reactions involved in the process of solid phase peptide synthesis. The step addition of amino acids is cycled for each individual amino acid building block and involves the deprotection post coupling, the activation of the building block to be added followed by a microwave driven coupling reaction. After the organic synthesis cycle is complete the terminus can optionally be capped, which depends on the peptide purpose. The synthesis reaction is then cleaved off the solid resin and purified by High Performance Liquid Chromatography (HPLC).

characteristics of the resin and for most commercially available resins ranges from 0.3 - 2.5 mmol of reactive groups per g of resin support. The optimum loading capacity depends on the specific characteristics of the peptide that is to be synthesised and it is an important consideration to achieve optimum yields. Generally this first coupling reaction can be UV monitored if a Fmoc protection scheme is used (see section 2.1.2); if the dry resin is treated by a piperdine/dimethylformamide (DMF) solution, the product of dibenzofulvene-piperdine is formed which has an absorption peak at 301 nm [435].

This method has the advantage of being fully automated in modern biochemistry, hence extensive labour is not required. Solid phase synthesis also allows the use of large excess of reagents and thus as a result the coupling reaction progresses to near completion. Further to this no intermediate purification after each coupling step is required and washing of the solid resin is sufficient to remove unreacted amino acids. Yet, this method uses large excess amounts

of amino acids and solvent that can become expensive especially for longer peptide sequences with a smaller final product yield. Generally the production of peptides in milligram quantities is possible, which allows for extensive biophysical characterisation of the compound of interest.

A.2.1.1.1 Chemical protecting groups

One of the most important features that allows for successful solid phase peptide synthesis is the use of temporary protecting groups that can be selectively deprotected at specific time points during the synthesis cycle.

The most common protecting groups for solid phase synthesis are *tert*-butoxy-carbonyl (Boc) group and the fluoren-9-ylmethyloxycarbonyl (Fmoc) group [433; 436; 437] . Fmoc is commonly used to protect the primary amine group of the amino acid to be coupled, and can easily be removed due to its sensitivity to bases like piperdine. Boc on the other hand is sensitive to strong acids such as TFA. Generally, Fmoc is the preferred protection option as the deprotection conditions are mild compared to Boc. Different sensitivity profiles allow for selective protection and temporal depotraction of different reactive groups during the synthesis cycle known as orthogonal protection (Figure A.2).

A.2.1.1.2 Solid resins and linkers

The most common solid support is polystyrene to which 1 - 2% divinylbenzene (DVB) is added to provide a reactive group and to cross link the functional linker to the solid support. DVB is insoluble in all common solvents and thus remains bound to the resin. Resins are normally small spheres (typically 35 - 150 μm in diameter) that allow for peptide coupling on all sides. Polystyrene tend to swell when hydrated in solvent. The swelling factor typically ranges from 2 - 6 times and depends on the solvent used. This is important as it will affect the accessibility to DVB by solvents as well as peptide clustering on the resin during the synthesis process, thereby influencing the overall efficiency of the synthesis reaction [433; 438].

Chemical linkers are the starting point for chemical synthesis and bridge the DVB-containing resin to the peptide to be synthesised. Many different linkers have been developed that show slightly different chemical profiles. The most important properties to consider are

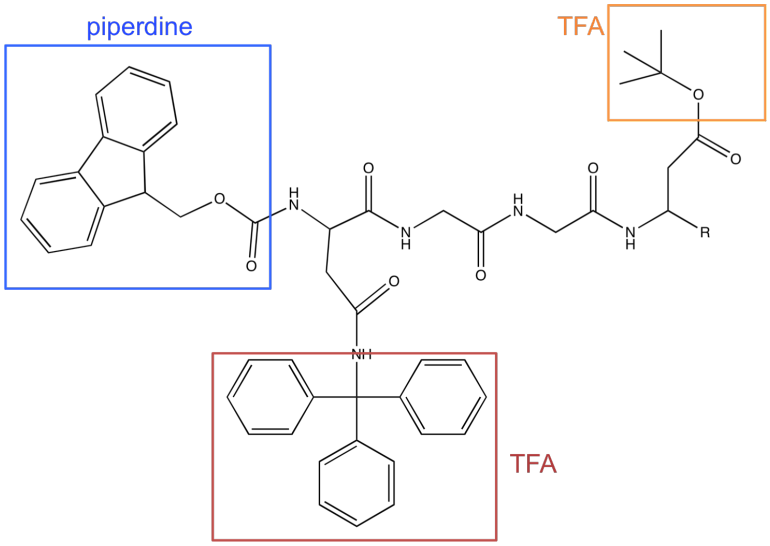

Figure A.2: A short peptide sequence is shown containing various protecting groups. The N-terminal is protected by a Fmoc group that is readily removed by a basic piperdine solution during the peptide synthesis (blue). The more liable trinyl group is removed by weak acidic conditions, most often by TFA (red) and the Boc group is cleaved in strong acidic conditions of concentrated TFA (orange).

the cleavage conditions to remove the peptide from the linker and the resulting chemical group that remains at the carboxyl end of the cleaved peptide. The most common linkers are Wang resin and MBHA resin, both use acidic conditions for cleavage and leave a remaining carboxylic acid group and an amide group respectively [434].

A.2.1.2 Peptide purity by MALDI-TOF

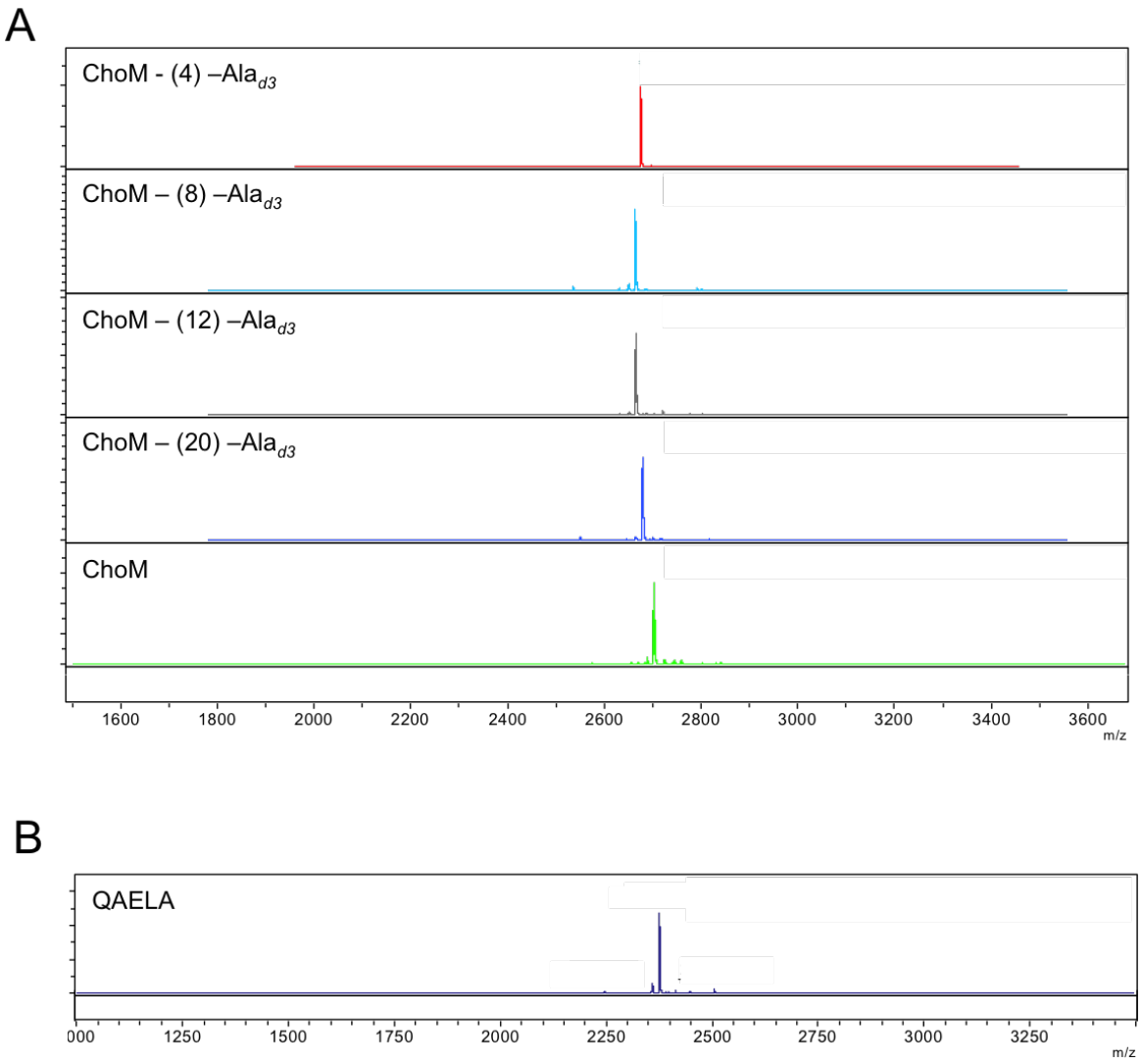

Figure A.3: The mass spectrometry (MALDI TOF) results for synthesised (A) ChoM and (B) QAELA peptides. (A) ChoM-(4)-Ala$_{d3}$: expected 2675.3, measured: 2675.4; ChoM-(8)-Ala$_{d3}$: expected 2661.3, measured: 2664.5; ChoM-(12)-Ala$_{d3}$: expected 2661.3, measured: 2665.1 ;ChoM-(20)-Ala$_{d3}$: expected 2675.3, measured 2678.1;ChoM: expected 2700, measured 2703.3; (B) QAELA: expected 2370.2, measured 2370.9.

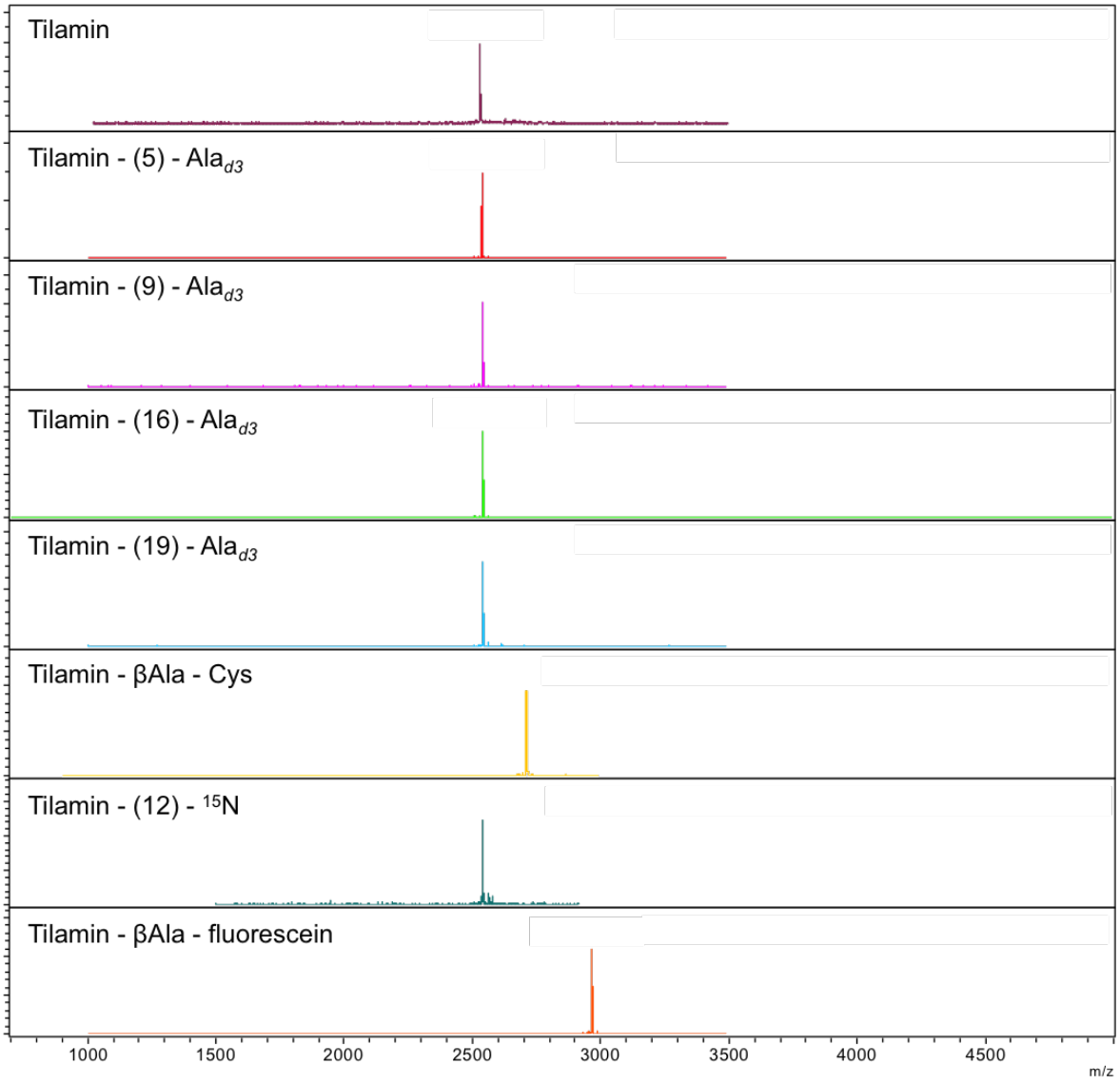

Figure A.4: The mass spectrometry (MALDI TOF) results for synthesised tilamin peptides. Tilamin: expected 2537.2, measured 2537.4; tilamin - Ala_{d3}: expected: 2540.2, measured 2540.8; tilamin - βAla - Cys: expected: 2711.4, measured: 2711.9; tilamin - (12) - ^{15}N: expected 2545.3, measured 2545.8; tilmain - βAls - fluorescein: expected 2965.5, measured: 2964.1.

A.2.2 Chapter 4

A.2.2.1 ^{2}H-NMR

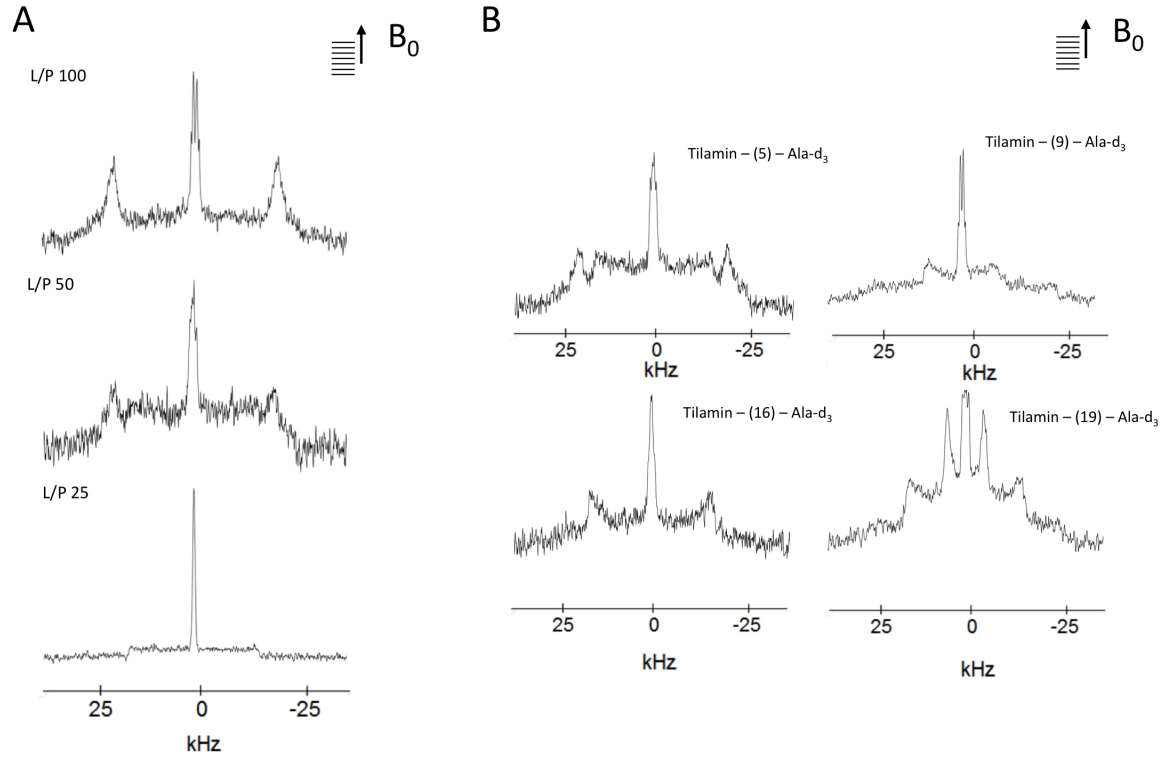

Figure A.5: The ^{2}H spectra of tilamin upon membrane interaction (DLPC:DLPG (3:1, molar ratio). (A) ^{2}H spectra showing tilamin-lipid interaction at different peptide to lipid molar ratios as indicted. The quadrupolar splitting collapses at a peptide to lipid molar ratio of 1:25, possibly due to significant bilayer disintegration. (B) The ^{2}H NMR spectra of the different deuterated Alanine residues are shown at peptide to lipid molar ratio of 1:50. Underlying powder patterns are observed for most spectra. Overall this indicates a higher potency of tilamin when interacting with saturated lipids (DLPC:DLPG (3:1, molar ratio).

A.2.2.2 ^{31}P-NMR

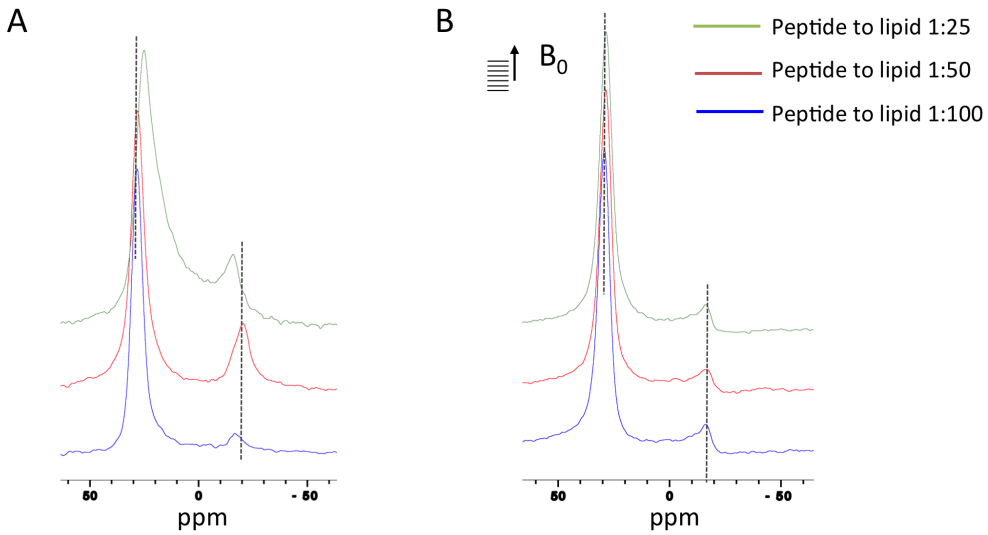

Figure A.6: Representative ^{31}P - NMR spectra are shown for mechanically aligned (A) DLPC:DLPG (3:1, molar ratio) and (B) POPG:POPC (3:1, molar ratio); in absence and presence of tilamin at different peptide to lipid molar ratios. Good lipid alignment was achieved for all samples, excluding DLPC:DLPG (3:1, molar ratio) in combination with tilamin at a molar ratio of 1:25, which is in agreement with an unresolved quadrupolar splitting for Ala-d_3 deuterated tilamin at this peptide to lipid molar ratio (Figure A.5 A).

A.2.2.3 MD simulations of tilamin

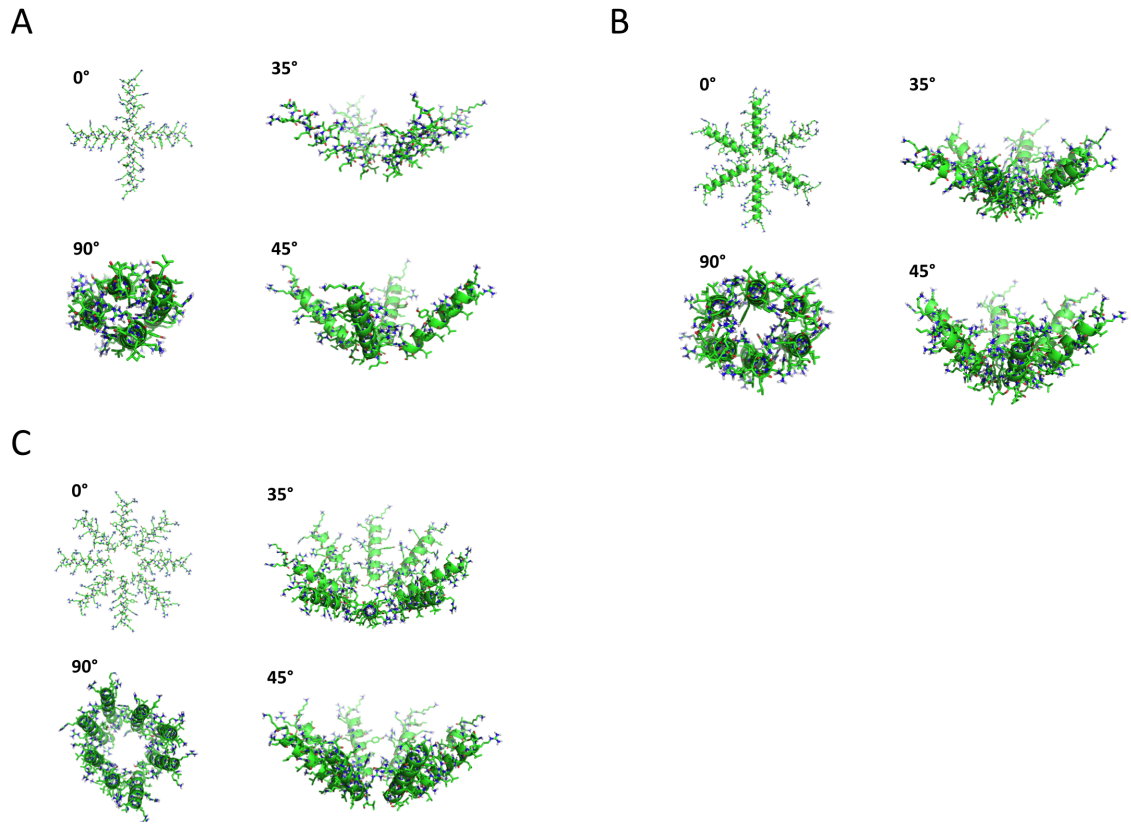

Figure A.7: The oligomeric tilamin assemblies used as starting points for MD simulations in POPC:POPG (3:1, molar ratio). All multimeric bundles were simulated at different relative tilt angles relative to the membrane plane in order to investigate potential bilayer penetration profiles. (A) Tetrameric assemblies; (B) hexameric assemblies and (C); octameric assemblies. All at different relative tilts.

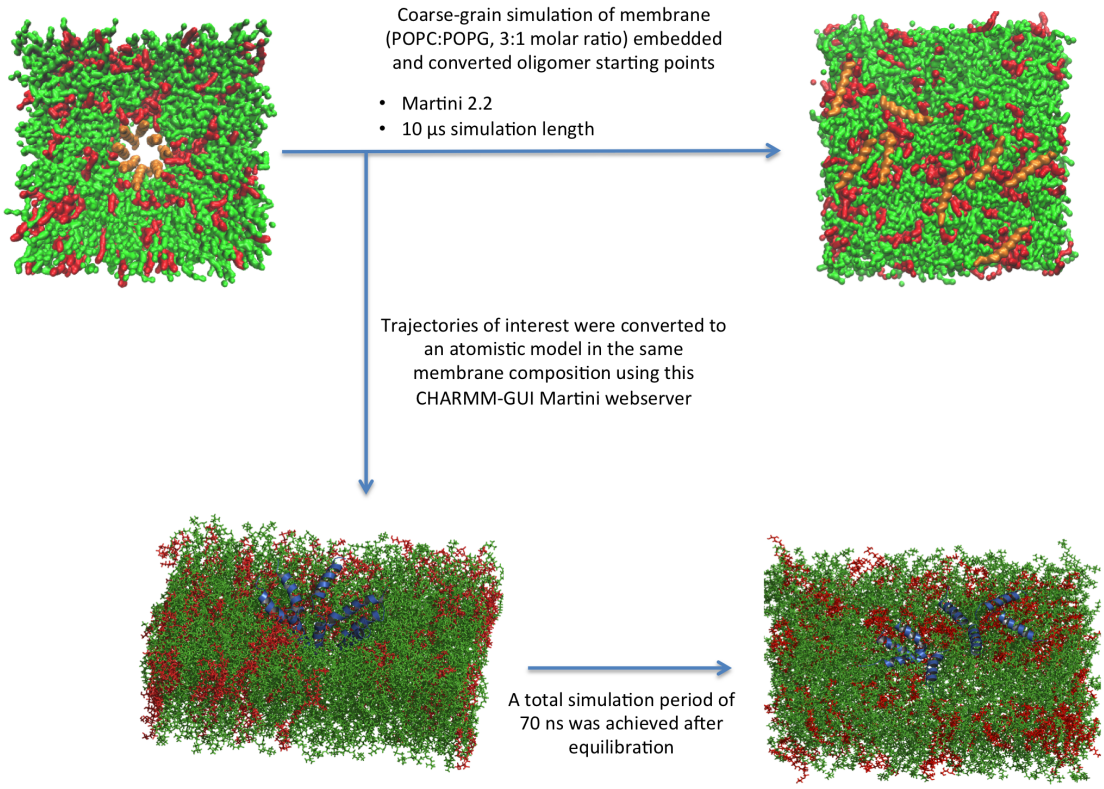

Figure A.8: All initial oligomeric configurations (as shown in Figure A.7) were converted to coarse-grain structures and manually placed into an equilibrated POPC:POPG (3:1, molar ratio) bilayer. MD simulations were run for a total of 10 μs. None of the tested assemblies was stable for the entire simulation span and thus individual trajectories of interest were converted to atomistic models and simulated for a short time period of 70 ns in order to evaluate if these configurations could be partially stable and of transient nature.

A.2.3 Chapter 7

A.2.3.1 Stitched 3p and 4p DEER trace of N-terminally labelled p7

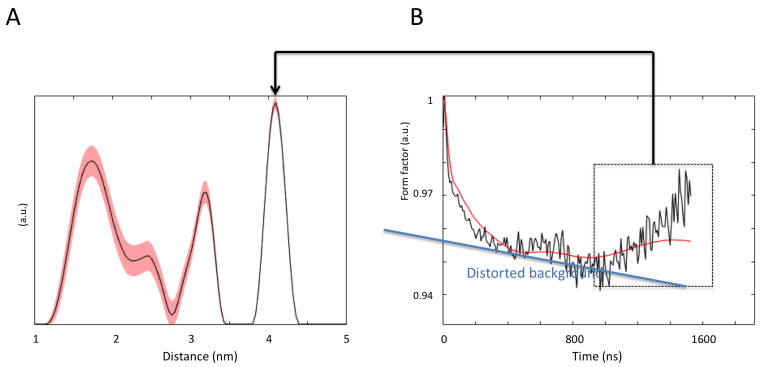

Figure A.9: The distance and time-dependent trace of p7 labelled at the N-terminus in DOPC:POPE (4:1, molar ratio) at a hexamer to lipid molar ratio of 1:150. (A) The resulting distance distribution by Tikhonov regularisation. (B) A combination of a 3p and 4p DEER traces that were stitched as described in [223]; at the benefit of allowing for a longer time-dependent trace utilising the 3p DEER sequence. A clear upwards trend is observed, resembling an unresolved oscillation of presumably non-specifically couples spins. This trend translates into a dominant distance around ∼4 nm (A), as also observed for the other DEER traces. This is probably attributed to the comparable high overall spin density in the membrane.

A.2.3.2 Static ^{31}P of p7 in DOPC:POPE(4:1, wt:wt)

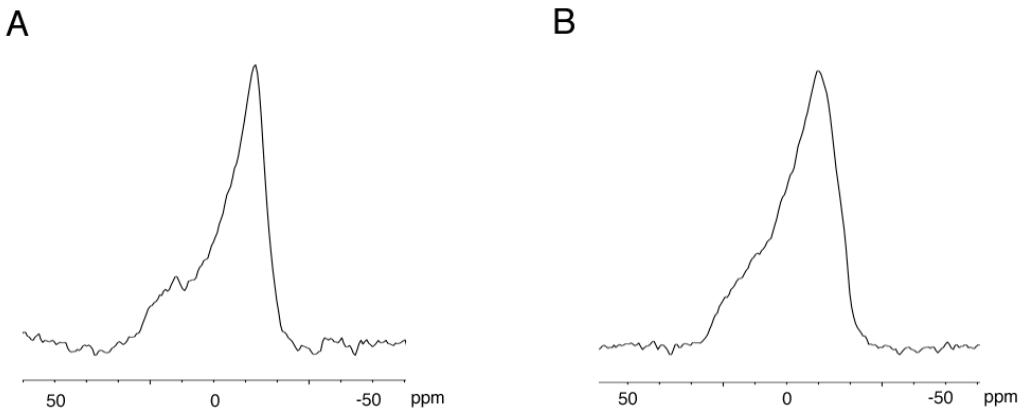

Figure A.10: Static ^{31}P NMR spectra of p7 in DOPC:POPE(1:4, wt:wt). (A) A hexamer to lipid molar ratio fo 1:2,000 and (B) A hexamer to lipid molar ratio of 1:150. Both spectra show a powder indicating vesicle formation in PE-rich membranes. The spectra were recorded at 30 °C and a phosphorus frequency of 323.78 MHz.

A.2.3.3 p7 S21C L51C mutation illustrated on PDB models

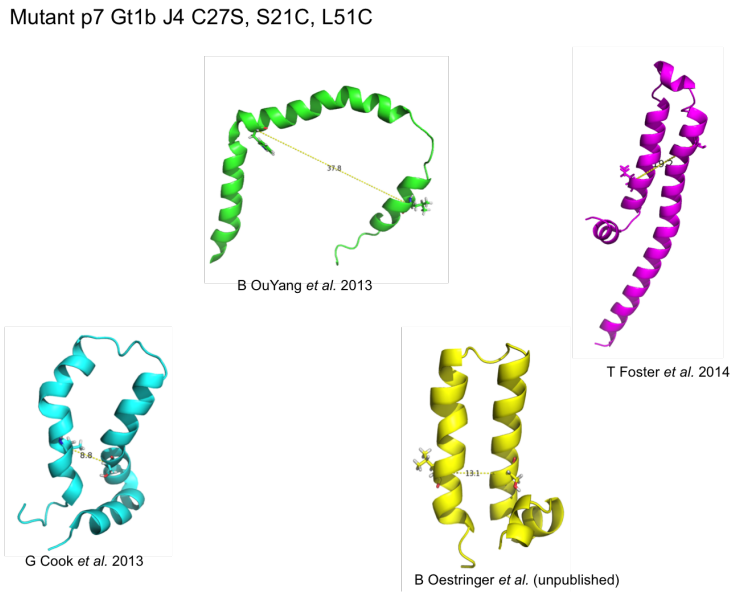

Figure A.11: The relative distances between C_α - C_α for residues 21 and 51, as labelled for DEER analysis, are shown for p7 models. Distances are: G Cook *et al.* 2013 8.8 Å; B OuYang *et al.* 2013 37.8 Å; B Oestringer *et al.* unpublished 13.1 Å; and T Foster *et al.* 2014 19.2Å. Note that these distances might be different from the experimentally measured distances as rotamer populations are not included in this illustration.

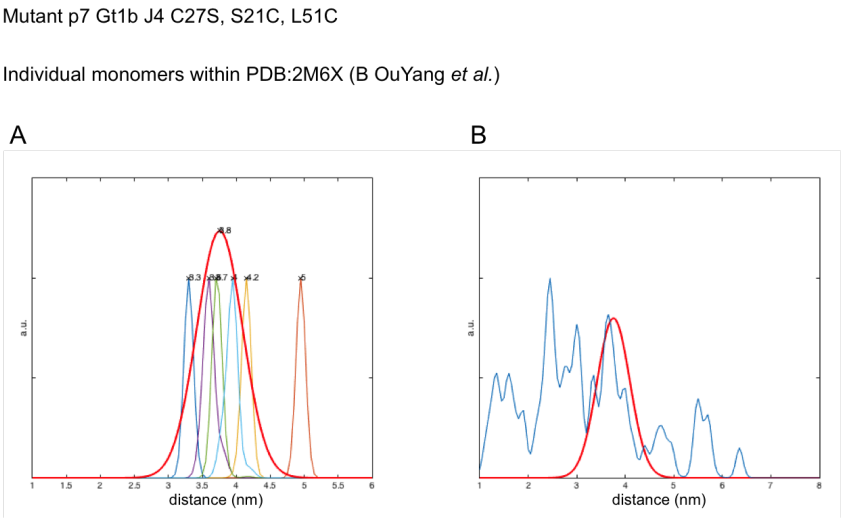

Figure A.12: The distance intramonomer distribution between residues 21 and 51 are shown for the oligomeric structure proposed by B OuYang *et al.* as simulated for rotamer populations attached at these residues. (A) The individual monomer distances for each of the six chains are shown in colour (treated individually as spin-pairs) and an average (Gaussian) is overlaid in red (bold). Note that the distances differ between the individual chains, which are not fully symmetric. (B) The average fitted in (A) is overlaid to a simulated distance distribution for an oligomer labelled at all chains, taking into account all spin-interactions including intermonomer interactions.

A.2.3.4 p7 K33R L51C mutation illustrated on PDB models

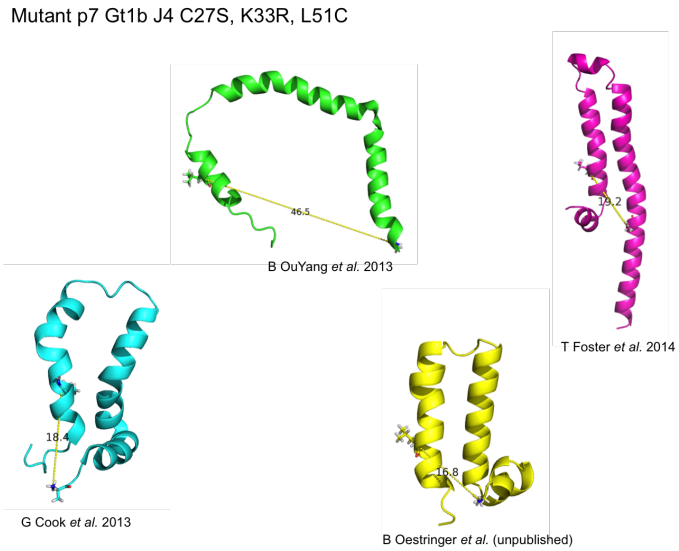

Figure A.13: The relative distances between C_α - C_α for residues 1 and 51, as labelled for DEER analysis, are shown for p7 models. Note that residue 1 is only an approximation as experimentally the N-terminus was directly labelled via the amide. Distances are: G Cook *et al.* 2013 18.4 Å; B OuYang *et al.* 2013 46.5 Å; B Oestringer *et al.* unpublished 16.8 Å;and T Foster *et al.* 2014 19.2 Å. Note that these distances might be different from the experimentally measured distances as rotamer populations are not included in this illustration.

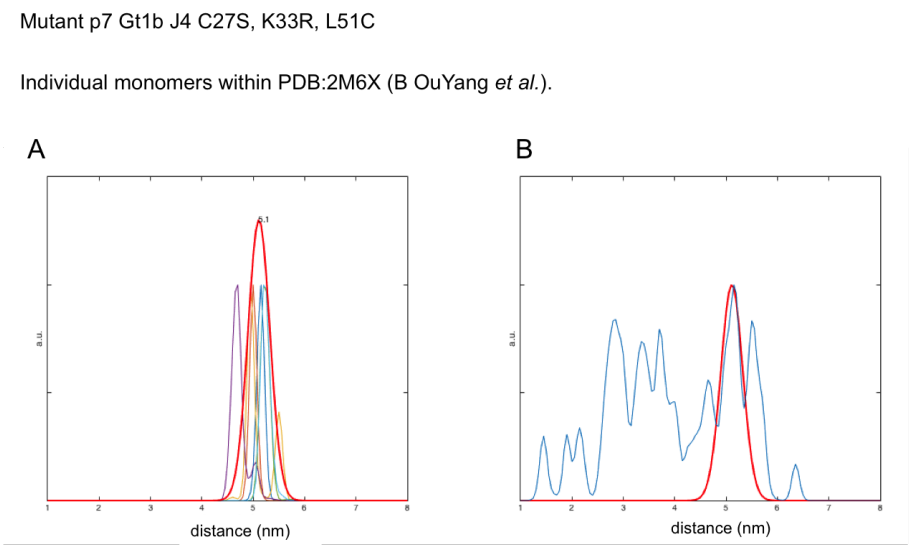

Figure A.14: The distance intramonomer distribution between residues 1 and 51 are shown for the oligomeric structure proposed by B OuYang *et al.* as simulated for rotamer populations attached at these residues. Note that residue 1 is only an approximation as experimentally the N-terminus was directly labelled via the amide. (A) The individual monomer distances for each of the six chains are shown in colour (treated individually as spin-pairs) and an average (Gaussian) is overlaid in red (bold). Note that the distances differ between the individual chains, which are not fully symmetric. (B) The average fitted in (A) is overlaid to a simulated distance distribution for an oligomer labelled at all chains, taking into account all spin-interactions including intermonomer interactions.

Table A.1: Summary of sample conditions for DEER

Figure	p7 mutant	Labelling efficiency (%)	D_2O	Cryoprotectant
7.7, 7.8, 7.10	p7 (Gt1b J4) G0 C-1	100	0	0
7.8, 7.9	p7 (Gt1b J4) G0 C-1	100	50	0
7.11	p7 (Gt1b J4) G64 C65	undetermined	40	15% ethylene glycol
7.15	p7 (Gt1b J4) S21C L51C	41	66	10% glycerol-d_8
7.16	p7 (Gt1b J4) S21C L51C	41	40	15% ethylene glycol
7.18 A, B	p7 (Gt1b J4) K33R L51C	undetermined	40	15% ethylene glycol
7.18 C,D	p7 (Gt1b J4) K33R L51C	undetermined	0	0

All samples contained 16 to 20mM sodium phosphate buffer (varying according to the addition of additives), pH 7.2. Note that reported spin-labelling efficiencies are prior to spin-dilution with unlablled protein; which was performed prior knowledge of the spin labelling efficiency, so that in those cases where the spin labelling efficiency was lower than 100%, the final spin dilution resulted greater than initially intended, but in such cases, this did not hamper the measurements and data analysis.

A.2.3.5 Construction of Chirp pulse for Gd^{3+} DEER

The Gadolinium DEER experiment were performed as previously described [407]. The observer pulses were aligned with the absorption spectrum maximum, of the central field splitting of Gadolinium. The pump pulses were applied as two separate frequency entities at lower and higher frequencies compared to the central field splitting respectively (Figure A.15 B). A similar set-up using squared and Gaussian shaped pulses was used for comparison. The frequency offset between the pump and observer pulses was varied between 160 - 300 MHz.

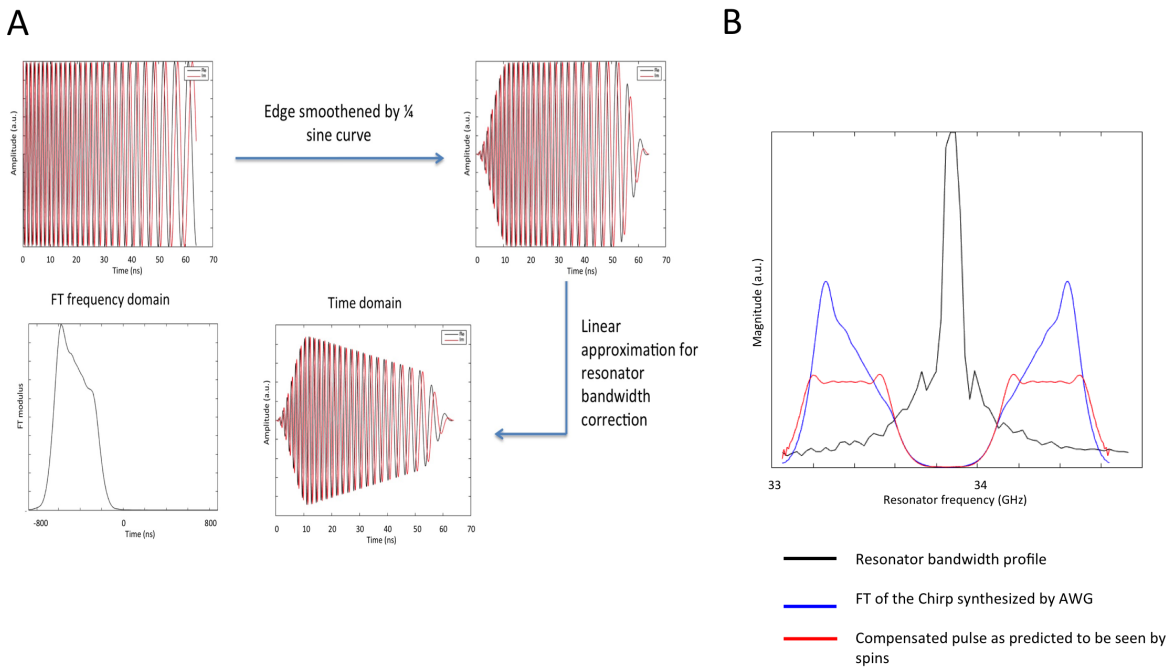

Figure A.15: The manual construction of a Chirp pulse. (A) The generic frequency chirp was generated using a 2D rotational matrix, where black is the real and red the imaginary part respectively.The edges were smoothened using a quarter of a sine curve. The resonator profile at the high and low frequencies (see (B), black) was approximated linearly and subtracted from the chirp pattern. The Fourier transformed pulse in the frequency domain is shown. (B) The resonator profile is shown in black, the chirp pulse generated by the arbitrary waveform generator (AWG) is shown in blue, and the compensated pulse as experienced by the local spins is shown in red. In collaboration with Will Myers (Department of Chemistry, Oxford).

Bibliography

[1] M. Luckey, *Membrane Structural Biology*. With Biochemical and Biophysical Foundations, Cambridge University Press, May 2014.

[2] S. J. Singer and G. L. Nicolson, "The fluid mosaic model of the structure of cell membranes," *Day and Good Membranes and viruses ...*, 1972.

[3] P. L. Yeagle, "Lipid regulation of cell membrane structure and function.," *The FASEB Journal*, vol. 3, pp. 1833–1842, May 1989.

[4] G. van Meer, D. R. Voelker, and G. W. Feigenson, "Membrane lipids: where they are and how they behave," *Nature Reviews Molecular Cell Biology*, vol. 9, pp. 112–124, Feb. 2008.

[5] L. Buehler, *Cell Membranes*. Garland Science, June 2015.

[6] N. Malanovic and K. Lohner, "Gram-positive bacterial cell envelopes: The impact on the activity of antimicrobial peptides," *Biochimica et Biophysica Acta (BBA) - Biomembranes*, vol. 1858, pp. 936–946, May 2016.

[7] L. V. Schäfer, D. H. de Jong, A. Holt, A. J. Rzepiela, A. H. de Vries, B. Poolman, J. A. Killian, and S. J. Marrink, "Lipid packing drives the segregation of transmembrane helices into disordered lipid domains in model membranes.," *Proceedings of the National Academy of Sciences of the United States of America*, vol. 108, pp. 1343–1348, Jan. 2011.

[8] G. W. Feigenson, "Phase behavior of lipid mixtures," *Nature chemical biology*, vol. 2, pp. 560–563, Nov. 2006.

[9] A. G. Lee, "Lipid phase transitions and phase diagrams II. Mixtures involving lipids," *Biochimica et Biophysica Acta (BBA) - Reviews on Biomembranes*, vol. 472, pp. 285–344, Nov. 1977.

[10] A. G. Marr and J. L. Ingraham, "Effect of temperature on the composition of fatty acids in E. coli.," *Journal of bacteriology*, vol. 84, pp. 1260–1267, Dec. 1962.

[11] J. N. Israelachvili, D. J. Mitchell, and B. W. Ninham, "Theory of self-assembly of hydrocarbon amphiphiles into micelles and bilayers," *J. Chem. Soc., Faraday Trans. 2*, vol. 72, pp. 1525–1568, Jan. 1976.

[12] K. Balasubramanian and A. J. Schroit, "Aminophospholipid asymmetry: A matter of life and death.," *Annual review of physiology*, vol. 65, no. 1, pp. 701–734, 2003.

[13] S. Manno, Y. Takakuwa, and N. Mohandas, "Identification of a functional role for lipid asymmetry in biological membranes: Phosphatidylserine-skeletal protein interactions modulate membrane stability.," *Proceedings of the National Academy of Sciences*, vol. 99, pp. 1943–1948, Feb. 2002.

[14] A. A. Gurtovenko and I. Vattulainen, "Lipid transmembrane asymmetry and intrinsic membrane potential: two sides of the same coin.," *Journal of the American Chemical Society*, vol. 129, pp. 5358–5359, May 2007.

[15] A. Zachowski, "Phospholipids in animal eukaryotic membranes: transverse asymmetry and movement.," *The Biochemical journal*, vol. 294 (Pt 1), pp. 1–14, Aug. 1993.

[16] P. F. Devaux, "Static and dynamic lipid asymmetry in cell membranes.," *Biochemistry*, vol. 30, pp. 1163–1173, Feb. 1991.

[17] R. F. Zwaal and A. J. Schroit, "Pathophysiologic implications of membrane phospholipid asymmetry in blood cells.," *Blood*, vol. 89, pp. 1121–1132, Feb. 1997.

[18] P. F. Devaux, "Protein involvement in transmembrane lipid asymmetry.," *Annual review of biophysics and biomolecular structure*, vol. 21, no. 1, pp. 417–439, 1992.

[19] M. Ikeda, A. Kihara, and Y. Igarashi, "Lipid Asymmetry of the Eukaryotic Plasma Membrane: Functions and Related Enzymes," *Biological and Pharmaceutical Bulletin*,

vol. 29, no. 8, pp. 1542–1546, 2006.
[20] J. Zhao, Q. Zhou, T. Wiedmer, and P. J. Sims, "Level of expression of phospholipid scramblase regulates induced movement of phosphatidylserine to the cell surface.," *The Journal of biological chemistry*, vol. 273, pp. 6603–6606, Mar. 1998.
[21] L. A. Woon, J. W. Holland, E. P. W. Kable, and B. D. Roufogalis, "Ca2+sensitivity of phospholipid scrambling in human red cell ghosts," *Cell calcium*, vol. 25, pp. 313–320, Apr. 1999.
[22] R. F. A. Zwaal, P. Comfurius, and E. M. Bevers, "Surface exposure of phosphatidylserine in pathological cells," *Cellular and Molecular Life Sciences CMLS*, vol. 62, no. 9, pp. 971–988, 2005.
[23] M. R. Yeaman and N. Y. Yount, "Mechanisms of antimicrobial peptide action and resistance.," *Pharmacological reviews*, vol. 55, pp. 27–55, Mar. 2003.
[24] P. Lasch, C. P. Schultz, and D. Naumann, "The Influence of Poly-(l-Lysine) and Porin on the Domain Structure of Mixed Vesicles Composed of Lipopolysaccharide and Phospholipid: An Infrared Spectroscopic Study," *Biophysical journal*, vol. 75, pp. 840–852, Aug. 1998.
[25] K. Matsuzaki, O. Murase, N. Fujii, and K. Miyajima, "An antimicrobial peptide, magainin 2, induced rapid flip-flop of phospholipids coupled with pore formation and peptide translocation.," *Biochemistry*, vol. 35, pp. 11361–11368, Sept. 1996.
[26] M. A. Kol, A. van Dalen, A. I. P. M. de Kroon, and B. de Kruijff, "Translocation of phospholipids is facilitated by a subset of membrane-spanning proteins of the bacterial cytoplasmic membrane.," *The Journal of biological chemistry*, vol. 278, pp. 24586–24593, July 2003.
[27] M. A. Kol, A. I. de Kroon, D. T. Rijkers, J. A. Killian, and B. de Kruijff, "Membrane-spanning peptides induce phospholipid flop: a model for phospholipid translocation across the inner membrane of E. coli.," *Biochemistry*, vol. 40, pp. 10500–10506, Sept. 2001.
[28] M. N. Melo, R. Ferre, and M. A. R. B. Castanho, "Antimicrobial peptides: linking partition, activity and high membrane-bound concentrations," *Nature Reviews Microbiology*, vol. 7, pp. 245–250, Mar. 2009.
[29] H. Nikaido and T. Nakae, "The outer membrane of Gram-negative bacteria.," *Advances in microbial physiology*, vol. 20, pp. 163–250, 1979.
[30] W. Vollmer and J.-V. Höltje, "The architecture of the murein (peptidoglycan) in gram-negative bacteria: vertical scaffold or horizontal layer(s)?," *Journal of bacteriology*, vol. 186, pp. 5978–5987, Sept. 2004.
[31] L. Gan, S. Chen, and G. J. Jensen, "Molecular organization of Gram-negative peptidoglycan.," *Proceedings of the National Academy of Sciences of the United States of America*, vol. 105, pp. 18953–18957, Dec. 2008.
[32] J. Errington, "L-form bacteria, cell walls and the origins of life," *Open biology*, vol. 3, pp. 120143–120143, Jan. 2013.
[33] T. Gutberlet, J. Frank, H. Bradaczek, and W. Fischer, "Effect of lipoteichoic acid on thermotropic membrane properties.," *Journal of bacteriology*, vol. 179, pp. 2879–2883, May 1997.
[34] D. Roversi, V. Luca, S. Aureli, Y. Park, M. L. Mangoni, and L. Stella, "How Many Antimicrobial Peptide Molecules Kill a Bacterium? The Case of PMAP-23," *ACS Chemical Biology*, vol. 9, pp. 2003–2007, July 2014.
[35] J. M. Freire, D. Gaspar, A. S. Veiga, and M. A. R. B. Castanho, "Shifting gear in antimicrobial and anticancer peptides biophysical studies: from vesicles to cells," *Journal of peptide science : an official publication of the European Peptide Society*, vol. 21, pp. 178–185, Mar. 2015.
[36] L. A. Clifton, S. A. Holt, A. V. Hughes, E. L. Daulton, W. Arunmanee, F. Heinrich, S. Khalid, D. Jefferies, T. R. Charlton, J. R. P. Webster, C. J. Kinane, and J. H. Lakey, "An accurate in vitro model of the E.coli envelope.," *Angewandte Chemie International Edition*, vol. 54, pp. 11952–11955, Oct. 2015.
[37] A. G. Lee, "How lipids and proteins interact in a membrane: a molecular approach," *Molecular Biosystems*, vol. 1, no. 3, pp. 203–212, 2005.
[38] P. F. Knowles, A. Watts, and D. Marsh, "Spin-label studies of lipid immobilization in dimyristoylphosphatidiylcholine-substituted cytochrome oxidase," *Biochemistry*, vol. 18, pp. 4480–4487, Oct. 1979.

[39] A. Watts, I. D. Volotovski, and D. Marsh, "Rhodopsin-lipid associations in bovine rod outer segment membranes. Identification of immobilized lipid by spin-labels," *Biochemistry*, vol. 18, pp. 5006–5013, Oct. 1979.
[40] J. A. Killian and T. K. M. Nyholm, "Peptides in lipid bilayers: the power of simple models.," *Current opinion in structural biology*, vol. 16, pp. 473–479, Aug. 2006.
[41] A. G. Lee, "How lipids affect the activities of integral membrane proteins.," *Biochimica et biophysica acta*, vol. 1666, pp. 62–87, Nov. 2004.
[42] T. J. McIntosh and S. A. Simon, "Roles of bilayer material properties in function and distribution of membrane proteins.," *Annual review of biophysics and biomolecular structure*, vol. 35, no. 1, pp. 177–198, 2006.
[43] M. R. de Planque, D. V. Greathouse, R. E. Koeppe, H. Schäfer, D. Marsh, and J. A. Killian, "Influence of lipid/peptide hydrophobic mismatch on the thickness of diacylphosphatidylcholine bilayers. A 2H NMR and ESR study using designed transmembrane alpha-helical peptides and gramicidin A.," *Biochemistry*, vol. 37, pp. 9333–9345, June 1998.
[44] P. C. A. van der Wel, E. Strandberg, J. A. Killian, and R. E. Koeppe II, "Geometry and Intrinsic Tilt of a Tryptophan-Anchored Transmembrane α-Helix Determined by 2H NMR," *Biophysical journal*, vol. 83, pp. 1479–1488, Sept. 2002.
[45] S. Ozdirekcan, D. T. S. Rijkers, R. M. J. Liskamp, and J. A. Killian, "Influence of flanking residues on tilt and rotation angles of transmembrane peptides in lipid bilayers. A solid-state 2H NMR study.," *Biochemistry*, vol. 44, pp. 1004–1012, Jan. 2005.
[46] T. M. Weiss, P. C. A. van der Wel, J. A. Killian, R. E. Koeppe, and H. W. Huang, "Hydrophobic mismatch between helices and lipid bilayers.," *Biophysical journal*, vol. 84, pp. 379–385, Jan. 2003.
[47] S. H. Park and S. J. Opella, "Tilt angle of a trans-membrane helix is determined by hydrophobic mismatch.," *Journal of molecular biology*, vol. 350, pp. 310–318, July 2005.
[48] T. A. Harroun, W. T. Heller, T. M. Weiss, L. Yang, and H. W. Huang, "Experimental evidence for hydrophobic matching and membrane-mediated interactions in lipid bilayers containing gramicidin.," *Biophysical journal*, vol. 76, pp. 937–945, Feb. 1999.
[49] M. R. R. de Planque, B. B. Bonev, J. A. A. Demmers, D. V. Greathouse, R. E. Koeppe, F. Separovic, A. Watts, and J. A. Killian, "Interfacial anchor properties of tryptophan residues in transmembrane peptides can dominate over hydrophobic matching effects in peptide-lipid interactions.," *Biochemistry*, vol. 42, pp. 5341–5348, May 2003.
[50] S. Sharpe, K. R. Barber, C. W. M. Grant, D. Goodyear, and M. R. Morrow, "Organization of model helical peptides in lipid bilayers: insight into the behavior of single-span protein transmembrane domains.," *Biophysical journal*, vol. 83, pp. 345–358, July 2002.
[51] E. Strandberg, S. Ozdirekcan, D. T. S. Rijkers, P. C. A. van der Wel, R. E. Koeppe, R. M. J. Liskamp, and J. A. Killian, "Tilt angles of transmembrane model peptides in oriented and non-oriented lipid bilayers as determined by 2H solid-state NMR.," vol. 86, pp. 3709–3721, June 2004.
[52] M. A. Carbone and P. M. Macdonald, "Cardiotoxin II segregates phosphatidylglycerol from mixtures with phosphatidylcholine: (31)P and (2)H NMR spectroscopic evidence.," *Biochemistry*, vol. 35, pp. 3368–3378, Mar. 1996.
[53] C. E. Dempsey and A. Watts, "A deuterium and phosphorus-31 nuclear magnetic resonance study of the interaction of melittin with dimyristoylphosphatidylcholine bilayers and the effects of contaminating phospholipase A2," *Biochemistry*, vol. 26, pp. 5803–5811, Sept. 1987.
[54] E. Kuchinka and J. Seelig, "Interaction of melittin with phosphatidylcholine membranes. Binding isotherm and lipid head-group conformation.," *Biochemistry*, vol. 28, pp. 4216–4221, May 1989.
[55] A. Watts, "Solid-state NMR approaches for studying the interaction of peptides and proteins with membranes.," *Biochimica et biophysica acta*, vol. 1376, pp. 297–318, Nov. 1998.
[56] M. Roux, J. M. Neumann, R. S. Hodges, P. F. Devaux, and M. Bloom, "Conformational changes of phospholipid headgroups induced by a cationic integral membrane peptide as seen by deuterium magnetic resonance.," *Biochemistry*, vol. 28, pp. 2313–2321, Mar. 1989.
[57] A. Engel and H. E. Gaub, "Structure and mechanics of membrane proteins.," *Annual review of biochemistry*, vol. 77, no. 1, pp. 127–148, 2008.

[58] E. Wallin and G. V. Heijne, "Genome-wide analysis of integral membrane proteins from eubacterial, archaean, and eukaryotic organisms," *Protein Science*, vol. 7, pp. 1029–1038, Apr. 1998.
[59] M. E. Gonzalez and L. Carrasco, "Viroporins," *FEBS letters*, vol. 552, pp. 28–34, July 2003.
[60] K. Wang, S. Xie, and B. Sun, "Viral proteins function as ion channels," *Biochimica et Biophysica Acta (BBA) - Biomembranes*, vol. 1808, pp. 510–515, Feb. 2011.
[61] L. F. Wetherill, K. K. Holmes, M. Verow, M. Müller, G. Howell, M. Harris, C. Fishwick, N. Stonehouse, R. Foster, G. E. Blair, S. Griffin, and A. Macdonald, "High-risk human papillomavirus E5 oncoprotein displays channel-forming activity sensitive to small-molecule inhibitors.," *Journal of virology*, vol. 86, pp. 5341–5351, May 2012.
[62] L. H. Pinto, L. J. Holsinger, and R. A. Lamb, "Influenza virus M2 protein has ion channel activity," *Cell*, vol. 69, pp. 517–528, May 1992.
[63] W. B. Fischer and H.-J. Hsu, "Viral channel forming proteins — Modeling the target," *Biochimica et Biophysica Acta (BBA) - Biomembranes*, vol. 1808, pp. 561–571, Feb. 2011.
[64] R. Acharya, V. Carnevale, G. Fiorin, B. G. Levine, A. L. Polishchuk, V. Balannik, I. Samish, R. A. Lamb, L. H. Pinto, W. F. DeGrado, and M. L. Klein, "Structure and mechanism of proton transport through the transmembrane tetrameric M2 protein bundle of the influenza A virus.," *Proceedings of the National Academy of Sciences of the United States of America*, vol. 107, pp. 15075–15080, Aug. 2010.
[65] S. H. Park, A. A. Mrse, A. A. Nevzorov, M. F. Mesleh, M. Oblatt-Montal, M. Montal, and S. J. Opella, "Three-dimensional Structure of the Channel-forming Trans-membrane Domain of Virus Protein "u" (Vpu) from HIV-1," *Journal of molecular biology*, vol. 333, pp. 409–424, Oct. 2003.
[66] B. OuYang, S. Xie, M. J. Berardi, X. Zhao, J. Dev, W. Yu, B. Sun, and J. J. Chou, "Unusual architecture of the p7 channel from hepatitis C virus.," *Nature*, vol. 498, pp. 521–525, June 2013.
[67] K. C. Duff and R. H. Ashley, "The transmembrane domain of influenza A M2 protein forms amantadine-sensitive proton channels in planar lipid bilayers.," *Virology*, vol. 190, pp. 485–489, Sept. 1992.
[68] D. Clarke, S. Griffin, L. Beales, C. S. Gelais, S. Burgess, M. Harris, and D. Rowlands, "Evidence for the formation of a heptameric ion channel complex by the hepatitis C virus p7 protein in vitro.," *The Journal of biological chemistry*, vol. 281, pp. 37057–37068, Dec. 2006.
[69] C. F. Chew, R. Vijayan, J. Chang, N. Zitzmann, and P. C. Biggin, "Determination of pore-lining residues in the hepatitis C virus p7 protein.," *Biophysical journal*, vol. 96, pp. L10–2, Jan. 2009.
[70] S. D. C. Griffin, L. P. Beales, D. S. Clarke, O. Worsfold, S. D. Evans, J. Jaeger, M. P. G. Harris, and D. J. Rowlands, "The p7 protein of hepatitis C virus forms an ion channel that is blocked by the antiviral drug, Amantadine," *FEBS letters*, vol. 535, pp. 34–38, Jan. 2003.
[71] D. Pavlović, D. C. A. Neville, O. Argaud, B. Blumberg, R. A. Dwek, W. B. Fischer, and N. Zitzmann, "The hepatitis C virus p7 protein forms an ion channel that is inhibited by long-alkyl-chain iminosugar derivatives.," *Proceedings of the National Academy of Sciences of the United States of America*, vol. 100, pp. 6104–6108, May 2003.
[72] T. Whitfield, A. J. Miles, J. C. Scheinost, J. Offer, P. Wentworth, R. A. Dwek, B. A. Wallace, P. C. Biggin, and N. Zitzmann, "The influence of different lipid environments on the structure and function of the hepatitis C virus p7 ion channel protein.," *Molecular membrane biology*, vol. 28, pp. 254–264, Aug. 2011.
[73] P. Luik, C. Chew, J. Aittoniemi, J. Chang, P. Wentworth, R. A. Dwek, P. C. Biggin, C. Vénien-Bryan, and N. Zitzmann, "The 3-dimensional structure of a hepatitis C virus p7 ion channel by electron microscopy.," *Proceedings of the National Academy of Sciences of the United States of America*, vol. 106, pp. 12712–12716, Aug. 2009.
[74] R. Montserret, N. Saint, C. Vanbelle, A. G. Salvay, J.-P. Simorre, C. Ebel, N. Sapay, J.-G. Renisio, A. Böckmann, E. Steinmann, T. Pietschmann, J. Dubuisson, C. Chipot, and F. Penin, "NMR structure and ion channel activity of the p7 protein from hepatitis C virus.," *The Journal of biological chemistry*, vol. 285, pp. 31446–31461, Oct. 2010.
[75] J. L. Nieva, V. Madan, and L. Carrasco, "Viroporins: structure and biological functions.," *Nature Reviews Microbiology*, vol. 10, pp. 563–574, Aug. 2012.

[76] T. Suzuki, Y. Orba, Y. Okada, Y. Sunden, T. Kimura, S. Tanaka, K. Nagashima, W. W. Hall, and H. Sawa, "The human polyoma JC virus agnoprotein acts as a viroporin.," *PLoS pathogens*, vol. 6, p. e1000801, Mar. 2010.
[77] S. Raghava, K. M. Giorda, F. B. Romano, A. P. Heuck, and D. N. Hebert, "SV40 late protein VP4 forms toroidal pores to disrupt membranes for viral release.," *Biochemistry*, vol. 52, pp. 3939–3948, June 2013.
[78] A. Helenius, "Unpacking the incoming influenza virus.," *Cell*, vol. 69, pp. 577–578, May 1992.
[79] E. R. Georgieva, P. P. Borbat, H. D. Norman, and J. H. Freed, "Mechanism of influenza A M2 transmembrane domain assembly in lipid membranes," *Scientific reports*, vol. 5, p. 11757, July 2015.
[80] S. Grambas, M. S. Bennett, and A. J. Hay, "Influence of amantadine resistance mutations on the pH regulatory function of the M2 protein of influenza A viruses.," *Virology*, vol. 191, pp. 541–549, Dec. 1992.
[81] S. Grambas and A. J. Hay, "Maturation of influenza A virus hemagglutinin–estimates of the pH encountered during transport and its regulation by the M2 protein.," *Virology*, vol. 190, pp. 11–18, Sept. 1992.
[82] A. L. Wozniak, S. Griffin, D. Rowlands, M. Harris, M. Yi, S. M. Lemon, and S. A. Weinman, "Intracellular proton conductance of the hepatitis C virus p7 protein and its contribution to infectious virus production.," *PLoS pathogens*, vol. 6, no. 9, p. e1001087, 2010.
[83] G. Vieyres, C. Brohm, M. Friesland, J. Gentzsch, B. Wölk, P. Roingeard, E. Steinmann, and T. Pietschmann, "Subcellular localization and function of an epitope-tagged p7 viroporin in hepatitis C virus-producing cells.," *Journal of virology*, vol. 87, pp. 1664–1678, Feb. 2013.
[84] H. Gouklani, C. Beyer, H. Drummer, E. J. Gowans, H. J. Netter, and G. Haqshenas, "Identification of specific regions in hepatitis C virus core, NS2 and NS5A that genetically interact with p7 and co-ordinate infectious virus production.," *Journal of viral hepatitis*, vol. 20, pp. e66–71, Apr. 2013.
[85] V. Jirasko, R. Montserret, J. Y. Lee, J. Gouttenoire, D. Moradpour, F. Penin, and R. Bartenschlager, "Structural and Functional Studies of Nonstructural Protein 2 of the Hepatitis C Virus Reveal Its Key Role as Organizer of Virion Assembly," *PLoS pathogens*, vol. 6, p. e1001233, Dec. 2010.
[86] Y. Ma, M. Anantpadma, J. M. Timpe, S. Shanmugam, S. M. Singh, S. M. Lemon, and M. Yi, "Hepatitis C virus NS2 protein serves as a scaffold for virus assembly by interacting with both structural and nonstructural proteins.," *Journal of virology*, vol. 85, pp. 86–97, Jan. 2011.
[87] G. A. Cook, L. A. Dawson, Y. Tian, and S. J. Opella, "Three-Dimensional Structure and Interaction Studies of Hepatitis C Virus p7 in 1,2-Dihexanoyl- sn-glycero-3-phosphocholine by Solution Nuclear Magnetic Resonance," *Biochemistry*, vol. 52, pp. 5295–5303, Aug. 2013.
[88] I. Agarkova, D. Dunigan, J. Gurnon, T. Greiner, J. Barres, G. Thiel, and J. L. Van Etten, "Chlorovirus-mediated membrane depolarization of Chlorella alters secondary active transport of solutes.," *Journal of virology*, vol. 82, pp. 12181–12190, Dec. 2008.
[89] V. Madan, A. Castelló, and L. Carrasco, "Viroporins from RNA viruses induce caspase-dependent apoptosis," *Cellular microbiology*, vol. 10, pp. 437–451, Feb. 2008.
[90] C. Scott and S. Griffin, "Viroporins: structure, function and potential as antiviral targets.," *The Journal of general virology*, vol. 96, pp. 2000–2027, Aug. 2015.
[91] W. L. Davies, R. R. Grunert, R. F. Haff, J. W. McGahen, E. M. Neumayer, M. Paulshock, J. C. Watts, T. R. Wood, E. C. Hermann, and C. E. Hoffmann, "Antiviral activity of Amantadine.," *Science (New York, N.Y.)*, vol. 144, pp. 862–863, May 1964.
[92] Y. Togo, R. B. Hornick, and A. T. Dawkins, "Studies on induced influenza in man. I. Double-blind studies designed to assess prophylactic efficacy of amantadine hydrochloride against a2/Rockville/1/65 strain.," *JAMA*, vol. 203, pp. 1089–1094, Mar. 1968.
[93] A. T. Dawkins, L. R. Gallager, Y. Togo, R. B. Hornick, and B. A. Harris, "Studies on induced influenza in man. II. Double-blind study designed to assess the prophylactic efficacy of an analogue of amantadine hydrochloride.," *JAMA*, vol. 203, pp. 1095–1099, Mar. 1968.
[94] W. L. Wingfield, D. Pollack, and R. R. GRUNERT, "Therapeutic efficacy of amantadine HCl and rimantadine HCl in naturally occurring influenza A2 respiratory illness in

man.," *The New England journal of medicine*, vol. 281, pp. 579–584, Sept. 1969.
[95] A. B. Sabin, "Amantadine hydrochloride. Analysis of data related to its proposed use for prevention of A2 influenza virus disease in human beings.," *JAMA*, vol. 200, pp. 943–950, June 1967.
[96] R. B. Couch, "Use of amantadine in the therapy and prophylaxis of A2 influenza.," *Bulletin of the World Health Organization*, vol. 41, no. 3, pp. 695–696, 1969.
[97] A. J. Hay, A. J. Wolstenholme, J. J. Skehel, and M. H. Smith, "The molecular basis of the specific anti-influenza action of amantadine.," *The EMBO journal*, vol. 4, pp. 3021–3024, Nov. 1985.
[98] J. R. Schnell and J. J. Chou, "Structure and mechanism of the M2 proton channel of influenza A virus.," *Nature*, vol. 451, pp. 591–595, Jan. 2008.
[99] S. D. Cady, K. Schmidt-Rohr, J. Wang, C. S. Soto, W. F. DeGrado, and M. Hong, "Structure of the amantadine binding site of influenza M2 proton channels in lipid bilayers.," *Nature*, vol. 463, pp. 689–692, Feb. 2010.
[100] S. D. Cady, T. V. Mishanina, and M. Hong, "Structure of amantadine-bound M2 transmembrane peptide of influenza A in lipid bilayers from magic-angle-spinning solid-state NMR: the role of Ser31 in amantadine binding.," *Journal of molecular biology*, vol. 385, pp. 1127–1141, Jan. 2009.
[101] F. Hu, W. Luo, S. D. Cady, and M. Hong, "Conformational plasticity of the influenza A M2 transmembrane helix in lipid bilayers under varying pH, drug binding, and membrane thickness.," *Biochimica et biophysica acta*, vol. 1808, pp. 415–423, Jan. 2011.
[102] S. Y. Liao, K. J. Fritzsching, and M. Hong, "Conformational analysis of the full-length M2 protein of the influenza A virus using solid-state NMR," *Protein Science*, vol. 22, pp. 1623–1638, Nov. 2013.
[103] K. C. Duff, P. J. Gilchrist, A. M. Saxena, and J. P. Bradshaw, "Neutron diffraction reveals the site of amantadine blockade in the influenza A M2 ion channel.," *Virology*, vol. 202, pp. 287–293, July 1994.
[104] J. Hu, T. Asbury, S. Achuthan, C. Li, R. Bertram, J. R. Quine, R. Fu, and T. A. Cross, "Backbone structure of the amantadine-blocked trans-membrane domain M2 proton channel from Influenza A virus.," *Biophysical journal*, vol. 92, pp. 4335–4343, June 2007.
[105] Y. Wu, B. Canturk, H. Jo, C. Ma, E. Gianti, M. L. Klein, L. H. Pinto, R. A. Lamb, G. Fiorin, J. Wang, and W. F. DeGrado, "Flipping in the Pore: Discovery of Dual Inhibitors That Bind in Different Orientations to the Wild-Type versus the Amantadine-Resistant S31N Mutant of the Influenza A Virus M2 Proton Channel," *Journal of the American Chemical Society*, vol. 136, pp. 17987–17995, Dec. 2014.
[106] C. Wang, R. A. Lamb, and L. H. Pinto, "Activation of the M2 ion channel of influenza virus: a role for the transmembrane domain histidine residue.," *Biophysical journal*, vol. 69, pp. 1363–1371, Oct. 1995.
[107] A. L. Stouffer, R. Acharya, D. Salom, A. S. Levine, L. Di Costanzo, C. S. Soto, V. Tereshko, V. Nanda, S. Stayrook, and W. F. DeGrado, "Structural basis for the function and inhibition of an influenza virus proton channel," *Nature*, vol. 451, pp. 596–599, Jan. 2008.
[108] G. Dong, C. Peng, J. Luo, C. Wang, L. Han, B. Wu, G. Ji, and H. He, "Adamantane-Resistant Influenza A Viruses in the World (1902–2013): Frequency and Distribution of M2 Gene Mutations," *PloS one*, vol. 10, p. e0119115, Mar. 2015.
[109] G. D. Ewart, K. Mills, G. B. Cox, and P. W. Gage, "Amiloride derivatives block ion channel activity and enhancement of virus-like particle budding caused by HIV-1 protein Vpu.," *European biophysics journal : EBJ*, vol. 31, pp. 26–35, Mar. 2002.
[110] W. Römer, Y. H. Lam, D. Fischer, A. Watts, W. B. Fischer, P. Göring, R. B. Wehrspohn, U. Gösele, and C. Steinem, "Channel activity of a viral transmembrane peptide in micro-BLMs: Vpu(1-32) from HIV-1.," *Journal of the American Chemical Society*, vol. 126, pp. 16267–16274, Dec. 2004.
[111] V. Lemaitre, R. Ali, C. G. Kim, A. Watts, and W. B. Fischer, "Interaction of amiloride and one of its derivatives with Vpu from HIV-1: a molecular dynamics simulation.," *FEBS letters*, vol. 563, pp. 75–81, Apr. 2004.
[112] C. G. Kim, V. Lemaitre, A. Watts, and W. B. Fischer, "Drug-protein interaction with Vpu from HIV-1: proposing binding sites for amiloride and one of its derivatives.," *Analytical and bioanalytical chemistry*, vol. 386, pp. 2213–2217, Dec. 2006.
[113] D. Willbold, S. Hoffmann, and P. Rösch, "Secondary structure and tertiary fold of

the human immunodeficiency virus protein U (Vpu) cytoplasmic domain in solution.," *European journal of biochemistry / FEBS*, vol. 245, pp. 581–588, May 1997.

[114] M. Wittlich, B. W. Koenig, M. Stoldt, H. Schmidt, and D. Willbold, "NMR structural characterization of HIV-1 virus protein U cytoplasmic domain in the presence of dodecylphosphatidylcholine micelles.," *The FEBS journal*, vol. 276, pp. 6560–6575, Nov. 2009.

[115] S. H. Park and S. J. Opella, "Conformational changes induced by a single amino acid substitution in the trans-membrane domain of Vpu: implications for HIV-1 susceptibility to channel blocking drugs.," *Protein science : a publication of the Protein Society*, vol. 16, pp. 2205–2215, Oct. 2007.

[116] S. H. Park, A. A. De Angelis, A. A. Nevzorov, C. H. Wu, and S. J. Opella, "Three-dimensional structure of the transmembrane domain of Vpu from HIV-1 in aligned phospholipid bicelles.," *Biophysical journal*, vol. 91, pp. 3032–3042, Oct. 2006.

[117] V. Lemaitre, D. Willbold, A. Watts, and W. B. Fischer, "Full length Vpu from HIV-1: combining molecular dynamics simulations with NMR spectroscopy.," *Journal of biomolecular structure & dynamics*, vol. 23, pp. 485–496, Apr. 2006.

[118] D. R. Hout, L. M. Gomez, E. Pacyniak, J.-M. Miller, M. S. Hill, and E. B. Stephens, "A single amino acid substitution within the transmembrane domain of the human immunodeficiency virus type 1 Vpu protein renders simian–human immunodeficiency virus (SHIVKU-1bMC33) susceptible to rimantadine," *Virology*, vol. 348, pp. 449–461, May 2006.

[119] D. R. Hout, M. L. Gomez, E. Pacyniak, L. M. Gomez, B. Fegley, E. R. Mulcahy, M. S. Hill, N. Culley, D. M. Pinson, W. Nothnick, M. F. Powers, S. W. Wong, and E. B. Stephens, "Substitution of the transmembrane domain of Vpu in simian–human immunodeficiency virus (SHIVKU1bMC33) with that of M2 of influenza A results in a virus that is sensitive to inhibitors of the M2 ion channel and is pathogenic for pig-tailed macaques," *Virology*, vol. 344, pp. 541–559, Jan. 2006.

[120] M. Sharma, C. Li, D. D. Busath, H.-X. Zhou, and T. A. Cross, "Drug sensitivity, drug-resistant mutations, and structures of three conductance domains of viral porins," *Biochimica et Biophysica Acta (BBA) - Biomembranes*, vol. 1808, pp. 538–546, Feb. 2011.

[121] D. Moradpour, F. Penin, and C. M. Rice, "Replication of hepatitis C virus.," *Nature Reviews Microbiology*, vol. 5, pp. 453–463, June 2007.

[122] A. Premkumar, L. Wilson, G. D. Ewart, and P. W. Gage, "Cation-selective ion channels formed by p7 of hepatitis C virus are blocked by hexamethylene amiloride.," *FEBS letters*, vol. 557, pp. 99–103, Jan. 2004.

[123] A. Sakai, M. S. Claire, K. Faulk, S. Govindarajan, S. U. Emerson, R. H. Purcell, and J. Bukh, "The p7 polypeptide of hepatitis C virus is critical for infectivity and contains functionally important genotype-specific sequences.," *Proceedings of the National Academy of Sciences*, vol. 100, pp. 11646–11651, Sept. 2003.

[124] E. Steinmann, F. Penin, S. Kallis, A. H. Patel, R. Bartenschlager, and T. Pietschmann, "Hepatitis C virus p7 protein is crucial for assembly and release of infectious virions.," *PLoS pathogens*, vol. 3, p. e103, July 2007.

[125] C. T. Jones, C. L. Murray, D. K. Eastman, J. Tassello, and C. M. Rice, "Hepatitis C virus p7 and NS2 proteins are essential for production of infectious virus.," *Journal of virology*, vol. 81, pp. 8374–8383, Aug. 2007.

[126] M. J. Bentham, T. L. Foster, C. McCormick, and S. Griffin, "Mutations in hepatitis C virus p7 reduce both the egress and infectivity of assembled particles via impaired proton channel function," *The Journal of general virology*, vol. 94, pp. 2236–2248, Oct. 2013.

[127] B. Boson, O. Granio, R. Bartenschlager, and F.-L. Cosset, "A concerted action of hepatitis C virus p7 and nonstructural protein 2 regulates core localization at the endoplasmic reticulum and virus assembly.," *PLoS pathogens*, vol. 7, p. e1002144, July 2011.

[128] V. Jirasko, R. Montserret, N. Appel, A. Janvier, L. Eustachi, C. Brohm, E. Steinmann, T. Pietschmann, F. Penin, and R. Bartenschlager, "Structural and functional characterization of nonstructural protein 2 for its role in hepatitis C virus assembly.," *The Journal of biological chemistry*, vol. 283, pp. 28546–28562, Oct. 2008.

[129] C.-I. Popescu, N. Callens, D. Trinel, P. Roingeard, D. Moradpour, V. Descamps, G. Duverlie, F. Penin, L. Héliot, Y. Rouillé, and J. Dubuisson, "NS2 protein of hepatitis

C virus interacts with structural and non-structural proteins towards virus assembly.," *PLoS pathogens*, vol. 7, no. 2, p. e1001278, 2011.

[130] P. Tedbury, S. Welbourn, A. Pause, B. King, S. Griffin, and M. Harris, "The subcellular localization of the hepatitis C virus non-structural protein NS2 is regulated by an ion channel-independent function of the p7 protein.," *The Journal of general virology*, vol. 92, pp. 819–830, Apr. 2011.

[131] K. A. Stapleford and B. D. Lindenbach, "Hepatitis C virus NS2 coordinates virus particle assembly through physical interactions with the E1-E2 glycoprotein and NS3-NS4A enzyme complexes.," *Journal of virology*, vol. 85, pp. 1706–1717, Feb. 2011.

[132] N. Hagen, K. Bayer, K. Rösch, and M. Schindler, "The intraviral protein interaction network of hepatitis C virus.," *Molecular & cellular proteomics : MCP*, vol. 13, pp. 1676–1689, July 2014.

[133] J. Gentzsch, C. Brohm, E. Steinmann, M. Friesland, N. Menzel, G. Vieyres, P. M. Perin, A. Frentzen, L. Kaderali, and T. Pietschmann, "hepatitis c Virus p7 is critical for capsid assembly and envelopment.," *PLoS pathogens*, vol. 9, no. 5, p. e1003355, 2013.

[134] S. Griffin, C. Stgelais, A. M. Owsianka, A. H. Patel, D. Rowlands, and M. Harris, "Genotype-dependent sensitivity of hepatitis C virus to inhibitors of the p7 ion channel.," *Hepatology (Baltimore, Md.)*, vol. 48, pp. 1779–1790, Dec. 2008.

[135] E. Steinmann, T. Whitfield, S. Kallis, R. A. Dwek, N. Zitzmann, T. Pietschmann, and R. Bartenschlager, "Antiviral effects of amantadine and iminosugar derivatives against hepatitis C virus.," *Hepatology (Baltimore, Md.)*, vol. 46, pp. 330–338, Aug. 2007.

[136] C. Stgelais, T. L. Foster, M. Verow, E. Atkins, C. W. G. Fishwick, D. Rowlands, M. Harris, and S. Griffin, "Determinants of hepatitis C virus p7 ion channel function and drug sensitivity identified in vitro.," *Journal of virology*, vol. 83, pp. 7970–7981, Aug. 2009.

[137] T. L. Foster, M. Verow, A. L. Wozniak, M. J. Bentham, J. Thompson, E. Atkins, S. A. Weinman, C. Fishwick, R. Foster, M. Harris, and S. Griffin, "Resistance mutations define specific antiviral effects for inhibitors of the hepatitis C virus p7 ion channel.," *Hepatology (Baltimore, Md.)*, vol. 54, pp. 79–90, July 2011.

[138] B. OuYang and J. J. Chou, "The minimalist architectures of viroporins and their therapeutic implications," *Biochimica et Biophysica Acta (BBA) - Biomembranes*, vol. 1838, pp. 1058–1067, Apr. 2014.

[139] T. L. Foster, G. S. Thompson, A. P. Kalverda, J. Kankanala, M. Bentham, L. F. Wetherill, J. Thompson, A. M. Barker, D. Clarke, M. Noerenberg, A. R. Pearson, D. J. Rowlands, S. W. Homans, M. Harris, R. Foster, and S. Griffin, "Structure-guided design affirms inhibitors of hepatitis C virus p7 as a viable class of antivirals targeting virion release.," *Hepatology (Baltimore, Md.)*, vol. 59, pp. 408–422, Feb. 2014.

[140] U. Mihm, N. Grigorian, C. Welsch, E. Herrmann, B. Kronenberger, G. Teuber, M. von Wagner, W.-P. Hofmann, M. Albrecht, T. Lengauer, S. Zeuzem, and C. Sarrazin, "Amino acid variations in hepatitis C virus p7 and sensitivity to antiviral combination therapy with amantadine in chronic hepatitis C.," *Antiviral therapy*, vol. 11, no. 4, pp. 507–519, 2006.

[141] C. A. Luscombe, Z. Huang, M. G. Murray, M. Miller, J. Wilkinson, and G. D. Ewart, "A novel Hepatitis C virus p7 ion channel inhibitor, BIT225, inhibits bovine viral diarrhea virus in vitro and shows synergism with recombinant interferon-α-2b and nucleoside analogues," *Antiviral research*, vol. 86, pp. 144–153, May 2010.

[142] J. H. Bowie, F. Separovic, and M. J. Tyler, "Host-defense peptides of Australian anurans. Part 2. Structure, activity, mechanism of action, and evolutionary significance.," *Peptides*, vol. 37, pp. 174–188, Sept. 2012.

[143] M.-A. Sani and F. Separovic, "How Membrane-Active Peptides Get into Lipid Membranes.," *Accounts of chemical research*, vol. 49, pp. 1130–1138, June 2016.

[144] Y. Shai, "Mode of action of membrane active antimicrobial peptides.," *Biopolymers*, vol. 66, no. 4, pp. 236–248, 2002.

[145] Y. Shai, "Mechanism of the binding, insertion and destabilization of phospholipid bilayer membranes by alpha-helical antimicrobial and cell non-selective membrane-lytic peptides.," *Biochimica et biophysica acta*, vol. 1462, pp. 55–70, Dec. 1999.

[146] Z. Wang and G. Wang, "APD: the Antimicrobial Peptide Database.," *Nucleic Acids Research*, vol. 32, pp. D590–2, Jan. 2004.

[147] G. Wang, X. Li, and Z. Wang, "APD2: the updated antimicrobial peptide database

and its application in peptide design.," *Nucleic Acids Research*, vol. 37, pp. D933–7, Jan. 2009.
[148] G. Wang, "Database-Guided Discovery of Potent Peptides to Combat HIV-1 or Superbugs.," *Pharmaceuticals (Basel, Switzerland)*, vol. 6, no. 6, pp. 728–758, 2013.
[149] G. Yim, H. H. Wang, and J. Davies, "Antibiotics as signalling molecules.," *Philosophical transactions of the Royal Society of London. Series B, Biological sciences*, vol. 362, pp. 1195–1200, July 2007.
[150] R. W. Hong, M. Shchepetov, J. N. Weiser, and P. H. Axelsen, "Transcriptional profile of the Escherichia coli response to the antimicrobial insect peptide cecropin A.," *Antimicrobial agents and chemotherapy*, vol. 47, pp. 1–6, Jan. 2003.
[151] C. B. Park, H. S. Kim, and S. C. Kim, "Mechanism of Action of the Antimicrobial Peptide Buforin II: Buforin II Kills Microorganisms by Penetrating the Cell Membrane and Inhibiting Cellular Functions," *Biochemical and Biophysical Research Communications*, vol. 244, pp. 253–257, Mar. 1998.
[152] S. Sharma, I. Verma, and G. K. Khuller, "Biochemical interaction of human neutrophil peptide-1 with Mycobacterium tuberculosis H37Ra," *Archives of microbiology*, vol. 171, no. 5, pp. 338–342, 1999.
[153] Y.-Q. Xiong, A. S. Bayer, and M. R. Yeaman, "Inhibition of intracellular macromolecular synthesis in Staphylococcus aureus by thrombin-induced platelet microbicidal proteins.," *Journal of Infectious Diseases*, vol. 185, pp. 348–356, Feb. 2002.
[154] Goran Kragol, Sandor Lovas, Gyorgyi Varadi, Barry A Condie, R. Hoffmann, and L. Otvos, "The Antibacterial Peptide Pyrrhocoricin Inhibits the ATPase Actions of DnaK and Prevents Chaperone-Assisted Protein Folding†," *Biochemistry*, vol. 40, pp. 3016–3026, Feb. 2001.
[155] N. Y. Yount and M. R. Yeaman, "Peptide antimicrobials: cell wall as a bacterial target," *Annals of the New York Academy of Sciences*, vol. 1277, pp. 127–138, Jan. 2013.
[156] J. H. Cho, B. H. Sung, and S. C. Kim, "Buforins: Histone H2A-derived antimicrobial peptides from toad stomach," *Biochimica et Biophysica Acta (BBA) - Biomembranes*, vol. 1788, pp. 1564–1569, Aug. 2009.
[157] S. K. Straus and R. E. W. Hancock, "Mode of action of the new antibiotic for Gram-positive pathogens daptomycin: Comparison with cationic antimicrobial peptides and lipopeptides," *Biochimica et Biophysica Acta (BBA) - Biomembranes*, vol. 1758, pp. 1215–1223, Sept. 2006.
[158] K. Matsuzaki, "Magainins as paradigm for the mode of action of pore forming polypeptides," *Biochimica et Biophysica Acta (BBA) - Reviews on Biomembranes*, vol. 1376, pp. 391–400, Nov. 1998.
[159] K. Matsuzaki, K.-i. Sugishita, M. Harada, N. Fujii, and K. Miyajima, "Interactions of an antimicrobial peptide, magainin 2, with outer and inner membranes of Gram-negative bacteria," *Biochimica et Biophysica Acta (BBA) - Biomembranes*, vol. 1327, pp. 119–130, July 1997.
[160] P. D. Rakowska, H. Jiang, S. Ray, A. Pyne, B. Lamarre, M. Carr, P. J. Judge, J. Ravi, U. I. M. Gerling, B. Koksch, G. J. Martyna, B. W. Hoogenboom, A. Watts, J. Crain, C. R. M. Grovenor, and M. G. Ryadnov, "Nanoscale imaging reveals laterally expanding antimicrobial pores in lipid bilayers.," *Proceedings of the National Academy of Sciences of the United States of America*, vol. 110, pp. 8918–8923, May 2013.
[161] L. Yang, T. A. Harroun, T. M. Weiss, L. Ding, and H. W. Huang, "Barrel-Stave Model or Toroidal Model? A Case Study on Melittin Pores," *Biophysical journal*, vol. 81, pp. 1475–1485, Sept. 2001.
[162] K. Bertelsen, J. Dorosz, S. K. Hansen, N. C. Nielsen, and T. Vosegaard, "Mechanisms of Peptide-Induced Pore Formation in Lipid Bilayers Investigated by Oriented 31 P Solid-State NMR Spectroscopy," *PloS one*, vol. 7, p. e47745, Oct. 2012.
[163] A. S. Ladokhin and S. H. White, "'Detergent-like' permeabilization of anionic lipid vesicles by melittin," *Biochimica et Biophysica Acta (BBA) - Biomembranes*, vol. 1514, pp. 253–260, Oct. 2001.
[164] D. W. Hoskin and A. Ramamoorthy, "Studies on anticancer activities of antimicrobial peptides," *Biochimica et Biophysica Acta (BBA) - Biomembranes*, vol. 1778, pp. 357–375, Feb. 2008.
[165] L. M. Harriss, B. Cronin, J. R. Thompson, and M. I. Wallace, "Imaging Multiple Conductance States in an Alamethicin Pore," *Journal of the American Chemical Society*,

vol. 133, pp. 14507–14509, Aug. 2011.
[166] D. Sengupta, H. Leontiadou, A. E. Mark, and S.-J. Marrink, "Toroidal pores formed by antimicrobial peptides show significant disorder," *Biochimica et Biophysica Acta (BBA) - Biomembranes*, vol. 1778, pp. 2308–2317, Oct. 2008.
[167] K. B. Smith-Dupont, L. Guo, and F. Gai, "Diffusion as a Probe of the Heterogeneity of Antimicrobial Peptide−Membrane Interactions," *Biochemistry*, vol. 49, pp. 4672–4678, June 2010.
[168] H. Leontiadou, A. E. Mark, and S. J. Marrink, "Antimicrobial Peptides in Action," *Journal of the American Chemical Society*, vol. 128, pp. 12156–12161, Sept. 2006.
[169] K. A. Brogden, "Antimicrobial peptides: pore formers or metabolic inhibitors in bacteria?," *Nature Reviews Microbiology*, vol. 3, pp. 238–250, Mar. 2005.
[170] E. S. Salnikov and B. Bechinger, "Lipid-controlled peptide topology and interactions in bilayers: structural insights into the synergistic enhancement of the antimicrobial activities of PGLa and magainin 2.," *Biophysical journal*, vol. 100, pp. 1473–1480, Mar. 2011.
[171] P. Tremouilhac, E. Strandberg, P. Wadhwani, and A. S. Ulrich, "Synergistic transmembrane alignment of the antimicrobial heterodimer PGLa/magainin.," *The Journal of biological chemistry*, vol. 281, pp. 32089–32094, Oct. 2006.
[172] R. W. Williams, R. Starman, K. M. P. Taylor, K. Gable, T. Beeler, M. Zasloff, and D. Covell, "Raman spectroscopy of synthetic antimicrobial frog peptides magainin 2a and PGLa," *Biochemistry*, vol. 29, pp. 4490–4496, May 2002.
[173] L. V. Allen, *Remington.* An Introduction to Pharmacy, 2013.
[174] C. D. Fjell, J. A. Hiss, R. E. W. Hancock, and G. Schneider, "Designing antimicrobial peptides: form follows function," *Nature reviews. Drug discovery*, vol. 11, pp. 37–51, Jan. 2012.
[175] G. Schneider and H.-J. Böhm, "Virtual screening and fast automated docking methods," *Drug Discovery Today*, vol. 7, pp. 64–70, Jan. 2002.
[176] T. Engel, "Basic Overview of Chemoinformatics†," *Journal of Chemical Information and Modeling*, vol. 46, pp. 2267–2277, Nov. 2006.
[177] C. D. Fjell, H. Jenssen, W. A. Cheung, R. E. W. Hancock, and A. Cherkasov, "Optimization of Antibacterial Peptides by Genetic Algorithms and Cheminformatics," *Chemical Biology & Drug Design*, vol. 77, pp. 48–56, Jan. 2011.
[178] Y. Yagi, K. Terada, T. Noma, K. Ikebukuro, and K. Sode, "In silico panning for a non-competitive peptide inhibitor," *BMC Bioinformatics*, vol. 8, p. 1, Jan. 2007.
[179] J. A. Beard, A. Bearden, and R. Striker, "Vitamin D and the anti-viral state," *Journal of Clinical Virology*, vol. 50, pp. 194–200, Mar. 2011.
[180] T. Nakatsuji and R. L. Gallo, "Antimicrobial peptides: old molecules with new ideas," *Journal of Investigative Dermatology*, 2012.
[181] Y. J. Gordon, L. C. Huang, E. G. Romanowski, K. A. Yates, R. J. Proske, and A. M. McDermott, "Human Cathelicidin (LL-37), a Multifunctional Peptide, is Expressed by Ocular Surface Epithelia and has Potent Antibacterial and Antiviral Activity," *Current Eye Research*, vol. 30, pp. 385–394, July 2009.
[182] T. W. Cullen, W. B. Schofield, N. A. Barry, E. E. Putnam, E. A. Rundell, M. S. Trent, P. H. Degnan, C. J. Booth, H. Yu, and A. L. Goodman, "Antimicrobial peptide resistance mediates resilience of prominent gut commensals during inflammation," *Science (New York, N.Y.)*, vol. 347, pp. 170–175, Jan. 2015.
[183] K. L. Strandberg, S. M. Richards, R. Tamayo, L. T. Reeves, and J. S. Gunn, "An Altered Immune Response, but Not Individual Cationic Antimicrobial Peptides, Is Associated with the Oral Attenuation of Ara4N-Deficient Salmonella enterica Serovar Typhimurium in Mice," *PloS one*, vol. 7, p. e49588, Nov. 2012.
[184] S. A. Kristian, V. Datta, C. Weidenmaier, R. Kansal, I. Fedtke, A. Peschel, R. L. Gallo, and V. Nizet, "D-alanylation of teichoic acids promotes group a streptococcus antimicrobial peptide resistance, neutrophil survival, and epithelial cell invasion.," *Journal of bacteriology*, vol. 187, pp. 6719–6725, Oct. 2005.
[185] C. B. Whitchurch, T. Tolker-Nielsen, P. C. Ragas, and J. S. Mattick, "Extracellular DNA Required for Bacterial Biofilm Formation," *Science (New York, N.Y.)*, vol. 295, pp. 1487–1487, Feb. 2002.
[186] H. Mulcahy, L. Charron-Mazenod, and S. Lewenza, "Extracellular DNA chelates cations and induces antibiotic resistance in Pseudomonas aeruginosa biofilms.," *PLoS pathogens*,

vol. 4, p. e1000213, Nov. 2008.
[187] A. Schmidtchen, I. M. Frick, E. Andersson, H. Tapper, and L. Björck, "Proteinases of common pathogenic bacteria degrade and inactivate the antibacterial peptide LL-37," *Molecular Microbiology*, vol. 46, pp. 157–168, Oct. 2002.
[188] Y.-L. Tzeng, K. D. Ambrose, S. Zughaier, X. Zhou, Y. K. Miller, W. M. Shafer, and D. S. Stephens, "Cationic antimicrobial peptide resistance in Neisseria meningitidis.," *Journal of bacteriology*, vol. 187, pp. 5387–5396, Aug. 2005.
[189] L. Ryan, B. Lamarre, T. Diu, J. Ravi, P. J. Judge, A. Temple, M. Carr, E. Cerasoli, B. Su, H. F. Jenkinson, G. Martyna, J. Crain, A. Watts, and M. G. Ryadnov, "Anti-antimicrobial peptides: folding-mediated host defense antagonists.," *The Journal of biological chemistry*, vol. 288, pp. 20162–20172, July 2013.
[190] P. Guterstam, F. Madani, H. Hirose, T. Takeuchi, S. Futaki, S. El-Andaloussi, A. Gräslund, and Ü. Langel, "Elucidating cell-penetrating peptide mechanisms of action for membrane interaction, cellular uptake, and translocation utilizing the hydrophobic counter-anion pyrenebutyrate," *Biochimica et Biophysica Acta (BBA) - Biomembranes*, vol. 1788, pp. 2509–2517, Dec. 2009.
[191] A. Rydström, S. Deshayes, K. Konate, L. Crombez, K. Padari, H. Boukhaddaoui, G. Aldrian, M. Pooga, and G. Divita, "Direct Translocation as Major Cellular Uptake for CADY Self-Assembling Peptide-Based Nanoparticles," *PloS one*, vol. 6, p. e25924, Oct. 2011.
[192] K. Ezzat, H. Helmfors, O. Tudoran, C. Juks, S. Lindberg, K. Padari, S. El-Andaloussi, M. Pooga, and Ü. Langel, "Scavenger receptor-mediated uptake of cell-penetrating peptide nanocomplexes with oligonucleotides.," *FASEB journal : official publication of the Federation of American Societies for Experimental Biology*, vol. 26, pp. 1172–1180, Mar. 2012.
[193] M. Green and P. M. Loewenstein, "Autonomous functional domains of chemically synthesized human immunodeficiency virus tat trans-activator protein," *Cell*, vol. 55, pp. 1179–1188, Dec. 1988.
[194] E. Vivès, P. Brodin, and B. Lebleu, "A truncated HIV-1 Tat protein basic domain rapidly translocates through the plasma membrane and accumulates in the cell nucleus.," *The Journal of biological chemistry*, vol. 272, pp. 16010–16017, June 1997.
[195] D. Derossi, S. Calvet, A. Trembleau, A. Brunissen, G. Chassaing, and A. Prochiantz, "Cell internalization of the third helix of the Antennapedia homeodomain is receptor-independent.," *The Journal of biological chemistry*, vol. 271, pp. 18188–18193, July 1996.
[196] E. Koren and V. P. Torchilin, "Cell-penetrating peptides: breaking through to the other side," *Trends in molecular medicine*, vol. 18, pp. 385–393, July 2012.
[197] M. Weingarth and M. Baldus, "CHAPTER 1 Introduction to Biological Solid-State NMR," *Advances in Biological Solid-State NMR*, pp. 1–17, 2014.
[198] H. Günther, *NMR Spectroscopy*. Basic Principles, Concepts and Applications in Chemistry, John Wiley & Sons, Dec. 2013.
[199] P. R. Cullis and B. d. Kruijff, *Lipid polymorphism and the functional roles of lipids in biological membranes*, vol. 559. Elsevier, Dec. 1979.
[200] T. Pott, J.-C. Maillet, C. Abad, A. Campos, J. Dufourcq, and E. J. Dufourc, "The lipid charge density at the bilayer surface modulates the effects of melittin on membranes," *Chemistry and physics of lipids*, vol. 109, pp. 209–223, Feb. 2001.
[201] T. Pott, M. Paternostre, and E. J. Dufourc, "A comparative study of the action of melittin on sphingomyelin and phosphatidylcholine bilayers," *European biophysics journal : EBJ*, vol. 27, no. 3, pp. 237–245, 1998.
[202] G. P. Holland, S. K. McIntyre, and T. M. Alam, "Distinguishing Individual Lipid Headgroup Mobility and Phase Transitions in Raft-Forming Lipid Mixtures with 31P MAS NMR," *Biophysical journal*, vol. 90, pp. 4248–4260, June 2006.
[203] L. S. Vermeer, "NMR struture determination and MD simultations of membrane peptides and proteins : a peptide derived from H+-V-ATPase subunit alpha, and MscL," Mar. 2009.
[204] M. Bak, J. T. Rasmussen, and N. C. Nielsen, "SIMPSON: A general simulation program for solid-state NMR spectroscopy," *Journal of Magnetic Resonance*, vol. 213, pp. 366–400, Dec. 2011.
[205] M. J. Duer, *Solid State NMR Spectroscopy*. Principles and Applications, Oxford, UK: John Wiley & Sons, Apr. 2008.

[206] A. Pines, M. G. Gibby, and J. S. Waugh, "Proton-enhanced NMR of dilute spins in solids," *The Journal of Chemical Physics*, vol. 59, pp. 569–590, July 1973.
[207] S. Hediger, B. H. Meier, and R. R. Ernst, "Adiabatic passage Hartmann-Hahn cross polarization in NMR under magic angle sample spinning," *Chemical Physics Letters*, vol. 240, pp. 449–456, July 1995.
[208] S. Hediger, B. H. Meier, N. D. Kurur, G. Bodenhausen, and R. R. Ernst, "NMR cross polarization by adiabatic passage through the Hartmann—Hahn condition (APHH)," *Chemical Physics Letters*, vol. 223, pp. 283–288, June 1994.
[209] H. J. Hogben, M. Krzystyniak, G. T. P. Charnock, P. J. Hore, and I. Kuprov, "Spinach – A software library for simulation of spin dynamics in large spin systems," *Journal of Magnetic Resonance*, vol. 208, pp. 179–194, Feb. 2011.
[210] G. Jeschke, "DEER Distance Measurements on Proteins," *dx.doi.org*, vol. 63, pp. 419–446, Apr. 2012.
[211] O. H. Griffith, D. W. Cornell, and H. M. McConnell, "Nitrogen Hyperfine Tensor and g Tensor of Nitroxide Radicals," *The Journal of Chemical Physics*, vol. 43, no. 8, p. 2909, 1965.
[212] V. A. Livshits, B. G. Dzikovski, and D. Marsh, "Anisotropic motion effects in CW non-linear EPR spectra: relaxation enhancement of lipid spin labels," *Journal of Magnetic Resonance*, vol. 162, pp. 429–442, June 2003.
[213] J. A. Weil and J. R. Bolton, "Electron paramagnetic resonance: elementary theory and practical applications," 2007.
[214] S. Stoll and A. Schweiger, "EasySpin, a comprehensive software package for spectral simulation and analysis in EPR," *Journal of Magnetic Resonance*, vol. 178, pp. 42–55, Jan. 2006.
[215] P. Fajer, A. Watts, and D. Marsh, "Saturation transfer, continuous wave saturation, and saturation recovery electron spin resonance studies of chain-spin labeled phosphatidylcholines in the low temperature phases of dipalmitoyl phosphatidylcholine bilayers. Effects of rotational dynamics and spin-spin interactions.," *Biophysical journal*, vol. 61, pp. 879–891, Apr. 1992.
[216] A. Watts, *Protein-Lipid Interactions*. Elsevier, Oct. 1993.
[217] D. Kurad, G. Jeschke, and D. Marsh, "Lateral Ordering of Lipid Chains in Cholesterol-Containing Membranes: High-Field Spin-Label EPR," *Biophysical journal*, vol. 86, pp. 264–271, Jan. 2004.
[218] C. S. Klug and J. B. Feix, "Methods and Applications of Site-Directed Spin Labeling EPR Spectroscopy," in *Biophysical Tools for Biologists, Volume One: In Vitro Techniques*, pp. 617–658, Elsevier, 2008.
[219] E. L. Hahn, "Spin Echoes," *Physical review*, vol. 80, pp. 580–594, Nov. 1950.
[220] H. Y. Carr and E. M. Purcell, "Effects of Diffusion on Free Precession in Nuclear Magnetic Resonance Experiments," *Physical review*, vol. 94, pp. 630–638, May 1954.
[221] A. D. Milov, A. B. Ponomarev, and Y. D. Tsvetkov, "Electron-electron double resonance in electron spin echo: Model biradical systems and the sensitized photolysis of decalin," *Chemical Physics Letters*, vol. 110, pp. 67–72, Sept. 1984.
[222] R. E. Martin, M. Pannier, and F. Diederich, "Determination of end-to-end distances in a series of TEMPO diradicals of up to 2.8 nm length with a new four-pulse double electron electron resonance experiment," *Angewandte Chemie ...*, 1998.
[223] J. E. Lovett, B. W. Lovett, and J. Harmer, "DEER-Stitch: Combining three- and four-pulse DEER measurements for high sensitivity, deadtime free data," *Journal of Magnetic Resonance*, vol. 223, pp. 98–106, Oct. 2012.
[224] M. A. Hemminga and L. Berliner, *ESR Spectroscopy in Membrane Biophysics*. Springer Science & Business Media, Feb. 2007.
[225] Y. Polyhach, E. Bordignon, R. Tschaggelar, S. Gandra, A. Godt, and G. Jeschke, "High sensitivity and versatility of the DEER experiment on nitroxide radical pairs at Q-band frequencies.," *Physical chemistry chemical physics : PCCP*, vol. 14, pp. 10762–10773, Aug. 2012.
[226] G. Weber, "Fluorescence-polarization spectrum and electronic-energy transfer in proteins.," *The Biochemical journal*, vol. 75, pp. 345–352, May 1960.
[227] J. M. Beechem and L. Brand, "Time-resolved fluorescence of proteins," *Annual review of biochemistry*, 1985.
[228] J. T. Vivian and P. R. Callis, "Mechanisms of Tryptophan Fluorescence Shifts in

Proteins," *Biophysical journal*, vol. 80, pp. 2093–2109, May 2001.
[229] J. G. Morin and J. W. Hastings, "Energy transfer in a bioluminescent system," *Journal of cellular physiology*, vol. 77, pp. 313–318, June 1971.
[230] O. Shimomura, "A Short Story of Aequorin," *Biological Bulletin*, vol. 189, p. 1, Aug. 1995.
[231] T. Jue, *Biomedical Applications of Biophysics*. Totowa, NJ: Springer Science & Business Media, Aug. 2010.
[232] M. Ryadnov and F. Hudecz, *Amino acids, peptides and proteins Volume 38*, vol. 40 of *Amino Acids, Peptides And Proteins*. Cambridge: Royal Society of Chemistry, Nov. 2013.
[233] L. Li, I. Vorobyov, and T. W. Allen, "The Different Interactions of Lysine and Arginine Side Chains with Lipid Membranes," *The journal of physical chemistry. B*, vol. 117, pp. 11906–11920, Oct. 2013.
[234] J. A. Killian and G. von Heijne, "How proteins adapt to a membrane–water interface," *Trends in biochemical sciences*, vol. 25, pp. 429–434, Sept. 2000.
[235] D. Hultmark, A. Engström, K. Andersson, H. Steiner, H. Bennich, and H. G. Boman, "Insect immunity. Attacins, a family of antibacterial proteins from Hyalophora cecropia.," *The EMBO journal*, vol. 2, no. 4, pp. 571–576, 1983.
[236] H. Stciner, D. Hultmark, A. Engström, and H. I. Bennich, "Séquence and spe-cificity of two antibacterial proteins involved in insect immunity," ..., 1981.
[237] H.-Y. Yi, M. Chowdhury, Y.-D. Huang, and X.-Q. Yu, "Insect antimicrobial peptides and their applications," *Applied Microbiology and Biotechnology*, vol. 98, pp. 5807–5822, May 2014.
[238] Y. Nakajima, X. M. Qu, and S. Natori, "Interaction between liposomes and sarcotoxin IA, a potent antibacterial protein of Sarcophaga peregrina (flesh fly).," *The Journal of biological chemistry*, vol. 262, pp. 1665–1669, Feb. 1987.
[239] Z.-q. Li, R. B. Merrifield, I. A. Boman, and H. G. Boman, "Effects on electrophoretic mobility and antibacterial spectrum of removal of two residues from synthetic sarcotoxin IA and addition of the same residues to cecropin B," *FEBS letters*, vol. 231, pp. 299–302, Apr. 1988.
[240] M. J. Arrowood, J. M. Jaynes, and M. C. Healey, "In vitro activities of lytic peptides against the sporozoites of Cryptosporidium parvum.," *Antimicrobial agents and chemotherapy*, vol. 35, pp. 224–227, Feb. 1991.
[241] S. C. Barr, D. Rose, and J. M. Jaynes, "Activity of Lytic Peptides against Intracellular Trypanosoma cruzi Amastigotes In vitro and Parasitemias in Mice," *The Journal of parasitology*, vol. 81, p. 974, Dec. 1995.
[242] M. Wachinger, A. Kleinschmidt, D. Winder, N. von Pechmann, A. Ludvigsen, M. Neumann, R. Holle, B. Salmons, V. Erfle, and R. Brack-Werner, "Antimicrobial peptides melittin and cecropin inhibit replication of human immunodeficiency virus 1 by suppressing viral gene expression.," *The Journal of general virology*, vol. 79, pp. 731–740, Apr. 1998.
[243] H. M. Chen, W. Wang, D. Smith, and S. C. Chan, "Effects of the anti-bacterial peptide cecropin B and its analogs, cecropins B-1 and B-2, on liposomes, bacteria, and cancer cells," *Biochimica et Biophysica Acta (BBA) - General Subjects*, vol. 1336, pp. 171–179, Aug. 1997.
[244] H. Suttmann, M. Retz, F. Paulsen, J. Harder, U. Zwergel, J. Kamradt, B. Wullich, G. Unteregger, M. Stöckle, and J. Lehmann, "Antimicrobial peptides of the Cecropin-family show potent antitumor activity against bladder cancer cells," *BMC Urology*, vol. 8, p. 1, Mar. 2008.
[245] T. A. Holak, A. Engstroem, P. J. Kraulis, G. Lindeberg, H. Bennich, T. A. Jones, A. M. Gronenborn, and G. M. Clore, "The solution conformation of the antibacterial peptide cecropin A: a nuclear magnetic resonance and dynamical simulated annealing study," *Biochemistry*, vol. 27, pp. 7620–7629, May 2002.
[246] S.-C. Hung, W. Wang, S. I. Chan, and H. M. Chen, "Membrane Lysis by the Antibacterial Peptides Cecropins B1 and B3: A Spin-Label Electron Spin Resonance Study on Phospholipid Bilayers," *Biophysical journal*, vol. 77, pp. 3120–3133, Dec. 1999.
[247] F. M. Marassi, S. J. Opella, P. Juvvadi, and R. B. Merrifield, "Orientation of Cecropin A Helices in Phospholipid Bilayers Determined by Solid-State NMR Spectroscopy," *Biophysical journal*, vol. 77, pp. 3152–3155, Dec. 1999.

[248] G. Beschiaschvili and J. Seelig, "Melittin binding to mixed phosphatidylglycerol/phosphatidylcholine membranes," *Biochemistry*, vol. 29, pp. 52–58, Jan. 1990.
[249] S. E. Blondelle and R. A. Houghten, "Hemolytic and antimicrobial activities of the twenty-four individual omission analogs of melittin," *Biochemistry*, vol. 30, pp. 4671–4678, May 1991.
[250] M. Dathe, H. Nikolenko, J. Meyer, M. Beyermann, and M. Bienert, "Optimization of the antimicrobial activity of magainin peptides by modification of charge," *FEBS letters*, vol. 501, pp. 146–150, July 2001.
[251] W. L. Maloy and U. P. Kari, "Structure–activity studies on magainins and other host defense peptides," *Biopolymers*, vol. 37, pp. 105–122, Jan. 1995.
[252] H. S. Sader, K. A. Fedler, R. P. Rennie, S. Stevens, and R. N. Jones, "Omiganan pentahydrochloride (MBI 226), a topical 12-amino-acid cationic peptide: spectrum of antimicrobial activity and measurements of bactericidal activity.," *Antimicrobial agents and chemotherapy*, vol. 48, pp. 3112–3118, Aug. 2004.
[253] E. Gazit, A. Boman, H. G. Boman, and Y. Shai, "Interaction of the Mammalian Antibacterial Peptide Cecropin P1 with Phospholipid Vesicles," *Biochemistry*, vol. 34, pp. 11479–11488, May 2002.
[254] A. Giacometti, O. Cirioni, F. Barchiesi, M. S. Del Prete, M. Fortuna, F. Caselli, and G. Scalise, "In vitro susceptibility tests for cationic peptides: comparison of broth microdilution methods for bacteria that grow aerobically.," *Antimicrobial agents and chemotherapy*, vol. 44, pp. 1694–1696, June 2000.
[255] J. A. Olivares Pacheco, A. Bernardini, G. Garcia-Leon, F. Corona, M. B. Sanchez, and J. L. Martinez, "The intrinsic resistome of bacterial pathogens," *Frontiers in Microbiology*, vol. 4, Apr. 2013.
[256] J. Haaber, C. Friberg, M. McCreary, R. Lin, S. N. Cohen, and H. Ingmer, "Reversible antibiotic tolerance induced in Staphylococcus aureus by concurrent drug exposure.," *Mbio*, vol. 6, no. 1, pp. e02268–14, 2015.
[257] C. J. Sullivan, J. L. Morrell, D. P. Allison, and M. J. Doktycz, "Mounting of Escherichia coli spheroplasts for AFM imaging," *Ultramicroscopy*, vol. 105, pp. 96–102, Nov. 2005.
[258] D. Oursel, C. Loutelier Bourhis, N. Orange, S. Chevalier, V. Norris, and C. M. Lange, "Lipid composition of membranes of Escherichia coli by liquid chromatography/tandem mass spectrometry using negative electrospray ionization," *Rapid Communications in Mass Spectrometry*, vol. 21, pp. 1721–1728, June 2007.
[259] J.-S. Ye, X.-J. Zheng, K. W. Leung, H. M. Chen, and F.-S. Sheu, "Induction of transient ion channel-like pores in a cancer cell by antibiotic peptide.," *Journal of biochemistry*, vol. 136, pp. 255–259, Aug. 2004.
[260] S. Srisailam, T. K. Kumar, A. I. Arunkumar, K. W. Leung, C. Yu, and H. M. Chen, "Crumpled structure of the custom hydrophobic lytic peptide cecropin B3.," *European journal of biochemistry / FEBS*, vol. 268, pp. 4278–4284, Aug. 2001.
[261] P. C. Jost, O. H. Griffith, R. A. Capaldi, and G. Vanderkooi, "Evidence for boundary lipid in membranes.," *Proceedings of the National Academy of Sciences*, vol. 70, pp. 480–484, Feb. 1973.
[262] P. J. Brophy, L. I. Horvath, and D. Marsh, "Stoichiometry and specificity of lipid-protein interaction with myelin proteolipid protein studied by spin-label electron spin resonance," *Biochemistry*, vol. 23, pp. 860–865, Feb. 1984.
[263] A. Watts, "Magnetic Resonance Studies of Protein-Lipid Interactions," in *Biological Membranes: Structure, Biogenesis and Dynamics*, pp. 79–92, Berlin, Heidelberg: Springer Berlin Heidelberg, 1994.
[264] J. M. Boggs, G. Rangaraj, and A. Watts, "Behavior of spin labels in a variety of interdigitated lipid bilayers," *Biochimica et Biophysica Acta (BBA) - Biomembranes*, vol. 981, pp. 243–253, June 1989.
[265] G. Cevc, *Phospholipids Handbook*. CRC Press, Aug. 1993.
[266] K. C. G, Liposomes:from physical structure to therapeutic applications. . Amsterdam: Elsevier, 1981.
[267] P. Jost, L. J. Libertini, V. C. Hebert, and O. H. Griffith, "Lipid spin labels in lecithin multilayers. A study of motion along fatty acid chains.," *Journal of molecular biology*, vol. 59, pp. 77–98, July 1971.
[268] H. M. McConnell and W. L. Hubbell, "Molecular motion in spin-labeled phospholipids and membranes," *Journal of the American Chemical Society*, vol. 93, pp. 314–326, Jan.

1971.
[269] A. Keith, G. Bulfield, and W. Snipes, "Spin-Labeled Neurospora Mitochondria," *Biophysical journal*, vol. 10, pp. 618–629, July 1970.
[270] M. Junk, "Assessing the Functional Structure of Molecular Transporters by EPR Spectroscopy," 2012.
[271] A. I. Kokorin, K. I. Zamaraev, G. L. Grigorian, V. P. Ivanov, and E. G. Rozantsev, "[Measurement of the distance between paramagnetic centers in solid solutions of nitrosyl radicals, biradicals and spin-labelled proteins].," *Biofizika*, vol. 17, pp. 34–41, Jan. 1972.
[272] M. D. Rabenstein and Y. K. Shin, "Determination of the distance between two spin labels attached to a macromolecule.," *Proceedings of the National Academy of Sciences*, vol. 92, pp. 8239–8243, Aug. 1995.
[273] E. J. Hustedt, R. A. Stein, L. Sethaphong, S. Brandon, Z. Zhou, and S. C. DeSensi, "Dipolar Coupling between Nitroxide Spin Labels: The Development and Application of a Tether-in-a-Cone Model," *Biophysical journal*, vol. 90, pp. 340–356, Jan. 2006.
[274] H. J. Steinhoff, N. Radzwill, W. Thevis, V. Lenz, D. Brandenburg, A. Antson, G. Dodson, and A. Wollmer, "Determination of interspin distances between spin labels attached to insulin: comparison of electron paramagnetic resonance data with the X-ray structure.," *Biophysical journal*, vol. 73, pp. 3287–3298, Dec. 1997.
[275] G. Jeschke, "Distance Measurements in the Nanometer Range by Pulse EPR," *ChemPhysChem*, vol. 3, pp. 927–932, Nov. 2002.
[276] B. Bechinger, M. Zasloff, and S. J. Opella, "Structure and orientation of the antibiotic peptide magainin in membranes by solid-state nuclear magnetic resonance spectroscopy," *Protein Science*, vol. 2, pp. 2077–2084, Dec. 1993.
[277] T. A. Cross, "[31] Solid-state nuclear magnetic resonance characterization of gramicidin channel structure," in *Solid-Phase Peptide Synthesis*, pp. 672–IN4, Elsevier, 1997.
[278] T. Vosegaard, M. Kamihira-Ishijima, A. Watts, and N. C. Nielsen, "Helix Conformations in 7TM Membrane Proteins Determined Using Oriented-Sample Solid-State NMR with Multiple Residue-Specific 15N Labeling," *Biophysical journal*, vol. 94, pp. 241–250, Jan. 2008.
[279] E. Strandberg, S. Esteban-Martín, J. Salgado, and A. S. Ulrich, "Orientation and Dynamics of Peptides in Membranes Calculated from 2H-NMR Data," *Biophysical journal*, vol. 96, pp. 3223–3232, Apr. 2009.
[280] C. Aisenbrey and B. Bechinger, "Tilt and rotational pitch angle of membrane-inserted polypeptides from combined 15N and 2H solid-state NMR spectroscopy.," *Biochemistry*, vol. 43, pp. 10502–10512, Aug. 2004.
[281] A. Seelig and J. Seelig, "Dynamic structure of fatty acyl chains in a phospholipid bilayer measured by deuterium magnetic resonance," *Biochemistry*, vol. 13, pp. 4839–4845, Nov. 1974.
[282] J. Seelig and W. Niederberger, "Deuterium-labeled lipids as structural probes in liquid crystalline bilayers. Deuterium magnetic resonance study," *Journal of the American Chemical Society*, vol. 96, pp. 2069–2072, Apr. 1974.
[283] D. Lu, I. Vavasour, and M. R. Morrow, "Smoothed acyl chain orientational order parameter profiles in dimyristoylphosphatidylcholine-distearoylphosphatidylcholine mixtures: a 2H-NMR study.," *Biophysical journal*, vol. 68, pp. 574–583, Feb. 1995.
[284] M. Lafleur, B. Fine, E. Sternin, P. R. Cullis, and M. Bloom, "Smoothed orientational order profile of lipid bilayers by 2H-nuclear magnetic resonance.," *Biophysical journal*, vol. 56, pp. 1037–1041, Nov. 1989.
[285] M. R. Morrow and D. Lu, "Universal behavior of lipid acyl chain order: chain length scaling," *Chemical Physics Letters*, vol. 182, pp. 435–439, Aug. 1991.
[286] F. Separovic and A. Naito, *Advances in Biological Solid-State NMR*. Proteins and Membrane-Active Peptides, Cambridge: Royal Society of Chemistry, 2014.
[287] E. Strandberg, N. Kanithasen, D. Tiltak, J. Bürck, P. Wadhwani, O. Zwernemann, and A. S. Ulrich, "Solid-state NMR analysis comparing the designer-made antibiotic MSI-103 with its parent peptide PGLa in lipid bilayers.," *Biochemistry*, vol. 47, pp. 2601–2616, Feb. 2008.
[288] J. H. Davis, "The description of membrane lipid conformation, order and dynamics by 2H-NMR," *Biochimica et Biophysica Acta (BBA) - Reviews on Biomembranes*, vol. 737, pp. 117–171, Mar. 1983.
[289] B. Bechinger, C. Aisenbrey, and P. Bertani, "The alignment, structure and dynamics of membrane-associated polypeptides by solid-state NMR spectroscopy," *Biochimica et*

Biophysica Acta (BBA) - Biomembranes, vol. 1666, pp. 190–204, Nov. 2004.

[290] J. H. Davis, K. R. Jeffrey, M. Bloom, M. I. Valic, and T. P. Higgs, "Quadrupolar echo deuteron magnetic resonance spectroscopy in ordered hydrocarbon chains," *Chemical Physics Letters*, vol. 42, pp. 390–394, Sept. 1976.

[291] M. Bak, R. Schultz, T. Vosegaard, and N. C. Nielsen, "Specification and Visualization of Anisotropic Interaction Tensors in Polypeptides and Numerical Simulations in Biological Solid-State NMR," *Journal of Magnetic Resonance*, vol. 154, pp. 28–45, Jan. 2002.

[292] C. J. Hartzell, M. Whitfield, T. Oas, and G. Drobny, "Determination of the nitrogen-15 and carbon-13 chemical shift tensors of L-[13C]alanyl-L-[15N]alanine from the dipole-coupled powder patterns," *Journal of the American Chemical Society*, vol. 109, pp. 5966–5969, May 2002.

[293] Q. Teng and T. A. Cross, "The in situ determination of the 15N chemical-shift tensor orientation in a polypeptide," *Journal of Magnetic Resonance (1969)*, vol. 85, pp. 439–447, Dec. 1989.

[294] N. D. Lazo, W. Hu, and T. A. Cross, "Low-Temperature Solid-State 15N NMR Characterization of Polypeptide Backbone Librations," *Journal of Magnetic Resonance, Series B*, vol. 107, pp. 43–50, Apr. 1995.

[295] T. G. Oas, C. J. Hartzell, F. W. Dahlquist, and G. P. Drobny, "The amide nitrogen-15 chemical shift tensors of four peptides determined from carbon-13 dipole-coupled chemical shift powder patterns," *Journal of the American Chemical Society*, vol. 109, pp. 5962–5966, Sept. 1987.

[296] C. Aisenbrey and B. Bechinger, "Investigations of polypeptide rotational diffusion in aligned membranes by 2H and 15N solid-state NMR spectroscopy.," *Journal of the American Chemical Society*, vol. 126, pp. 16676–16683, Dec. 2004.

[297] M. Elder, P. Hitchcock, R. Mason, and G. G. Shipley, "A Refinement Analysis of the Crystallography of the Phospholipid, 1,2-Dilauroyl-DL-Phosphatidylethanolamine, and Some Remarks on Lipid-Lipid and Lipid-Protein Interactions," *Proceedings of the Royal Society of London A: Mathematical, Physical and Engineering Sciences*, vol. 354, pp. 157–170, May 1977.

[298] J. F. Nagle and S. Tristram-Nagle, "Structure of lipid bilayers," *Biochimica et Biophysica Acta (BBA) - Reviews on Biomembranes*, vol. 1469, pp. 159–195, Nov. 2000.

[299] E. S. Salnikov, A. J. Mason, and B. Bechinger, "Membrane order perturbation in the presence of antimicrobial peptides by 2H solid-state NMR spectroscopy," *Biochimie*, vol. 91, pp. 734–743, June 2009.

[300] B. A. Lewis and D. M. Engelman, "Lipid bilayer thickness varies linearly with acyl chain length in fluid phosphatidylcholine vesicles," *Journal of molecular biology*, vol. 166, pp. 211–217, May 1983.

[301] N. Kučerka, M.-P. Nieh, and J. Katsaras, "Fluid phase lipid areas and bilayer thicknesses of commonly used phosphatidylcholines as a function of temperature," *Biochimica et Biophysica Acta (BBA) - Biomembranes*, vol. 1808, pp. 2761–2771, Nov. 2011.

[302] B. Bechinger and E. S. Salnikov, "The membrane interactions of antimicrobial peptides revealed by solid-state NMR spectroscopy," *Chemistry and physics of lipids*, vol. 165, pp. 282–301, Apr. 2012.

[303] C. Mendonça Moraes and B. Bechinger, "Peptide-related alterations of membrane-associated water: deuterium solid-state NMR investigations of phosphatidylcholine membranes at different hydration levels," *Magnetic Resonance in Chemistry*, vol. 42, pp. 155–161, Feb. 2004.

[304] M. B. Ulmschneider, M. S. P. Sansom, and A. Di Nola, "Evaluating Tilt Angles of Membrane-Associated Helices: Comparison of Computational and NMR Techniques," *Biophysical journal*, vol. 90, pp. 1650–1660, Mar. 2006.

[305] Kresten Bertelsen, Jan M Pedersen, Brian S Rasmussen, Troels Skrydstrup, N. C. Nielsen, , and T. Vosegaard, *Membrane-Bound Conformation of Peptaibols with Methyl-Deuterated α-Amino Isobutyric Acids by 2H Magic Angle Spinning Solid-State NMR Spectroscopy*, vol. 129. American Chemical Society, Nov. 2007.

[306] J. H. D. R S Prosser, "Dynamics of an integral membrane peptide: a deuterium NMR relaxation study of gramicidin.," *Biophysical journal*, vol. 66, pp. 1429–1440, May 1994.

[307] Z. Song, F. A. Kovacs, J. Wang, J. K. Denny, S. C. Shekar, J. R. Quine, and T. A. Cross, "Transmembrane Domain of M2 Protein from Influenza A Virus Studied by Solid-State 15N Polarization Inversion Spin Exchange at Magic Angle NMR," *Biophysical journal*,

vol. 79, pp. 767–775, Aug. 2000.

[308] A. Ramamoorthy, F. M. Marassi, M. Zasloff, and S. J. Opella, "Three-dimensional solid-state NMR spectroscopy of a peptide oriented in membrane bilayers," *Journal of biomolecular NMR*, vol. 6, no. 3, pp. 329–334, 1995.

[309] L. Thøgersen, B. Schiøtt, T. Vosegaard, N. C. Nielsen, and E. Tajkhorshid, "Peptide Aggregation and Pore Formation in a Lipid Bilayer: A Combined Coarse-Grained and All Atom Molecular Dynamics Study," *Biophysical journal*, vol. 95, pp. 4337–4347, Nov. 2008.

[310] J.-H. Sachse, M. D. King, and D. Marsh, "ESR determination of lipid translational diffusion coefficients at low spin-label concentrations in biological membranes, using exchange broadening, exchange narrowing, and dipole-dipole interactions," *Journal of Magnetic Resonance (1969)*, vol. 71, pp. 385–404, Feb. 1987.

[311] M. D. King, J.-H. Sachse, and D. Marsh, "Unconstrained optimization method for interpreting the concentration and temperature dependence of the linewidths of interacting nitroxide spin labels. Application to the measurement of translational diffusion coefficients of spin-labeled phospholipids in membranes," *Journal of Magnetic Resonance (1969)*, vol. 72, pp. 257–267, Apr. 1987.

[312] T. C. Squier, J. E. Mahaney, J. J. Yin, C. S. Lai, and J. R. Lakowicz, "Resolution of phospholipid conformational heterogeneity in model membranes by spin-label EPR and frequency-domain fluorescence spectroscopy.," *Biophysical journal*, vol. 59, pp. 654–669, Mar. 1991.

[313] B. Bechinger, "Insights into the mechanisms of action of host defence peptides from biophysical and structural investigations," *Journal of Peptide Science*, vol. 17, pp. 306–314, Feb. 2011.

[314] M. N. Melo and M. A. R. B. Castanho, "Omiganan interaction with bacterial membranes and cell wall models. Assigning a biological role to saturation," *Biochimica et Biophysica Acta (BBA) - Biomembranes*, vol. 1768, pp. 1277–1290, May 2007.

[315] G. G. Perron, M. Zasloff, and G. Bell, "Experimental evolution of resistance to an antimicrobial peptide," *Proceedings of the Royal Society of London B: Biological Sciences*, vol. 273, pp. 251–256, Jan. 2006.

[316] E. Strandberg, D. Tiltak, S. Ehni, P. Wadhwani, and A. S. Ulrich, "Lipid shape is a key factor for membrane interactions of amphipathic helical peptides," *Biochimica et Biophysica Acta (BBA) - Biomembranes*, vol. 1818, pp. 1764–1776, July 2012.

[317] B. Bechinger and K. Lohner, "Detergent-like actions of linear amphipathic cationic antimicrobial peptides.," *Biochimica et biophysica acta*, vol. 1758, pp. 1529–1539, Sept. 2006.

[318] A. J. Mason, I. N. H. Chotimah, P. Bertani, and B. Bechinger, "A spectroscopic study of the membrane interaction of the antimicrobial peptide Pleurocidin.," *Molecular membrane biology*, vol. 23, pp. 185–194, Mar. 2006.

[319] R. M. Epand and R. F. Epand, "Lipid domains in bacterial membranes and the action of antimicrobial agents," *Biochimica et Biophysica Acta (BBA) - Biomembranes*, vol. 1788, pp. 289–294, Jan. 2009.

[320] A. Mecke, D.-K. Lee, A. Ramamoorthy, B. G. Orr, and M. M. Banaszak Holl, "Membrane Thinning Due to Antimicrobial Peptide Binding: An Atomic Force Microscopy Study of MSI-78 in Lipid Bilayers," *Biophysical journal*, vol. 89, pp. 4043–4050, Dec. 2005.

[321] F. Jean-François, S. Castano, B. Desbat, B. Odaert, M. Roux, M.-H. Metz-Boutigue, and E. J. Dufourc, "Aggregation of Cateslytin β-Sheets on Negatively Charged Lipids Promotes Rigid Membrane Domains. A New Mode of Action for Antimicrobial Peptides?†," *Biochemistry*, vol. 47, pp. 6394–6402, May 2008.

[322] A. J. Mason, A. Martinez, C. Glaubitz, O. Danos, A. Kichler, and B. Bechinger, "The antibiotic and DNA-transfecting peptide LAH4 selectively associates with, and disorders, anionic lipids in mixed membranes.," *FASEB journal : official publication of the Federation of American Societies for Experimental Biology*, vol. 20, pp. 320–322, Feb. 2006.

[323] O. K. Abou-Zied, A. Barbour, N. A. Al-Sharji, and K. Philip, "Elucidating the mechanism of peptide interaction with membranes using the intrinsic fluorescence of tryptophan: perpendicular penetration of cecropin B-like peptides into Pseudomonas aeruginosa," *RSC Advances*, vol. 5, no. 19, pp. 14214–14220, 2015.

[324] S. Gruenheid and H. Le Moual, "Resistance to antimicrobial peptides in Gram-negative bacteria," *FEMS microbiology letters*, vol. 330, pp. 81–89, May 2012.

[325] A. Pyne, M.-P. Pfeil, I. Bennett, J. Ravi, P. Iavicoli, B. Lamarre, A. Roethke, S. Ray, H. Jiang, A. Bella, B. Reisinger, D. Yin, B. Little, J. C. Muñoz-García, E. Cerasoli, P. J. Judge, N. Faruqui, L. Calzolai, A. Henrion, G. J. Martyna, C. R. M. Grovenor, J. Crain, B. W. Hoogenboom, A. Watts, and M. G. Ryadnov, "Engineering monolayer poration for rapid exfoliation of microbial membranes," *Chemical Science*, 2016.

[326] M.-T. Lee, T.-L. Sun, W.-C. Hung, and H. W. Huang, "Process of inducing pores in membranes by melittin.," *Proceedings of the National Academy of Sciences of the United States of America*, vol. 110, pp. 14243–14248, Aug. 2013.

[327] N. N. Gosvami, E. Parsons, C. Marcovich, M. L. Berkowitz, B. W. Hoogenboom, and S. Perkin, "Resolving the structure of a model hydrophobic surface: DODAB monolayers on mica," *RSC Advances*, vol. 2, pp. 4181–4188, May 2012.

[328] A. M. Di Bisceglie, "Hepatitis C and hepatocellular carcinoma," *Hepatology (Baltimore, Md.)*, vol. 26, pp. 34S–38S, Dec. 1997.

[329] P. L. Yang, M. Gao, K. Lin, Q. Liu, and V. A. Villareal, "Anti-HCV drugs in the pipeline," *Current opinion in virology*, vol. 1, pp. 607–616, Dec. 2011.

[330] H. Polenakovik, "New Therapies for Hepatitis C Virus.," *Prilozi (Makedonska akademija na naukite i umetnostite. Oddelenie za medicinski nauki)*, vol. 36, no. 2, pp. 119–132, 2015.

[331] B. R. Edlin, "Access to treatment for hepatitis C virus infection: time to put patients first," *The Lancet Infectious Diseases*, vol. 16, pp. e196–e201, Sept. 2016.

[332] N. Zitzmann, A. S. Mehta, S. Carrouée, T. D. Butters, F. M. Platt, J. McCauley, B. S. Blumberg, R. A. Dwek, and T. M. Block, "Imino sugars inhibit the formation and secretion of bovine viral diarrhea virus, a pestivirus model of hepatitis C virus: implications for the development of broad spectrum anti-hepatitis virus agents.," *Proceedings of the National Academy of Sciences*, vol. 96, pp. 11878–11882, Oct. 1999.

[333] J. R. Peterson, A. Ora, P. N. Van, and A. Helenius, "Transient, lectin-like association of calreticulin with folding intermediates of cellular and viral glycoproteins.," *Molecular Biology of the Cell*, vol. 6, pp. 1173–1184, Sept. 1995.

[334] D. Durantel, N. Branza-Nichita, S. Carrouée-Durantel, T. D. Butters, R. A. Dwek, and N. Zitzmann, "Study of the mechanism of antiviral action of iminosugar derivatives against bovine viral diarrhea virus.," *Journal of virology*, vol. 75, pp. 8987–8998, Oct. 2001.

[335] S.-F. Wu, C.-J. Lee, C.-L. Liao, R. A. Dwek, N. Zitzmann, and Y.-L. Lin, "Antiviral effects of an iminosugar derivative on flavivirus infections.," *Journal of virology*, vol. 76, pp. 3596–3604, Apr. 2002.

[336] T. Harada, N. Tautz, and H. J. Thiel, "E2-p7 region of the bovine viral diarrhea virus polyprotein: processing and functional studies.," *Journal of virology*, vol. 74, pp. 9498–9506, Oct. 2000.

[337] I. C. Bollen and J. A. Higgins, "Phospholipid asymmetry in rough- and smooth-endoplasmic-reticulum membranes of untreated and phenobarbital-treated rat liver," *The Biochemical journal*, vol. 189, pp. 475–480, Sept. 1980.

[338] S. C. Davison and E. D. Wills, "Studies on the lipid composition of the rat liver endoplasmic reticulum after induction with phenobarbitone and 20-methylcholanthrene," *The Biochemical journal*, vol. 140, pp. 461–468, June 1974.

[339] A. Watts and T. W. Poile, "Direct determination by 2H-NMR of the ionization state of phospholipids and of a local anaesthetic at the membrane surface," *Biochimica et Biophysica Acta (BBA) - Biomembranes*, vol. 861, pp. 368–372, 1986.

[340] A. Watts, "Magnetic Resonance Studies of Lipid-Protein Interfaces and Lipophilic Molecule Partitioning," *Annals of the New York Academy of Sciences*, vol. 625, pp. 653–666, June 1991.

[341] A. W. A S Ulrich, "Molecular response of the lipid headgroup to bilayer hydration monitored by 2H-NMR.," *Biophysical journal*, vol. 66, pp. 1441–1449, May 1994.

[342] J. Seelig, P. M. MacDonald, and P. G. Scherer, "Phospholipid head groups as sensors of electric charge in membranes," *Biochemistry*, vol. 26, pp. 7535–7541, Dec. 1987.

[343] M. F. Brown and J. Seelig, "Ion-induced changes in head group conformation of lecithin bilayers," *Nature*, vol. 269, no. 5630, pp. 721–723, 1977.

[344] H. Akutsu and J. Seelig, "Interaction of metal ions with phosphatidylcholine bilayer membranes," *Biochemistry*, vol. 20, pp. 7366–7373, Dec. 1981.

[345] M. Roux, J. M. Neumann, M. Bloom, and P. F. Devaux, "2H and 31P NMR

study of pentalysine interaction with headgroup deuterated phosphatidylcholine and phosphatidylserine," *European biophysics journal : EBJ*, vol. 16, no. 5, pp. 267–273, 1988.
[346] T. J. T. Pinheiro, A. A. Duralski, and A. Watts, "Phospholipid Headgroup-Headgroup Electrostatic Interactions in Mixed Bilayers of Cardiolipin with Phosphatidylcholines Studied by 2H NMR," *Biochemistry*, vol. 33, pp. 4896–4902, Apr. 1994.
[347] F. Sixl and A. Watts, "Headgroup interactions in mixed phospholipid bilayers.," *Proceedings of the National Academy of Sciences*, vol. 80, pp. 1613–1615, Mar. 1983.
[348] M.-A. Sani, D. K. Weber, F. Delaglio, F. Separovic, and J. D. Gehman, "A practical implementation of de-Pake-ing via weighted Fourier transformation.," *PeerJ*, vol. 1, p. e30, 2013.
[349] T. D. Butters, L. A. G. M. van den Broek, G. W. J. Fleet, T. M. Krulle, M. R. Wormald, R. A. Dwek, and F. M. Platt, "Molecular requirements of imino sugars for the selective control of N-linked glycosylation and glycosphingolipid biosynthesis," *Tetrahedron: Asymmetry*, vol. 11, pp. 113–124, Jan. 2000.
[350] L. Panicker, V. Sugandhi, and K. P. Mishra, "Interaction of keratolytic drug, salicylic acid with dipalmitoyl phosphatidylethanolamine vesicles," *Phase Transitions*, vol. 81, pp. 361–378, Apr. 2008.
[351] L. Panicker and K. P. Mishra, "Nuclear magnetic resonance and thermal studies on the interaction between salicylic acid and model membranes," *Biophysical chemistry*, vol. 120, pp. 15–23, Mar. 2006.
[352] A. Marczak, A. Kowalczyk, A. Wrzesienkus, T. Robak, and Z. Jozwiak, "Interaction of doxorubicin and idarubicin with red blood cells from acute myeloid leukaemia patients," *Cell Biology International*, vol. 30, pp. 127–132, Feb. 2006.
[353] F. Lindström, P. T. F. Williamson, and G. Gröbner, "Molecular insight into the electrostatic membrane surface potential by 14n/31p MAS NMR spectroscopy: nociceptin-lipid association.," *Journal of the American Chemical Society*, vol. 127, pp. 6610–6616, May 2005.
[354] J. Ma, L. Domicevica, J. R. Schnell, and P. C. Biggin, "Position and orientational preferences of drug-like compounds in lipid membranes: a computational and NMR approach.," *Physical chemistry chemical physics : PCCP*, vol. 17, pp. 19766–19776, Aug. 2015.
[355] A. A. Bothner-By, R. L. Stephens, J. Lee, C. D. Warren, and R. W. Jeanloz, "Structure determination of a tetrasaccharide: transient nuclear Overhauser effects in the rotating frame," *Journal of the American Chemical Society*, vol. 106, pp. 811–813, May 1984.
[356] G. A. Cook and S. J. Opella, "Secondary structure, dynamics, and architecture of the p7 membrane protein from hepatitis C virus by NMR spectroscopy," *Biochimica et Biophysica Acta (BBA) - Biomembranes*, vol. 1808, pp. 1448–1453, June 2011.
[357] S. Carrère-Kremer, C. Montpellier-Pala, L. Cocquerel, C. Wychowski, F. Penin, and J. Dubuisson, "Subcellular localization and topology of the p7 polypeptide of hepatitis C virus.," *Journal of virology*, vol. 76, pp. 3720–3730, Apr. 2002.
[358] G. A. Cook and S. J. Opella, "NMR studies of p7 protein from hepatitis C virus.," *European biophysics journal : EBJ*, vol. 39, pp. 1097–1104, June 2010.
[359] S. J. Opella, "Relating structure and function of viral membrane-spanning miniproteins.," *Current opinion in virology*, vol. 12, pp. 121–125, June 2015.
[360] T. A. Cross, D. T. Murray, and A. Watts, "Helical membrane protein conformations and their environment," *European biophysics journal : EBJ*, vol. 42, no. 10, pp. 731–755, 2013.
[361] D. E. Chandler, F. Penin, K. Schulten, and C. Chipot, "The p7 Protein of Hepatitis C Virus Forms Structurally Plastic, Minimalist Ion Channels," *PLoS Comput Biol*, vol. 8, p. e1002702, Sept. 2012.
[362] M. M. Kalita, S. Griffin, J. J. Chou, and W. B. Fischer, "Genotype-specific differences in structural features of hepatitis C virus (HCV) p7 membrane protein," *Biochimica et Biophysica Acta (BBA) - Biomembranes*, vol. 1848, pp. 1383–1392, June 2015.
[363] N. Holzmann, C. Chipot, F. Penin, and F. Dehez, "Assessing the physiological relevance of alternate architectures of the p7 protein of hepatitis C virus in different environments," *Bioorganic & Medicinal Chemistry*, July 2016.
[364] A. A. De Angelis and S. J. Opella, "Bicelle samples for solid-state NMR of membrane proteins," *Nature protocols*, vol. 2, pp. 2332–2338, Oct. 2007.
[365] S. H. Park, S. Berkamp, G. A. Cook, M. K. Chan, and H. Viadiu, "Nanodisc vs.

Macrodisc for NMR of Membrane Proteins," 9999.
[366] N. Das, D. T. Murray, and T. A. Cross, "Lipid bilayer preparations of membrane proteins for oriented and magic-angle spinning solid-state NMR samples," *Nature protocols*, vol. 8, pp. 2256–2270, Nov. 2013.
[367] A. Ramamoorthy, C. H. Wu, and S. J. Opella, "Experimental Aspects of Multidimensional Solid-State NMR Correlation Spectroscopy," *Journal of Magnetic Resonance*, vol. 140, pp. 131–140, Sept. 1999.
[368] C. H. Wu, A. Ramamoorthy, and S. J. Opella, "High-Resolution Heteronuclear Dipolar Solid-State NMR Spectroscopy," *Journal of Magnetic Resonance, Series A*, vol. 109, pp. 270–272, Aug. 1994.
[369] S. Jayanthi, N. Sinha, and K. V. Ramanathan, "24-SEMA as a sensitive and offset compensated SLF sequence," *Journal of Magnetic Resonance*, vol. 207, pp. 206–212, Dec. 2010.
[370] R. Fu, C. Tian, H. Kim, S. A. Smith, and T. A. Cross, "The effect of Hartmann–Hahn mismatching on polarization inversion spin exchange at the magic angle," *Journal of Magnetic Resonance*, vol. 159, pp. 167–174, Dec. 2002.
[371] A. A. Nevzorov and S. J. Opella, "A "Magic Sandwich" pulse sequence with reduced offset dependence for high-resolution separated local field spectroscopy," *Journal of Magnetic Resonance*, vol. 164, pp. 182–186, Sept. 2003.
[372] G. A. Cook, S. Stefer, and S. J. Opella, "Expression and purification of the membrane protein p7 from hepatitis C virus," *Biopolymers*, vol. 96, pp. 32–40, Jan. 2011.
[373] E. Racker, T. F. Chien, and A. Kandrach, "A cholate-dilution procedure for the reconstitution of the Ca++ pump, 32Pi—ATP exchange, and oxidative phosphorylation," *FEBS letters*, vol. 57, pp. 14–18, Sept. 1975.
[374] E. Racker, B. Violand, S. O'neal, M. Alfonzo, and J. Telford, "Reconstitution, a way of biochemical research; some new approaches to membrane-bound enzymes," *Archives of Biochemistry and Biophysics*, vol. 198, pp. 470–477, Dec. 1979.
[375] H. W. Rémigy, D. Caujolle-Bert, K. Suda, A. Schenk, M. Chami, and A. Engel, "Membrane protein reconstitution and crystallization by controlled dilution," *FEBS letters*, vol. 555, pp. 160–169, Nov. 2003.
[376] J. H. Kleinschmidt, *Lipid-Protein Interactions*, vol. 974 of *Methods and Protocols*. Totowa, NJ: Humana Press, Feb. 2013.
[377] M. Kamihira, T. Vosegaard, A. J. Mason, S. K. Straus, N. C. Nielsen, and A. Watts, "Structural and orientational constraints of bacteriorhodopsin in purple membranes determined by oriented-sample solid-state NMR spectroscopy," *Journal of Structural Biology*, vol. 149, pp. 7–16, Jan. 2005.
[378] M. B. William Dowhan, "Lipid-Dependent Membrane Protein Topogenesis," *Annual review of biochemistry*, vol. 78, no. 1, pp. 515–540, 2009.
[379] J. Radoicic, G. J. Lu, and S. J. Opella, "NMR structures of membrane proteins in phospholipid bilayers.," *Quarterly reviews of biophysics*, vol. 47, pp. 249–283, Aug. 2014.
[380] M. A. Scull, W. M. Schneider, B. R. Flatley, R. Hayden, C. Fung, C. T. Jones, M. van de Belt, F. Penin, and C. M. Rice, "The N-terminal Helical Region of the Hepatitis C Virus p7 Ion Channel Protein Is Critical for Infectious Virus Production," *PLoS pathogens*, vol. 11, p. e1005297, Nov. 2015.
[381] L. A. Dawson, "The NMR Structure and Oligomerization State of the Membrane Associated p7 Protein from Hepatitis C Virus," Jan. 2015.
[382] V. Madan and R. Bartenschlager, "Structural and Functional Properties of the Hepatitis C Virus p7 Viroporin," *Viruses*, vol. 7, pp. 4461–4481, Aug. 2015.
[383] H. Gouklani, C. Beyer, H. Drummer, E. J. Gowans, H. J. Netter, and G. Haqshenas, "Identification of specific regions in hepatitis C virus core, NS2 and NS5A that genetically interact with p7 and co-ordinate infectious virus production," *Journal of viral hepatitis*, vol. 20, pp. e66–e71, Apr. 2013.
[384] S. Griffin, D. Clarke, C. McCormick, D. Rowlands, and M. Harris, "Signal peptide cleavage and internal targeting signals direct the hepatitis C virus p7 protein to distinct intracellular membranes.," *Journal of virology*, vol. 79, pp. 15525–15536, Dec. 2005.
[385] G. Haqshenas, J. M. Mackenzie, X. Dong, and E. J. Gowans, "Hepatitis C virus p7 protein is localized in the endoplasmic reticulum when it is encoded by a replication-competent genome," *The Journal of general virology*, vol. 88, pp. 134–142, Jan. 2007.
[386] I. H. Stein, V. Schüller, P. Böhm, P. Tinnefeld, and T. Liedl, "Single-Molecule FRET

Ruler Based on Rigid DNA Origami Blocks," *ChemPhysChem*, vol. 12, pp. 689–695, Feb. 2011.
[387] K. Kawano, Y. Yano, K. Omae, S. Matsuzaki, and K. Matsuzaki, "Stoichiometric Analysis of Oligomerization of Membrane Proteins on Living Cells Using Coiled-Coil Labeling and Spectral Imaging," *Analytical Chemistry*, vol. 85, pp. 3454–3461, Mar. 2013.
[388] B. H. Meyer, J.-M. Segura, K. L. Martinez, R. Hovius, N. George, K. Johnsson, and H. Vogel, "FRET imaging reveals that functional neurokinin-1 receptors are monomeric and reside in membrane microdomains of live cells.," *Proceedings of the National Academy of Sciences*, vol. 103, pp. 2138–2143, Feb. 2006.
[389] B. D. Adair and D. M. Engelman, "Glycophorin A Helical Transmembrane Domains Dimerize in Phospholipid Bilayers: A Resonance Energy Transfer Study," *Biochemistry*, vol. 33, pp. 5539–5544, May 1994.
[390] K. Kawano, Y. Yano, and K. Matsuzaki, "A Dimer Is the Minimal Proton-Conducting Unit of the Influenza A Virus M2 Channel," *Journal of molecular biology*, vol. 426, pp. 2679–2691, July 2014.
[391] A. Giannoulis, R. Ward, E. Branigan, J. H. Naismith, and B. E. Bode, "PELDOR in rotationally symmetric homo-oligomers.," *Molecular physics*, vol. 111, pp. 2845–2854, Oct. 2013.
[392] G. Jeschke, M. Sajid, M. Schulte, and A. Godt, "Three-spin correlations in double electron–electron resonance," *Physical Chemistry Chemical Physics*, vol. 11, no. 31, pp. 6580–6591, 2009.
[393] G. Jeschke, G. Panek, A. Godt, A. Bender, and H. Paulsen, "Data analysis procedures for pulse ELDOR measurements of broad distance distributions," *Applied Magnetic Resonance*, vol. 26, no. 1-2, pp. 223–244, 2004.
[394] Y.-W. Chiang, P. P. Borbat, and J. H. Freed, "Maximum entropy: A complement to Tikhonov regularization for determination of pair distance distributions by pulsed ESR," *Journal of Magnetic Resonance*, vol. 177, pp. 184–196, Dec. 2005.
[395] G. Hagelueken, W. J. Ingledew, H. Huang, B. Petrovic Stojanovska, C. Whitfield, H. ElMkami, O. Schiemann, and J. H. Naismith, "PELDOR Spectroscopy Distance Fingerprinting of the Octameric Outer-Membrane Protein Wza from Escherichia coli.," *Angewandte Chemie International Edition*, vol. 48, pp. 2904–2906, Apr. 2009.
[396] C. Pliotas, R. Ward, E. Branigan, A. Rasmussen, G. Hagelueken, H. Huang, S. S. Black, I. R. Booth, O. Schiemann, and J. H. Naismith, "Conformational state of the MscS mechanosensitive channel in solution revealed by pulsed electron-electron double resonance (PELDOR) spectroscopy.," *Proceedings of the National Academy of Sciences of the United States of America*, vol. 109, pp. E2675–82, Oct. 2012.
[397] T. von Hagens, Y. Polyhach, M. Sajid, A. Godt, and G. Jeschke, "Suppression of ghost distances in multiple-spin double electron–electron resonance," *Physical Chemistry Chemical Physics*, vol. 15, no. 16, pp. 5854–5866, 2013.
[398] B. E. Bode, D. Margraf, J. Plackmeyer, G. Dürner, T. F. Prisner, and O. Schiemann, "Counting the monomers in nanometer-sized oligomers by pulsed electron-electron double resonance.," *Journal of the American Chemical Society*, vol. 129, pp. 6736–6745, May 2007.
[399] M. Sharma, M. Yi, H. Dong, H. Qin, E. Peterson, D. D. Busath, H.-X. Zhou, and T. A. Cross, "Insight into the Mechanism of the Influenza A Proton Channel from a Structure in a Lipid Bilayer," *Science (New York, N.Y.)*, vol. 330, pp. 509–512, Oct. 2010.
[400] L. B. Andreas, M. T. Eddy, R. M. Pielak, J. Chou, and R. G. Griffin, "Magic Angle Spinning NMR Investigation of Influenza A M218−60: Support for an Allosteric Mechanism of Inhibition," *Journal of the American Chemical Society*, vol. 132, pp. 10958–10960, July 2010.
[401] E. Bordignon and Y. Polyhach, "EPR Techniques to Probe Insertion and Conformation of Spin-Labeled Proteins in Lipid Bilayers," in *Cell-Penetrating Peptides*, pp. 329–355, Totowa, NJ: Humana Press, Dec. 2012.
[402] L. Cristian, J. D. Lear, and W. F. DeGrado, "Use of thiol-disulfide equilibria to measure the energetics of assembly of transmembrane helices in phospholipid bilayers.," *Proceedings of the National Academy of Sciences*, vol. 100, pp. 14772–14777, Dec. 2003.
[403] B. A. Lewis and D. M. Engelman, "Bacteriorhodopsin remains dispersed in fluid phospholipid bilayers over a wide range of bilayer thicknesses," *Journal of molecular biology*, vol. 166, pp. 203–210, May 1983.

[404] V. Raicu and A. Popescu, *Integrated Molecular and Cellular Biophysics*. Dordrecht: Springer Science & Business Media, June 2008.
[405] Y. Polyhach, E. Bordignon, and G. Jeschke, "Rotamer libraries of spin labelled cysteines for protein studies.," *Physical chemistry chemical physics : PCCP*, vol. 13, pp. 2356–2366, Feb. 2011.
[406] G. A. Cook, H. Zhang, S. H. Park, Y. Wang, and S. J. Opella, "Comparative NMR studies demonstrate profound differences between two viroporins: p7 of HCV and Vpu of HIV-1," *Biochimica et Biophysica Acta (BBA) - Biomembranes*, vol. 1808, pp. 554–560, Feb. 2011.
[407] A. Doll, M. Qi, N. Wili, S. Pribitzer, A. Godt, and G. Jeschke, "Gd(III)–Gd(III) distance measurements with chirp pump pulses," *Journal of Magnetic Resonance*, vol. 259, pp. 153–162, Oct. 2015.
[408] Arnold M Raitsimring, Chidambaram Gunanathan, Alexey Potapov, Irena Efremenko, Jan M L Martin, D. Milstein, , and Daniella Goldfarb, *Gd3+ Complexes as Potential Spin Labels for High Field Pulsed EPR Distance Measurements*, vol. 129. American Chemical Society, Oct. 2007.
[409] E. Matalon, T. Huber, G. Hagelueken, B. Graham, V. Frydman, A. Feintuch, G. Otting, and D. Goldfarb, "Gadolinium(III) Spin Labels for High-Sensitivity Distance Measurements in Transmembrane Helices," *Angewandte Chemie International Edition*, vol. 52, pp. 11831–11834, Nov. 2013.
[410] A. Feintuch, G. Otting, and D. Goldfarb, "Gd3+ Spin Labeling for Measuring Distances in Biomacromolecules," in *Electron Paramagnetic Resonance Investigations of Biological Systems by Using Spin Labels, Spin Probes, and Intrinsic Metal Ions, Part A*, pp. 415–457, Elsevier, 2015.
[411] D. T. Edwards, T. Huber, S. Hussain, K. M. Stone, M. Kinnebrew, I. Kaminker, E. Matalon, M. S. Sherwin, D. Goldfarb, and S. Han, "Determining the Oligomeric Structure of Proteorhodopsin by Gd3+-Based Pulsed Dipolar Spectroscopy of Multiple Distances," *Structure (London, England : 1993)*, vol. 22, pp. 1677–1686, Nov. 2014.
[412] G. Patargias, N. Zitzmann, R. Dwek, and W. B. Fischer, "Protein−Protein Interactions: Modeling the Hepatitis C Virus Ion Channel p7," *Journal of Medicinal Chemistry*, vol. 49, pp. 648–655, Jan. 2006.
[413] T. L. Foster, M. Verow, A. L. Wozniak, M. J. Bentham, J. Thompson, E. Atkins, S. A. Weinman, C. Fishwick, R. Foster, M. Harris, and S. Griffin, "Resistance mutations define specific antiviral effects for inhibitors of the hepatitis C virus p7 ion channel," *Hepatology (Baltimore, Md.)*, vol. 54, pp. 79–90, July 2011.
[414] L. J. Holsinger and R. Alams, "Influenza virus M2 integral membrane protein is a homotetramer stabilized by formation of disulfide bonds," *Virology*, vol. 183, pp. 32–43, July 1991.
[415] S. D. C. Griffin, R. Harvey, D. S. Clarke, W. S. Barclay, M. Harris, and D. J. Rowlands, "A conserved basic loop in hepatitis C virus p7 protein is required for amantadine-sensitive ion channel activity in mammalian cells but is dispensable for localization to mitochondria," *The Journal of general virology*, vol. 85, pp. 451–461, Feb. 2004.
[416] H.-X. Zhou and T. A. Cross, "Modeling the membrane environment has implications for membrane protein structure and function: Influenza A M2 protein," *Protein Science*, vol. 22, pp. 381–394, Apr. 2013.
[417] N. Grigorieff, T. A. Ceska, K. H. Downing, J. M. Baldwin, and R. Henderson, "Electron-crystallographic Refinement of the Structure of Bacteriorhodopsin," *Journal of molecular biology*, vol. 259, pp. 393–421, June 1996.
[418] E. Glattard, E. S. Salnikov, C. Aisenbrey, and B. Bechinger, "Investigations of the synergistic enhancement of antimicrobial activity in mixtures of magainin 2 and PGLa," *Biophysical chemistry*, vol. 210, pp. 35–44, Mar. 2016.
[419] M. Ieronimo, S. Afonin, K. Koch, M. Berditsch, P. Wadhwani, and A. S. Ulrich, "19F NMR Analysis of the Antimicrobial Peptide PGLa Bound to Native Cell Membranes from Bacterial Protoplasts and Human Erythrocytes," *Journal of the American Chemical Society*, vol. 132, pp. 8822–8824, June 2010.
[420] Katsuyuki Nishimura, Sanguk Kim, L. Zhang, , and T A Cross, *The Closed State of a H+ Channel Helical Bundle Combining Precise Orientational and Distance Restraints from Solid State NMR†*, vol. 41. American Chemical Society, Oct. 2002.
[421] S. H. Park, F. M. Marassi, D. Black, and S. J. Opella, "Structure and Dynamics of the

Membrane-Bound Form of Pf1 Coat Protein: Implications of Structural Rearrangement for Virus Assembly," *Biophysical journal*, vol. 99, pp. 1465–1474, Sept. 2010.
[422] S. H. Park, B. B. Das, F. Casagrande, Y. Tian, H. J. Nothnagel, M. Chu, H. Kiefer, K. Maier, A. A. De Angelis, F. M. Marassi, and S. J. Opella, "Structure of the chemokine receptor CXCR1 in phospholipid bilayers," *Nature*, vol. 491, pp. 779–783, Nov. 2012.
[423] B. B. Das, S. H. Park, and S. J. Opella, "Membrane protein structure from rotational diffusion.," *Biochimica et biophysica acta*, vol. 1848, pp. 229–245, Jan. 2015.
[424] A. Peschel and H.-G. Sahl, "The co-evolution of host cationic antimicrobial peptides and microbial resistance," *Nature Reviews Microbiology*, vol. 4, pp. 529–536, July 2006.
[425] P. Vlieghe, V. Lisowski, J. Martinez, and M. Khrestchatisky, "Synthetic therapeutic peptides: science and market," *Drug Discovery Today*, vol. 15, pp. 40–56, Jan. 2010.
[426] A. Lehmann, "Ecallantide (DX-88), a plasma kallikrein inhibitor for the treatment of hereditary angioedema and the prevention of blood loss in on-pump cardiothoracic surgery," *Expert opinion on biological therapy*, vol. 8, pp. 1187–1199, July 2008.
[427] D. C. Birdsell and E. H. Cota-Robles, "Production and ultrastructure of lysozyme and ethylenediaminetetraacetate-lysozyme spheroplasts of Escherichia coli.," *Journal of bacteriology*, vol. 93, pp. 427–437, Jan. 1967.
[428] P. L. Gor'kov, E. Y. Chekmenev, C. Li, M. Cotten, J. J. Buffy, N. J. Traaseth, G. Veglia, and W. W. Brey, "Using low-E resonators to reduce RF heating in biological samples for static solid-state NMR up to 900MHz," *Journal of Magnetic Resonance*, vol. 185, pp. 77–93, Mar. 2007.
[429] F. Delaglio, S. Grzesiek, G. W. Vuister, G. Zhu, J. Pfeifer, and A. Bax, "NMRPipe: A multidimensional spectral processing system based on UNIX pipes," *Journal of biomolecular NMR*, vol. 6, no. 3, pp. 277–293, 1995.
[430] Y. Qi, H. I. Ingólfsson, X. Cheng, J. Lee, S. J. Marrink, and W. Im, "CHARMM-GUI Martini Maker for Coarse-Grained Simulations with the Martini Force Field," *Journal of Chemical Theory and Computation*, vol. 11, pp. 4486–4494, Aug. 2015.
[431] D. H. de Jong, G. Singh, W. F. D. Bennett, C. Arnarez, T. A. Wassenaar, L. V. Schäfer, X. Periole, D. P. Tieleman, and S. J. Marrink, "Improved Parameters for the Martini Coarse-Grained Protein Force Field," *Journal of Chemical Theory and Computation*, vol. 9, pp. 687–697, Nov. 2012.
[432] G. Jeschke, V. Chechik, P. Ionita, A. Godt, H. Zimmermann, J. Banham, C. R. Timmel, D. Hilger, and H. Jung, "DeerAnalysis2006—a comprehensive software package for analyzing pulsed ELDOR data," *Applied Magnetic Resonance*, vol. 30, no. 3-4, pp. 473–498, 2006.
[433] R. B. Merrifield, "Solid Phase Peptide Synthesis. I. The Synthesis of a Tetrapeptide," *Journal of the American Chemical Society*, vol. 85, pp. 2149–2154, July 1963.
[434] J. M. Palomo, "Solid-phase peptide synthesis: an overview focused on the preparation of biologically relevant peptides," *RSC Advances*, vol. 4, no. 62, pp. 32658–32672, 2014.
[435] I. Coin, M. Beyermann, and M. Bienert, "Solid-phase peptide synthesis: from standard procedures to the synthesis of difficult sequences," *Nature protocols*, vol. 2, pp. 3247–3256, Dec. 2007.
[436] L. A. Carpino and G. Y. Han, "9-Fluorenylmethoxycarbonyl function, a new base-sensitive amino-protecting group," *Journal of the American Chemical Society*, vol. 92, pp. 5748–5749, Sept. 1970.
[437] R. B. Merrifield, *Solid phase synthesis*. Science, 1986.
[438] R. B. Merrifield, "Solid Phase Synthesis (Nobel Lecture)," *Angewandte Chemie International Edition*, vol. 24, pp. 799–810, Oct. 1985.